Mechano-energetic uncoupling in Barth syndrome cardiomyopathy

Mechano-energetische Entkopplung bei der Barth Syndrom Kardiomyopathie

Doctoral thesis for a doctoral degree
at the Graduate School of Life Sciences,
Julius-Maximilians-Universität Würzburg,
Section Biomedicine

submitted by

Edoardo Bertero

from

Genova

Würzburg 2021

Submitted on:

…………………………………………………………….………

Office stamp

Members of the Thesis Committee

Chairperson: Prof. Dr. Georg Gasteiger

Primary Supervisor: Prof. Dr. Christoph Maack

Supervisor (Second): Prof. Dr. Stefan Frantz

Supervisor (Third): Prof. Dr. Almut Schulze

Supervisor (Fourth): Dr. Michael Kohlhaas
(If applicable)

Date of Public Defence: ……………………………………………….……

Date of Receipt of Certificates: ………………………………………...

Table of contents

Summary

This Thesis comprises four studies whose unifying theme is the role of calcium (Ca^{2+}) as a link between excitation-contraction coupling and mitochondrial oxidative metabolism in the heart - a process termed *mechano-energetic coupling* - under physiological and pathological conditions. While excess Ca^{2+} uptake inside mitochondria has catastrophic consequences for oxidative phosphorylation and causes cell death, physiological Ca^{2+} fluxes via the mitochondrial Ca^{2+} uniporter (MCU) stimulate the Krebs cycle-dependent generation of reducing equivalents that fuel both the electron transport chain and mitochondrial antioxidant systems, thereby playing an essential role for both ATP production and reactive oxygen species (ROS) elimination.

In the first study, "*Mitochondria do not survive calcium overload during transplantation",* we refuted the feasibility of mitochondria transplantation in the setting of myocardial ischemia. Mitochondria transplantation is a therapeutic approach that entails injection of autologous skeletal muscle mitochondria into the damaged myocardium after an acute ischemic event. According to the proposed mechanism of action, transplanted mitochondria should be incorporated in dysfunctional cardiac myocytes and contribute to ATP production within the host cell. However, mitochondria cannot survive the high Ca^{2+} concentration of the extracellular environment, since Ca^{2+} overload elicits opening of a large pore in the mitochondrial membranes, termed the permeability transition pore (PTP). Besides its implication for mitochondrial transplantation, this study demonstrates the destructive consequences of excess Ca^{2+} uptake via the MCU. Indeed, Ca^{2+} overload and consequent PTP opening is considered a major responsible of cardiac myocyte death in the context of ischemia/reperfusion (I/R) injury.

The subsequent study, "*CaMKII does not control mitochondrial calcium uptake in cardiac myocytes*", investigates whether the Ca^{2+}/calmodulin-dependent protein kinase II (CaMKII) modulates mitochondrial Ca^{2+} uptake. Previous studies indicate that the MCU is a target of CaMKII activity, and that upon phosphorylation, the MCU current is increased, thus promoting Ca^{2+} overload and cell death in response to I/R injury. In contrast, we did not detect any differences in mitochondrial Ca^{2+} uptake, redox state, and production of reactive oxygen species (ROS) in mice lacking both CaMKIIδ and γ, the two dominant cardiac CaMKII isoforms, specifically in the heart, and in mice lacking

the CaMKIIδ isoform in the entire organism. Therefore, CaMKII does not modulate mitochondrial Ca^{2+} uptake in the heart under physiological conditions.

The study "*Selective NADH communication from α-ketoglutarate dehydrogenase to mitochondrial transhydrogenase prevents reactive oxygen species formation under reducing conditions in the heart*" addresses the question whether the Krebs cycle enzyme α-ketoglutarate dehydrogenase (α-KGDH) is as a source or rather a sink of ROS in cardiac myocytes. On the one hand, α-KGDH contains a flavin group that might become a source of superoxide under certain conditions; on the other hand, α-KGDH regenerates the reduced form of NADH that provides reducing equivalents also to mitochondrial antioxidant systems via the nicotinamide nucleotide transhydrogenase (NNT) reaction. Our results indicate that NADH derived from α-KGDH preferentially shuttles electrons to NNT for NADPH formation rather than to the respiratory chain for ATP production and thereby, plays an important role in ROS elimination rather than being a source of superoxide in the heart.

Finally, we investigated the consequences of perturbed mitochondrial Ca^{2+} handling in the context of a rare human disease, Barth syndrome, in which the altered phospholipid composition of the inner mitochondrial membrane affects the structural organization of several protein complexes, including the MCU. In the study "*Mechano-energetic uncoupling underlies lack of contractile reserve in Barth syndrome cardiomyopathy*" we discovered that loss of the MCU in cardiac, but not skeletal muscle mitochondria hinders the Ca^{2+}-induced adaptation of mitochondrial oxidative metabolism during workload transitions. This mechano-energetic uncoupling impairs the physiological increase in contractile force during physical exercise and might predispose Barth syndrome patients to the development of arrhythmias.

Zusammenfassung

Diese Doktorarbeit umfasst vier Studien, deren verbindendes Thema die Rolle von Calcium (Ca^{2+}) als Verbindung zwischen elektromechanischer Kopplung und mitochondrialem oxidativen Metabolismus im Herzen unter physiologischen und pathologischen Bedingungen ist. Dieser Prozess wird als mechano-energetische Kopplung bezeichnet. Während eine übermäßige Ca^{2+} Aufnahme in Mitochondrien katastrophale Folgen für die oxidative Phosphorylierung hat und zum Zelltod führt, stimuliert die physiologische Ca^{2+}-Aufnahme über den mitochondrialen Ca^{2+} uniporter (MCU) die Krebs-Zyklus abhängige Erzeugung von Reduktionsäquivalenten, die sowohl die Atmungskette als auch die mitochondrialen Antioxidationssysteme antreiben, und spielt somit eine wesentliche Rolle sowohl für die ATP Produktion als auch für die Eliminierung reaktiver Sauerstoffspezies (ROS).

In der ersten Studie „*Mitochondria do not survive calcium overload during transplantation*" haben wir die Machbarkeit einer Mitochondrien-Transplantation bei Myokardischämie in Frage gestellt. Die Mitochondrien-Transplantation ist ein therapeutischer Ansatz, bei dem autologe Skelettmuskel-Mitochondrien nach einem akuten ischämischen Ereignis in das geschädigte Myokard injiziert werden. Gemäß dem vorgeschlagenen Wirkungsmechanismus sollten transplantierte Mitochondrien in dysfunktionale Herzmuskelzellen eingebaut werden und zur ATP Produktion in der Wirtszelle beitragen. Mitochondrien können jedoch die hohe Ca^{2+} Konzentration der extrazellulären Umgebung nicht überleben, da durch Ca^{2+} Überladung eine große Pore in der innere Mitochondrienmembran geöffnet wird, die sog. *permeability transition pore* (PTP). Neben ihrer Bedeutung für die mitochondriale Transplantation zeigt diese Studie die zerstörerischen Folgen einer übermäßigen Ca^{2+} Aufnahme über den MCU. In der Tat wird die Ca^{2+} Überladung und die daraus resultierende PTP-Öffnung als Hauptursache für den Tod von Herzmuskelzellen im Zusammenhang mit Ischämie/Reperfusions-Schaden angesehen.

Die nachfolgende Studie „*CaMKII does not control mitochondrial calcium uptake in cardiac myocytes*" untersucht, ob die Ca^{2+} / Calmodulin-abhängige Proteinkinase II (CaMKII) die mitochondriale Ca^{2+} Aufnahme moduliert. Frühere Studien zeigen, dass der MCU durch CaMKII reguliert wird und dass bei Phosphorylierung der MCU-Strom erhöht wird, wodurch die Ca^{2+} Überladung und der Zelltod nach kardialer Ischämie/ Reperfusion gefördert werden. Im Gegensatz dazu konnten wir bei Mäusen, denen sowohl die CaMKIIδ als auch γ, die beiden dominanten kardialen CaMKII-Isoformen,

im Herzen fehlten, keine Unterschiede in der mitochondrialen Ca^{2+} Aufnahme, dem Redoxstatus und der Produktion von reaktiven Sauerstoffspezies (ROS) feststellen. Gleiche Ergebnisse wurden bei Mäusen, denen die CaMKIIδ-Isoform im gesamten Organismus fehlten, erzielt. Daher moduliert CaMKII die mitochondriale Ca^{2+} Aufnahme im Herzen unter physiologischen Bedingungen nicht.

Die Studie „*Selective NADH communication from α-ketoglutarate dehydrogenase to mitochondrial transhydrogenase prevents reactive oxygen species formation under reducing conditions in the heart*" befasst sich mit der Frage, ob das Krebszyklus Enzym α-Ketoglutarat-Dehydrogenase (α-KGDH) als Quelle oder vielmehr als „Senke" von ROS in Herzmuskelzellen dient. Einerseits enthält die α-KGDH eine Flavin-Gruppe, die unter bestimmten Bedingungen zu einer Superoxidquelle werden kann. Andererseits regeneriert α-KGDH die reduzierte Form von NADH, die über die Nikotinamid-Nucleotid-Transhydrogenase (NNT)-Reaktion auch für mitochondriale Antioxidationssysteme reduzierende Äquivalente liefert. Unsere Ergebnisse zeigen, dass von α-KGDH abgeleitetes NADH Elektronen bevorzugt zur NADPH-Bildung zur NNT und nicht zur Atmungskette für die ATP-Produktion transportiert und somit eine wichtige Rolle bei der ROS-Eliminierung spielt, anstatt eine Quelle für Superoxid im Herzen zu sein.

Schließlich untersuchten wir die Folgen einer gestörten mitochondrialen Ca^{2+} Aufnahme im Zusammenhang mit einer seltenen Krankheit, dem Barth-Syndrom, bei der die veränderte Phospholipid-Zusammensetzung der inneren mitochondrialen Membran die strukturelle Organisation mehrerer Proteinkomplexe, einschließlich des MCU, beeinflusst. In der Studie „*Mechano-energetic uncoupling underlies lack of contractile reserve in Barth syndrome cardiomyopathy*" stellten wir fest, dass der Verlust des MCU in Herz-, aber nicht in Skelettmuskel-Mitochondrien, die Ca^{2+}-induzierte Anpassung des mitochondrialen oxidativen Metabolismus während erhöhter Herzmuskelzellbelastung behindert. Diese mechano-energetische Entkopplung beeinträchtigt den physiologischen Anstieg der Kontraktionskraft des Herzens während körperlicher Betätigung und könnte Patienten mit Barth-Syndrom für die Entwicklung von Arrhythmien prädisponieren.

Introduction

1. Mitochondrial oxidative metabolism

1.1 Chemiosmotic coupling

To maintain their high degree of organization, living organisms continuously exchange materials and energy with their surroundings. In eukaryotes, energy conversion is predominantly performed in two types of specialized organelles: chloroplasts, which occur in plants and green algae, and mitochondria, found in virtually all other eukaryotic cells. Mitochondria originated from aerobic bacteria that were engulfed by and evolved in symbiosis with one ancestral anaerobic cell. Mitochondria retain vestiges of their bacterial progenitor, including a double membrane, their own circular DNA, and a primordial protein synthesis machinery. Furthermore, mitochondria, chloroplasts, and prokaryotes share the same fundamental strategy for energy conversion, whereby electrons derived from different sources – oxidation of chemical fuels in mitochondria, pigments excited by sunlight in chloroplasts – are channelled through protein complexes comprising a series of electron acceptors of increasing reduction potential (a measure of their affinity for electrons), together denoted as the electron transport chain (ETC). With each transfer, electrons release a small amount of energy that is used to pump protons (H^+) across the membrane where the ETC complexes are embedded. The result is the generation of an electrochemical gradient that is harnessed to catalyse the phosphorylation of adenosine diphosphate (ADP) to form adenosine triphosphate (ATP) (1). This process is coined *chemiosmotic coupling*, reflecting the conversion of transmembrane gradients ("osmotic") into chemical energy, and contributes to maintain the ATP hydrolysis reaction far from its thermodynamic equilibrium, thus rendering ATP breakdown highly exergonic.

In mitochondria, the ETC consists of the three protein complexes (I, III, and IV) located in the inner membrane (IMM) (**Figure 1**). Complex I receives electrons from the reduced form of nicotine adenine dinucleotide (NADH), the major electron carrier in mitochondria, and therefore is also referred to as NADH dehydrogenase. Subsequently, electrons are shuttled via ubiquinone to complex III, which transfers them to the soluble electron carrier cytochrome *c*. In addition, succinate dehydrogenase (also known as complex II) is another integral IMM protein that feeds electrons into complex III by reducing ubiquinone; however, succinate dehydrogenase does not pump H^+ across the IMM, and therefore it is not considered to be part of the ETC. Finally, complex IV oxidizes cytochrome *c* and transfers electrons to molecular oxygen (O_2), the final electron acceptor, to form water (H_2O). Electron transfer between consecutive complexes is favoured by the association of complex I, III, and IV into large supercomplexes that are stabilized by cardiolipin, a phospholipid predominantly found in the IMM. Cardiolipin is deemed to function as a hydrophobic glue and is essential for the structural and functional organization of the ETC supercomplexes and several other macromolecular complexes embedded in the IMM (2).

While the outer mitochondrial membrane is freely permeable to ions and small molecules, the IMM is impermeable to H^+, and thereby the H^+-pumping activity of complex I, III, and IV generates the electrical ($\Delta\Psi_m$) and chemical (ΔpH) potential that constitutes the proton-motive force ($\Delta\mu_H$). The F_1-F_o ATP synthase (complex V) harnesses $\Delta\mu_H$ to catalyse ADP phosphorylation, thus completing the conversion of energy obtained from oxidation of nutrients to the phosphate bond of ATP – a process known as *oxidative phosphorylation*.

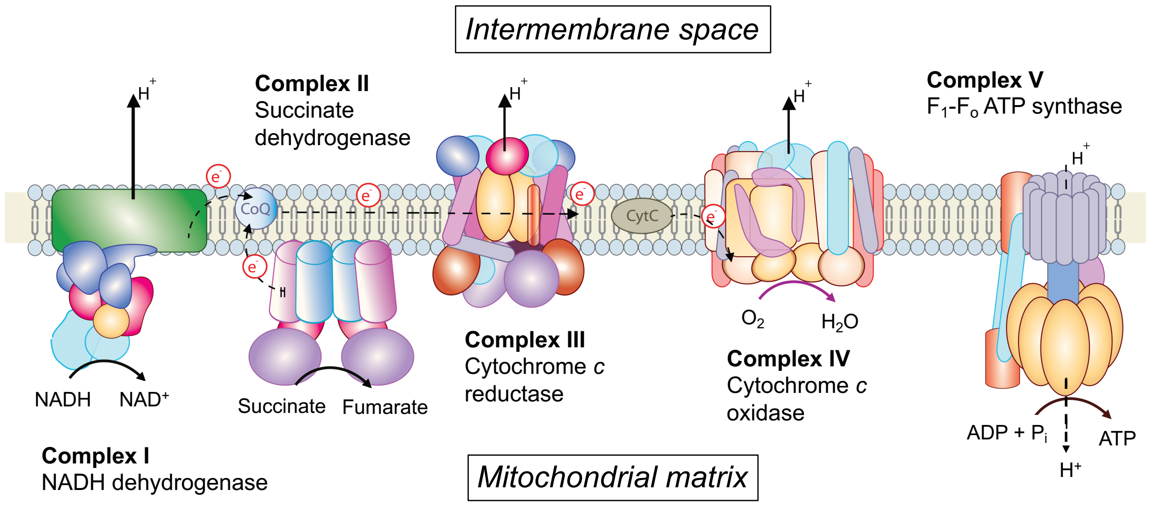

Figure 1. The mitochondrial electron transport chain. Abbreviations not used in the text: CoQ, coenzyme Q; CytC, cytochrome *c*; e^-, electron. Courtesy of Vasco Sequeira.

1.2 The Krebs cycle

The reducing equivalents that fuel oxidative phosphorylation are primarily produced by the Krebs cycle, a series of enzymatic reactions that oxidize two-carbon units in the form of acetyl-coenzyme A (acetyl-CoA) to carbon dioxide (CO_2). The Krebs cycle, also known as the tricarboxylic acid cycle or citric acid cycle, is a central hub in cellular metabolism; in fact, it is not only the final oxidative pathway for acetyl-CoA produced from oxidative decarboxylation of pyruvate, β-oxidation of fatty acids, and degradation of certain amino acids, but also a source of precursors for a wide range of molecules. To compensate for intermediates that are siphoned off the Krebs cycle, a number of *anaplerotic* reactions serve to replenish it and maintain its activity, a prominent example being the carboxylation of pyruvate to form oxaloacetate.

The Krebs cycle reactions are represented in **Figure 2**. First, acetyl-CoA is condensed with oxaloacetate to form the six-carbon compound citrate, and the latter is isomerized to isocitrate by aconitase. Subsequently, two consecutive oxidative decarboxylation reactions yield CO_2 and use the energy of this oxidation to regenerate NADH from NAD^+. Specifically, isocitrate is oxidized to α-ketoglutarate (α-KG) by isocitrate dehydrogenase, and in turn α-KG is oxidized by the α-KG dehydrogenase (α-KGDH) complex to form succinyl-CoA. Succinyl-CoA is the substrate for the only Krebs cycle reaction that yields ATP or GTP, catalysed by succinyl-CoA synthetase. The product of the latter reaction, succinate, is the electron donor for the flavin adenine dinucleotide (FAD) covalently bound to succinate dehydrogenase (complex II). The succinate dehydrogenase product fumarate is hydrated to form malate, which is oxidized to oxaloacetate in the final NADH-yielding reaction of the cycle. Altogether, one turn of the Krebs cycle results in the oxidation of one acetyl group to two CO_2 molecules, and the energy obtained from these reactions is stored in the form of three NADH, one $FADH_2$, and one ATP or GTP (**Figure 2**).

The flux through the Krebs cycle is regulated at several points. One tightly regulated step is the entry of pyruvate into the cycle, which is mediated by the oxidative decarboxylation reaction catalysed by pyruvate dehydrogenase (PDH). The activity of the PDH complex is allosterically inhibited by its products, i.e. acetyl-CoA and NADH, and by the phosphorylation state of the enzyme. In particular, phosphorylation by PDH kinase inhibits, and dephosphorylation by PDH phosphatase activates PDH. Additional points of regulation are represented by the three highly exergonic reactions of the cycle, i.e. those catalysed by citrate synthase, isocitrate dehydrogenase, and α-KGDH. Similar to PDH and to many other regulated reactions in intermediary metabolism, these three enzymes are inhibited by accumulation of their products, including NADH. Therefore, the Krebs cycle activity is primarily regulated by the availability of nutrients and the redox state of mitochondrial pyridine nucleotides. Moreover, in the skeletal and cardiac muscle of vertebrates, free matrix calcium (Ca^{2+}) is a potent activator of PDH, isocitrate dehydrogenase, and α-KGDH, thereby comprising an additional layer of regulation that is essential for the metabolic adaptation to acute increases in ATP demand. The physiological relevance of the Ca^{2+}-induced activation of the Krebs cycle is discussed in detail in **Chapter 2**.

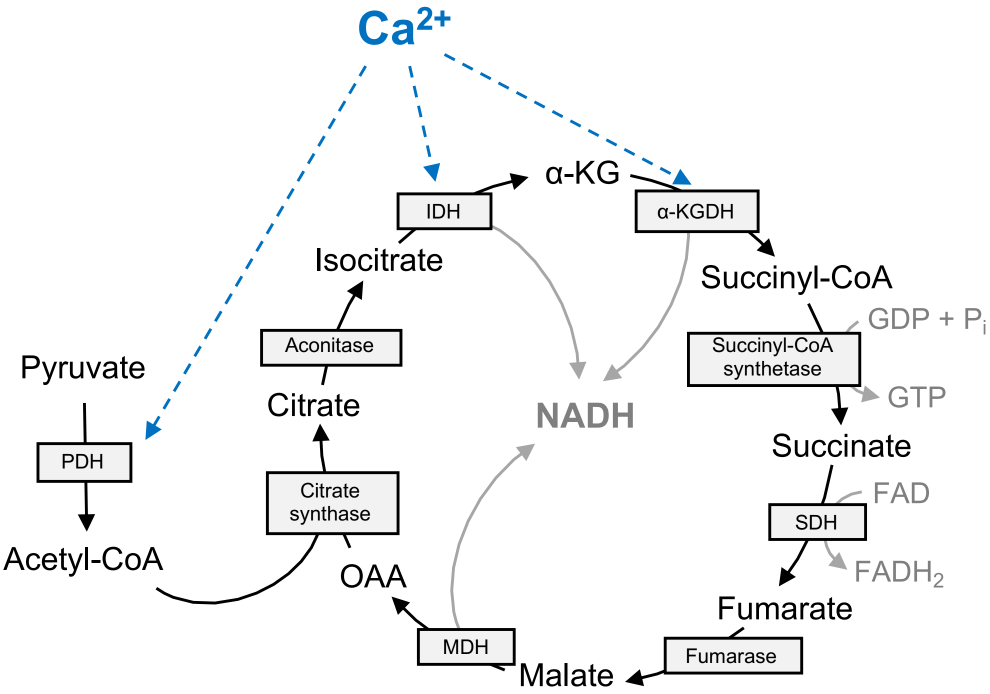

Figure 2. **The Krebs cycle.** Abbreviations not found in the text: OAA, oxaloacetate; SDH, succinate dehydrogenase.

1.3 Mitochondrial production and elimination of reactive oxygen species

The high affinity of O_2 for electrons accounts for the large amount of energy released upon its reduction to H_2O, which enables cells to harness substantially more energy from oxidative metabolism than it can be obtained from anaerobic metabolism. For the same reason, however, the electron transfer pathway can become a source of highly reactive free radicals with potentially devastating consequences on cellular lipids, proteins, and nucleic acids. In fact, O_2 can be incompletely reduced by acquiring one single electron, and the resulting superoxide radical ($O_2^{\cdot-}$) is extremely reactive and has a strong tendency to subtract three electrons to other molecules. Free radicals derived from O_2 such as superoxide and the product of its dismutation, hydrogen peroxide (H_2O_2), are collectively known as reactive oxygen species (ROS). The mitochondrial ETC, and complexes I and III in particular, is considered the major source of ROS in most mammalian cells (3).

Experiments performed in isolated mitochondria demonstrated that substantial ROS production can be observed in two conditions: (i) when the proton-motive force is maximal and the ubiquinone pool fully reduced in the absence of ADP phosphorylation, and (ii) when the matrix $NADH/NAD^+$ ratio is high (3). The latter situation favours the back up of electrons onto the flavin mononucleotide group of complex I, which can react with O_2 to form superoxide. Alternatively, a fully reduced ubiquinone pool favours superoxide production at complex I via reverse electron transport, which happens when a high proton-motive force induces (reverse) electron flow from ubiquinone to complex I. This mode of mitochondrial ROS formation is relevant in the context of ischemia and subsequent reperfusion, when succinate accumulation induced by ischemia feeds superoxide formation at complex I via reverse electron transport once O_2 becomes again available for oxidation at complex IV. This represents one major mechanism of tissue damage when the supply of O_2 and nutrients is restored after an ischemic event, a process denoted as ischemia/reperfusion injury (4). In addition to the ETC, matrix enzymes that catalyse redox reactions represent potential sources of mitochondrial ROS. Studies performed in isolated brain and skeletal muscle mitochondria indicate that the flavin group of the α-KGDH complex might become one major site of ROS formation under conditions of elevated $NADH/NAD^+$ ratio (5).

Mitochondria are protected from oxidative damage by enzymatic systems that efficiently eliminate ROS. First, superoxide is converted to H_2O_2 by the manganese-dependent superoxide dismutase (MnSOD), which is present in micromolar concentrations in the mitochondrial matrix – largely exceeding the picomolar levels of superoxide – and has the highest catalytic efficiency known in nature ($k \simeq 2 \times 10^9\ M^{-1} \times s^{-1}$). In turn, each H_2O_2 molecule is converted to two H_2O by matrix peroxidases, including peroxiredoxin (Prx) and glutathione peroxidases (Gpx). The reduction of H_2O_2 to H_2O catalysed by Prx and Gpx is coupled to the oxidation of two electron donors, thioredoxin (Trx) and glutathione (GSH), respectively, that are regenerated in their reduced (i.e., active) state by a cascade of redox reactions that depend on NADPH as a source of reducing equivalents (**Figure 3**). Catalase, another H_2O_2-eliminating enzyme that is mostly found within peroxisomes, might be present in the mitochondrial matrix in certain tissues, such as the heart (6). In contrast to Prx and Gpx, catalase decomposes H_2O_2 to H_2O and O_2, and is not in a redox couple with other proteins. Nevertheless, catalase is tightly bound to NADPH, which is required to protect the enzyme from inactivation by its substrate (7). Therefore, the redox state of the mitochondrial NADPH pool is pivotal to H_2O_2 elimination in the mitochondrial matrix.

The main sources of reduced NADPH in mitochondria are the nicotinamide nucleotide transhydrogenase (NNT), which catalyses the transfer of electrons from NADH to NADP$^+$ coupled to H$^+$ transfer from the intermembrane space to the matrix, together with isocitrate dehydrogenase type 2 (IDH2) and NADP-linked malate dehydrogenase (MEP), which use the Krebs cycle intermediates isocitrate and malate, respectively, as electron donors. Therefore, the reducing equivalents produced by the Krebs cycle are essential not only to sustain ADP phosphorylation, but also to regenerate the active forms of the H_2O_2-eliminating enzymes in the mitochondrial matrix (**Figure 3**).

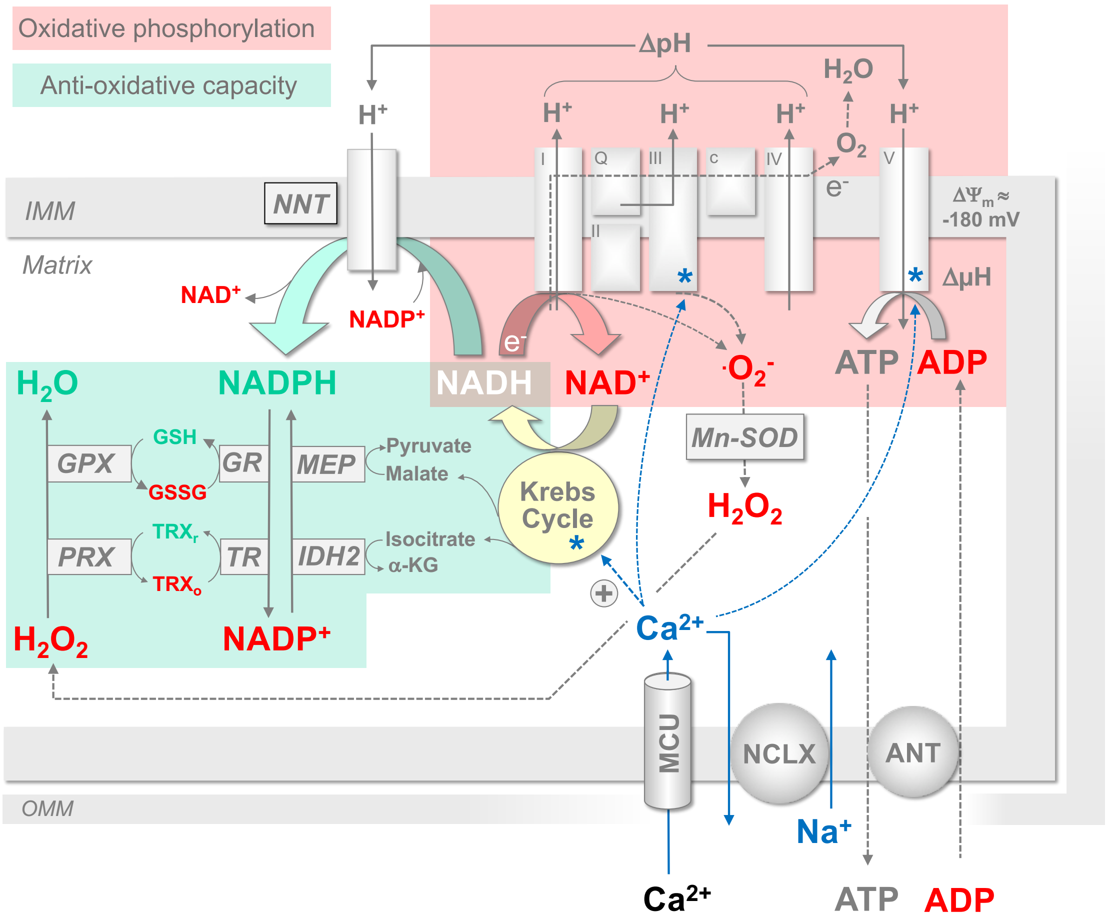

Figure 3. Mitochondrial ROS production and elimination. Stars (*) indicate the sites of Ca^{2+}-induced activation. Abbreviations not found in the text: ANT, adenine nucleotide translocator; GR, glutathione reductase; GSH and GSSG, reduced and oxidized glutathione, respectively; MCU, mitochondrial Ca^{2+} uniporter; NCLX, mitochondrial Na$^+$/Ca^{2+} exchanger; TR, thioredoxin reductase; TRX$_r$ and TRX$_o$, reduced and oxidized thioredoxin, respectively. Modified with permission from (8).

1.4 Redox-optimized ROS balance

The concept that mitochondrial ROS production is maximal under conditions of low or absent ADP phosphorylation, high proton-motive force, and high $NADH/NAD^+$ ratio is grounded in a vast body of experimental evidence. A caveat to this model is that it cannot be extrapolated to the intact cell or tissue, as it primarily reflects the mode of operation of isolated mitochondria. In fact, the NADH pool is never as reduced, and electron flow never as low in cells as it is in isolated mitochondria preparations energized with saturating amounts of substrates and in the absence of ADP – the only exceptions being perhaps hypoxia or significant damage to the ETC. When mitochondria are in their physiological context of intact cells, they operate in an intermediate redox state that maximizes ADP phosphorylation while keeping ROS production at a minimum, and oxidative stress is induced from extreme reduction or oxidation of the redox couples that govern oxidative phosphorylation (i.e., $NADH/NAD^+$) and ROS elimination ($NADPH/NADP^+$). Under conditions of extreme reduction, ROS production at the ETC outweighs mitochondrial antioxidant systems, whereas extreme oxidation depletes the reducing equivalents required to maintain these systems operational. This model, coined “redox-optimized ROS balance”, provides a conceptual framework that integrates the metabolic state of a cell with ROS production and elimination in mitochondria (9).

2. Cardiac mechano-energetic coupling

2.1 Mitochondrial oxidative metabolism in the heart

With an estimated rate of ATP turnover of ~0.5 µmol × g wet weight^{-1} × s^{-1} at rest, the heart is one of the most energy-demanding organs of the human body (10). In cardiac myocytes, the majority of ATP (60-70%) is consumed by the contractile apparatus, and the remaining 30-40% fuels ion handling in the cytosol. These intense energy requirements are covered for ~95% by oxidative phosphorylation in mitochondria (11).

In the healthy heart, ~60-90% of the acetyl-CoA that enters the Krebs cycle derives from β-oxidation of fatty acids, and ~10-40% from oxidative decarboxylation of pyruvate, which in turn is obtained in equal amounts from glycolysis and reduction of lactate (10). In addition, ketones might become an important carbon source for the heart during fasting (12) and in the diseased heart (13-15). In fact, the relative contribution of different substrates to ATP production changes dynamically in response to changes in ATP demand, substrate availability, and hormonal signalling. The ability of the heart to swiftly adapt substrate preference without consequences on cardiac function is termed *metabolic flexibility*, and is the result of a complex regulatory network that modulates the flux through metabolic pathways via allosteric modulation of enzyme activity, substrate/product availability, and regulation of gene expression (16).

Another hallmark of cardiac metabolism is the tight coupling between the rate of oxidative phosphorylation in mitochondria and ATP turnover in the cytosol. At rest, the heart operates at ~15-25% of its maximal oxidative capacity (11), which can be rapidly recruited in response to an increase in energy demand to maintain a constant ATP concentration even during elevations of cardiac workload. This process, termed *mechano-energetic coupling*, reflects the existence of a functional continuum between excitation-contraction coupling and mitochondrial oxidative metabolism in the healthy heart (8).

2.2 Cardiac excitation-contraction coupling

The term *excitation-contraction* (EC) *coupling* describes the processes linking electrical excitation to mechanical work development in the heart. EC coupling is initiated by the propagation of an action potential across the myocardium, which triggers the opening of the voltage-gated L-type Ca^{2+} channels on the sarcolemma of cardiac myocytes. The resulting inward Ca^{2+} current (I_{Ca}) induces Ca^{2+} release from the sarcoplasmic reticulum (SR) via the ryanodine receptor type 2 (RyR2), leading to a transient increase in cytosolic Ca^{2+} ($[Ca^{2+}]_c$) (17). This *Ca^{2+}-induced Ca^{2+} release* is favoured by the spatial proximity between the T tubules, invaginations of the sarcolemma where L-type Ca^{2+} channels are located, and RyR2 channels found on the subsarcolemmal cisternae of the SR. In human ventricular myocytes, Ca^{2+} influx via I_{Ca} accounts for ~30% of the increase in $[Ca^{2+}]_c$ during an action potential, while the remaining ~70% derives from the SR. In the cytosol, Ca^{2+} ignites the contractile machinery by binding to troponin C, which induces a conformational change in tropomyosin and thereby enables the interaction of the myosin head with actin. The actin and myosin filaments slide over each other as the myosin head extends, pulling together the two ends of a sarcomere. Due to the strong myofilament cooperativity with respect to $[Ca^{2+}]_c$, the force developed is related to $[Ca^{2+}]_c$ in a non-linear manner (17).

The rise in $[Ca^{2+}]_c$ that triggers contraction ultimately also induces I_{Ca} inactivation, which stops Ca^{2+} influx via L-type Ca^{2+} channels and thereby, also Ca^{2+} release from the SR. Consequently, $[Ca^{2+}]_c$ starts to decline as Ca^{2+} is removed from the cytosol by the SR Ca^{2+} ATPase (SERCA), which takes Ca^{2+} back into the SR, and the sarcolemmal Na^+/Ca^{2+} exchanger (NCX), which extrudes Ca^{2+} to the extracellular space in exchange for 3 Na^+ ions. Because "Ca^{2+} influx must match efflux" (a phrase made famous by David Eisner) during steady-state cardiac function, SERCA and NCX contribute to Ca^{2+} removal from the cytosol to the same extent that Ca^{2+} release from the SR and influx via I_{Ca}, respectively, contribute to the increase in $[Ca^{2+}]_c$ (18). Additionally, the sarcolemmal Ca^{2+} ATPase contributes to Ca^{2+} removal, although to a minimal extent. Finally, while it has been suggested that also mitochondria remove Ca^{2+} from the cytosol during diastole (17), the prevailing view is that mitochondrial accumulate Ca^{2+} via the uniporter (MCU) during systole and release it during diastole (8). Anyway, mitochondrial Ca^{2+} fluxes are relatively small compared to those of SERCA and the NCX, and thus likely inconsequential for cytosolic Ca^{2+} dynamics, but are pivotal to the metabolic adaptation to elevations of cardiac workload, as outlined in detail below (8).

2.3 Cardiac mechano-energetic coupling

During physical exercise, the heart is capable of increasing its output of blood by 4- to 6-fold in a matter of seconds. Sympathetic nervous system activation is a key driver of this adaptation: stimulation of β-adrenergic receptors (β-AR) increases heart rate, enhances contractile force, and accelerates relaxation – termed positive chronotropic, inotropic, and lusitropic effects, respectively – primarily by inducing phosphorylation of key target proteins via protein kinase A (PKA). Mechanistically, β-AR stimulation activates a GTP-binding protein that induces cyclic adenosine monophosphate (cAMP) production by adenylate kinase. Upon binding cAMP, PKA phosphorylates L-type Ca^{2+} and RyR2 channels, thereby increasing I_{Ca} and Ca^{2+} release from the SR, respectively, and phospholamban, which relieves its inhibition on SERCA. Consequently, the amplitude of $[Ca^{2+}]_c$ transients is increased, and Ca^{2+} reuptake in the SR is accelerated. The combination of increased Ca^{2+} influx from the extracellular space and faster SERCA-mediated Ca^{2+} reuptake results in an increase in the SR Ca^{2+} content, which together with the increase in I_{Ca} contributes to the positive inotropic effect of β-AR activation. Furthermore, PKA phosphorylates sarcomeric proteins, namely troponin I and myosin binding protein C, with the result of decreasing the affinity of the myofilaments for Ca^{2+}. Although the faster dissociation of Ca^{2+} from the myofilaments contributes to accelerate cytosolic Ca^{2+} removal, phospholamban phosphorylation is considered by far the most important driver of the lusitropic effect associated with β-adrenergic stimulation (19).

The changes in EC coupling induced by sympathetic activation are accompanied by a rapid surge in ATP consumption, primarily from sarcomeric proteins and ion pumps, thus increasing the flux of ADP to mitochondria via the creatine shuttle. As a result, the redox state of mitochondrial NADH and $FADH_2$ is transiently oxidized, but this is rescued by Ca^{2+} accumulation inside the mitochondrial matrix, which stimulates the Krebs cycle to regenerate the reduced forms of NAD^+ and FAD (20). The increase in free matrix Ca^{2+} during β-AR stimulation is due to the mismatch between the rate of Ca^{2+} uptake via the MCU and of its extrusion via the mitochondrial Na^+/Ca^{2+} exchanger (NCLX), the latter being substantially slower than the former. The NCLX is the primary mitochondrial Ca^{2+} efflux pathway in excitable cells, and it extrudes 1 Ca^{2+} to the cytosol in exchange for 3 Na^+ ions (21). The physiological relevance of mitochondrial Ca^{2+} accumulation during β-AR stimulation is underscored by the observation that in mice lacking the MCU exclusively in cardiac myocytes, the delayed metabolic adaptation caused by loss of mitochondrial Ca^{2+} uptake blunts the increase in cardiac contractile performance induced by isoproterenol (22). Therefore, rapid mitochondrial Ca^{2+} uptake via the MCU in the heart is essential to the metabolic and inotropic response to elevations of cardiac workload.

The MCU complex has a low apparent affinity for Ca^{2+} (k_D 20-30 μM) (23), which implies that Ca^{2+} flux across the MCU requires Ca^{2+} concentrations that are markedly higher than the physiological $[Ca^{2+}]_c$ range. These high Ca^{2+} concentrations might be achieved in a spatially localized "Ca^{2+} microdomain" created by the close apposition of the SR with mitochondria (24). The existence of these Ca^{2+} microdomains might depend on specialized proteins that physically tether the SR to mitochondria, such as mitofusin (Mfn) 1 and 2 (25) and FUNDC1 (26). Mitofusins are GTPases found on the OMM and ER membranes that were initially identified as essential mediators of mitochondrial fusion. Subsequently, mitochondrial Mfn2 was discovered to engage homo- and heterotypic interactions with mitofusins on ER membranes to maintain the close communication between the two organelles (25). Lending support to this concept, deletion of Mfn2 gene in cardiac myocytes reduces the length of SR-mitochondria contact sites and hinders the Ca^{2+}-stimulated regeneration of mitochondrial NAD(P)H and $FADH_2$ during elevations of workload (27). Of note, the role of Mfn2 as an ER-mitochondria tether has been challenged (28), and the debate on the function of mitofusins is still ongoing.

Importantly, the Ca^{2+}-dependent metabolic adaptation of mitochondrial oxidative metabolism has been mostly characterized in mice, but its physiological role might be more relevant in humans than in small rodents because of the larger contractile reserve of the human heart. Mice have a resting heart rate of 500-600 beats per minute (bpm) that can increase to 700-800 bpm during exercise, whereas humans can increase from 60-80 bpm at rest to 170-190 bpm. Similarly, the force-frequency relationship is blunted in mice compared to humans: contractile force (assessed by measuring isometric force development in cardiac trabeculae *ex vivo*) increases only marginally between 8 and 12 Hz in mice, whereas human cardiac trabeculae develop 81-168% more force when stimulation frequency is increased from 0.5 to 2.5 Hz (29). Consequently, the increase in ATP demand imposed by elevations of cardiac workload is substantially larger in humans than in mice.

Furthermore, there are important differences in EC coupling between small rodents and humans that have important implications for mechano-energetic coupling. One critical difference is the higher cytosolic Na^+ concentration ($[Na^+]_c$) of mice (9-14 mmol/L) compared to humans (4-8 mmol/L). Because the main driver of NCLX activity is the Na^+ gradient across the IMM (30), mitochondrial Ca^{2+} efflux should be faster in mice than in humans, likely to prevent excess Ca^{2+} accumulation in the matrix. In contrast, $[Na^+]_c$ should have a larger influence on the rate of Ca^{2+} efflux in human mitochondria, allowing a wider range of free Ca^{2+} regulation in the mitochondrial matrix.

Altogether, these observations indicate that the Ca^{2+}-mediated stimulation of oxidative metabolism might be more relevant to cardiac function in humans than it is in mice.

2.4 Mechano-energetic uncoupling and oxidative stress in heart failure

Heart failure (HF) is the clinical syndrome resulting from structural and functional cardiac abnormalities that reduce cardiac output and/or increase intracardiac pressures at rest or during exercise (31). HF is a progressive condition initiated by an index event that can either acutely damage the myocardium, such as myocardial infarction, or chronically hinder its ability to relaxate or generate force, such as arterial hypertension. Regardless of the nature of this index event, asymptomatic ventricular dysfunction progresses toward overt HF due to a series of structural and functional alterations that on the long term result in maladaptive remodelling and deterioration of cardiac function (32). Depending on whether contraction or relaxation is primarily affected, HF can be divided in *systolic* or *diastolic*, respectively. In the clinical arena, left ventricular (LV) ejection fraction (LVEF) is the prime parameter used to evaluate cardiac contractile function, and thus HF is classified in HF with reduced (LVEF <40%), mid-range (40-49%), or preserved LVEF (≥50%), respectively (31).

Derangements in cardiac EC coupling are central in the pathophysiology of *systolic* HF and contribute to the progression of the disease (8). The SR Ca^{2+} content is diminished, thus blunting the amplitude of $[Ca^{2+}]_c$ transients and consequently the development of force during systole (33). In addition, cytosolic Ca^{2+} removal is slowed, and steady-state diastolic $[Ca^{2+}]_c$ is increased, thereby enhancing ventricular wall tension during diastole (34). Furthermore, $[Na^+]_c$ is elevated in failing cardiac myocytes. Several mechanisms conspire to increase $[Na^+]_c$ in HF, including decreased activity of the Na^+/K^+ ATPase (35), increased activity of the Na^+/H^+ exchanger (36), and enhancement of the late Na^+ current (37). As described above, Na^+ and Ca^{2+} handling are intertwined via the NCX, which in the healthy heart predominantly functions to remove Ca^{2+} from the cytosol (i.e. in *forward* mode). In HF, decreased systolic $[Ca^{2+}]_c$ and increased $[Na^+]_c$ shift the NCX toward *reverse* mode during the initial phases of the action potential (38, 39). In fact, during diastole, elevated $[Na^+]_c$ decreases the Na^+ gradient driving Ca^{2+} extrusion via the *forward* mode of the NCX; during the action potential, elevated $[Na^+]_c$ favours Ca^{2+} influx via the *reverse* mode of the NCX (40). Action potential prolongation in failing cardiac myocytes further promotes Ca^{2+} influx via the NCX (39). On the one hand, enhanced NCX reverse mode may positively affect inotropy by compensating for decreased SR Ca^{2+} release (41), but on the other hand, impaired diastolic Ca^{2+} removal hinders relaxation (40) and increases the risk of arrhythmias (42).

Derangements in cytosolic Na^+ and Ca^{2+} handling occurring in HF conspire to hinder mitochondrial Ca^{2+} uptake and enhance Ca^{2+} extrusion from mitochondria (**Figure 4**) (8). First, because of the physical and functional coupling of mitochondria and SR, the decrease in SR Ca^{2+} load hinders mitochondrial Ca^{2+} uptake via the MCU (43). In addition, elevated $[Na^+]_c$ increases the driving force for Ca^{2+} efflux from the mitochondrial matrix via the NCLX (30). Moreover, the MCU open probability is decreased in the failing human myocardium (44). Finally, structural modifications of the SR-mitochondria contact sites might further impair Ca^{2+} exchange between the two organelles in HF (45). Altogether, these alterations hinder mitochondrial Ca^{2+} accumulation in the failing heart, consequently impairing the Krebs cycle-mediated regeneration of reducing equivalents that supply electrons to the ETC and to mitochondrial antioxidant systems (46), ultimately causing bioenergetic deficit and oxidative stress. One additional mechanism that contributes to deplete mitochondrial antioxidative capacity in HF is the reversal of the NNT reaction. In the healthy heart, the NNT is one major source of reduced NADPH in mitochondria (47). In response to pathological afterload elevations, the NNT can function in *reverse* mode, i.e. regenerating NADH at the expense of the NADPH pool. In fact, during pressure overload, NADH oxidation is not matched by an adequate increase in TCA cycle activity, and therefore the reversal of NNT reaction becomes thermodynamically favourable (47).

Altogether, alterations in mechano-energetic coupling contribute to bioenergetic deficit and oxidative stress, two major drivers of systolic HF (**Figure 4**) (48, 49).

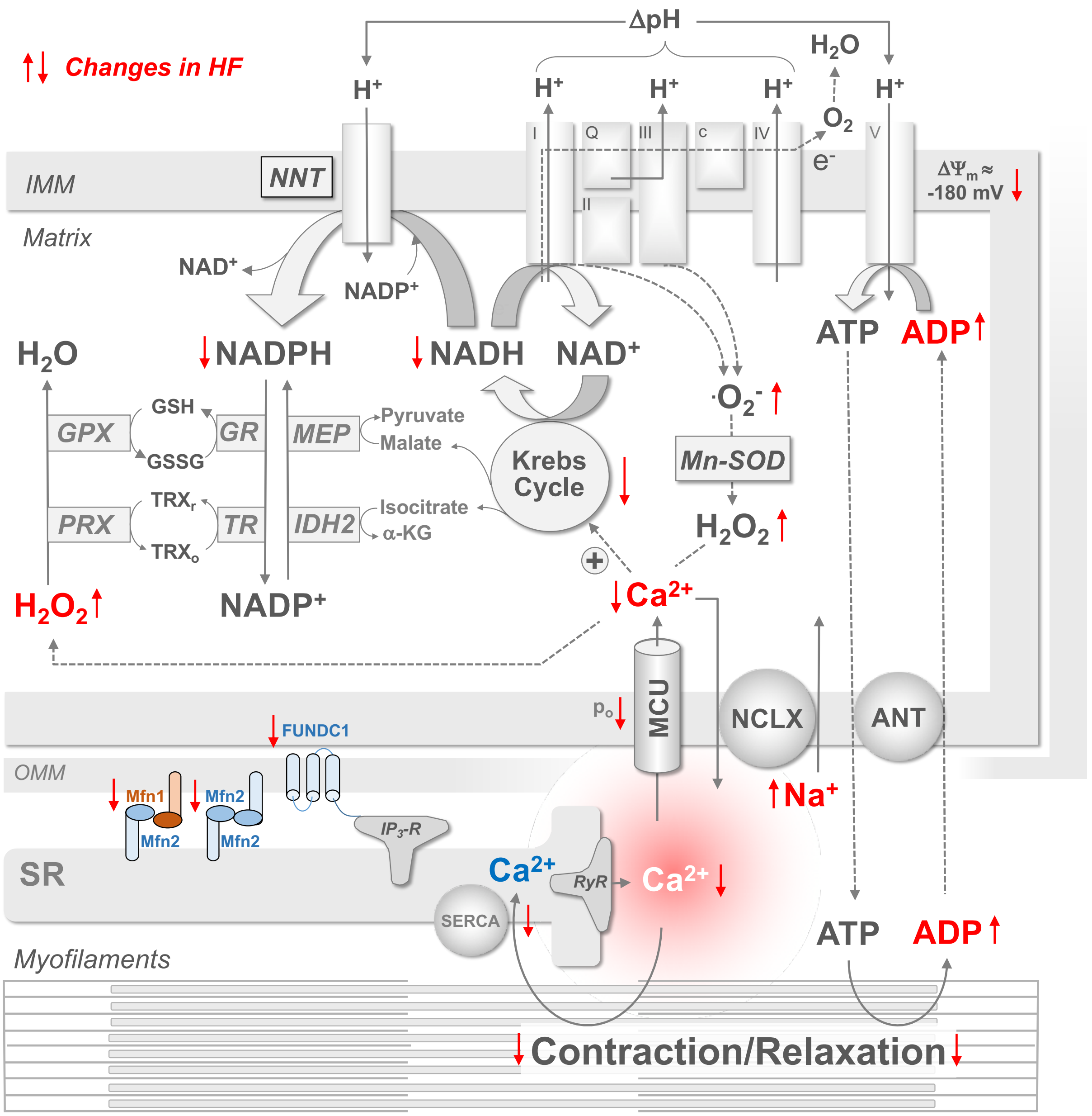

Figure 4. Cardiac mechano-energetic uncoupling in heart failure.

Modified with permission from (8). Abbreviations not found in the text: ANT, adenine nucleotide translocator; e^-, electron; GR, glutathione reductase; GSH and GSSG, reduced and oxidized glutathione, respectively; IP_3-R, inositol trisphosphate receptor; MCU, mitochondrial Ca^{2+} uniporter; NCLX, mitochondrial Na^+/Ca^{2+} exchanger; p_o, open probability; TR, thioredoxin reductase; TRX_r and TRX_o, reduced and oxidized thioredoxin, respectively.

3. Barth syndrome

Barth syndrome (BTHS) is an X-linked multisystem disorder characterized by the infantile onset of cardiomyopathy, skeletal myopathy, recurrent neutropenia, and growth retardation (50). BTHS was first described in 1983 in one Dutch kindred with high infant mortality due to HF and infections (51), and was initially classified together with other metabolic disorders characterized by urinary excretion of high levels of 3-methylglutaconic acid, a product of leucine breakdown. More than one decade later, mutations in the gene encoding the mitochondrial enzyme tafazzin (*TAZ*) were discovered to be the cause of BTHS (52). Tafazzin is a mitochondrial transacylase ubiquitously expressed in human tissues that catalyses the final step in the remodelling of CL (53). To understand the functional consequences of *TAZ* mutations and how they result in a systemic disorder, the following paragraphs summarize CL biosynthesis and function, describe the current knowledge of the pathophysiology of BTHS obtained by cellular and animal models of the disease, and finally, outline the main clinical characteristics of the human disease.

3.1 Cardiolipin synthesis and function

A number of enzymes essential for mitochondrial oxidative metabolism are integral IMM proteins. The phospholipid composition of the IMM is pivotal to ensure proper integration, structural organization, and function of several of these proteins, and in particular those that assemble in multi-protein complexes such as the ETC. The fact that an abnormal composition of the CL pool causes BTHS, a systemic and potentially lethal disorder, underscores the importance of protein-phospholipid interactions for mitochondrial function. In contrast to other phospholipids, CL is unique in that it consists of a double glycerophosphate backbone and four fatty acyl chains arranged in a cone-shaped structure (54). This peculiar conformation might contribute to shaping the curvature of the highly bent regions within the mitochondrial cristae (55). Furthermore, while most phospholipids are synthesized in the ER and then distributed throughout the cell, CL is synthesized at the site of its final localization, i.e. the mitochondrial membranes (56). After the initial biosynthetic steps summarized in **Figure 5**, CL undergoes a process termed *remodelling* or *maturation*, consisting in de-acylation (i.e., removal of three of the four acyl chains) to form monolyso-cardiolipin (MLCL), which is subsequently re-acylated to form mature CL (57). The process of CL maturation appears particularly important in tissues with high metabolic activity, such as the heart, where a large proportion of the CL pool contains polyunsaturated acyl chains. Tafazzin catalyses the synthesis of tetralinoleoyl-CL, the most abundant form of mature CL in mammalian cardiac and skeletal muscle mitochondria (58). As indicated by its name, the acyl chains of tetralinoleoyl-CL consist of four linoleic acid molecules, a fatty acid with eighteen carbons and two unsaturated bonds. The integration of CL in protein complexes requires the presence of these unsaturated "tails", and prolongs the half-life of CL by preventing its enzymatic degradation (59). Because premature CL cannot interact with IMM proteins, defective CL remodelling accelerates CL turnover and induces the accumulation of MLCL, the precursor of tetralinoleoyl-CL (59). Indeed, an increase in the MLCL/CL ratio is the most accurate parameter for BTHS diagnosis (60).

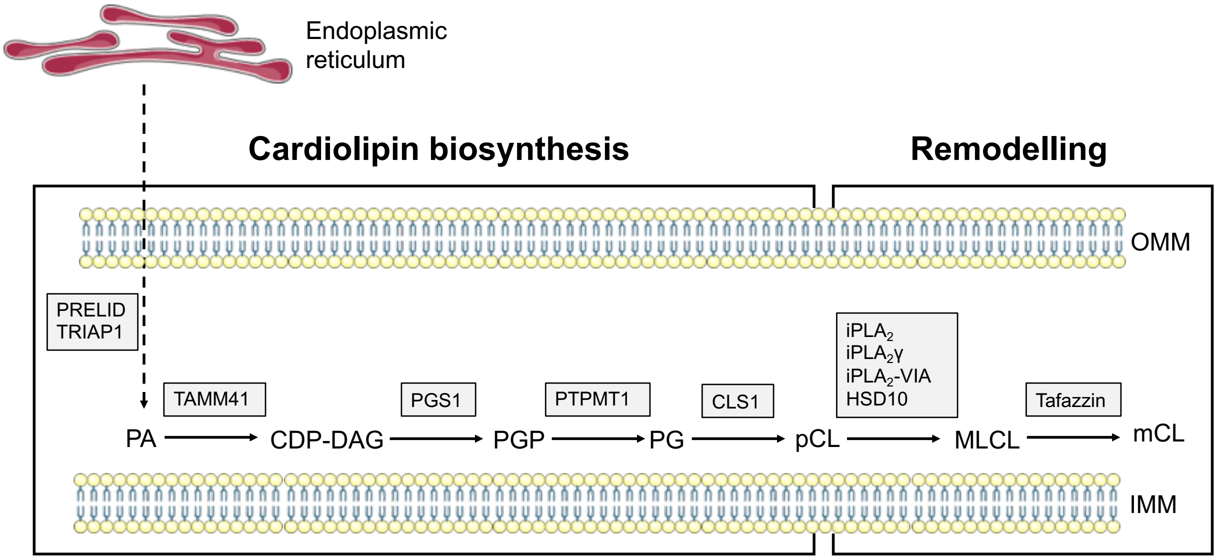

Figure 5. Cardiolipin synthesis and remodelling.

Abbreviations not used in the text: CDP-DAG, cytidindiphosphate-diacylglycerol; CLS1, cardiolipin synthase 1; iPLA2/iPLA2γ/ iPLA2-VIA/HSD10: Ca^{2+}-independent phospholipases; MLCL, monolysocardiolipin; mCL, mature cardiolipin; OMM, outer mitochondrial membrane; pCL, precardiolipin; PGS1, phosphatidylglycerol phosphate synthase 1; PA, phosphatidic acid; PG, phosphatidylglycerol; PGP, phosphatidylglycerol phosphate; PTPMT1, protein-tyrosine phosphatase mitochondrial 1; TAMM41, CDP-DAG synthase.

Modified with permission from (61).

CL stabilizes supramolecular complexes by forming an interface between membrane domains of proteins and the lipid phase of the IMM (61). As mentioned in **Chapter 1**, the stabilization of the ETC supercomplexes requires the presence of mature CL (62). CL-deficient cells display an increase in the monomeric form of complex IV and decreased levels of the supercomplexes composed of complex I, one complex III dimer, and a variable number of complex IV subunits (2). Remodelling of ETC respirasomes is accompanied by impaired mitochondrial respiration, suggesting that CL increases the efficiency of electron transfer between complexes (62). In addition, CL is required for the structural organization of the α-KGDH and the succinate dehydrogenase complexes (63, 64), and might favour the interaction between PDH and its activating phosphatase. Indeed, PDH activity is decreased in CL-deficient cells due to enhanced PDH phosphorylation (65). Therefore, mature CL is important for both oxidative phosphorylation and Krebs cycle activity.

CL is involved in numerous mitochondrial processes besides oxidative metabolism. Mitochondrial protein import is mediated by a group of integral membrane proteins denoted as translocases of the outer and inner membrane (TOM and TIM, respectively), which also require CL for their structural organization (66). Furthermore, CL favours the oligomerization of dynamin-1-like protein 1 (Drp1) and optic atrophy 1 (Opa1), two GTPases that are essential for mitochondrial fission and fusion, respectively (67, 68). In addition, CL is involved in the removal and degradation of damaged mitochondria, a process termed mitophagy, and in the intrinsic (mitochondrial) apoptotic pathway. In response to mitochondrial damage, CL is externalized to the outer mitochondrial membrane, where it mediates specific targeting to mitochondria of proteins involved in autophagy and apoptosis (69, 70). The latter are only some prominent examples of mitochondrial functions that require CL; a list of processes with known CL requirements is provided in **Table 1**. Altogether, the presence of CL and the composition of its acyl side chains are essential for mitochondrial and cellular homeostasis. As outlined in detail below, experimental evidence from cellular and animal models of BTHS indicates that alterations in certain CL-dependent processes might be particularly relevant for the pathogenesis of BTHS.

Table 1. Mitochondrial functions involving cardiolipin.

Function	Role of cardiolipin	Ref.
Mitochondrial biogenesis	Structural organization of integrity of mitochondrial translocases mediating protein import and membrane protein complex assembly	(66, 71-73)
Mitochondrial dynamics (fission and fusion)	Oligomerization and regulation of the activity of dynamin-like proteins mediating mitochondrial fission and fusion	(67, 68, 74, 75)
Mitochondrial cristae morphology	Physical properties of CL, promoting membrane bending	(76)
	Structural organization of the mitochondrial cristae organizing system (MICOS) complex	(77)
Oxidative phosphorylation	Structural integrity of respirasome, interaction with individual respiratory complexes	(2, 62, 64, 78, 79)
	Interaction with the adenine nucleotide translocator (ANT)	(80)
Intermediary metabolism	Interaction of pyruvate dehydrogenase (PDH) with PDH phosphatase	(65)
	Interaction with the carnitine/acylcarnitine carrier (CACT)	(81)
	Structural organization and activity of succinate dehydrogenase	(64)
Mitophagy and apoptosis	Regulation of Beclin 1 and LC3 recruitment to mitochondrial membranes	(69, 82)
	Cytochrome *c* peroxidase activity and mitochondrial permeability transition	(83, 84)
	Recruitment and oligomerization of pro-apoptotic Bcl-2 proteins on the outer mitochondrial membrane	(85, 86)

Modified with permission from (61).

3.2 Cellular and animal models of Barth syndrome

The consequences of *TAZ* mutations on mitochondrial function have been investigated in numerous cell systems, including fibroblasts, lymphoblasts, and inducible pluripotent stem cells (iPSCs)-derived cardiac myocytes, as well as in animal models, including fruit fly, zebrafish, and mouse. The main findings of the studies using cellular and animal models of BTHS are summarized in **Tables 2** and **3**, respectively.

Tafazzin-deficient cells exhibit several common features, including alterations in mitochondrial morphology and destabilization of the ETC supercomplexes. In the majority of studies, ETC remodelling was accompanied by decreased baseline and/or uncoupled respiration and increased mitochondrial ROS production. In one study employing an engineered BTHS "heart-on-chip" tissue, iPSC-derived cardiac myocytes displayed sarcomere disarray, impaired contractility, and increased mitochondrial ROS production, and these defects could be rescued by mitoTEMPO, a mitochondria-targeted antioxidant (87). On these grounds, it was proposed that defective oxidative phosphorylation and increased ROS formation at the ETC due to remodelling of respirasomes is one dominant driver of BTHS cardiomyopathy.

To overcome the limitations associated with cellular and non-mammalian models, a mouse model of BTHS was generated by global short hairpin RNA (shRNA)-mediated knockdown (KD) of *Taz* gene (88). To induce degradation of *Taz* mRNA, transcription of the shRNA is induced by administration of doxycycline. *Taz*-KD mice have a normal life span, but develop cardiac dysfunction that is usually detected at 7-8 months of age (88-92). Studies using the *Taz*-KD model of BTHS reported different phenotypes of cardiomyopathy. The most commonly reported feature is an impairment in cardiac contractility, reflected by an increase in LV end-systolic diameter without significant changes in LV chamber dimension, thus resulting in a lower LVEF and cardiac output. In other studies, *Taz*-KD mice exhibited increased LV wall thickness and lower LV volumes, recapitulating the phenotype of hypertrophic cardiomyopathy (93). *Taz*-KD have lower exercise capacity compared to wild-type (WT) littermates, but they do not exhibit signs of cardiac decompensation, such as oedema, and do not die of sudden cardiac death. One notable exception is the report by Phoon and colleagues, who observed high perinatal lethality and abnormal cardiac development in *Taz*-KD mice. The authors attributed these differences to the higher dose of doxycycline used for induction of *Taz* knockdown (94). However, the reason for the heterogeneous cardiac phenotypes observed in *Taz*-KD mice is currently unclear, given that the genetic background of the mice was the same (i.e., C57BL/129S6) in all studies.

In line with results obtained in cellular models of BTHS, loss of tafazzin function in mice results in a marked decrease in mitochondrial CL content and a proportional increase in more saturated CL species, reflecting the shift in CL composition observed in human BTHS (88). This is accompanied by ultrastructural and functional abnormalities of cardiac and skeletal muscle mitochondria, such as abnormal morphology of mitochondrial cristae and disruption of mitochondria-SR contact sites (88). In addition, and also in agreement with tafazzin-deficient cell systems, defective CL remodelling destabilizes the ETC supercomplexes in *Taz*-KD mice. Respiration of isolated cardiac mitochondria supplied with the complex I substrates pyruvate and malate or with fatty acids is decreased in *Taz*-KD mice compared with WT, and most studies attributed this defect to the destabilization of ETC respirasomes. However, mitochondrial respiration is higher in *Taz*-KD than WT when glutamate is used as substrate (95, 96), suggesting that rewiring of intermediary metabolism, rather than ETC remodelling, accounts for the shift in substrate preference in *Taz*-KD mitochondria. In one report, defective pyruvate- and fatty acid-supported respiration could be partially rescued by supplying mitochondria with CoA, indicating that deficiency of this essential acyl carrier might impair oxidation of substrates that enter the Krebs cycle in the form of acyl-CoA (96).

In contrast with cellular models of BTHS, the majority of studies using the *Taz*-KD mouse model did not observe an increase in ROS production from isolated cardiac mitochondria, nor signs of oxidative stress in the myocardium, that could account for the development of cardiac dysfunction. A recent report that analysed individually all the most important sites of ROS production in cardiac and skeletal muscle mitochondria of *Taz*-KD mice did not identify differences in the maximum capacity of superoxide/H_2O_2 formation compared to WT mitochondria (97). Most important, crossing *Taz*-KD mice with mice overexpressing catalase in the mitochondrial matrix does not prevent the development of cardiomyopathy (93). Altogether, evidence obtained in mouse models of BTHS argues against oxidative stress playing a major role in the pathogenesis of cardiac dysfunction in mice, and therefore the mechanisms linking aberrant CL biogenesis to HF in BTHS remain poorly understood.

Table 2. Cellular models of Barth syndrome.

Cell type	Main findings	Ref.
Patient-derived skin fibroblasts	Impaired ETC function	(50)
	Destabilization of ETC supercomplexes, α-KDGH complex, branched-chain ketoacid dehydrogenase (BCKDH) complex. ↑ abundance of the mitochondrial contact site and cristae organizing system (MICOS) and the sorting and assembly machinery (SAM) complexes	(63)
	Adeno-associated virus *TAZ* gene transduction improves mitochondrial morphology, ↓ ATP content, and ↑ ROS production	(98)
Mouse embryonic fibroblasts	↓ ROS production under hypoxic conditions hinders activation of hypoxia-induced factor-1α (HIF-1α) signalling	(99)
Rat neonatal ventricular fibroblasts	↑ ROS production and impaired cell cycle progression	(100)
Patient-derived lymphoblasts	Unchanged susceptibility to death-receptor mediated apoptosis	(101)
	Unchanged ATP levels and membrane potential	(102)
	Destabilization of ETC supercomplexes	(78)
	Destabilization of ETC supercomplexes, ↓ levels of complex V, ↑ mitochondrial mass, inhibition of intrinsic apoptotic pathway due to impaired caspase 8 binding to mitochondria	(103, 104)
	Expression of monolysocardiolipin acyltransferase-1 (MLCL AT-1) ↑ CL, ↑ basal respiration, ↓ proton leak, superoxide production	(105)
Neonatal rat ventricular myocytes	↓ ATP levels, AMPK activation, ↑ mitochondrial density, cellular hypertrophy	(9)
	Treatment with mito-Tempo ↓ ROS production, ↑ ATP levels, and ↓ AMPK activation	(106)

Mouse myoblasts	↓ transferrin receptor (iron import), ↑ ferroportin (iron export), ↓ activity of mitochondria iron-sulfur cluster enzymes, ↓ Yfh1/frataxin (iron-sulfur biogenesis)	(107)
iPSC-derived cardiac myocytes	Destabilization of ETC supercomplexes, ↓ levels and activity of succinate dehydrogenase	(62)
	Fragmentation of mitochondrial network, ↓ ATP production, ↑ basal O_2 consumption because of inefficient F_1/F_o ATP synthase activity, abnormal sarcomere assembly, ↑ mitochondrial ROS production	(87)
	Destabilization of ETC supercomplexes, ↓ respiration, ROS production	(64)
	↑ glucose and ↓ fatty acid uptake, ↑ lactate production, ↓ pyruvate carboxylation, ↑ cellular acylcarnitine levels	(108)

Table 3. Animal models of Barth syndrome.

Animal model	Main findings	Ref.
Fruit fly	Male sterility, rescued by inactivation of iPLA2-VIA, a Ca^{2+}-independent phospholipase A_2	(109)
Zebrafish	Abnormal cardiac development, bradycardia, pericardial diffusion, generalized oedema, embryonic lethality	(110)
Taz-knockdown mouse	Cardiac dysfunction at 8 months of age; abnormal mitochondrial morphology in heart and skeletal muscle	(88)
	↓ force development and abnormal mitochondrial morphology in skeletal muscle at 2 months, ↓ LVEF at 7 months of age	(92)
	Abnormal cardiac development, LV hypertrabeculation, early diastolic dysfunction, abnormal mitochondrial morphology	(94)
	↓ complex III and V activity, ↓ pyruvate-supported and ↑ glutamate-supported respiration of isolated cardiac mitochondria	(95)
	O_2 consumption rate unchanged at baseline, but unable to increase during exercise, ↑ lactate levels during exercise	(91)

	↓ expression of genes encoding ETC subunits, ↑ expression of enzymes involved in amino acid and one-carbon metabolism in the heart	(89)
	↓ complex I, III, IV enzymatic activity; exercise training ↑ complex III activity	(111)
	↓ mitochondrial respiration; overexpression of catalase in mitochondria does not rescue cardiomyopathy	(93)
	Abnormal mitochondrial and SR morphology, unchanged respiration and H_2O_2 production of isolated cardiac mitochondria	(90)
	Treatment with bezafibrate (PPAR agonist) for 4 months rescues LVEF, but not exercise capacity at 7 months of age. Bezafibrate ↑ expression of genes related to metabolism, including those involved in mitochondrial oxidation of FA and ketones	(112)
	Adeno-associated virus *Taz* gene transduction ameliorates cardiac and skeletal muscle dysfunction and reverts changes in protein expression	(113, 114)
	High-fat diet induces triglyceride accumulation, LV hypertrophy, and HF. Resveratrol partially rescues the high-fat diet-induced cardiomyopathy and ↓ oxidative stress	(115)
	Unchanged superoxide and ROS production in cardiac and skeletal muscle mitochondria	(97)
	↓ pyruvate- and FA-supported, but ↑ glutamate-supported respiration, ↑ H_2O_2 emission of isolated cardiac mitochondria. Addition of coenzyme A partially rescues defective pyruvate- and FA-supported respiration	(96)
Taz-knockout mouse	Global *Taz*-KO: high perinatal lethality, growth retardation, muscular weakness, dilated cardiomyopathy. Adeno-associated virus *TAZ* gene transduction rescues perinatal lethality. Cardiomyocyte-specific *Taz*-KO: LV dysfunction and dilatation at 2 months, myocardial fibrosis. Adeno-associated virus *TAZ* gene transduction prevents cardiomyopathy	(116)

3.3 Clinical features of Barth syndrome

Cardiomyopathy is the major clinical feature and cause of death in BTHS. The most frequent presentation of cardiac disease is LV dilation, but hypertrophic cardiomyopathy can also occur (117). In addition, up to 50% of patients display non-compaction cardiomyopathy, a pathological hypertrabeculation of the myocardium that reflects an abnormal development of the ventricular wall. The related clinical picture is also heterogeneous: while the most severe cases require cardiac transplantation or result in death in the first months of life, some patients exhibit a milder form of ventricular dysfunction that responds to HF medical therapy and eventually stabilizes during childhood. In the largest prospective studies performed thus far, the mean LVEF in a cohort of 31 BTHS patients was 50±10%, with 16 patients having preserved (≥50%) LVEF, and remained stable over a 2-year follow-up (118). However, BTHS patients exhibit a blunted inotropic reserve, as reflected by a lower increase in LVEF during treadmill exercise compared with healthy subjects (119). Furthermore, BTHS patients carry an increased risk of developing cardiac conduction defects and ventricular arrhythmias that can lead to sudden cardiac death (120). Importantly, the risk of these events is unrelated to the severity of cardiac dysfunction (118).

Skeletal myopathy is another hallmark of BTHS. It can be evident at birth as generalized hypotonia and muscle wasting, and during infancy it delays the achievement of the main motor developmental milestones. Later in life, skeletal myopathy is only minimally progressive but nevertheless, can become a major limiting factor for physical activity (119). Indeed, exercise intolerance and chronic fatigue are common symptoms in children and adolescents with BTHS. During exercise, BTHS patients exhibit impaired skeletal muscle utilization of fatty acids, which might contribute to muscular weakness by impairing metabolic adaptation in response to elevations in ATP demand (121).

BTHS patients also frequently suffer from persistent or recurrent neutropenia that predisposes to bacterial infections. Besides HF, sepsis is another frequent cause of hospitalization and death in BTHS (122). Neutropenia is sometimes accompanied by an increase in circulating monocytes (123). These features suggest that Taz deficiency might alter myelopoiesis, but this aspect of the disease has not been investigated thus far. Children with BTHS often exhibit a pre-pubertal growth delay, which is often compensated by a remarkable growth spurt after puberty. Weight and height are usually below average in adolescents, but tend to normalize after 18 years (124).

Numerous metabolic abnormalities have been identified in BTHS patients. As mentioned above, BTHS is characterized by increased urinary excretion of 3-methylglutaconic acid, the product of leucine breakdown, and this feature is shared with other inherited mitochondrial disorders (125). Another indication that amino acid metabolism might be affected in BTHS is that circulating levels of amino acids are frequently abnormal: BTHS patients have markedly lower plasma arginine, and higher proline, compared to healthy individuals of the same age (126). In addition, lactic acidosis, hypoglycaemia, hyperammonaemia, hypocholesterolaemia, and low carnitine levels have been reported in BTHS (126, 127).

3.4 From tafazzin deficiency to cardiomyopathy

As outlined in **Chapter 2**, the functional continuum between mitochondrial oxidative metabolism and EC coupling is essential to normal cardiac function. Despite the increasingly detailed knowledge of the mechanisms of mitochondrial dysfunction caused by tafazzin deficiency, none of the studies on the BTHS models addressed the fundamental question how these defects impact on EC coupling. In contrast, the concept that ROS production at the ETC is a primary culprit of cardiac and skeletal myopathy in BTHS has fostered the investigation of pharmacological and genetic interventions aimed at augmenting mitochondrial antioxidative capacity.

In this Thesis, we investigated the consequences of CL deficiency on mechano-energetic coupling in the *Taz*-KD mouse model of BTHS. We discovered that aberrant remodelling of CL alters the structural organization of the MCU complex, hindering Ca^{2+} uptake in the mitochondrial matrix. Consequently, the Ca^{2+}-dependent stimulation of Krebs cycle-related regeneration of NADH and $FADH_2$ is impaired, compromising energetic adaptation of cardiac myocytes during workload transitions. This mechano-energetic uncoupling prevents the physiological increase in systolic force, explaining for the lack of inotropic reserve during physical exercise in BTHS patients.

Materials and Methods

1. Materials

1.1 Chemicals

Chemical	Abbreviation	Manufacturer
Acrylamide/bisacrylamide (30%)		Bio-Rad GmbH
Adenosine diphosphate	ADP	Sigma-Aldrich
α-ketoglutarate	α-KG	Sigma-Aldrich
Amplex^{TM} UltraRed	AmR	Thermo Fischer Scientific
Ascorbic acid (sodium ascorbate)		Sigma-Aldrich
Adenosine triphosphate	ATP	Sigma-Aldrich
B-27^{TM} Supplement, minus Insulin		Thermo Fischer Scientific
BES		Sigma-Aldrich
Bovine serum albumin	BSA	Sigma-Aldrich
2,3-butanedione monoxime	BDM	Sigma-Aldrich
Caffeine		Sigma-Aldrich
Calcium chloride	$CaCl_2$	Sigma-Aldrich
Calcium Green^{TM}-5N		Invitrogen
Carbonyl cyanide-4-(trifluoromethoxy)-phenylhydrazone	FCCP	Sigma-Aldrich
CGP-37157	CGP	Sigma-Aldrich
cOmplete^{TM} Protease Inhibitor cocktail		Roche
Cyanide	CN	Sigma-Aldrich
Cyclosporine A	CsA	Sigma-Aldrich
DAPI stain		Merck
2',7'-dichlorodihydrofluorescein diacetate	DCF	Thermo Fischer Scientific
Dimethyl sulfoxide	DMSO	Sigma-Aldrich
2,4-dinitrochlorbenzol	DCNB	Sigma-Aldrich
2,4-dinitrophenol	DNP	Sigma-Aldrich
Ethylenediaminetetraacetic acid	EDTA	Sigma-Aldrich
Ethylene glycol-bis(β-aminoethyl ether)-N,N,N′,N′-tetraacetic acid	EGTA	Sigma-Aldrich
Ethanol	EtOH	VWR

Foetal calf serum	FCS	Thermo Fischer Scientific
Glucose		Sigma-Aldrich
Glycine		VWR
Heparin		Braun AG
Hydrogen peroxide (30%)	H_2O_2	Merck
4-(2-hydroxyethyl)-1-piperazineethanesulfonic acid	HEPES	Sigma-Aldrich
1-hydroxy-3-methoxycarbonyl-2,2,5,5-tetramethylpyrrolidine	CMH	Enzo Life Sciences
HMR-1098		Sigma-Aldrich
Indo-1 acetoxymethyl ester	Indo-1-AM	Thermo Fischer Scientific
Indo-1 pentapotassium salt		Thermo Fischer Scientific
Isoflurane		Abbott GmbH & Co. KG
Isoprenaline/isoproterenol	Iso	Sigma-Aldrich
Isopropanol		Merck
IWP-2		Sigma-Aldrich
Ketamine		Zoetis Deutschland GmbH
Lactobionic acid		Sigma-Aldrich
Laminin		Roche Diagnostics
Magnesium chloride	$MgCl_2$	Merck
Magnesium sulfate	$MgSO_4$	Sigma-Aldrich
Malic acid (sodium malate)		Sigma-Aldrich
Mannitol		Sigma-Aldrich
Methanol		Sigma-Aldrich
3-Methyl-2-Oxovalerat	KMV	Sigma-Aldrich
MitoSOX		Thermo Fischer Scientific
N-Ethylmaleimide	NEM	Sigma-Aldrich
Oligomycin		Sigma-Aldrich
PeqGold TriFast^{TM}		VWR
Phenol red		Sigma-Aldrich
Phosphocreatine	PCr	Sigma-Aldrich
PhosSTOP^{TM} (phosphatase inhibitor)		Sigma-Aldrich
Pinacidil		Sigma-Aldrich
Potassium bicarbonate	$KHCO_3$	Sigma-Aldrich
Potassium chloride	KCl	Sigma-Aldrich
Potassium dihydrogen phosphate	KH_2PO_4	Merck

Pyruvic acid (sodium pyruvate)		Sigma-Aldrich
Rhod-2-acetoxymethyl esther	Rhod- 2-AM	Thermo Fischer Scientific
Rotenone		Sigma-Aldrich
RPMI 1640 medium		Thermo Fischer Scientific
Sodium chloride	NaCl	Carl Roth
Sodium bicarbonate	$NaHCO_3$	VWR
Sodium dodecylsulfate	SDS	Carl Roth
Sodium hydrogen phosphate	Na_2HPO_4	VWR
Sucrose		Merck
Taurine		Merck
Tetramethylethylenediamine	TEMED	Sigma-Aldrich
Tetramethylrhodamine methyl ester	TMRM	Thermo Fischer Scientific
Tissue Tek® O.C.T. compound		Sakura
Tris Base		Carl Roth
Tris-HCl		Carl Roth
Triton-X100		Thermo Fischer Scientific
Tween® 20		Sigma-Aldrich
Vectashield® mounting medium		Vector Laboratories
Versene™ solution		Thermo Fischer Scientific
Xylazin		Bayer AG

1.2 Enzymes

Enzyme	Abbreviation	Manufacturer
Collagenase type II		Worthington
DNAse		VWR
HighCap cDNA RT Kit		Applied Biosystems
Horseradish peroxidase	HRP	Sigma-Aldrich
Liberase TH (Thermolysin high)		Roche Diagnostics
Proteinase, bacterial, type XXIV		Sigma-Aldrich
Proteinase K		Thermo Fischer Scientific
Subtilisin A		Sigma-Aldrich
Superoxide dismutase	SOD	Sigma-Aldrich
TaqMan GenEx Mastermix		Applied Biosystems

1.3 Antibodies

Antigen	Manufacturer	Catalogue number
Actin (α-sarcomeric)	Sigma-Aldrich	Cat#A2172
Catalase	Cell Signaling Technology	Cat#14097S
Cytochrome c oxidase subunit 4	Abcam	Cat#ab14744
Cytochrome c oxidase subunit 5	Generated by Peter Rehling	N/A
EMRE (C22orf32)	Santa Cruz Biotechnology	Cat#sc-86337
Glutathione peroxidase 1	Abcam	Cat#ab108427
Glyceraldehyde-3-phosphate dehydrogenase (GAPDH)	Millipore	Cat#MAB374
MICU1	Cell Signaling Technology	Cat#12524S
MICU2	Abcam	Cat#b101465
Mitochondrial H^+/Ca^{2+} exchanger	Generated by Peter Rehling	N/A
MCUa	Cell Signaling Technology	Cat#14997S
MCUb (Ccdc109b)	Abcam	Cat#ab170715
MCUR1	Cell Signaling Technology	Cat#13706S
NADH dehydrogenase 1 beta subcomplex subunit 8 (NDUFB8)	Generated by Peter Rehling	N/A
Peroxiredoxin 1	Cell Signaling Technology	Cat#8499
Peroxiredoxin 2	Abcam	Cat#ab50862
Peroxiredoxin 3	Ab Frontier	Cat#LF-PA0030
Superoxide dismutase 1	Santa Cruz Biotechnology	Cat#sc-11407
Superoxide dismutase 2	Santa Cruz Biotechnology	Cat#sc-30080
Ubiquinol-cytochrome c reductase, Rieske iron-sulfur polypeptide 1 (UQCRFS1)	Generated by Peter Rehling	N/A
Total OXPHOS rodent Ab cocktail	Abcam	Cat#ab110413
Voltage-dependent anion-selective channel 3 (VDAC3)	Generated by Peter Rehling	N/A
8-OHdG	Abcam	Cat#ab10802
2^{ary} Ab goat anti-mouse	Bio-Rad	Cat#170-6516
2^{ary} Ab rabbit anti-goat	Bio Rad	Cat#172-1034

1.4 Solutions

Solutions for experiments with isolated cardiac myocytes

Solution	Chemicals	AfCS
Isolation solution (pH 7.46)	NaCl	113 mM
	KCl	4.7 mM
	KH_2PO_4	0.6 mM
	Na_2HPO_4	0.6 mM
	$MgSO_4$	1.2 mM
	$NaHCO_3$	12 mM
	$KHCO_3$	10 mM
	HEPES	10 mM
	Phenol red	32 µM
	BDM	10 mM
	Taurine	30 mM
	Glucose	5.5 mM

The other solutions required for cardiac myocytes isolation are prepared by adding the following components to the isolation solution (from now on referred to as “solution A”):

- solution B: Liberase TH 0.08 mg/mL, trypsin 0.14 mg/mL, $CaCl_2$ 12.5 µM;
- solution C: FCS 10%, $CaCl_2$ 12.5 µM;
- solution D: FCS 5%, $CaCl_2$ 12.5 µM.

Normal Tyrode (NT) solution was used for cardiac myocyte perfusion during experiments in the IonOptix setup.

Solution	Chemicals	Concentration
Normal Tyrode (pH 7.54)	NaCl	130 mM
	KCl	5 mM
	$MgCl_2$	1 mM
	HEPES	10 mM
	Sodium pyruvate	2 mM
	Sodium ascorbate	0.3 mM
	Glucose	10 mM
	$CaCl_2$	1 mM

Solutions for experiments with isolated mitochondria

Solution	Chemicals	Concentration
Isolation solution (pH 7.4)	Mannitol	225 mM
	Sucrose	75 mM
	HEPES	2 mM
	EGTA	1 mM
Mitochondria suspending solution (pH 7.4)	Mannitol	225 mM
	Sucrose	75 mM
	HEPES	2 mM
Basic medium (pH 7.0)	KCl	140 mM
	HEPES	20 mM
	$MgCl_2$	5 mM
	EGTA	1 mM
Homogenization medium (pH 7.0)	KCl	140 mM
	HEPES	20 mM
	$MgCl_2$	5 mM
	EGTA	1 mM
	ATP	1 mM
	BSA	1%
Respiration buffer (pH 7.2)	KCl	134 mM
	$MgCl_2$	2.5 mM
	KH_2PO_4	2 mM
	EGTA	0.5 mM
	HEPES	20 mM
MiR05 (pH 7.1)	Sucrose	110 mM
	Lactobionic acid	60 mM
	Taurine	20 mM
	HEPES	20 mM
	KH_2PO_4	10 mM
	$MgCl_2$	3 mM
	EGTA	0.5 mM
Buffer for permeability transition pore (PTP) assay	KCl	120 mM
	Mannitol	70 mM
	Sucrose	25 mM
	HEPES	20 mM
	KH_2PO_4	5 mM
	EGTA	0.02 mM

Solutions for gel electrophoresis and Western blotting

Solution	Chemicals	Concentration
Tris-buffered saline (TBS)	Tris Base	500 mM
	NaCl	150 mM
TBS + Tween	Tween 20 (polysorbate 20)	0.001%
Electrophoresis buffer (pH 8.2-8.4)	Tris-HCl	25 mM
	SDS	0.1%
	Glycine	200 mM
Blotting buffer	Tris-HCl	25 mM
	Glycine	192 mM
	Methanol	20%

1.5 Mouse lines

Mouse line	Origin	Characteristics	Ref.
C57BL/N	Purchased from Charles River, Wilmington, MA, USA		
C57BL/J		Truncating mutation of *Nnt*	(128)
CaMKIIδ knockout (KO)	Courtesy of Prof. Johannes Backs	Global, constitutive knockout of *Camk2d*	(129)
CaMKIIδ/γ double knockout (DKO)		Tamoxifen-inducible, cardiomyocyte-specific knockout of *Camk2d* and *Camk2g*	(130)
Dlst$^{+/-}$	Generated by Prof. Gary E. Gibson. Courtesy of Prof. Stéphane Heymans and Dr. Ward Heggermont	Global, heterozygous knockout of *Dlst*	(131)
Taz-knockdown	Purchased from The Jackson Laboratories	Global, shRNA-mediated, doxycycline-inducible knockdown of *Taz*	(88)
Mito-roGFP2-Orp1 *Taz*-KD	Generated by Prof. Leticia Prates Roma	Expresses the H_2O_2-specific redox sensor Orp1 coupled to roGFP2 in the mitochondrial matrix	(132)

2. Methods

This section provides a detailed description of the methods for isolation of mitochondria and ventricular myocytes and the related experiments. The majority of experiments included in this Thesis are based on these methods. Additional methods are described in the Methods section of each study.

2.1 Ethical approval of animal experiments

Animal experiments were performed in accordance with guidelines of the local animal ethics committee. Animal licence numbers are reported in the Methods section of each study.

2.2 Isolation of adult mouse cardiac myocytes

Isolation of adult ventricular myocytes from mouse heart is performed using a modified Langendorff perfusion system, as described by O'Connell and colleagues (AfCS Research Reports; Vol. 1 No. 5 CM). In the Langendorff system, the heart is perfused in reverse fashion, i.e. from the aorta to the ventricles, and the backward pressure induced by retrograde perfusion causes the aortic valve to close, thus forcing the perfusate to flow through the coronary vessels.

For cardiac myocyte isolation, mice were anaesthetized with 5% isoflurane, 250 I.U. unfractionated heparin, and 0.33 mg carprofen. When pedal reflexes could not be elicited anymore, the heart was exposed and excised together with the aortic arch, the aorta was cannulated, and retrograde perfusion was started. Before reaching the heart, the perfusate was warmed up to 37°C by flowing through a glass coil immersed in a water bath at 37°C. The composition of the solutions used in the isolation is provided in the table below.

First, the heart was perfused with solution A for 4 minutes to remove the remaining blood from the coronary vessels; subsequently, the heart was digested with solution B for 5 to 8 minutes. Solution B contains Liberase TH, a mixture of collagenase I, II, and the protease thermolysin, which degrades intercellular junctions. To stop digestion of the tissue, the heart was removed from the Langendorff apparatus, the ventricles were opened and rinsed with a 1:1 to mixture of solutions A and C at room temperature. Intact cardiac myocytes were released by softly rinsing the heart in the solution A/C mixture for 2-3 minutes, after which the solution was transferred to a 15 mL tube. The cell pellet obtained by sedimentation was resuspended in 5 to 10 mL (depending on cell viability and the yield of the isolation) of solution D and transferred to a Petri dish.

Finally, cardiac myocytes were gradually re-exposed to the physiological concentration of extracellular Ca^{2+} in 5 steps, each step lasting 4 minutes: 50 µM → 100 µM → 200 µM → 500 µM → 1 mM $CaCl_2$. Thereafter, the solution was again transferred to a 15 mL tube and cardiac myocytes were obtained by sedimentation for 8-10 minutes. The pellet was resuspended in 10 mL of culture medium (M199 + FCS 5% + penicillin and streptomycin 1% + 10 mM HEPES) and stored at 37°C.

2.3 Fluorescence measurements in isolated cardiac myocytes

Description of the IonOptix setup

Experiments with intact ventricular myocytes were performed using a customized IonOptix setup (IonOptix, Milton, MA, USA) consisting of the components described below and represented in **Figure 6**. The components are described following the path of excitation and emission light during recording of fluorescence signals.

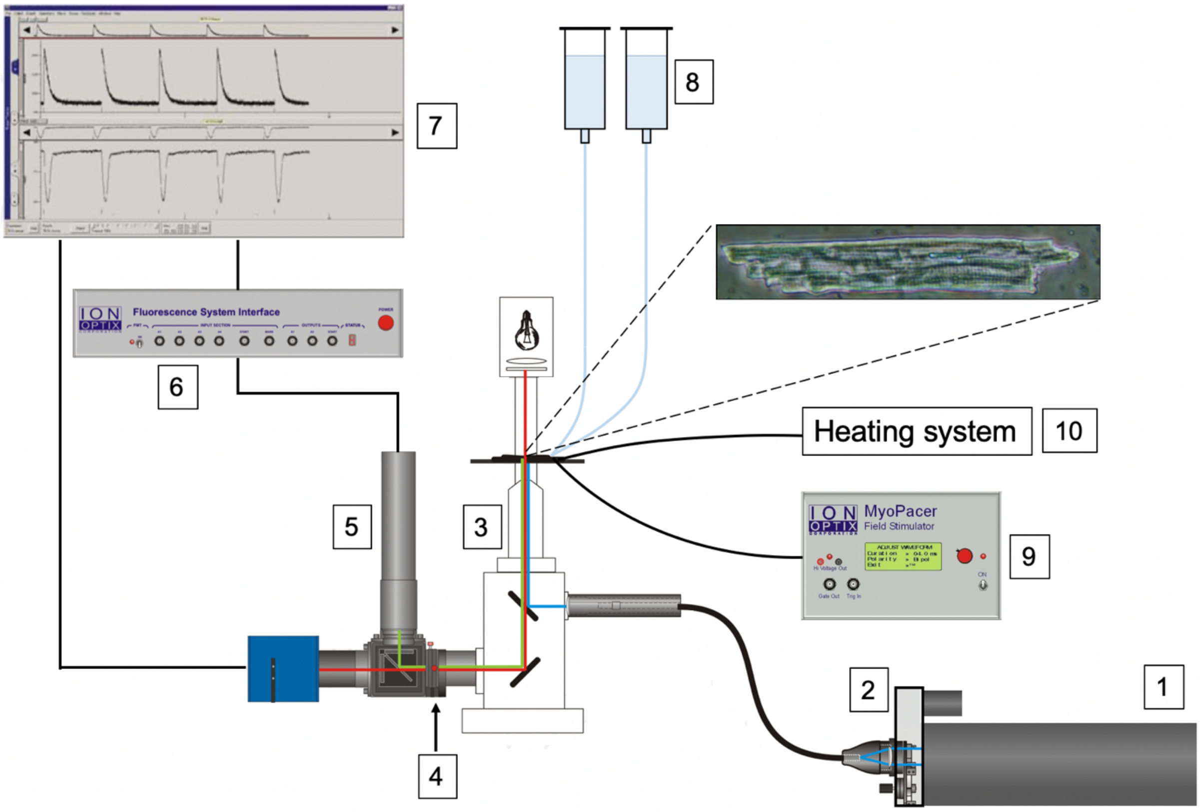

Figure 6. Scheme of the IonOptix setup used for fluorescence measurements.

1. Xenon arc lamp (Xenon Short Arc-75XE, Ushio Inc., Tokyo, Japan): produces excitation light with a usable wavelength range between 300 and 700 nm.
2. Filter wheel (IonOptix μStep): the Xenon arc lamp housing is coupled with a six-position filter wheel controlled by a stepper motor (a scheme of the filter wheel is shown in **Figure 7**). During the experiment, the wheel automatically rotates between one or more excitation filters to deliver the desired excitation wavelength to the microscope with a sampling frequency selected by the investigator. The wheel automatically returns to the nearest shutter (closed) position between sampling periods to minimize light exposure and consequent bleaching of the dye. To enable continuous recording of cytosolic Ca^{2+} with the dye indo-1, an additional excitation filter was placed in one of the shutter positions. The excitation light (represented by the blue beam in **Figure 6**) is transmitted to the microscope via a liquid light guide and a microscope-specific adapter.
3. Inverted microscope (Eclipse Ti, Nikon GmbH, Düsseldorf, Germany): fluorescence measurements were performed with an inverted epifluorescence microscope. The *excitation* light reaches the base of the microscope and is reflected upwards (toward the cells) by a dichroic mirror (89017bs F/TR). The *emission* light (green beam in **Figure 6**) passes through the dichroic mirror and is reflected toward the cell framing adapter (described below) by another mirror. The same mirror also reflects the microscope light (>660 nm; red beam in **Figure 6**) that illuminates the cells from above, enabling visualization of the microscope field throughout the experiment.
4. Cell framing adapter: contains an adjustable iris that frames a rectangular area of the microscope field. The area is adjusted by the investigator to match the cell size, so that only the signal derived from one cell is recorded during the experiment. The cell framing adapter also contains a charged-coupled device (CCD) camera (MyoCam) to visualize the selected area and a dichroic mirror and emitter to reflect and filter fluorescence emission before it is collected by the photomultiplier(s). The use of a red filter in the microscope condenser permits the transmitted image to be visualized during photometry recording.
5. Photomultiplier 400 sub-system: the setup is equipped with 3 photomultiplier tubes (PMT, only one is represented in **Figure 6**) that convert incident photons into electrical signals. Interchangeable dichroic mirrors are used to direct specific wavelengths toward the PMTs, enabling detection and recording of more than one fluorescence signal from the same cell.

6. IonOptix fluorescence system interface: provides the control hardware required for fluorescence measurements. Receives signals from the PMTs and transduces them to the computer.
7. Computer: the signal recorded by the CCD camera and transmitted from the fluorescence system interface is visualized and recorded on a table computer.

Altogether, these components enable measurement of fluorescent signals from intact cardiac myocytes. The setup is additionally equipped with components that enable electrical field-stimulation, continuous superfusion, and temperature control of the cells during the experiment.

8. Customized perfusion and suction systems: during the experiment, cells are placed on a laminin-coated coverslip housed in a superfusion chamber. The superfusion chamber consists of a plastic frame (chamber holder) equipped with one needle for inflow of solution and one aspirator. This inflow/outflow system maintains a stable solution level at low bath volume (<0.5 mL) and achieves nearly laminar flow at a rate of 1 mL/min.
9. Field-stimulation: the superfusion chamber is additionally equipped with two electrodes for cell field-stimulation. The electrodes are powered by an external supply that enables control of stimulation frequency during the experiment.
10. Temperature controller and heater: temperature of the superfusion chamber and of the perfusate is maintained at 37°C throughout the experiment by a temperature controller.

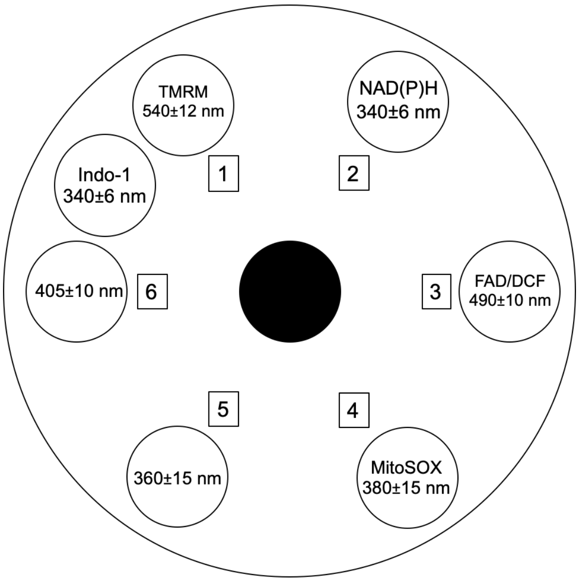

Figure 7. Scheme of the filter wheel containing the excitation filters.

Fluorescence recordings

Table 4 summarizes fluorescence dyes and the excitation and emission wavelengths (λ_{exc} and λ_{em}, respectively) used for fluorescence measurements in isolated cardiac myocytes.

Table 4. Excitation and emission wavelengths

Parameter	Dye	Loading	λ_{exc} (nm)	λ_{em} (nm)
NAD(P)H	None (autofluorescence)		340	450
FAD			485	525
Cytosolic Ca^{2+}	Indo-1 AM	15 min incubation with 1-5 µM indo-1 at RT	340	405-485
ROS	DCF	15 min incubation with 0.75-4 µM DCF at 37°C	485	525
Mitochondrial superoxide	MitoSOX	30 min incubation with 3.3 µM MitoSOX at RT	380	580
Mitochondrial membrane potential	TMRM	5 min incubation with 25-100 nM TMRM at RT	540	605

For measurements of NAD(P)H and FAD autofluorescence, at the end of each experiment the signal was calibrated by superfusing cardiac myocytes with the protonophore FCCP (5 µM) and subsequently with the complex IV inhibitor cyanide (4 mM) to induce complete oxidation and reduction of the mitochondrial pyridine nucleotide pool, respectively.

For experiments with DCF and MitoSOX, external H_2O_2 (10 mM) or the complex III inhibitor antimycin A (150 µM), respectively, were applied as positive controls at the end of each experiment, and only cells exhibiting a clear increase in fluorescence signal in response to H_2O_2/antimycin A were included in the analysis.

All experiments were performed at 37°C and cardiac myocytes were field-stimulated at either 0.5 or 5 Hz frequency. Data were acquired and analysed with IonWizard. Experimental protocols are described separately in the “Methods” section of each study.

2.4 Isolation of mitochondria from mouse heart and skeletal muscle

Isolation of cardiac mitochondria

For mitochondria isolation, mice were sacrificed by intraperitoneal injection of ketamine hydrochloride (100 mg/kg; Pfizer, Karlsruhe, Germany) and xylazine hydrochloride (10 mg/kg; Bayer Healthcare, Berlin, Germany). The protocol for mitochondria isolation from adult mouse heart was first described by Mela and Seitz (133). All media used in the procedure were ice-cold, and all steps were performed on ice or at 4°C. After the animal was sacrificed, the heart was excised and rinsed in a Petri dish filled with isotonic isolation solution. Atrial and non-cardiac tissue was removed, and ventricles were opened to remove blood clots. The heart was then transferred into a 2 mL tube containing 500 µL isolation solution and minced with scissors. Subsequently, the minced heart was transferred to a 5 mL homogenizer (Teflon pestle) and manually homogenized in 1 mL isolation solution for 14 minutes. The homogenate was centrifuged at low speed (400 g) in a pre-cooled (4°C) centrifuge for 5 minutes to remove cell debris. The supernatant obtained from the first centrifugation was centrifuged at high speed (7,700 g) for 10 minutes, and the pellet - containing mitochondria - was washed in 1 mL mitochondrial suspension solution and centrifuged again twice at high speed (7700 g) for 10 minutes. The pellet obtained from the final centrifugation step was resuspended in 100-150 µL mitochondrial suspension solution and used for experiments.

Isolation of skeletal muscle mitochondria

The protocol for mitochondria isolation from mouse skeletal muscle was first described by Chappel and Perry (134). All media used in the procedure were ice-cold, and all steps were performed on ice or at 4°C. After the animal was sacrificed, hindlimb skeletal muscle was rapidly excised and rinsed in a Petri dish filled with basic medium. Connective tissue or adipose tissue was removed and skeletal muscle was placed in a 2 mL tube containing 500 µL homogenization medium containing 1 U of subtilisin A, a serine protease produced by *Bacillus subtilis*, and minced with scissors. The skeletal muscle was then transferred to a 5 mL homogenizer (Teflon pestle) and manually homogenized in 1,5 mL homogenization medium for 14 minutes. The homogenate was centrifuged at low speed (800 g) in a pre-cooled (4°C) centrifuge for 10 minutes to remove cellular debris. The supernatant obtained from the first centrifugation was centrifuged at high speed (12,000 g) for 10 minutes, and the pellet, containing mitochondria, was resuspended in 200 µL basic medium.

2.5 Experiments with isolated mitochondria

Mitochondrial respiration

For three of the studies included in this Thesis [(135, 136), and Bertero *et al.*, *Mechano-energetic uncoupling underlies lack of inotropic reserve in Barth syndrome cardiomyopathy*], mitochondrial respiration was measured polarographically using a Clark electrode (Hansatech) covered with an ultrathin Teflon membrane (Hansatech), while in (137) an Oroboros Oxygraph-2k (Oroboros Instruments, Innsbruck, Austria) was used. Experimental procedures were the same for both instruments.

For each experiment, 400 µg mitochondria were suspended in 2 mL air-saturated respiration buffer [MiR05 in (137)] inside the oxygraph chamber (State 1). Subsequently, mitochondria were supplied with saturating concentrations of the complex I substrates pyruvate and malate (5 mM each). Under this condition, which we refer to as respiratory State 2, respiration is limited by the low level of ADP, and O_2 consumption is mainly due to H^+ leak across the IMM. Thereafter, oxidative phosphorylation was stimulated by the addition of ADP (final concentration: 1 mM), achieving respiratory State 3. Finally, State 4 was obtained by adding the complex V inhibitor oligomycin (1.25 µM) and O_2 consumption drops again. It must be noted that the definitions of respiratory states adopted in this Thesis differ from the ones proposed in the original studies by Chance and Williams (138-141), as summarized in **Table 5**.

Table 5. Definition of respiratory states according to Chance and Williams and adopted in the Thesis.

Respiratory state	Definition by Chance and Williams	Definition adopted in the Thesis
State 1	Mitochondria	Mitochondria
State 2	Mitochondria + ADP	Mitochondria + substrates
State 3	Mitochondria + ADP + substrates	
State 4	ADP depleted by phosphorylation	Complex V inhibition with oligomycin

Mitochondrial H_2O_2 emission

H_2O_2 emission from isolated mitochondria was measured with Amplex UltraRed, a sensitive and H_2O_2-specific indicator that is converted to the fluorescent molecule resorufin (λ_{exc} 535 nm; λ_{em} 595 nm) upon reaction with H_2O_2. Oxidation of Amplex UltraRed by H_2O_2 is catalyzed by horseradish peroxidase (HRP). The assay was performed at 37°C using a fluorescence plate reader (Infinite M200Pro, Tecan) in a 96-well transparent bottom plate. The experiment was conducted with 200 µL respiration buffer containing 165 µg mitochondria per well and the following concentrations of assay reagents: Amplex UltraRed 10 µM, HRP 0.5 U/mL, and SOD 100 U/mL. Respiratory state 1, 2, and 3 were obtained using the same substrates used for mitochondrial respiration measurements; subsequently, the complex III blocker antimycin A (15 µM) was added as a positive control to induce superoxide formation at the ETC. Results were calculated by averaging at least 3 replicates of the same experimental condition. Background fluorescence in the absence of mitochondria was measured for each condition and subtracted accordingly.

It is important to note that Amplex UltraRed does not enter mitochondria, and therefore the H_2O_2 measured with this indicator is the net result of its production and detoxification by mitochondrial antioxidant systems; additionally, H_2O_2 production in the intermembrane space and outer mitochondrial membrane might be relevant under certain conditions (3). Therefore, measurement of H_2O_2 with Amplex UltraRed should not be interpreted as a readout of H_2O_2 *production* at the ETC or in the mitochondrial matrix. On these grounds, the term H_2O_2 *emission* was used when referring to the H_2O_2 detection with this assay.

Permeability transition pore (PTP) assay

Ca^{2+} retention capacity of isolated mitochondria was determined by exposing mitochondria to repeated Ca^{2+} pulses (final free Ca^{2+} concentration 10 µM each pulse) and simultaneously measuring extramitochondrial Ca^{2+} levels with the fluorescence indicator Calcium Green 5-N (λ_{exc} 503 nm; λ_{em} 535 nm) using a fluorescence plate reader (Infinite M200Pro, Tecan). The assay was performed at 37°C in a 96-well transparent bottom plate. For each replicate, 165 µg mitochondria were dissolved in 200 µL PTP buffer. Mitochondria were incubated with potassium glutamate (5 mM) and sodium malate (2.5 mM) with or without the PTP inhibitor cyclosporine A (2 µM) for 15 minutes. Calcium Green 5-N (1 µM) was added immediately before starting the experiment. Ca^{2+} was added by an automatic injector to each well every 120 s. The amount of Ca^{2+} required to obtain 10 µM free Ca^{2+} for each addition was calculated with Maxchelator (http://maxchelator.stanford.edu/CaEGTA-TS.htm). Results were calculated by averaging at least 2 technical replicates of the same experimental condition.

Enzyme activity

Aconitase activity was determined by measuring absorption changes of NAD(P)H every minute at 340 nm using a fluorescence plate reader (Infinite M200Pro, Tecan). The assay was performed in a total volume of 200 µL reaction buffer at 37°C after one freeze/thaw cycle to break mitochondria. For each replicate, 25 µg of mitochondria or cytosol were supplied with (in mM) Tris-HCl 36, cysteine 0.8, $MgCl_2$ 0.4, $NADP^+$ 0.2, citrate 30 (pH 7.4).

Mitochondria do not survive calcium overload during transplantation

Edoardo Bertero, Brian O'Rourke & Christoph Maack

Circulation Research. 2020 March 13;126(6):784-786.

Autologous mitochondrial transplantation was recently proposed as a novel therapeutic strategy to restore cardiac function after myocardial infarction (142). For this intervention, functional mitochondria are isolated from skeletal muscle and then injected directly into the ischemic heart or coronary arteries of the same subject (142). The declared treatment goal is to replace mitochondria in cardiac myocytes damaged by ischemia with respiration-competent mitochondria, whose ATP formation supposedly sustains cardiac vitality and contraction. This approach was tested in preclinical models of ischemia/reperfusion injury (142) and subsequently applied to pediatric patients with myocardial ischemia in an open-label, single-armed clinical trial (NCT02851758). We recently argued that the translation of this approach to the clinical arena may be premature, since it appears unlikely that injected mitochondria withstand high Ca^{2+} concentrations in the extracellular environment (143). In response to our article, McCully and colleagues, who had introduced this approach (142), emphasized that "donor mitochondria are viable in both the isolated perfused heart, where Ca^{2+} concentration was 1.7 mM and in *in vitro* cell studies where Ca^{2+} concentration was 1.8 mM" (144).

It is widely accepted that upper micromolar Ca^{2+} concentrations induce mitochondrial Ca^{2+} overload with fatal activation of the permeability transition pore. However, high extramitochondrial Na^+ concentrations in the bloodstream or extracellular fluid may potentially protect mitochondria from Ca^{2+} overload by inducing Ca^{2+} efflux via the mitochondrial Na^+/Ca^{2+} exchanger. To address this hypothesis, we isolated skeletal muscle mitochondria (as used in the studies by McCully *et al.* (142)) from mice and determined oxygen (O_2) consumption and the mitochondrial membrane potential ($\Delta\psi_m$; using the potentiometric dye tetramethylrhodamine methyl ester, TMRM). Mitochondria were resuspended in either conventional Ca^{2+}-free respiration buffer (RB) or – to mimic the extracellular environment – in Normal Tyrode's solution (NT), containing 140 mM Na^+, 5 mM K^+, and 1 mM Ca^{2+}. Using pyruvate and malate as complex I substrates, respiration was stimulated by increasing concentrations of ADP. In Ca^{2+}-free RB, ADP accelerated O_2 consumption, while in Ca^{2+}-containing NT, respiration was abrogated (**Figure 1a**). This effect was irreversible, since respiration could not be restored by resuspending mitochondria in Ca^{2+}-free RB after 10 min incubation in NT (**Figure 1b**).

When acutely applying 1 mM Ca^{2+} during ADP-stimulated respiration in RB, O_2 consumption slightly and transiently accelerated, but shortly thereafter ceased (**Figures 1c, d**). Immediately after Ca^{2+} addition, $\Delta\psi_m$ depolarized within 20 s and did not repolarize when the ATP synthase was inhibited with oligomycin. Moreover, the mitochondrial uncoupler 2,4-dinitrophenol (DNP) did not further depolarize Ca^{2+}-exposed mitochondria (**Figure 1d**). These data indicate that after Ca^{2+} addition, $\Delta\psi_m$ dissipates completely and is uncoupled from the control by ADP via the ATP synthase. To interrogate whether this effect requires Ca^{2+} uptake via the mitochondrial Ca^{2+} uniporter (MCU), mitochondria were preincubated with the MCU inhibitor ruthenium red. Under these conditions, $\Delta\psi_m$ was only partially depolarized by Ca^{2+} addition, and ADP-induced control of respiration was maintained at levels comparable to that of mitochondria in Ca^{2+}-free RB (**Figures 1e** and **f**).

We conclude that skeletal muscle mitochondria are unable to withstand the ionic milieu of blood or the extracellular space, characterized by millimolar Ca^{2+} and Na^+ concentrations, since mitochondria are immediately and irreversibly damaged by depolarization of $\Delta\psi_m$ as a result of rapid MCU-mediated Ca^{2+} overload. These results argue against the plausibility of the proposed concept of mitochondrial transplantation, according to which a) extracellular mitochondria provide ATP to ischemic myocardium and b) functional mitochondria eventually become internalized into cardiac myocytes to replace mitochondria damaged by ischemic injury (142, 143). Therefore, although the scientific question behind our experiments may appear trivial, the question how mitochondria can survive a “high Ca^{2+} shock” during mitochondrial transplantation, especially when applied to patients, should no longer be ignored.

Instead, our results raise the new question whether the *contents* of permeabilized mitochondria (e.g., peptides, glutathione, adenosine di- or triphosphate, mitochondrial DNA etc.) might account for the beneficial effects reported by McCully and colleagues (142, 143) in a *paracrine* fashion rather than the mitochondria directly contributing to respiration. In this context, it is possible that mitochondria act as delivery vehicles for molecules released into the interstitial space of the myocardium, which could then act as damage-associated molecular patterns (145) to shape the immune response to myocardial ischemia in a protective manner, similar to the model recently proposed to explain the benefits of stem cell therapy after myocardial infarction (146). If this is the case, the increased membrane permeability induced by the Ca^{2+} shock could even be a *requirement*, rather than a *threat*, for the efficiency of this novel and intriguing treatment strategy. In conclusion, our results may guide the focus of emerging research in this area towards further clarifying the mechanisms that underlie the cardioprotective effects before this procedure is further applied in humans.

Figure and Legend

Figure 1.

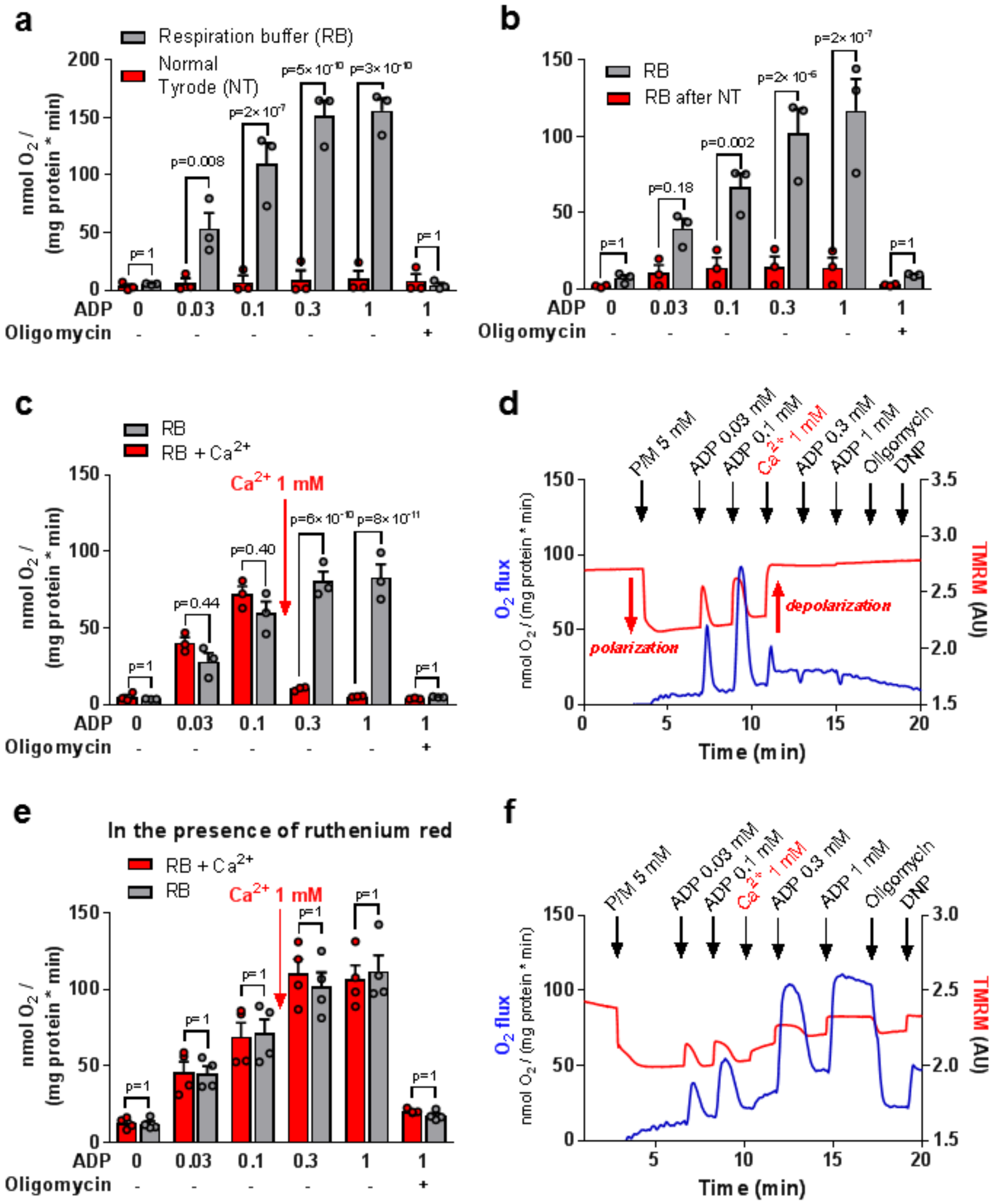

a, Mitochondria were isolated from murine musculus quadriceps and resuspended either in respiration buffer (RB) containing (in mM) EGTA 0.5, taurine 20, $MgCl_2$ 3, sucrose 110, K-lactobionate 60, KH_2PO_4 10, K-HEPES 20, BSA 1 mg/mL or Normal Tyrode´s solution (NT), containing (in mM): NaCl 130, KCl 5, $MgCl_2$ 1, $CaCl_2$ 1, Na-HEPES 10, glucose 10, sodium pyruvate 2 and ascorbic acid 0.3. Mitochondria were supplied with pyruvate and malate (5 mM, respectively) as complex I substrates, and respiration (measured by an Oroboros O2k system) was induced by sequential additions of increasing concentrations of ADP ("State 3" respiration), before oligomycin (1.2 µM) was added to block the ATP synthase. **b**, Similar conditions as in **a**, unless that mitochondria were incubated in NT for 10 min and then centrifuged at 12.000 rpm for 5 min and resuspended in Ca^{2+}-free RB. The control group was treated in the same way except that mitochondria were preincubated with Ca^{2+}-free RB. **C**, Similar conditions as the RB groups in **a** and **b**, unless that in one group (RB + Ca^{2+}), 1 mM Ca^{2+} was added during state 3 respiration. **d**, representative example of the group RB + Ca^{2+} from **C**, showing (besides respiration) also the fluorescence of TMRM (1 µM). Upon polarization, TMRM fluorescence decreases due to quenching of TMRM fluorescence, while upon depolarization, fluorescence increases due to dequenching of the signal. ADP concentrations are given in mM. Oligomycin (1.2 µM) and DNP (5 µM) were added at the end of the protocol. **e** and **f,** similar conditions as in **c** and **d**, except that all experiments were performed in the presence of the MCU blocker ruthenium red (25 µM). Animal procedures were approved by the local animal ethics committee and conducted in accordance with institutional guidelines. All cumulative data are the means ±SEM of n=3 experiments, respectively. The Shapiro-Wilk normality test was performed to determine data distribution. Data were analyzed with 2-way analysis of variance (ANOVA) followed by Bonferroni's post-hoc test. The *p*-values presented are corrected for multiple testing. A *p*-value <0.05 was considered statistically significant.

CaMKII does not control mitochondrial Ca^{2+} uptake in cardiac myocytes

Alexander G. Nickel*, Michael Kohlhaas*, Edoardo Bertero, Daniel Wilhelm, Michael Wagner, Vasco Sequeira, Michael M. Kreusser, Matthias Dewenter, Reinhard Kappl, Markus Hoth, Jan Dudek, Johannes Backs, Christoph Maack

*Alexander G. Nickel and Michael Kohlhaas contributed equally to this work.

The Journal of Physiology. 2020 April;598(7):1361-1376.

Abstract

Mitochondria are the main source of ATP and reactive oxygen species (ROS) in cardiac myocytes. Furthermore, activation of the mitochondrial permeability transition pore (mPTP) induces programmed cell death. These processes are essentially controlled by Ca^{2+}, which is taken up into mitochondria via the Ca^{2+} uniporter (MCU). It was recently proposed that Ca^{2+}/calmodulin-dependent protein kinase II (CaMKII) regulates Ca^{2+} uptake by interacting with the MCU, thereby affecting mPTP activation and programmed cell death. Here, we addressed the role of CaMKII under physiological conditions in which mitochondrial Ca^{2+} uptake matches energy supply to demand of cardiac myocytes. To this end, we measured mitochondrial Ca^{2+} uptake in isolated mitochondria and cardiac myocytes harvested from cardiomyocyte-specific CaMKII δ and γ double KO (CaMKIIδ/γ DKO) and global CaMKIIδ KO mice. To simulate a physiological workload increase, cardiac myocytes were subjected to β-adrenergic stimulation (by isoproterenol superfusion) and increase in stimulation frequency (from 0.5 to 5 Hz). No differences in mitochondrial Ca^{2+} accumulation were detected in isolated mitochondria or cardiac myocytes from both CaMKII KO models compared with wild-type (WT) littermates. Mitochondrial redox state and ROS production were unchanged in CaMKIIδ/γ DKO, whereas we observed a mild oxidation of mitochondrial redox state and an increase in H_2O_2 emission from CaMKIIδ KO cardiac myocytes exposed to an increase in workload. In conclusion, our results argue against a relevant regulation of mitochondrial Ca^{2+} uptake via the MCU or mPTP activation by CaMKII in cardiac myocytes under physiological conditions.

Introduction

The processes of cardiac excitation-contraction (EC) coupling are initiated by the propagation of an action potential across the sarcolemma, which induces calcium (Ca^{2+}) influx from the extracellular space by opening of voltage-gated L-type Ca^{2+} channels (LTCC). In turn, this Ca^{2+} influx triggers an even greater release of Ca^{2+} from the sarcoplasmic reticulum (SR) via ryanodine receptors 2 (RyR2), a process coined Ca^{2+}-induced Ca^{2+} release. The increase in intracellular Ca^{2+} concentration ($[Ca^{2+}]_c$) initiates cross-bridge cycling and thereby, contraction of the myofilaments (17). During diastole, Ca^{2+} is taken back up into the SR via the SR Ca^{2+} ATPase (SERCA) or extruded to the extracellular space by the sarcolemmal sodium (Na^+)/Ca^{2+} exchanger. The processes of EC coupling consume large amounts of ATP, which is mainly regenerated by oxidative phosphorylation in mitochondria (17). Besides being the main producer of ATP, mitochondria represent also the dominant source of reactive oxygen species (ROS) in cardiac myocytes. ROS production leads to oxidative stress, which has been causally related to maladaptive remodeling, arrhythmogenesis and progression of heart failure (HF) (147, 148).

Ca^{2+} is an essential regulator of both ATP production and ROS elimination in mitochondria (8). When β-adrenergic stimulation triggers an increase in cardiac workload, the increase in amplitude and frequency of cytosolic Ca^{2+} transients drives Ca^{2+} accumulation in the mitochondrial matrix. Here, Ca^{2+} stimulates the Krebs cycle dehydrogenases to regenerate reduced NADH and $FADH_2$, which in turn donate electrons to the electron transport chain (ETC) for ATP production, thereby matching the increase in energy demand with an increase in ATP supply (149). Furthermore, the Krebs cycle products isocitrate, malate and NADH are required for the regeneration of reduced NADPH, which maintains mitochondrial H_2O_2-detoxifying systems in their active form (46, 148). Finally, mitochondria are crucial mediators of the intrinsic pathway of programmed cell death, and Ca^{2+} plays a pivotal role also in this process. In fact, mitochondrial Ca^{2+} overload leads to sustained opening of the mitochondrial permeability transition pore (mPTP), a pore in the inner mitochondrial membrane which enables release of ions and solutes from the mitochondrial matrix and thereby, triggers programmed cell death (150).

Mitochondrial Ca^{2+} uptake is predominantly mediated by a protein complex residing in the inner mitochondrial membrane denoted as the mitochondrial Ca^{2+} uniporter (MCU). The MCU is composed of a pore-forming subunit (MCUa) (151, 152), a dominant-negative subunit (MCUb) (153), an essential regulatory element (EMRE) (154) and a dimer of regulatory subunits termed MICU1/MICU2 (155, 156), which partly accounts for the complex physiological properties of the MCU (8). Since Ca^{2+} uptake via the MCU is driven by the large negative mitochondrial membrane potential ($\Delta\Psi_m$), the MICU1/MICU2 dimer operates as a gate-keeper, preventing mitochondrial Ca^{2+} overload and consequent mPTP opening (155, 157). For this reason, the Ca^{2+} affinity of the MCU is apparently low (K_d 10-20 μM), and efficient mitochondrial Ca^{2+} uptake is enabled by the close apposition of mitochondria and the SR. It has been proposed that specialized Ca^{2+} microdomains are formed between sites of Ca^{2+} release from the SR and mitochondria to achieve a spatially localized increase in $[Ca^{2+}]_c$ required to overcome the low apparent affinity of the uniporter (158). It is currently unknown whether the molecular complexity of MCU is sufficient to explain its physiological properties, and it cannot be excluded that MCU activity is modulated by intracellular signaling pathways.

The multifunctional Ca^{2+}/calmodulin-dependent protein kinase II (CaMKII) is a serine/threonine phosphokinase which is activated upon Ca^{2+}/calmodulin binding in response to increases in $[Ca^{2+}]_c$ (159). In addition, several Ca^{2+}-independent regulators of CaMKII activity have been identified, including oxidative modification (160), S-nitrosylation (161) and O-linked glycosylation (162), suggesting that CaMKII is a central hub integrating various forms of stress towards cellular Ca^{2+} handling, but also transcriptional regulation of cardiac hypertrophy. The four CaMKII isoforms (α, β, γ and δ) display distinct tissue expression patterns, with CaMKIIδ and γ being the predominant isoforms in the heart (163). CaMKII phosphorylation targets include several key proteins involved in EC coupling, such as LTCC, RyR2 and phospholamban, and the phosphorylation state of these proteins fine-tunes intracellular Ca^{2+} handling (159). For instance, CaMKII was recently shown to mediate the cardiac contractile response to exercise training by modulating cytosolic Ca^{2+} handling via phospholamban phosphorylation (164). Although little is known about CaMKII function in the healthy heart (159), the role of CaMKII in cardiac disease has been extensively investigated, revealing that its kinase activity plays a key role in the transduction of pathological Ca^{2+} signals, ultimately contributing to maladaptive remodeling and cardiac dysfunction. In fact, CaMKII expression and activity are enhanced in HF, and this overactivation may contribute to the increase in intracellular Na^+ and Ca^{2+} concentrations and SR Ca^{2+} depletion observed in the failing heart (165).

Furthermore, CaMKII modulates the expression of a wide set of genes, and was shown to induce pro-hypertrophic gene expression by phosphorylating histone deacetylase 4 (HDAC4) (166, 167). Finally, CaMKII regulates apoptosis of cardiac myocytes, although its effects may be either pro- or anti-apoptotic depending on the isoforms (168, 169).

A wealth of experimental studies demonstrated that genetic or pharmacological CaMKII inhibition has cardioprotective effects in ischemia/reperfusion injury and pathological pressure overload (129, 130, 170), indicating that CaMKII activation in response to cardiac stressors is a key mediator of maladaptive remodeling. However, mechanisms underlying the beneficial effects associated with CaMKII inhibition are not completely resolved. A recent study by Joiner *et al.* (171) proposed that CaMKII regulates mitochondrial Ca^{2+} uptake in the heart by phosphorylating the MCU, consequently impacting on mPTP activation and programmed cell death during ischemia/reperfusion. However, the results of this study were challenged by Fieni *et al.* (172), who did not detect effects of CaMKII on MCU current density in experiments employing patch-clamping of isolated mitochondria. One point of controversy was that Fieni *et al.* (172) argued that the purported MCU current measured by Joiner *et al.* (171) was at least two orders of magnitude higher than previously reported MCU currents, possibly due to compromised integrity of mitochondria. Furthermore, Joiner and colleagues tested for an effect of CaMKII on the MCU exclusively by mutating two putative phosphorylation sites on MCUa, and therefore direct evidence demonstrating MCU phosphorylation by CaMKII is currently lacking. Thus, it is still controversial whether CaMKII modulates MCU-dependent mitochondrial Ca^{2+} uptake. However, the mentioned studies neither used knock-out (KO) technology nor addressed the role of CaMKII under physiological conditions in which mitochondrial Ca^{2+} uptake matches energy supply to demand of cardiac myocytes. Here, we investigated the functional consequences of genetic deletion of CaMKII on mitochondrial function in two mouse models characterized by global constitutive deletion of CaMKIIδ (CaMKIIδ KO) and conditional cardiomyocyte-specific deletion of CaMKIIδ and γ (CaMKIIδ/γ DKO), respectively. Whereas CaMKII activity is totally abolished in cardiac myocytes of CaMKIIδ/γ DKO mice (130), CaMKIIδ KO mice retain expression of the minority γ isoform, which might partially compensate for the lack of CaMKIIδ–dependent phosphorylation (130, 169). Our results argue against a relevant role of CaMKII for mitochondrial Ca^{2+} handling, redox state and ROS production under physiological conditions.

Methods

Ethical approval and animal experiments

Animal procedures were approved by the local animal ethics committees (Animal Experiment Review Board of the state of Baden-Württenberg, Germany; ethics committee approval reference number: G-268/16) and conform to the principles and regulations as described by Grundy (173). For cardiac myocyte isolation, mice received carprofen (12 mg/kg) and heparin (10,000 IE/kg) and were anaesthetized with isoflurane (5% at 0.5 L/min). When mice became insensible to pedal reflex, the heart was excised and processed depending on the experiment. For mitochondria isolation from mouse hearts, mice were sacrificed by intraperitoneal injection of ketamine hydrochloride (100 mg/Kg; Pfizer, Karlsruhe, Germany) and xylazine hydrochloride (10 mg/kg; Bayer Healthcare, Berlin, Germany).

Mouse strains

Generation and characterization of CaMKIIδ KO and CaMKIIδ/γ DKO mice were described previously (129, 130, 174, 175). Global CaMKIIδ KO and tamoxifen-inducible cardiac-specific CaMKIIδ/CaMKIIγ double knockout (CaMKIIδ/γ DKO) mice were born in the expected mendelian ratios and developed normally until adulthood.

Experiments on isolated cardiac myocytes

Most methods employed were performed as reported previously (47, 176). Briefly, for the experiments in **Figures 3** and **7**, isolated adult ventricular myocytes were field-stimulated at 37°C with a stimulation rate of 0.5 Hz and superfused with Normal Tyrode´s (NT) solution containing (in mM): NaCl 130, KCl 5, $MgCl_2$ 1, $CaCl_2$ 1, Na-HEPES 10, glucose 10, sodium pyruvate 2 and ascorbic acid 0.3, pH 7.4. After 120 s, cardiac myocytes were superfused with NT solution containing 30 nM isoproterenol, and after 60 s, the stimulation rate was increased to 5 Hz for 180 s. Finally, the stimulation rate was set back to 0.5 Hz and isoproterenol was washed out. During this stress protocol, sarcomere length, NAD(P)H and FAD autofluorescence (for **Figure 3**), MitoSOX and 5-(-6)-chloromethyl-2,7-dichlorohydrofluorescein di-acetate (CM-H_2DCFDA, in the following denoted as DCF) fluorescence (for **Figure 7**) were recorded using an IonOptix set-up. MitoSOX is a mitochondria-targeted fluorogenic dye which emits fluorescence upon reaction with superoxide ($\cdot O_2^-$). While DCF fluorescence derives from both the cytosol and mitochondria, previous studies suggest that most of its fluorescence derives from mitochondria under the conditions employed (177). In other experiments, we monitored cytosolic Ca^{2+} concentrations together with the mitochondrial membrane potential ($\Delta\psi_m$) of intact cardiac myocytes by loading the cells with the fluorescent Ca^{2+} indicator indo-1 acetoxymethyl ester (AM) and tetramethyl-rhodamine methyl ester (TMRM), a potentiometric marker of $\Delta\psi_m$.

To determine mitochondrial Ca^{2+} levels in isolated cardiac myocytes (**Figure 2**), we used a patch-clamp-based dual-fluorescence approach as previously described (27, 30, 46). Briefly, cardiac myocytes were incubated for 2 hours with rhod-2-AM, a mitochondria-located Ca^{2+} indicator, and then cytosolic remnants of rhod-2-AM were eliminated by dialyzing the cytosol with a rhod-2-free pipette solution. At the same time, the pipette solution contained 75 µM of indo-1 penta-K^+ salt which, by its inability to pass membranes, reports specifically $[Ca^{2+}]_c$ (30). Besides indo-1, the pipette solution contained (in mM): potassium glutamate 130, KCl 19, $MgCl_2$ 0.5, Na-HEPES 15, Mg-ATP 5, pH 7.2. Subsequently, cardiac myocytes were voltage-clamped in whole-cell configuration (37°C, pipette resistance 2-4 MΩ) and subjected to the same experimental stress protocol described above by depolarizing the cell from -80 to +10 mV for 50 ms at 0.5 and 5 Hz.

Experiments on isolated mitochondria

Mitochondria were isolated from mouse hearts, and respiration was measured at 30°C with a Clark electrode as described previously (47). State 2 respiration was obtained by adding sodium pyruvate 5 mM and sodium malate 5 mM. After 180 s, increasing ADP concentrations (0.03, 0.1, 0.3 and 1 mM) were added to induce state 3 respiration. Finally, state 4 respiration was estimated by inhibiting F_1-F_o ATP synthase with oligomycin (1.2 µM).

Ca^{2+}-retention assays (mPTP assays) were performed with minor modifications compared with our previous work (47): mitochondria were preincubated with 5 mM K-glutamate/2.5 mM malate in the absence or presence of cyclosporine A (1 µM) for 5 min. In a separate set of experiments, mitochondria were also preincubated with 100 µM H_2O_2.

Superoxide ($\cdot O_2^-$) production from mitochondria was measured by electron paramagnetic resonance (EPR) using a Bruker spectrometer (ESP300e). The redox activated cyclic hydroxylamine spin trap CMH (1-hydroxy-3-methoxycarbonyl-2,2,5,5 tetramethyl-pyrrolidine) was added before the experiment in 300 µM to monitor superoxide ($\cdot O_2^-$) production, as outlined in more detail previously (47).

H_2O_2 emission from mitochondria was measured using 10 µM of H_2O_2-specific fluorescent dye Amplex® UltraRed (AUR, Life Technologies, Molecular Probes, Carlsbad, CA, USA). Upon horseradish peroxidase-catalyzed reaction with H_2O_2, AUR forms the fluorescent product Resorufin (excitation 535 nm, emission 590 nm). Assay component concentrations were 10 µM for AUR, 0.5 U ml^{-1} HRP, 100 U ml^{-1} SOD. Experiments were performed with 30 µM mitochondria per well in triplicate in 96-well plates using the Tecan GENios Pro Reader (Tecan Group Ltd, Männedorf, Switzerland) and were conducted in respiration buffer as in previous studies (47). H_2O_2 was quantified from a calibration curve obtained with defined H_2O_2 concentrations.

Both $\cdot O_2^-$ and H_2O_2 production were measured after treatment with 2,4-dinitrophenol (DNP) as a mitochondrial uncoupler, antimycin A (15 µM) to provoke superoxide ($\cdot O_2^-$) production at complex III of the ETC, 1 mM ADP and in the presence of pyruvate/malate (both 5 mM).

Measurements of enzyme activities

Methods for measurement of enzyme activities were described previously (47).

Statistical analyses

Results are displayed as mean ± standard error of the mean (SEM). Two-way ANOVA with Bonferroni's multiple comparisons test and unpaired t-tests were performed using GraphPad Prism version 7.0 for Windows (GraphPad Software, La Jolla, CA, USA).

Results

Mitochondrial Ca^{2+} uptake is not affected by CaMKII deletion

In the study by Joiner *et al.* (171), mitochondrial expression of a CaMKII inhibitory peptide protected mitochondria challenged with high Ca^{2+} concentrations from $\Delta\Psi_m$ depolarization and mPTP opening. To evaluate the consequences of CaMKII deletion on mitochondrial Ca^{2+} uptake and permeability transition, we exposed isolated cardiac mitochondria to repetitive Ca^{2+} pulses (10 µM every 120 s) while monitoring extramitochondrial Ca^{2+} concentrations with a fluorescent Ca^{2+} indicator

(CalciumGreen). The experiment was performed in the absence and presence of cyclosporine A (1 µM), a pharmacological inhibitor of mPTP opening. We did not observe any difference in mitochondrial Ca^{2+} uptake or retention capacity between WT and CaMKIIδ KO or CaMKIIδ/γ DKO, neither in the absence (**Figure 1A**) nor presence (**Figure 1B**) of cyclosporine A, suggesting that CaMKII has no effect on MCU activity and mPTP opening in this context. In addition to Ca^{2+} accumulation, which is an essential permissive factor for permeability transition, mPTP open probability can be increased by ROS and oxidation of mitochondrial pyridine nucleotides (178). To test whether CaMKII deletion interfered with ROS-dependent mPTP opening, we performed the experiments described above using mitochondria preincubated with H_2O_2 (100 µM). Also in this setting, no differences were detected in mitochondrial Ca^{2+} retention capacity between WT and CaMKIIδ KO or CaMKIIδ/γ DKO (**Figures 1C, D**).

These results do not rule out that CaMKII regulates mitochondrial Ca^{2+} uptake and permeability transition by acting on extra-mitochondrial proteins involved in Ca^{2+} handling (171). Therefore, we investigated whether genetic silencing of CaMKII influences mitochondrial Ca^{2+} accumulation when mitochondria are integrated in their natural context of cardiac myocytes subjected to an increase in workload. To this end, isolated cardiac myocytes were loaded with the mitochondria-located Ca^{2+} indicator rhod-2-AM. Subsequently, cells were patch-clamped in whole-cell configuration and the cytosolic remnants of rhod-2-AM were eliminated by dialysing the cytosol with a pipette solution containing the Ca^{2+} indicator indo-1, as described previously (30). To simulate an increase in workload, cardiac myocytes were superfused with the β-adrenergic agonist isoproterenol and stimulation frequency was increased from 0.5 to 5 Hz for 180 s. As previously reported, β-adrenergic stimulation and increased stimulation frequency increased the amplitude of cytosolic and mitochondrial Ca^{2+} transients and led to Ca^{2+} accumulation in mitochondria (30, 46). In agreement with previous studies (129, 130, 179), despite a small trend towards larger cytosolic Ca^{2+} transients in CaMKIIδ KO myocytes, no significant difference in amplitude and kinetics of cytosolic Ca^{2+} transients between WT and CaMKIIδ KO or CaMKIIδ/γ DKO cardiac myocytes (**Figure 2A**) could be observed, confirming that CaMKII deletion does not alter cytosolic Ca^{2+} handling. Finally, and consistent with the results obtained in isolated mitochondria, mitochondrial Ca^{2+} accumulation did not differ between WT and CaMKIIδ KO or CaMKIIδ/γ DKO (**Figure 2B**). Taken together, these results indicate that CaMKII does neither affect cytosolic nor mitochondrial Ca^{2+} handling in cardiac myocytes under physiological conditions.

Effects of CaMKII deletion on mitochondrial redox state

Mitochondrial Ca^{2+} uptake is an important regulator of the mitochondrial redox state, since the activity of rate-limiting enzymes of the Krebs cycle is stimulated by Ca^{2+} accumulation in the mitochondrial matrix (149). Conditions associated with defective Ca^{2+} uptake or accelerated Ca^{2+} efflux from mitochondria oxidize the mitochondrial pyridine nucleotide pool during physiological workload transitions (30, 46). To evaluate the consequences of CaMKII deletion on the mitochondrial redox state, we determined the autofluorescence of reduced and oxidized forms of the pyridine nucleotides $NAD(P)^+$ and FAD in intact cardiac myocytes exposed to a simulated increase in cardiac workload (i.e., β-adrenergic stimulation and increased stimulation frequency, as described above). As previously demonstrated, the increase of ADP flux to mitochondria associated with this workload transition accelerates electron flow along the ETC, thereby inducing a mild and transient oxidation of the $NAD(P)H/NAD(P)^+$ and $FADH_2/FAD$ redox states and the NAD(P)H/FAD ratio, a sensitive index of mitochondrial redox state which eliminates movement artifacts. Subsequently, the increase in energy demand is compensated by mitochondrial Ca^{2+} uptake and Ca^{2+}-dependent stimulation of the Krebs cycle, which promotes regeneration of reduced NAD(P)H and $FADH_2$ (20, 30, 46). We did not observe any difference in NAD(P)H and FAD autofluorescence and the NAD(P)H/FAD ratio in CaMKIIδ/γ DKO compared with WT cardiac myocytes subjected to this physiological increase in workload (**Figure 3A, B**). In contrast, CaMKIIδ KO cardiac myocytes displayed a slight oxidation of mitochondrial redox state at baseline compared with WT, which was maintained throughout the stress protocol (**Figure 3A, B**). To exclude that this finding resulted from decreased activity of the Krebs cycle, we measured the activity of four key Krebs cycle enzymes, namely aconitase, isocitrate, α-ketoglurarate and malate dehydrogenases, but did not observe any difference in their enzymatic activities between different genotypes (**Figure 4**). However, we cannot exclude that activity of Krebs cycle enzymes is regulated by CaMKII in intact cardiac myocytes, because any regulatory mechanism dependent on mitochondrial integrity would be disrupted within this assay. Finally, and consistent with previous studies (129, 130, 179), CaMKII deletion did not have any effect on sarcomere shortening and relaxation (**Figure 5**), indicating that CaMKII activity is dispensable for contractility of cardiac myocytes both at baseline and under conditions of acutely increased workload.

Effects of CaMKII deletion on mitochondrial respiration and ROS production

Mitochondria are the main source of ROS in cardiac myocytes, and ROS production can induce mitochondrial permeability transition and subsequent cell death. In the heart challenged with pathological pressure overload, activation of pro-hypertrophic signaling pathways leads to impaired mitochondrial respiration and ROS generation in a CaMKIIδ-dependent manner (180). To probe whether CaMKIIδ KO or CaMKIIδ/γ DKO influenced mitochondrial respiration and ROS production at the ETC under physiological conditions, we measured oxygen (O_2) consumption, superoxide ($\cdot O_2^-$) production and hydrogen peroxide (H_2O_2) formation in isolated cardiac mitochondria supplied with pyruvate and malate in the absence and presence of different concentrations of ADP to simulate an increase in energy demand. In agreement with our previous studies, ADP increased oxygen consumption and decreased $\cdot O_2^-$ and H_2O_2 emission (47). We did neither detect any differences in O_2 consumption (**Figure 6A**) nor ROS production (**Figure 6B, C**) between WT, CaMKIIδ KO and CaMKIIδ/γ DKO mitochondria, respectively.

To interrogate whether mitochondrial ROS production is affected in intact cells, cardiac myocytes were loaded with the mitochondria-targeted fluorogenic indicator MitoSOX, and fluorescence was measured during the experimental stress protocol described above (β-adrenergic stimulation and increased stimulation frequency). In agreement with our results obtained in isolated mitochondria, mitochondrial superoxide formation was not changed in CaMKIIδ KO and CaMKIIδ/γ DKO compared with WT cardiac myocytes (**Figure 7A, B**). In addition to increased ROS generation at the ETC, mitochondrial ROS emission can result from a decrease in mitochondrial antioxidative capacity. In fact, the mitochondrial manganese-dependent superoxide dismutase (Mn-SOD) very efficiently converts $\cdot O_2^-$ to H_2O_2, which in turn is detoxified by two enzymatic systems whose activities are maintained by the Krebs cycle-dependent regeneration of reduced NADPH. To evaluate whether CaMKII deletion affected ROS emission in intact cardiac myocytes, the latter were loaded with the ROS indicator DCF, and accumulation of DCF fluorescence was assessed during the experimental stress protocol described above. While we did not detect any differences in ROS emission in CaMKIIδ/γ DKO compared with WT cardiac myocytes, accumulation of DCF fluorescence diverged early during the stress protocol in CaMKIIδ KO cardiac myocytes and became significantly higher than the one in littermate WT cells during 5 Hz stimulation (**Figure 7C, D**). These results suggest that ROS generation is increased in CaMKIIδ KO cardiac myocytes subjected to a physiological increase in workload. This finding is not explained by a defect of the ETC or mitochondrial antioxidative capacity *per se*, since we did not observe an increase in mitochondrial $\cdot O_2^-$ or H_2O_2 emission from isolated mitochondria (**Figure 6**).

Finally, since the mitochondrial membrane potential ($\Delta\psi_m$) is important for the regulation of mitochondrial Ca^{2+} uptake and ROS formation, we determined it in WT and CaMKIIδ/γ DKO myocytes using TMRM. This was unaffected by the physiological stress protocol and unchanged in CaMKIIδ/γ DKO compared to WT myocytes (**Figure 7E**).

Discussion

The role of CaMKII in the transduction of pathological Ca^{2+} signals in cardiac disease has been extensively investigated, revealing that CaMKII lies downstream of various cardiac stressors and mediates maladaptive cardiac remodeling in response to pressure overload (179) and ischemia/reperfusion injury (174). Thus, CaMKII inhibition is emerging as a viable therapeutic strategy to prevent the transition from compensated cardiac dysfunction to overt HF. However, it is currently unclear whether CaMKII plays a relevant role in the heart under physiological conditions, which could potentially limit the development of CaMKII inhibition as a therapeutic approach (159). Recently, the development of mouse models characterized by genetic deletion of CaMKII enabled scientists to overcome the limitations of previous studies in which CaMKII activity was inhibited with peptides (e.g. AC3-I) or small molecules (e.g. KN93) that were likely associated with off-target effects (129). In this study, we investigated the consequences of CaMKII deletion on mitochondrial function, revealing that CaMKII does not play a relevant role in the modulation of mitochondrial Ca^{2+} uptake, redox state and ROS generation under physiological conditions.

CaMKII is dispensable for cytosolic Ca^{2+} handling and cellular contractility

Because CaMKII phosphorylation targets include several proteins involved in EC coupling, it was surprising to observe that CaMKII deletion does not have any substantial consequence on cytosolic Ca^{2+} handling and cellular contractility. While in CaMKIIδ KO mice, this finding can be partly explained by the compensatory activation of CaMKIIγ (179), previous studies reported that cardiac CaMKII activity is almost completely abolished in CaMKIIδ/γ DKO mice (130). In agreement with those previous studies (129, 130, 179), we confirmed that kinetics of cytosolic Ca^{2+} transients and cellular contractility are preserved in both mouse models, and we observed that this is also maintained when cardiac myocytes are challenged with a short-term increase in workload through β-adrenergic stimulation. These findings are of translational relevance, because any detrimental effect of CaMKII deletion on Ca^{2+} handling in cardiac myocytes would preclude the development of therapeutic approaches based on CaMKII inhibition. However, a limitation of this study is that we examined the effects of CaMKII genetic ablation exclusively in cardiac myocytes, and therefore our results do not rule out that CaMKII inhibition could negatively affect the functioning myocardium.

CaMKII and mitochondrial Ca^{2+} uptake

Joiner *et al.* (171) reported that CaMKII increases MCU current via direct phosphorylation of the uniporter. Although this study mainly focused on the effects of CaMKII inhibition in the setting of ischemia/reperfusion injury, their results in patch-clamped mitoplasts suggested that CaMKII modulates MCU currents also under physiological conditions. To address this question, we measured mitochondrial Ca^{2+} uptake in isolated cardiac mitochondria and patch-clamped cardiac myocytes subjected to an increase in workload. Both approaches indicated that CaMKII deletion does not affect mitochondrial Ca^{2+} accumulation. It is important to note that any effect of CaMKII on mitochondrial Ca^{2+} uptake under physiological conditions would have represented an important caveat against its development as a therapeutic target. In fact, mitochondrial Ca^{2+} uptake is crucial for both energy supply-and-demand matching and mitochondrial antioxidative capacity (8, 30, 46). Because of their high basal heart rate, mice cannot increase cardiac output more than 0.5-fold (181), whereas in humans, cardiac output needs to be increased up to 4- to 5-fold during physical exertion (182). Therefore, it is likely that metabolic adaptations driven by mitochondrial Ca^{2+} are even more relevant in humans than in mice (8), and thus the consequences of mitochondrial Ca^{2+} uptake inhibition in human hearts are not trivial to predict.

Mitochondrial permeability transition is a well-established mechanism of cardiac myocyte death during ischemia/reperfusion injury, and mPTP opening can be triggered by Ca^{2+} overload and ROS production (178). Pharmacological inhibition with Ru360 in rats (183) or cardiomyocyte-specific genetic deletion of the MCU in mice (22, 184) ameliorates ischemia/reperfusion injury, indicating that Ca^{2+} overload is a dominant trigger of mPTP opening in this setting. In this context, Joiner *et al.* (2012) proposed that by decreasing MCU-dependent Ca^{2+} uptake, CaMKII inhibition prevents mPTP opening during ischemia/reperfusion, thereby exerting a cardioprotective effect. Here, we report that CaMKII deletion does not interfere with mPTP opening in isolated cardiac mitochondria challenged with supraphysiological Ca^{2+} concentrations, and this finding was also confirmed when mitochondria were preincubated with H_2O_2, which further sensitizes to mPTP opening. Therefore, these results argue against CaMKII regulating mitochondrial permeability transition in the heart under pathological conditions. Of note, our results are corroborated by our recent study which demonstrated that neither deletion of CaMKIIδ alone nor of both CaMKIIδ and γ protected from acute myocardial damage shortly after ischemia/reperfusion injury (I/R), but rather ameliorated post-infarct remodeling due to reducing chemoattractant signaling and leukocyte invasion about three days after I/R (174).

CaMKII and mitochondrial redox state

In line with the absence of a significant effect of CaMKII deletion on mitochondrial Ca^{2+} uptake, CaMKIIδ/γ DKO cardiac myocytes challenged with an increase in workload did not display any difference in mitochondrial redox state, which is tightly regulated by the Ca^{2+}-dependent stimulation of the Krebs cycle (20, 30). In contrast, we observed a mild oxidation of NAD(P)H/FAD redox states at baseline which was maintained (but not aggravated) during workload transitions in CaMKIIδ KO cardiac myocytes. Interestingly, oxidation of mitochondrial redox state was associated with an increase in ROS emission from CaMKIIδ KO cardiac myocytes, which we did not detect in CaMKIIδ/γ DKO. These findings stand to some degree at odds with previous studies in which CaMKIIδ was pinpointed as a key mediator of mitochondrial reprogramming during pathological pressure overload, ultimately leading to mitochondrial oxidative stress and cell death (180). One might speculate that the trend towards increased amplitude of cytosolic Ca^{2+} transients observed in CaMKIIδ KO during workload transitions increases energy expenditure at the myofilaments, and since this is not accompanied by a concomitant increase in mitochondrial Ca^{2+} accumulation (**Figure 2B**), the ensuing elevation of ADP flux could create a mismatch between energy supply and demand, potentially oxidizing NAD(P)H/FAD redox states in CaMKIIδ KO cardiac myocytes. In turn, since mitochondrial H_2O_2–detoxifying systems are maintained in their active form by reduced NADPH, this could impair H_2O_2 detoxification during workload transitions. However, we believe this is not the case, since *i)* the (non-significant) increase in amplitude of cytosolic Ca^{2+} transients does not lead to an increase in sarcomere shortening of cardiac myocytes (**Figure 5**), which would be required to augment ATP consumption at the myofilaments; and *ii)* the mitochondrial redox state is already oxidized at baseline in CaMKIIδ KO cardiac myocytes, and this oxidation is not further aggravated during workload transitions. Another important point to consider is the fundamental difference between the two mouse models used in this study: while CaMKIIδ/γ DKO is cardiomyocyte-specific and inducible, CaMKIIδ KO is global and constitutive. The differences observed in the CaMKIIδ KO mouse model suggest that factors outside of cardiac myocytes, e.g. a paracrine effect of other cardiac cell types, may impact mitochondrial redox regulation. However, considering the dominating question of our study, the experiments performed on the CaMKIIδ/γ DKO mouse provide the most relevant information. In conclusion, we cannot provide a mechanistic insight into the mild increase in ROS emission observed in CaMKIIδ KO cardiac myocytes, but we can rule out that this depended on impaired mitochondrial Ca^{2+} accumulation or a primary defect of the ETC leading to enhanced mitochondrial ROS formation.

Conclusions

Taken together, our results using CaMKII KO technology argue against a regulation of mitochondrial Ca^{2+} uptake via the MCU or mPTP opening by CaMKII in cardiac myocytes under physiological conditions.

Figures and Legends

Figure 1. Mitochondrial Ca^{2+} uptake and retention capacity in isolated cardiac mitochondria.

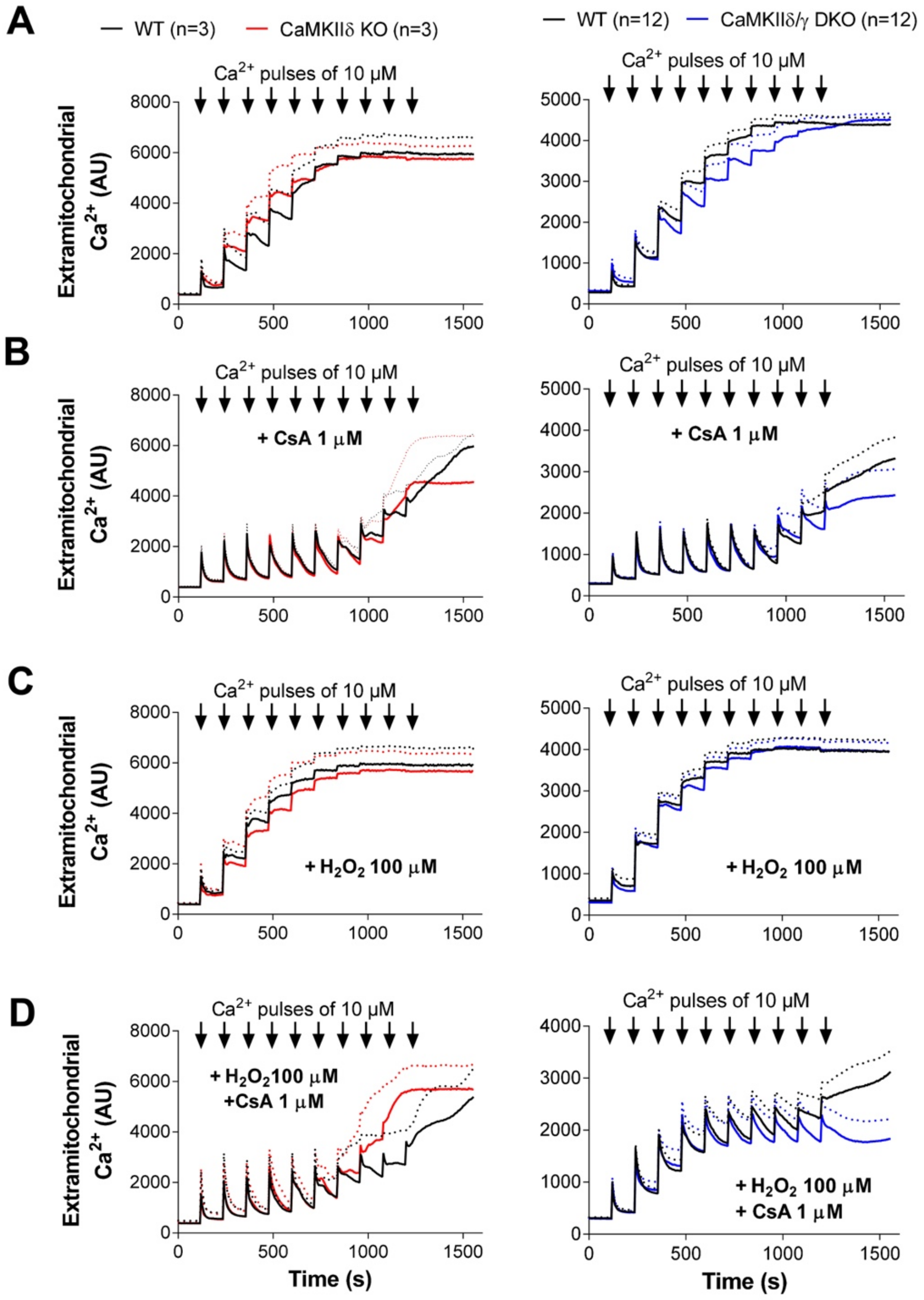

Isolated cardiac mitochondria from WT, CaMKIIδ KO (left side) and CaMKIIδ/γ DKO (right side) were exposed to repetitive Ca^{2+} pulses (10 μM every 120 s), and extramitochondrial Ca^{2+} concentrations were measured with the fluorescent Ca^{2+} indicator CalciumGreen 5N (1 μM). The experiments were performed in the absence (**A**) and presence (**B**) of cyclosporine A (CsA, 1 μM) to prevent mitochondrial permeability transition.

Figure 2. Mitochondrial Ca^{2+} uptake in patch-clamped cardiac myocytes.

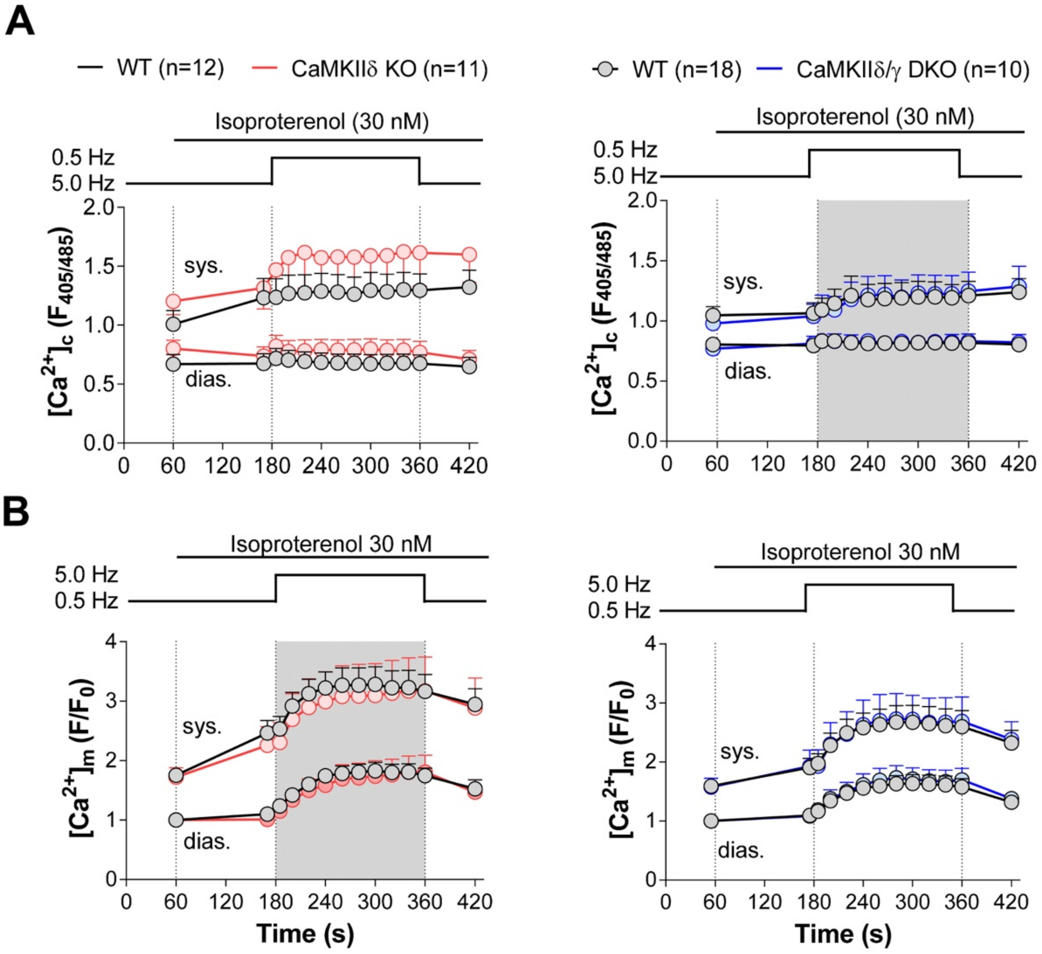

Isolated murine cardiac myocytes from WT, CaMKIIδ KO (left side) and CaMKIIδ/γ DKO (right side) were loaded with the mitochondria-located Ca^{2+} indicator rhod-2-AM. Subsequently, cardiac myocytes were patch-clamped in whole-cell configuration, and cytosolic remnants of rhod-2-AM were eliminated by dialysing the cytosol with a pipette solution containing the Ca^{2+} indicator indo-1 penta-K^+ salt. Cardiac myocytes were exposed to a physiological stress protocol by increasing electrical stimulation from 0.5 Hz to 5 Hz during superfusion with the β-adrenergic receptor agonist isoproterenol (30 nM). During this stress protocol, cytosolic (indo-1) (**A**) and mitochondrial (rhod-2-AM) Ca^{2+} levels were measured (**B**).

Figure 3. Mitochondrial redox state.

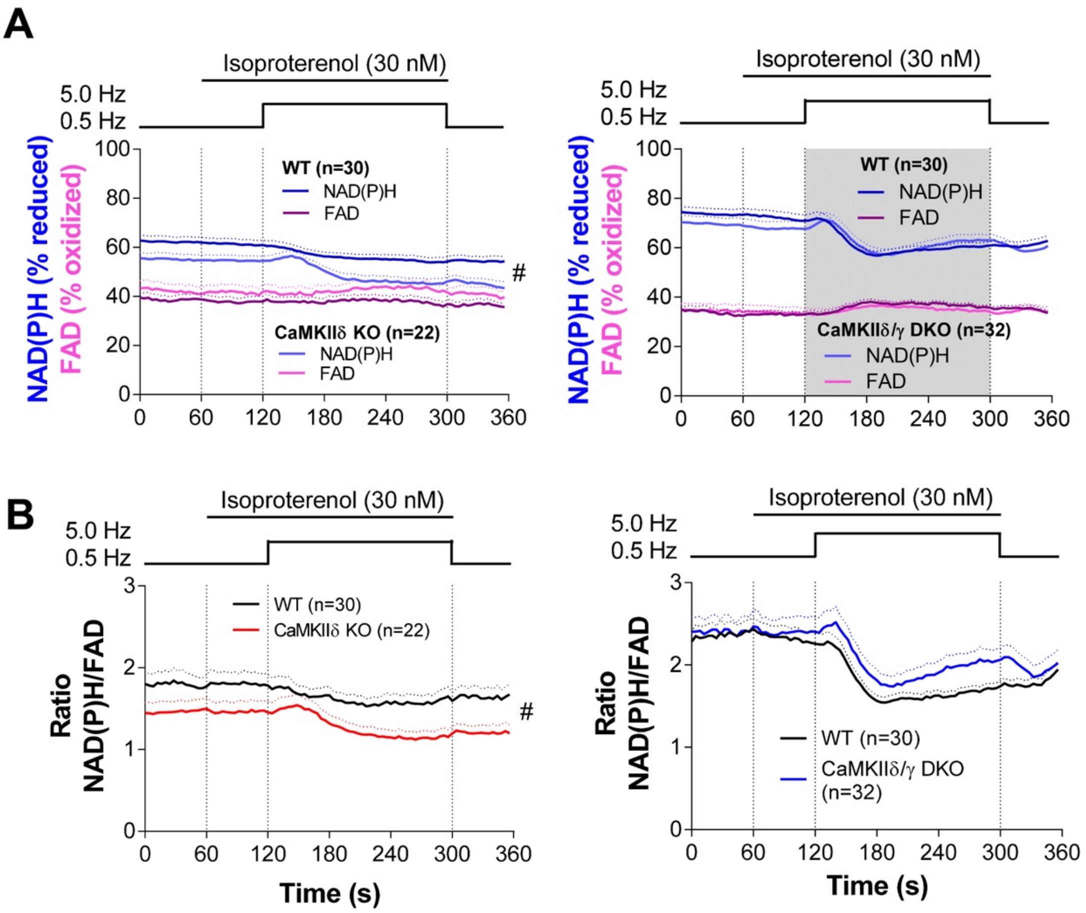

Isolated cardiac myocytes from WT, CaMKIIδ KO (left side) and CaMKIIδ/γ DKO (right side) were exposed to a physiological stress protocol by increasing electrical field stimulation from 0.5 Hz to 5 Hz during superfusion with the β-adrenergic receptor agonist isoproterenol (30 nM). During this stress protocol, the autofluorescences of NAD(P)Hand FAD were measured and calibrated (**A**), and the ratio of reduced NAD(P)H to oxidized FAD was calculated (data from A) as an indicator of the mitochondrial redox state (**B**).

Figure 4. Enzymatic activity of key Krebs cycle enzymes.

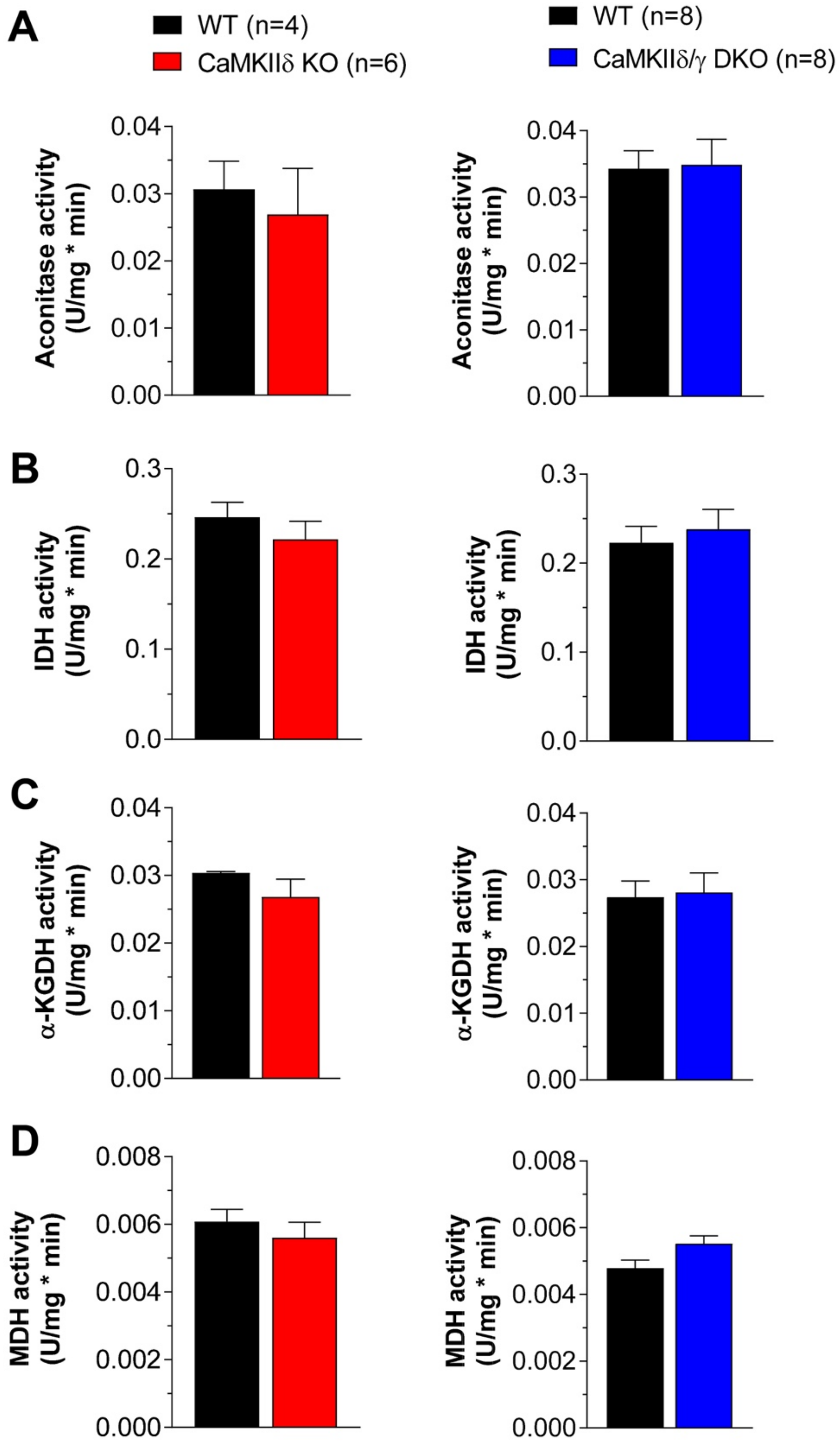

Enzymatic activities of aconitase (**A**), isocitrate dehydrogenase (IDH) (**B**), α-ketoglutarate dehydrogenase (α-KGDH) (**C**) and malic enzyme (MDH) (**D**) were measured in mitochondrial preparations from WT, CaMKIIδ KO (left side) and CaMKIIδ/γ DKO (right side), respectively.

Figure 5. Cellular contractility of intact cardiac myocytes.

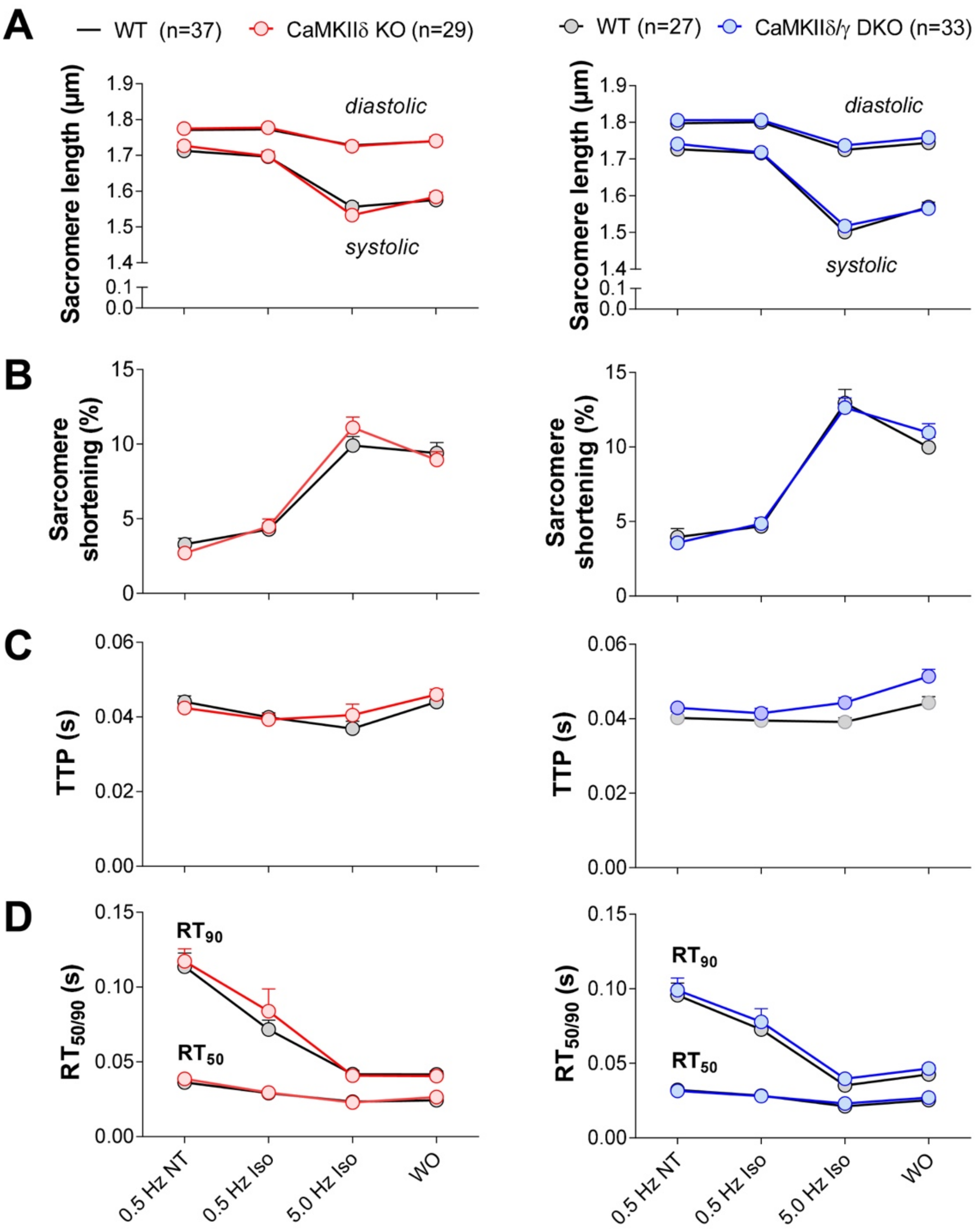

Sarcomere length (**A**), fractional sarcomeric shortening (**B**), time to peak sarcomere shortening (TTP) (**C**) and sarcomere relengthening time (RT) (**D**) were measured in isolated cardiac myocytes from WT, CaMKIIδ KO (left side) and CaMKIIδ/γ DKO (right side) exposed to the same stress protocols described for Figures 2 and 3, respectively.

Figure 6. O_2 consumption and ROS production in isolated cardiac mitochondria.

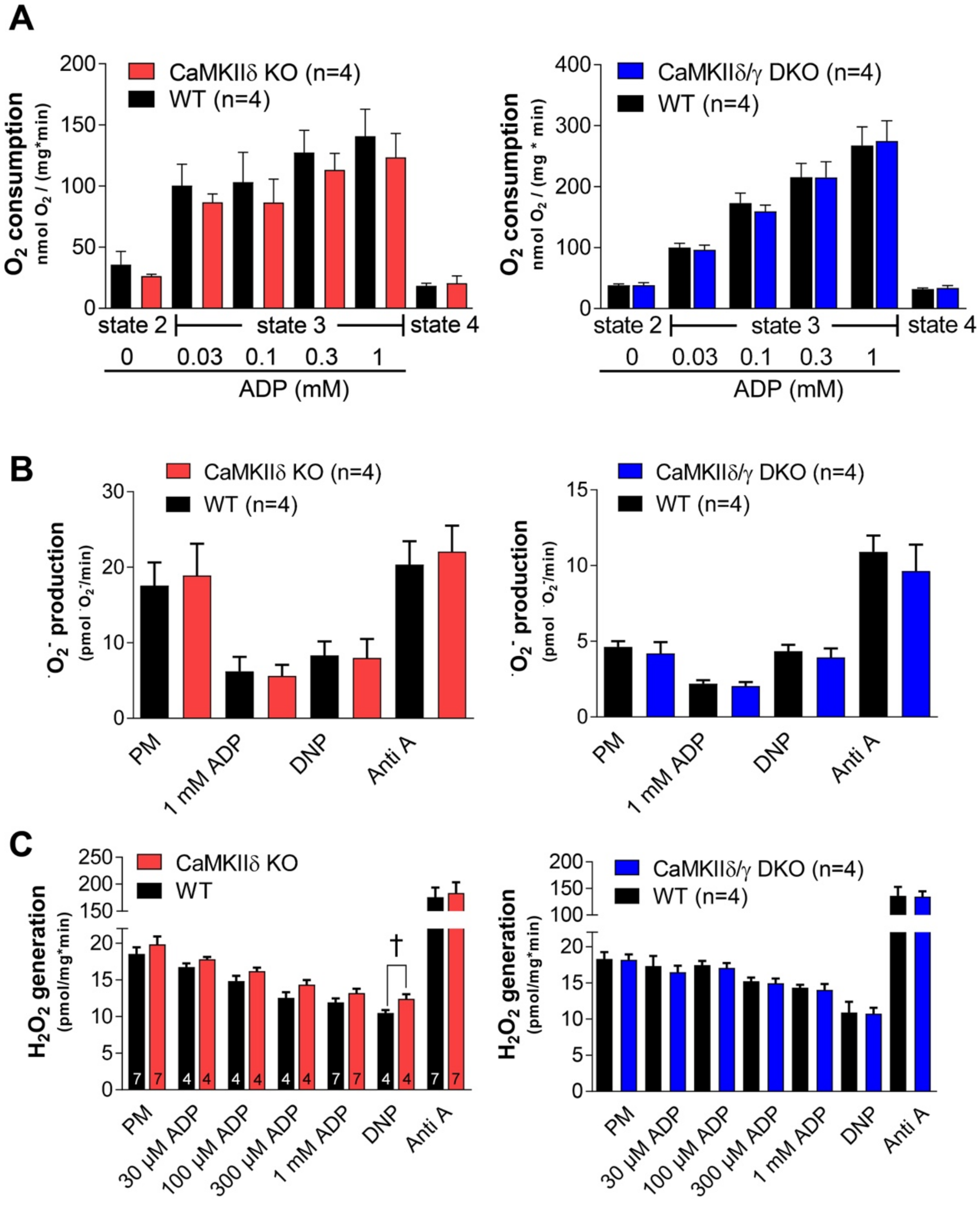

O_2 consumption (**A**), net formation of $\cdot O_2^-$ (EPR) (**B**) and emission of H_2O_2 (Amplex Ultra-Red) (**C**) were measured in/from isolated cardiac mitochondria supplied with pyruvate and malate (P/M, both 5 mM) in the absence (state 4) and presence of different ADP concentrations as indicated (state 3). Furthermore, $\cdot O_2^-$ formation and H_2O_2 emission were measured after uncoupling the electron transport chain from ATP production with 2,4-dinitrophenol (DNP) or after cytochrome *c* reductase inhibition with antimycin A (AntiA), respectively.

Figure 7. ROS production in intact cardiac myocytes.

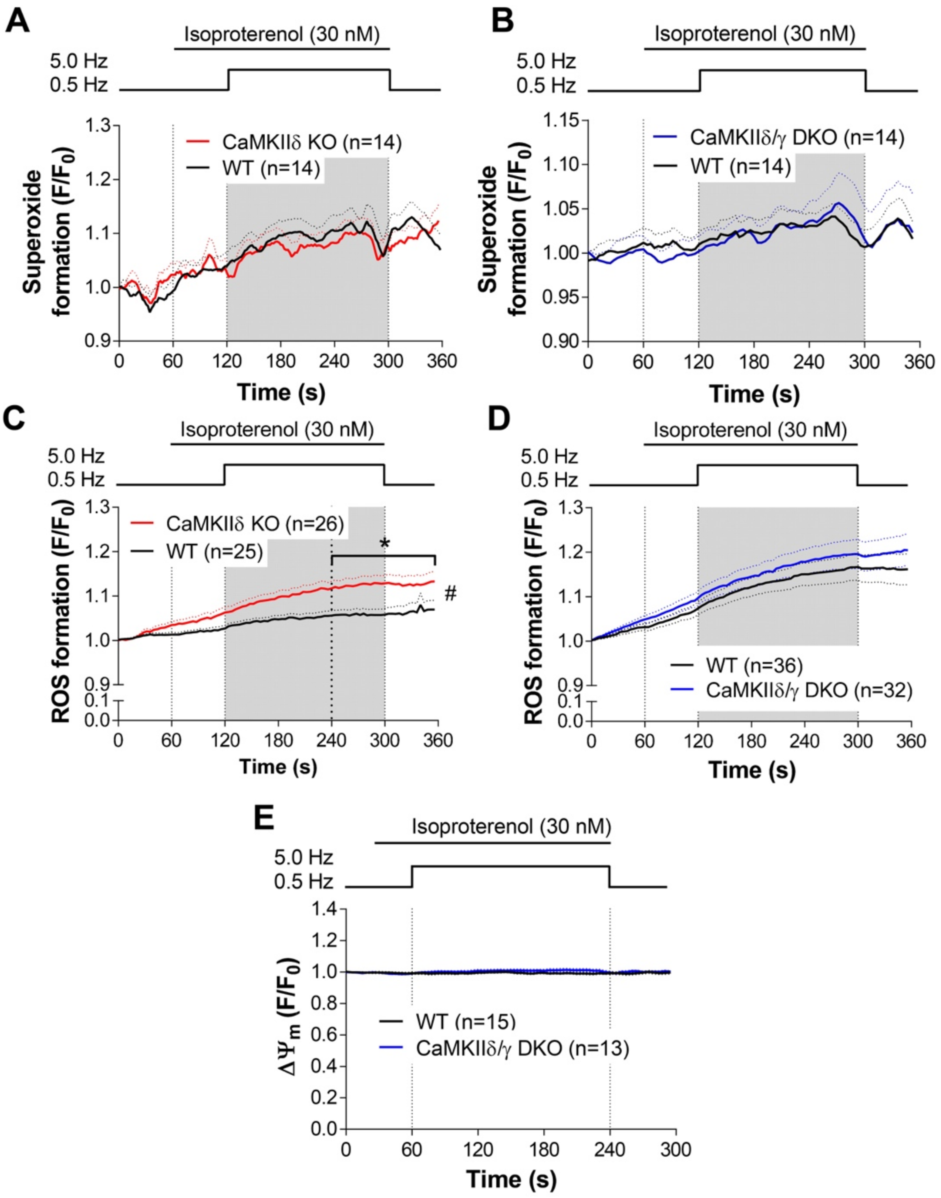

Isolated cardiac myocytes from WT, CaMKIIδ KO (**A, C**) and CaMKIIδ/γ DKO (**B, D**) loaded with the mitochondrial superoxide indicator MitoSOX (**A**, **B**) or the ROS indicator DCF (**C**, **D**) were exposed to the same stress protocol as described for Figures 2 and 3, respectively. In a separate set of experiments (**E**), we subjected CaMKIIδ/γ DKO cardiac myocytes to the same stress protocol and monitored mitochondrial membrane potential ($\Delta\psi_m$) with the fluorescent indicator TMRM. MitoSOX data are smoothened by averaging 5 consecutive time points.

Data are presented as mean ± standard error of the mean (SEM); # indicates $p<0.05$ (2-way ANOVA); * = $p<0.05$ (Sidak's post-test); † $p<0.05$ (unpaired *t*-test).

Additional information

Competing interest

No competing interests are to be reported in relation to the work presented.

Author contributions

A.G.N., M.K., E.B., D.W., M.W., V.S., M.K., M.D., R.K., and M.H. designed and performed the experiments. E.B., V.S., J.D., J.B., and C.M. designed the experiments, drafted the manuscript and revised it critically for important intellectual content. All authors approved the final version of the manuscript and agree to be accountable for all aspects of the work in ensuring that questions related to the accuracy or integrity of any part of the work are appropriately investigated and resolved. All persons designated as authors qualify for authorship, and all those who qualify for authorship are listed.

Funding

C.M. is supported by the Deutsche Forschungsgemeinschaft (DFG; SFB-894, MA 2528/7-1, TRR-219) and the German Ministry of Education and Science (BMBF; 01EO1504, CF.3 and RC.2). M.H. is supported by DFG (SFB 894). J.B. was/is supported by grants from the DFG (BA 2258/2-1 and SFB 1118), the European Commission (FP7-Health-2010 and MEDIA-261409) and the Deutsches Zentrum für Herz-Kreislauf-Forschung (DZHK; German Centre for Cardiovascular Research) and by the BMBF.

Acknowledgements

We thank Michelle Gulentz and Nina Schnellbach for technical assistance.

Selective NADH communication from α-ketoglutarate dehydrogenase to mitochondrial transhydrogenase prevents reactive oxygen species formation under reducing conditions in the heart

Michael Wagner*, Edoardo Bertero*, Alexander Nickel, Michael Kohlhaas, Gary E. Gibson, Ward Heggermont, Stephane Heymans, Christoph Maack
Michael Wagner and Edoardo Bertero contributed equally to this manuscript.

Basic Research in Cardiology. 2020 August 3;115(5):53.

Abstract

Aims. In heart failure, a functional block of complex I of the respiratory chain provokes superoxide generation, which is transformed to H_2O_2 by dismutation. The Krebs cycle produces NADH, which delivers electrons to complex I, and NADPH for H_2O_2 elimination via isocitrate dehydrogenase and transhydrogenase (NNT). At high NADH levels, α-ketoglutarate dehydrogenase (α-KGDH) is a major source of superoxide in *skeletal* muscle mitochondria with low NNT activity. Here, we analyzed how α-KGDH and NNT control H_2O_2 emission in *cardiac* mitochondria.

Results. In cardiac mitochondria from NNT-competent BL/6N mice, H_2O_2 emission is equally low with pyruvate/malate (P/M) or α-ketoglutarate (α-KG) as substrates. Complex I inhibition with rotenone increases H_2O_2 emission from P/M-, but not α-KG respiring mitochondria, which is potentiated by depleting H_2O_2-eliminating capacity. Conversely, in NNT-deficient BL/6J mitochondria, H_2O_2 emission is higher with α-KG than with P/M as substrate, and further potentiated by complex I blockade. Prior depletion of H_2O_2-eliminating capacity increases H_2O_2 emission from P/M-, but not α-KG respiring mitochondria. In cardiac myocytes, downregulation of α-KGDH activity impaired dynamic mitochondrial redox adaptation during workload transitions, without increasing H_2O_2 emission.

Conclusions. NADH from α-KGDH selectively shuttles to NNT for NADPH formation rather than to complex I of the respiratory chain for ATP production. Therefore, α-KGDH plays a key role for H_2O_2 elimination, but is not a relevant source of superoxide in heart. In heart failure, α-KGDH/NNT-dependent NADPH formation ameliorates oxidative stress imposed by complex I blockade. Downregulation of α-KGDH may therefore predispose to oxidative stress in heart failure.

Introduction

Mitochondria are the major source of cellular adenosine triphosphate (ATP), but also reactive oxygen species (ROS). Chronic heart failure is associated with derangements at multiple levels in the processes of substrate utilization, mitochondrial oxidative metabolism, and shuttling of ATP from mitochondria to the cytosol (185), and these abnormalities lead to energetic deficit (48, 186) and oxidative stress (187). In heart failure, ROS production is increased in mitochondria (188), but also from other sources such as NADPH oxidase (187, 189) and xanthine oxidase (190). Within mitochondria, canonical sites for ROS formation are complexes I and III of the electron transport chain (ETC) (191), and a functional block of complex I provokes elevated ROS production in heart failure (188).

The overflow of ROS from mitochondria in heart failure is not solely explained by the increase in ROS formation, but is also accounted for by the inability of mitochondria to efficiently eliminate ROS (148). Conversion of hydrogen peroxide (H_2O_2) to water is catalyzed by glutathione peroxidase and peroxiredoxin, which are in turn regenerated by a cascade of redox reactions requiring the reduced form of nicotinamide adenine dinucleotide phosphate (NADPH) as an electron donor. Furthermore, catalase might contribute to H_2O_2 elimination in cardiac mitochondria (6), and NADPH is required to protect catalase against inactivation by its substrate (7, 192). In the failing heart, the dynamic regulation of the mitochondrial antioxidative capacity is hampered by maladaptive changes of excitation-contraction (EC) coupling (8). Specifically, decreased calcium (Ca^{2+}) release from the sarcoplasmic reticulum (43) and elevated cytosolic sodium (Na^+) concentrations (46, 193) in failing cardiac myocytes decrease Ca^{2+} uptake and accelerate Ca^{2+} efflux from the mitochondrial matrix, respectively. Consequently, the Ca^{2+}-dependent stimulation of the Krebs cycle dehydrogenases is hindered, leading to a decrease in the $NAD(P)H/NAD(P)^+$ ratio. Oxidation of mitochondrial pyridine nucleotides limits the supply of electrons to the ETC (30) and to the antioxidant systems required for H_2O_2 elimination (46). Thus, disrupted intracellular Ca^{2+} handling in heart failure limits regeneration of antioxidative capacity, resulting in ROS emission from mitochondria (46, 158).

The mitochondrial nicotinamide nucleotide transhydrogenase (NNT) represents an essential interface between the NADPH and NADH pools in the heart. Under physiological conditions, the NNT harnesses the protonmotive force ($\Delta\mu_H$) to transfer hydride ion equivalents (H^-) from NADH to NADPH, thus maintaining the mitochondrial $NADPH/NADP^+$ ratio several fold higher than the $NADH/NAD^+$ ratio. In the heart, pathological elevations of workload reverse the direction of the NNT reaction, which then consumes NADPH to regenerate NADH, thereby depleting mitochondrial antioxidative capacity. This model is corroborated by the observation that the C57BL/6J mouse strain (BL/6J), which carries a loss-of-function mutation of *Nnt* (128), is protected from mitochondrial oxidative stress and maladaptive cardiac remodeling upon pressure overload compared with the C57BL/6N strain (BL/6N), which harbors a functional NNT (194).

In addition to the ETC complexes, numerous other sites within mitochondria might become a source of ROS under certain conditions (3). Studies performed in isolated mitochondria indicate that the α-ketoglutarate (α-KG) dehydrogenase (α-KGDH) complex, which catalyzes the rate-limiting reaction of the Krebs cycle (195), is the major source of mitochondrial ROS under conditions of elevated $NADH/NAD^+$ ratios (5, 196, 197). The α-KGDH complex catalyzes the reaction of α-ketoglutarate (α-KG) and the cofactors thiamine pyrophosphate, NAD^+ and coenzyme A to succinyl-CoA, CO_2, and NADH. It is a multienzyme complex consisting of multiple copies of the three subunits α-ketoglutarate dehydrogenase (OGDH, or E1 component), dihydrolipoyl succinyltransferase (DLST, or E2 component), and dihydrolipoyl dehydrogenase (DLD, or E3 component) (198). Experiments performed in isolated α-KGDH preparations indicate that the flavin group of the DLD (E3) component of the complex might act as electron donor for superoxide formation, thus accounting for the high rate of H_2O_2 emission from mitochondria respiring on α-KG (199). Furthermore, α-KGDH is also susceptible to oxidative damage, and thus represents both a target and a source of mitochondrial ROS (200).

On the other hand, our own previous studies imply that NAD(P)H regeneration by the Krebs cycle dehydrogenases is required to maintain mitochondrial antioxidative capacity, and thereby prevent overflow of ROS from cardiac mitochondria (46, 194). Importantly, NADH derived from α-KGDH reaction might contribute to NADPH regeneration via the NNT, but experiments pinpointing α-KGDH as a major source of ROS were performed in skeletal muscle or brain mitochondria (5, 196, 197), where NNT activity is substantially lower than in the heart (194). Unraveling the role of α-KGDH in the redox balance of cardiac mitochondria has important implications for heart failure, since we recently observed that pathological elevations of cardiac workload decrease α-KGDH expression and activity secondary to microRNA146a-mediated downregulation of the DLST subunit (131).

Here, we analyzed NAD(P)H production and respiration of isolated cardiac mitochondria supplied with α-KG or the complex I substrates pyruvate and malate (P/M), and assessed whether NADH generated by the α-KGDH complex contributes to mitochondrial antioxidative capacity via the NNT in cardiac mitochondria. Furthermore, we investigated how impaired α-KGDH activity affects the Ca^{2+}-dependent regeneration of NAD(P)H when mitochondria are integrated in their physiological context of intact cardiac myocytes. Altogether, our results indicate that NADH produced by α-KGDH is preferentially used to regenerate antioxidative NADPH via the NNT, suggesting an important antioxidant role of the α-KGDH and arguing against its role as a primary ROS source in cardiac mitochondria.

Materials and Methods

Ethical approval and animal experiments

All animal experiments were performed in accordance to guidelines of the local animal ethics committee. C57BL/6 mice were purchased from Charles River (BL/6N, C57BL/6NCrl, strain code 027; and BL/J, C57BL/6J, JAX Mice Stock Number 000664). *Dlst*$^{+/-}$ mice and corresponding wild-type (WT) littermates were generated by Prof. Gary E. Gibson (Weill Cornell Medical College, New York) and received through Prof. Stéphane Heymans and Dr. Ward Heggermont (KU Leuven).

For cardiac myocyte isolation, mice received carprofen (12 mg kg^{-1}) and heparin (10,000 IE kg^{-1}) and were anaesthetized with isoflurane (5% at 0.5 L min^{-1}). The heart was excised as soon as mice became insensible to pedal reflex. For mitochondria isolation from mouse hearts, mice were sacrificed by intraperitoneal injection of ketamine hydrochloride (100 mg kg^{-1}; Pfizer, Karlsruhe, Germany) and xylazine hydrochloride (10 mg kg^{-1}; Bayer Healthcare, Berlin, Germany)

Experiments in isolated cardiac myocytes

Most methods employed in this study were described previously (194). For the experiments in **Figure 5d-g** and **Supplementary Figure 4**, isolated murine ventricular myocytes were field-stimulated at 0.5 Hz and perfused with Normal Tyrode's (NT) solution containing (in mM): NaCl 130, KCl 5, $MgCl_2$ 1, $CaCl_2$ 1, Na-HEPES 10, glucose 10, sodium pyruvate 2 and ascorbic acid 0.3, pH 7.4. After 120 s, cardiac myocytes were perfused with NT solution containing the β-adrenergic receptor agonist isoproterenol (30 nM) and pacing frequency was increased to 5 Hz for 180 s. Finally, isoproterenol was washed out by perfusing the cells again with NT, and a 0.5 Hz pacing frequency was restored. During this experimental stress protocol, sarcomere length, NAD(P)H and FAD autofluorescence, and 5-(-6)-chloromethyl-2,7-dichlorohydrofluorescein di-acetate (CM-H_2DCFDA, denoted as DCF in the Results) fluorescence were measured with an IonOptix setup.

Experiments in isolated mitochondria

Mitochondria were isolated from murine hearts as previously described (194). O_2 consumption was measured at 37°C with a Clarke electrode (Hansatech, Pentney, Norfolk, UK). State 2 respiration was obtained by using sodium pyruvate and sodium malate or α-KG as substrates (5 mM each). Increasing concentrations of ADP (0.03, 0.1, 0.3 and 1 mM) or a single addition of a saturating concentration of ADP (1 mM) were used to induce state 3 respiration. Finally, state 4 respiration was induced by adding the F_1/F_o ATP synthase (complex V) inhibitor oligomycin (1.2 µM).

Hydrogen peroxide (H_2O_2) emission from isolated cardiac mitochondria was determined using the H_2O_2-specific dye Amplex® UltraRed (purchased from Thermo Fisher Scientific, Waltham, Massachusetts, USA). The reaction of Amplex® UltraRed with H_2O_2 is catalyzed by horseradish peroxidase (HRP) and forms the fluorescent product resorufin (λ_{Ex} = 535 nm, λ_{Em} = 590 nm). The concentrations used in the assay were 10 µM Amplex® UltraRed, 0.5 U ml^{-1} HRP and 100 U ml^{-1} superoxide dismutase.

H_2O_2 emission was measured in the presence of ADP (1 mM), the complex I inhibitor rotenone (8 µM) or the α-KGDH inhibitor 3-methyl-2-oxovaleric acid (KMV, 10 mM). To deplete mitochondrial antioxidative capacity, mitochondria were pretreated with 2,4-dinitrochlorobenzene (DNCB, 25 µM; purchased from Sigma-Aldrich), which alkylates glutathione and is an irreversible inhibitor of thioredoxin reductase.

For simultaneous measurement of NAD(P)H and mitochondrial membrane potential ($\Delta\Psi_m$), isolated cardiac mitochondria were preincubated with the potentiometric marker tetramethylrhodamine methyl ester (TMRM) for 10 minutes before the experiment. Subsequently, NAD(P)H autofluorescence (λ_{Ex} = 340 nm, λ_{Em} = 450 nm) and TMRM fluorescence (λ_{Ex} = 560 nm, λ_{Em} = 600 nm) were determined with the same concentrations of substrates and effectors described above.

For both H_2O_2 emission and concomitant assessment of NAD(P)H and $\Delta\Psi_m$, fluorescence or absorption was measured in the fluorescence plate reader Infinite M200Pro (Tecan, Männedorf, Switzerland) using Falcon® 96-well plate black/clear (Corning Inc., Corning, NY, USA) for Amplex® UltraRed or UV flat bottom Microtiter® plates (Thermo Fisher Scientific, Waltham, Massachusetts, USA) for NAD(P)H and TMRM. We used 60 µg mitochondria per well in triplicates in a total volume of 200 µl respiration buffer at 37°C.

Enzyme activities

All enzyme activities were determined by measuring absorption changes of NAD(P)H every minute at 340 nm in a total volume of 200 µl reaction buffer at 37°C after one freeze/thaw cycle to break mitochondria. For isocitrate dehydrogenase type 2 (IDH2) activity, 5 µg of mitochondria or cytosol were supplemented with (in mM) TRIS-HCl (pH 8.0) 10, $NADP^+$ 0.2, $MgCl_2$ 5, isocitrate 2. For aconitase activity, 25 µg of mitochondria or cytosol were supplemented with (in mM) TRIS-HCl (pH 7.4) 36, cysteine 0.8, $MgCl_2$ 0.4, $NADP^+$ 0.2, citrate 30; dependence on H_2O_2 was tested by adding H_2O_2 to the reaction buffer. For α-KGDH, 10 µg of mitochondria were supplemented with (in mM) KH_2PO_4 25, EGTA 0.5, $MgCl_2$ 5, NAD^+ 1, α-KG 2.5, thiamine pyrophosphate 0.2, rotenone 0.008. The reaction was started by adding 0.1 mM coenzyme A. For malate dehydrogenase (MDH) activity, 10 µg of mitochondria or cytosol were supplemented with (in mM) TRIS-HCl (pH 7.4) 50, $NADP^+$ 0.2, $MgCl_2$ 5, malate 5.

Statistical analysis

All values are displayed as means ± standard error of the mean. One-way/two-way ANOVA followed by Bonferroni's multiple comparisons test and unpaired Student's t-test were performed using GraphPad Prism version 7.00 for Windows (GraphPad Software, La Jolla, CA, USA).

Results

Functional NNT is required for α-KGDH-dependent regeneration of mitochondrial antioxidative capacity

The Krebs cycle enzyme α-KGDH is a major source of NADH within mitochondria, but its contribution to NADPH regeneration and thereby, the maintenance of mitochondrial antioxidative capacity is not known. To address this, we determined H_2O_2 emission from cardiac mitochondria isolated from BL/6N mice in the presence of pyruvate/malate (P/M) or α-KG. The rate of H_2O_2 emission did not differ when mitochondria were supplied with P/M or α-KG (**Figure 1a**, blue traces; direct comparison in **Supplementary Figure 1a**). Intriguingly, complex I inhibition with rotenone induced a marked increase in H_2O_2 emission from mitochondria supplied with P/M, while it had no effect in the presence of α-KG (**Figure 1a**, red traces). Furthermore, the addition of the α-KGDH inhibitor 3-methyl-2-oxovaleric acid (KMV) increased H_2O_2 emission from mitochondria supplied with P/M, but not with α-KG, suggesting that the α-KGDH complex is not a major source of ROS under these conditions (**Figure 1a**, green traces), but rather contributes to H_2O_2 elimination.

Rotenone induces ROS production by blocking the coenzyme Q-binding site of complex I, thereby leading to a back-up of NADH-derived electrons onto the flavin group of the complex, where superoxide is produced by the reaction of electrons with oxygen (3). To explain why rotenone does not exacerbate H_2O_2 emission from mitochondria supplied with α-KG, we hypothesized that NADH derived from the α-KGDH reaction is preferentially used for NADPH regeneration via the NNT, whereas NADH generated by pyruvate and malate dehydrogenase is shuttled to complex I, where it fuels ROS production (scheme in **Figure 1b**). To test this hypothesis, we assessed H_2O_2 emission under the same conditions in mitochondria isolated from BL/6J mice, a strain carrying a loss-of-function mutation of *Nnt* (128). In BL/6J mitochondria provided with α-KG as substrate, the rate of H_2O_2 emission at baseline and in particular, upon complex I inhibition with rotenone was significantly higher compared to the one observed in the presence of P/M (**Figure 2a**, blue and red traces). On the contrary, α-KGDH inhibition with KMV decreased H_2O_2 emission, indicating that the α-KGDH complex might become a relevant source of ROS under these conditions (**Figure 2a**, green trace). These observations support our hypothesis and indicate that NADPH regeneration becomes exclusively dependent on the NNT reaction when α-KG is provided as substrate (scheme in **Figure 2b**).

To further investigate this, we repeated the experiment after incubation of mitochondria with 2,4-dinitrochlorobenzene (DNCB), which leads to alkylation of free glutathione and thereby, depletes mitochondrial antioxidative capacity. As expected, the rate of H_2O_2 emission from BL/6N and BL/6J mitochondria treated with DNCB was substantially higher compared to mitochondria with an intact antioxidative capacity (**Figure 3a-c,** direct comparison with **Figure 1** shown in **Supplementary Figure 1**). In the presence of P/M, H_2O_2 emission did not differ between BL/6N and BL/6J mitochondria and was exacerbated to the same extent by rotenone addition in both strains (**Figure 3a-c**). Intriguingly, when DNCB-treated mitochondria were supplied with α-KG, complex I blockade with rotenone increased H_2O_2 emission from BL/6J, but not from BL/6N mitochondria, and the latter strain displayed a rate of H_2O_2 emission that was comparable to the one of BL/6J mitochondria with an intact antioxidative capacity (**Figure 3a-c**, **Supplementary Figure 1**).

To explain why DNCB increases H_2O_2 emission only in the presence of P/M as substrates, we reasoned that under these conditions, both the isocitrate dehydrogenase (IDH) type 2 (IDH2, i.e. the $NADP^+$-dependent isocitrate dehydrogenase, IDH3 being NAD^+-dependent) and NNT contribute to maintain the antioxidative capacity via NADPH regeneration (**Figure 1b**, left panel; **Supplementary Figure 1**). We previously reported that IDH2 is the main source of NADPH in cardiac mitochondria and its activity does not differ between BL/6N and BL/6J mitochondria (194). We also did not detect differences in the activity of the other two Krebs cycle enzymes upstream of α-KGDH, i.e. citrate synthase and aconitase (**Supplementary Figure 2**). In contrast, the observation that DNCB does not affect the rate of H_2O_2 emission from BL/6N mitochondria supplied with α-KG corroborates the hypothesis that NADPH regeneration is exclusively dependent on the NNT under these conditions, and that the NADH generated from α-KGDH is shuttled to a higher extent to the NNT than to the ETC (**Figure 1b**, right panel).

Pyruvate/malate and α-ketoglutarate yield different maxima of NAD(P)H, membrane potential and respiration in isolated cardiac mitochondria

The mitochondrial formation of ROS critically depends on the NADH/NAD$^+$ ratio and the mitochondrial membrane potential ($\Delta\Psi_m$) (3). Previous studies investigating ROS production by the α-KGDH complex employed conditions with full reduction of the NADH/NAD$^+$ pool, but did not clarify to what extent α-KG by itself is able to reduce NAD(P)$^+$ and generate $\Delta\Psi_m$. To interrogate whether the differences in H_2O_2 emission from BL/6N and BL/6J mitochondria might be explained by differences in redox state or membrane potential between the two genotypes, we measured changes in NAD(P)H levels (by autofluorescence) and $\Delta\Psi_m$ (by TMRM fluorescence) in BL/6N and BL/6J cardiac mitochondria supplied with either P/M or α-KG. The addition of P/M to isolated mitochondria rapidly increased NAD(P)H autofluorescence and $\Delta\Psi_m$, independent of the genotype, although we noted a trend toward higher NAD(P)H levels in BL/6N compared to BL/6J mitochondria. In the presence of α-KG, the net increase and rate of increase in NAD(P)H and $\Delta\Psi_m$ were substantially lower compared to the ones induced by P/M in both strains (**Figure 4a**). In mitochondria supplied with P/M, adenosine diphosphate (ADP) addition partially dissipated $\Delta\Psi_m$ and oxidized the NAD(P)H pool, whereas a mild increase in NAD(P)H levels in response to ADP was observed in BL/6N and BL/6J mitochondria respiring on α-KG (**Figure 4b**). This effect might be attributable to the ADP-mediated stimulation of the α-KGDH complex (201).

In a separate experiment, the addition of substrates was followed by complex I inhibition with rotenone, which completely dissipated $\Delta\Psi_m$ independent of the genotype and substrate used (**Figure 4c**). In mitochondria supplied with P/M, rotenone did not affect NAD(P)H levels, implying that the NAD(P)H/NAD(P)$^+$ pool is almost fully reduced in the presence of P/M. In contrast, we observed a marked increase in NAD(P)H autofluorescence after rotenone addition when α-KG was used as substrate (**Figure 4c**). Again, we did not detect differences between BL/6N and BL/6J mitochondria. Finally, we compared the capacity of P/M and α-KG to support mitochondrial respiration. In agreement with the lower efficiency of α-KG-induced NAD(P)H production, ADP-stimulated (i.e., state 3) respiration was substantially lower when mitochondria were respiring on α-KG (**Figure 4d**). Mitochondrial O_2 consumption was similar in BL/6J and BL/6N mitochondria respiring on P/M, but tended to be higher in BL/6J than in BL/6N mitochondria supplied with α-KG alone. Altogether, these results indicate that the pronounced difference in H_2O_2 emission between BL/6N and BL/6J mitochondria in the presence of α-KG alone and upon complex I inhibition is neither explained by differences in NADH/NAD$^+$ ratio nor in membrane potential. On the contrary, NAD(P)H levels tended to be higher in BL/6N compared to BL/6J mitochondria, which would induce an even larger increase in ROS production by virtue of the higher NADH/NAD$^+$ ratio.

Impaired α-KGDH activity does not affect ROS emission from isolated mitochondria

To further investigate the functional role of the α-KGDH reaction in cardiac mitochondria, we used a mouse model characterized by global heterozygous deletion of the gene encoding the DLST subunit of the α-KGDH complex (*Dlst*$^{+/-}$ mice). While homozygous *Dlst* knockout is embryonically lethal, *Dlst*$^{+/-}$ mice exhibit ~25% lower α-KGDH activity in the heart (**Supplementary Figure 3a**). However, we observed that after cardiac myocyte isolation, the differences in α-KGDH activity between *Dlst*$^{+/-}$ and

WT mice, as sampled *from the very same* digested hearts as the cell experiments were performed from, were slightly less pronounced (**Supplementary Figure 3b**), possibly explained by post-translational modifications of α-KGDH induced by the isolation procedure (i.e., oxidation (200)). Therefore, we re-grouped WT and *Dlst*$^{+/-}$ myocytes into those with low, intermediate, and high α-KGDH activity depending on whether the α-KGDH in the respective tissue was below 60%, between 60% and 80% or above 80%, respectively, compared to the one of WT myocytes with the highest α-KGDH activity (**Figure 5a**). The activity of aconitase, IDH2, and malate dehydrogenase did not differ between the three groups (**Supplementary Figure 3c-e**). Because α-KGDH activity was only partially reduced, α-KG alone supported respiration of cardiac mitochondria isolated from *Dlst*$^{+/-}$ mice, although O_2 consumption tended to be lower in the low- and intermediate-α-KGDH activity groups compared to mitochondria with high α-KGDH activity (**Figure 5b**).

To address the consequences of impaired α-KGDH activity on mitochondrial ROS formation, we measured H_2O_2 emission from *Dlst*$^{+/-}$ cardiac mitochondria supplied with α-KG. In the presence of α-KG alone and upon addition of increasing concentrations of ADP, mitochondrial H_2O_2 emission did not differ between the three groups of α-KGDH activity (**Figure 5c**), thus arguing against α-KGDH being a dominant source of mitochondrial ROS under these conditions.

Decreased α-KGDH activity oxidizes mitochondrial redox state but does not affect ROS emission in intact cardiac myocytes

The ATP demand of cardiac myocytes changes continuously in response to variations in cardiac workload, and Ca^{2+} plays a key role in the process of energy supply-and-demand matching in the heart (8). In fact, elevations of cardiac workload (and thus, ATP demand) are accompanied by an increase in the amplitude and frequency of cytosolic Ca^{2+} transients that drives Ca^{2+} accumulation in the mitochondrial matrix, where Ca^{2+} stimulates pyruvate-, isocitrate- and α-KG dehydrogenases to regenerate NAD^+ to NADH. To interrogate whether decreased α-KGDH activity has an impact on mitochondrial redox state in cardiac myocytes challenged with an increase in energy demand, we measured the autofluorescence of NAD(P)H and oxidized flavin adenine dinucleotide (FAD) in cardiac myocytes harvested from *Dlst*$^{+/-}$ and WT mice during an experimental stress protocol that simulates a physiological transition of cardiac workload. Specifically, cardiac myocytes were superfused with the β-adrenergic receptor agonist isoproterenol, and pacing frequency was increased from 0.5 to 5 Hz for 180 s. As previously observed, the increase in ATP demand accelerates electron flow from mitochondrial pyridine nucleotides to the ETC complexes, thereby inducing a mild oxidation of the NAD(P)H/NAD^+ and $FADH_2$/FAD redox states (**Figure 5d** and **e**). Interestingly, mitochondrial redox state was not different at baseline (0.5 Hz stimulation frequency), but underwent a substantially larger oxidation in cardiac myocytes with low α-KGDH activity compared with the ones with high- or intermediate α-KGDH activity in response to this workload transition (**Figure 5d** and **e**). Cardiac myocytes contractility and relaxation kinetics did not differ depending on α-KGDH activity (**Supplementary Figure 4**).

Because the Ca^{2+}-dependent stimulation of Krebs cycle dehydrogenases is also relevant for the regeneration of mitochondrial H_2O_2-detoxifying capacity, we investigated whether impaired α-KGDH activity aggravated the overflow of ROS in intact cardiac myocytes. To this end, cells were loaded with the ROS indicator DCF and subjected to the experimental stress protocol described above. Accumulation of

DCF fluorescence did not differ between the three groups of α-KGDH activity, indicating similar levels of ROS emission (**Figure 5f**). However, when cardiac myocytes were challenged with external H_2O_2 to assess their H_2O_2-eliminating capacity, DCF fluorescence increased almost 2-fold in cardiac myocytes with high α-KGDH activity compared to the ones with low and intermediate α-KGDH activity (**Figure 5g**). Altogether, these results indicate that decreased α-KGDH activity impairs energetic adaptation to elevated cardiac workload, but does not affect mitochondrial antioxidative capacity under physiological conditions.

Discussion

Oxidative stress results from an imbalance between ROS formation and their elimination by cellular antioxidative systems. Mitochondria are a major source of ROS in the heart, and a wealth of preclinical evidence indicates that both increased ROS formation and impaired mitochondrial antioxidative capacity are implicated in the progression of heart failure (8). Within mitochondria, complex I and III of the respiratory chain are generally considered the major sources of ROS, but other potential sites of ROS production have been identified (3). Specifically, it has been proposed that mitochondrial dehydrogenases, and in particular the α-KGDH complex, might become dominant ROS sources under conditions of high $NADH/NAD^+$ ratio (5, 196, 197). In fact, the flavin groups of complex I and other matrix dehydrogenases become fully reduced under these conditions, thus maximizing the possibility of ROS formation upon leakage of electrons to O_2. On the other hand, NADPH produced by the Krebs cycle dehydrogenases and the NNT reaction is pivotal to regenerating mitochondrial antioxidative capacity in the heart, and studies evaluating α-KGDH-dependent ROS production were performed in skeletal muscle and brain mitochondria, where NNT activity is negligible compared to the heart (43, 46, 194). Here, we investigated the role of α-KGDH-derived NADH in the regulation of mitochondrial redox state and ROS emission in isolated cardiac mitochondria and intact cardiac myocytes.

NADH produced by α-ketoglutarate dehydrogenase is preferentially shuttled to NADPH via the NNT under non-phosphorylating conditions

The central observation of our work is that in cardiac mitochondria from NNT-competent BL/6N mice, H_2O_2 emission is equally low with P/M or α-KG as substrates, but complex I inhibition with rotenone exacerbates H_2O_2 emission exclusively in mitochondria supplied with P/M, while having no effect on mitochondria supplied with α-KG (**Figure 1a**). Conversely, in NNT-deficient BL/6J mitochondria, H_2O_2 emission is higher with α-KG than P/M as substrate, and further potentiated by complex I blockade (**Figure 2a**). Importantly, addition of rotenone completely dissipated $\Delta\Psi_m$ (**Figure 4c**) and thus, the difference in H_2O_2 production upon complex I inhibition cannot be accounted for by a difference in mitochondrial membrane potential between the two strains. These results suggest that NADH derived from the α-KGDH reaction is preferentially used for NADPH regeneration via the NNT, which represents the dominant source of NADPH in the presence of α-KG alone. In fact, the observation that rotenone cannot increase H_2O_2 emission from BL/6N mitochondria supplied with α-KG (**Figure 1a**) implies that the mitochondrial antioxidative capacity is preserved, while ROS formation at the respiratory chain (or in any other mitochondrial ROS sources that can be fueled by NADH) is blunted under these conditions (scheme in **Figure 1b**). In contrast, the rotenone-induced increase in H_2O_2 emission from BL/6J mitochondria supplied with α-KG is higher than that observed in the presence of P/M (**Figure 2a**), indicating that (i) mitochondrial H_2O_2–eliminating capacity is depleted and (ii) ROS production is exacerbated by shuttling of α-KGDH-derived NADH toward complex I and, potentially, the flavin groups of mitochondrial dehydrogenases.

This concept is substantiated by our observations in mitochondria depleted of their antioxidative capacity via pre-incubation with DNCB. In the presence of P/M, DNCB treatment led to a substantial increase in rotenone-induced H_2O_2 emission from both BL/6N and BL/6J mitochondria compared with mitochondria with an intact antioxidative capacity. This implies that P/M metabolism produces NADPH required for regenerating the reduced form of peroxiredoxin and glutathione reductase and to protect catalase from H_2O_2-mediated inactivation independent of the NNT, most likely via the IDH2 reaction. This is in agreement with our previous observation that $NADP^+$-sensitivity and maximal efficacy of IDH2 are higher than of NNT in cardiac mitochondria [26]. It must also be noted that aconitase, the Krebs cycle enzyme upstream of IDH, is particularly sensitive to oxidative damage (202). Therefore, under conditions of oxidative stress, as in the presence of rotenone in our experiments or with a functional block at complex I as reported for heart failure (188), ROS-mediated aconitase inactivation might further limit the flux of substrates into IDH and α-KGDH and thereby, further compromise mitochondrial antioxidative capacity, eliciting an adverse feed-forward mechanisms of mitochondrial oxidative stress.

In contrast, DNCB treatment did not affect the (already high) rate of H_2O_2 emission from BL/6J mitochondria supplied with α-KG (**Figures 2a** and **3b**, directly compared in **Supplementary Figure 1b**), indicating that α-KG alone does not support NADPH regeneration in the absence of a functional NNT (scheme in **Figure 2b**). Consequently, mitochondrial H_2O_2-eliminating capacity is extremely low under these conditions and not further depleted by DNCB. Furthermore, also when mitochondrial antioxidative systems were exhausted with DNCB, rotenone did not exacerbate H_2O_2 emission from BL/6N mitochondria (**Figure 3a**). This further substantiates the notion that NADH produced by α-KGDH shuttles preferentially to the NNT for NADPH formation and not (or to a much lesser extent) to complex I (scheme in **Figure 1b**). Otherwise, one would have expected an increase in ROS formation in the face of DNCB-induced depletion of antioxidative capacity. Altogether, these results indicate that the NNT reaction is a dominant source of NADPH when mitochondria are supplied with α-KG alone and, upon complex I inhibition, it functions as an antioxidative “safety valve escape” that concomitantly regenerates mitochondrial H_2O_2-eliminating systems and prevents NADH-mediated ROS production by the flavin groups of complex I and mitochondrial dehydrogenases.

The results of a recent study based on a mouse model of homozygous deletion of the *Nnt* (*Nnt*$^{-/-}$ mice) corroborate this concept. In their experiments, Ronchi and colleagues (203) exposed liver mitochondria from WT and *Nnt*$^{-/-}$ mice to an exogenous organic peroxide (*t*-BOOH) to induce a transient oxidation of the NAD(P)H pool. Subsequently, they monitored the time required to restore baseline levels of NAD(P)H in the presence of different substrate couples, including P/M and glutamate/malate (G/M). Glutamate enters mitochondria in exchange for aspartate and is channeled into the Krebs cycle after conversion to α-KG, and thus relies on the α-KGDH for further oxidation to succinyl-CoA. In WT mitochondria, NADPH regeneration was equally efficient independent of the substrate used. In contrast, mitochondria lacking a functional NNT could restore baseline levels of NAD(P)H only when supplied with P/M as substrates, whereas no recovery was observed with G/M (203). These results indicate that, when mitochondria are supplied with G/M or α-KG alone, NADPH regeneration under non-phosphorylating conditions is largely dependent on the NNT.

Reduced α-ketoglutarate dehydrogenase activity does not affect ROS elimination in isolated cardiac myocytes

To examine whether α-KGDH-derived NADH regulates mitochondrial redox balance under more physiological conditions, we investigated how α-KGDH activity influences ROS emission and mitochondrial redox state of isolated mitochondria and cardiac myocytes challenged with an increase in energy demand. In cardiac mitochondria respiring on α-KG, lower α-KGDH activity is associated with a trend toward decreased O_2 consumption (**Figure 4d**), but does not affect H_2O_2 emission (**Figure 5c**). In isolated cardiac myocytes, lower α-KGDH activity does not influence mitochondrial redox state at baseline, but impairs metabolic adaptation to increased workload, as evidenced by the pronounced oxidation of the NAD(P)H/FAD ratio elicited by concomitant β-adrenergic stimulation and elevated pacing frequency (**Figures 5d** and **5e**). This observation highlights the importance of the Ca^{2+}-stimulated Krebs cycle dehydrogenases for NAD(P)H regeneration during elevated cardiac workload. However, we did not detect an increase in ROS overflow within intact cardiac myocytes with low α-KGDH activity (**Figure 5f**), indicating that on one hand, α-KGDH is unlikely a relevant source of ROS under physiological conditions in cardiac myocytes. On the other hand, these results also suggest that the contribution of α-KGDH-derived NADH and subsequently, NADPH, is not essential for ROS elimination under physiological conditions. This may be explained by the fact that in cardiac myocytes, IDH2 has the highest contribution towards NADPH regeneration compared to NNT and malate dehydrogenase (194).

Together with our observations in isolated mitochondria, this result supports the emerging concept that the contribution of the NNT reaction to mitochondrial antioxidative capacity is higher under non-phosphorylating conditions (e.g., complex I inhibition with rotenone) than during states of high energy demand (203). Such conditions may apply to pancreatic islet cells, in which glucose-dependent ATP production serves to close ATP-dependent K^+ channels and thereby, increase Ca^{2+} influx and insulin release. In these cells, ATP demand is lower than in cardiac myocytes, resembling closer non-phosphorylating conditions, and in fact, NNT deletion provokes ROS formation and disruption of glucose-induced insulin release (128, 204).

Implications for cardiac hypertrophy and failure

Intriguingly, a recent study by our groups indicates that pathological elevations of cardiac afterload lead to a decrease in α-KGDH activity (131). Mechanistically, mouse models of pressure overload and left ventricular biopsies of patients with aortic stenosis display an increased expression of microRNA-146a, which targets and induces degradation of DLST, the E2 component of the α-KGDH complex. From a pathophysiological standpoint, conditions that downregulate α-KGDH expression and/or activity impair energetic adaptation and NADPH regeneration, which may have an adverse effect on intracellular redox balance and energetics. Accordingly, genetic deletion of microRNA-146a restored α-KGDH activity and partially prevented metabolic and structural remodeling of the pressure-overloaded mouse heart (131). Our findings in isolated cardiac myocytes suggest that the protective effect obtained by maintaining α-KGDH activity might be mediated by the preservation of mitochondrial redox balance under conditions of elevated cardiac workload.

Heart failure is common, costly, disabling, and deadly (205). Treatment of heart failure with reduced ejection fraction, the clinical correlate of the animal models used to investigate heart failure, is largely based on medications that reduce the detrimental activation of the renin-angiotensin-aldosterone and sympathetic nervous system (206). Although experimental evidence supports a crucial role of mitochondrial dysfunction in the progression of heart failure, no specific mitochondria-targeted treatment is currently used in clinical practice. Nevertheless, several clinical trials are currently ongoing to validate preclinical findings in the human setting (e.g. with elamipretide (207, 208)). We believe that our data contribute to shed more light on the complex mitochondrial biology that underlies pathological metabolic remodeling and energy starvation in heart failure.

Limitations

This study has limitations: first, all experiments were conducted in isolated mitochondria or unloaded cardiac myocytes, thus removing the natural context of the intact, beating heart. In addition, the Amplex® UltraRed assay used in **Figures 1** to **3** reports exclusively extramitochondrial H_2O_2, whereas we did not assess ROS *formation* selectively in the mitochondrial matrix. Furthermore, NAD(P)H and $\Delta\Psi_m$ measurements shown in **Figure 4a-c** are semiquantitative, and therefore we cannot draw conclusions on the absolute values of NAD(P)H and $\Delta\Psi_m$ in our mitochondria preparation. *Dlst*$^{+/-}$ cardiac myocytes displayed only a modest decrease in α-KGDH activity, and this led us to re-group WT and *Dlst*$^{+/-}$ mice used for our cellular experiments based on the actual activity of the enzyme, rather than their genotype. We acknowledge that an approach based on genetic silencing to reduce the enzymatic activity of α-KGDH would have been preferable; however, because α-KGDH activity was determined in the same digested hearts as the cell experiments were performed from, we believe that the results shown in **Figure 5d-g** actually capture the effect of varying degrees of α-KGDH activity on mitochondrial NAD(P)H/FAD redox state and cellular ROS production. Finally, the biological significance of the NAD(P)H/FAD oxidation in the cellular experiments of **Figure 5d** and **e** is presently unclear. However, in previous work, a similar oxidation of NAD(P)H at elevated cytosolic Na^+ concentrations (30) proved to be of biological significance since preventing such Na^+-dependent mitochondrial oxidation with an inhibitor of the mitochondrial Na^+/Ca^{2+} exchanger prevented maladaptive cardiac remodeling, dysfunction, and arrhythmias (193, 209).

Conclusions

In conclusion, our results indicate that in cardiac mitochondria, the α-KGDH is a sink rather than a source of ROS, since NADH produced from α-KGDH is preferentially shuttled towards the NNT rather than to complex I. Of note, the experiments that identified the α-KGDH complex as a major source of ROS were performed in *skeletal* muscle and *brain* mitochondria. We showed previously that in contrast to *cardiac* mitochondria, these have negligible NNT activity (194), thereby preventing the antioxidative “safety valve escape” of NADH shuttling to NADPH under reducing conditions. Therefore, our data resolve a seeming paradox of α-KGDH being a source or a sink for ROS in mitochondria under various conditions. Furthermore, downregulation of α-KGDH by microRNA-146a during cardiac hypertrophy and failure [5] may contribute to redox imbalance during situations of elevated cardiac workload.

Declarations

Funding

CM is supported by the German Research Foundation (DFG; Ma 2528/7-1; SFB 894; TRR-219), the Federal Agency of Research and Education (BMBF; 01EO1504; CF.3, RC.2) and the Corona Foundation. SH acknowledges the support from the Netherlands Cardiovascular Research Initiative, an initiative with support of the Dutch Heart Foundation, CVON2016-Early HFPEF, 2015-10, CVON She-PREDICTS, grant 2017-21 and CVON Arena-PRIME, 2017-18. We acknowledge the support of the ERA-Net-CVD project MacroERA, 01KL1706. GEG is supported by NIH grant P01AG014930.

Conflicts of interest

No competing financial interests exist.

Ethics approval

All animal experiments were performed in accordance to guidelines of the local animal ethics committee.

Figures and Legends

Figure 1. H_2O_2 emission from cardiac mitochondria supplied with pyruvate/malate or α-ketoglutarate.

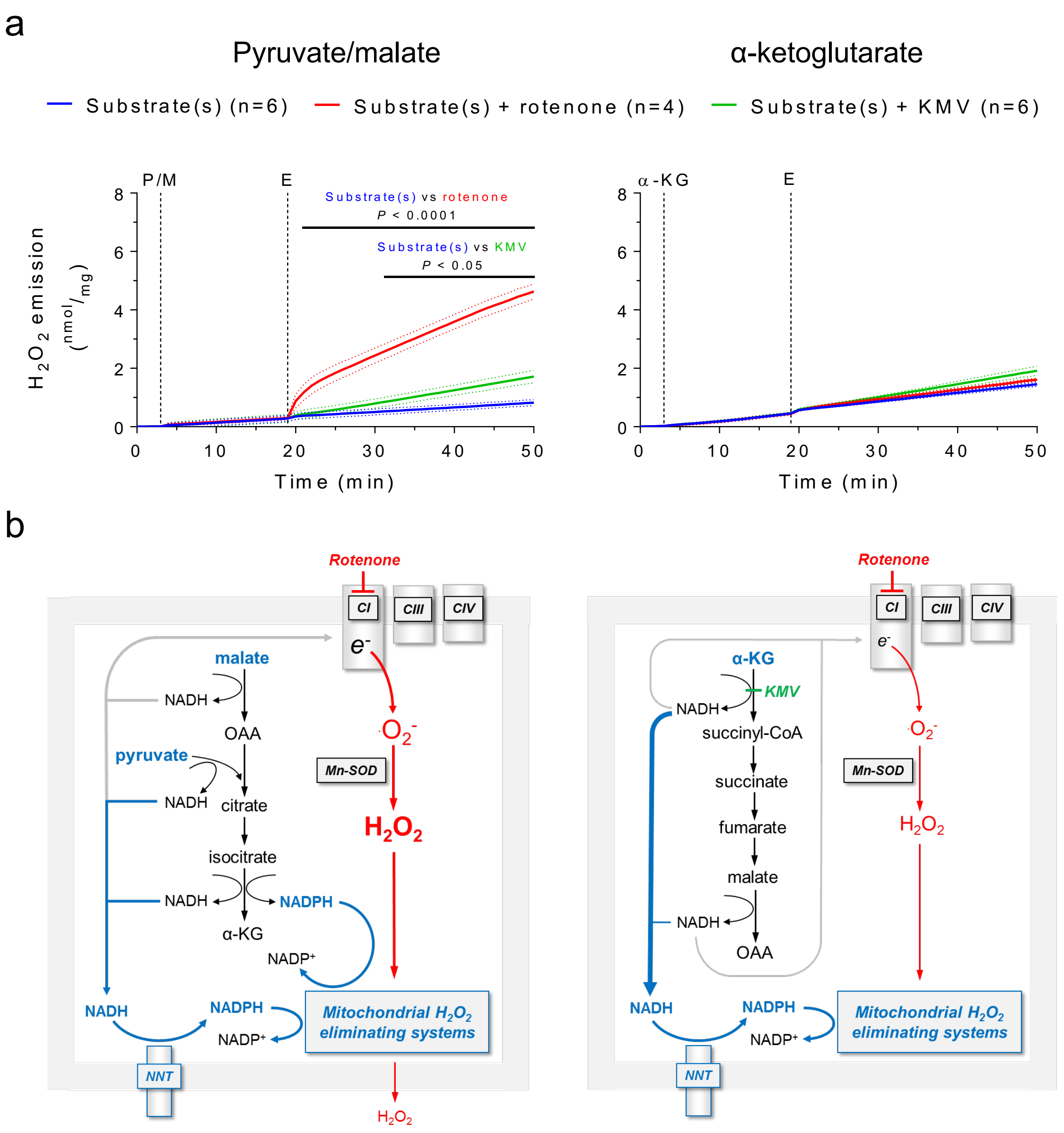

(**a**) H_2O_2 emission (by Amplex® UltraRed) of isolated cardiac mitochondria harvested from BL/6N mice was measured in the presence of pyruvate and malate (5 mM each) or α-ketoglutarate (5 mM) as substrates (added at time point S) and in response to addition of DMSO (blue trace), complex I inhibition with rotenone (8 µM, red trace) or the α-ketoglutarate dehydrogenase inhibitor KMV (10 mM, green trace) at time point E (effectors).

(**b**) The mitochondrial hydrogen peroxide (H_2O_2)-eliminating systems, i.e. glutathione peroxidase and peroxiredoxin, are maintained in their active form by a series of redox reactions requiring NADPH as an electron donor. In mitochondria respiring on pyruvate and malate (left panel), NADPH regeneration is mainly mediated by the nicotinamide nucleotide transhydrogenase (NNT) and the isocitrate dehydrogenase type 2 reactions. Upon complex I inhibition with rotenone, the increase in the $NADH/NAD^+$ ratio induces leakage of electrons and consequent superoxide ($\cdot O_2^-$) formation at complex I of the respiratory chain. The mitochondrial superoxide dismutase (Mn-SOD) converts $\cdot O_2^-$ to H_2O_2, which overcomes the mitochondrial detoxifying capacity and accounts for the H_2O_2 emission observed in (**a**). In BL/6N mitochondria supplied with α-KG (right panel), the NADH produced via the α-KGDH reaction is preferentially used for NADPH regeneration via the NNT rather than being shuttled to complex I, where it would induce $\cdot O_2^-$ formation, thereby leading to very low levels of H_2O_2 emission as seen in (**a**).

Results are shown as mean ± standard error of the mean; n = number of mice. Significance was calculated using two-way ANOVA with Bonferroni's post-hoc test. Continuous black lines above traces indicate statistically significant differences (defined as $P < 0.05$) between experimental groups by Bonferroni's post-hoc test.

Figure 2. H_2O_2 emission from cardiac mitochondria of BL/6J mice supplied with pyruvate/malate or α-ketoglutarate.

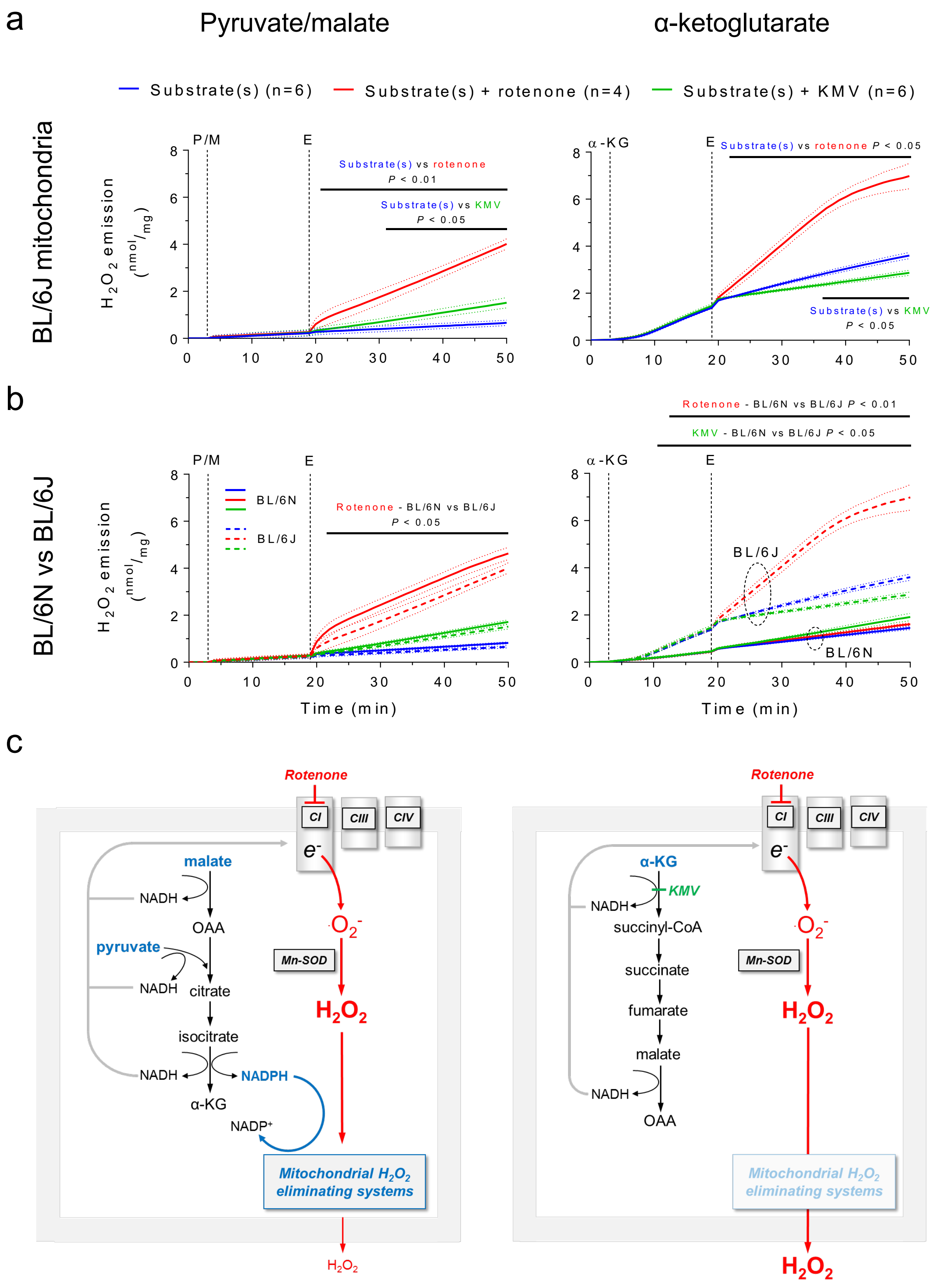

(**a**) H_2O_2 emission (by Amplex® UltraRed) of isolated cardiac mitochondria harvested from mice lacking a functional NNT (BL/6J) was measured in the presence of pyruvate and malate (5 mM each) or α-ketoglutarate (5 mM) as substrates (added at time point S) and in response to addition of DMSO (blue trace), complex I inhibition with rotenone (8 µM, red trace) or the α-ketoglutarate dehydrogenase inhibitor KMV (10 mM, green trace) at time point E (effectors).

(**b**) Direct comparison of H_2O_2 emission from BL/6N and BL/6J mitochondria supplied with pyruvate and malate or α-ketoglutarate [data from **Figure 1a** and panel (**a**)].

(**c**) In mitochondria lacking a functional NNT (BL/6J) provided with pyruvate and malate (left panel), the isocitrate dehydrogenase reaction is sufficient to maintain mitochondrial H_2O_2-eliminating capacity, leading to a rate of H_2O_2 emission comparable to that of BL/6N mitochondria. In contrast, the mitochondrial antioxidative capacity cannot be regenerated in BL/6J mitochondria supplied with α-KG alone (right panel), and α-KGDH-derived NADH fuels ROS production at the respiratory chain when complex I is inhibited with rotenone, leading to the highest rate of H_2O_2 emission observed in the four experimental conditions.

Results are shown as mean ± standard error of the mean; n = number of mice. Significance was calculated using two-way ANOVA with Bonferroni's post-hoc test. Continuous black lines above traces indicate statistically significant differences (defined as $P < 0.05$) between experimental groups by Bonferroni's post-hoc test.

Figure 3. H_2O_2 emission from cardiac mitochondria depleted of their antioxidative capacity.

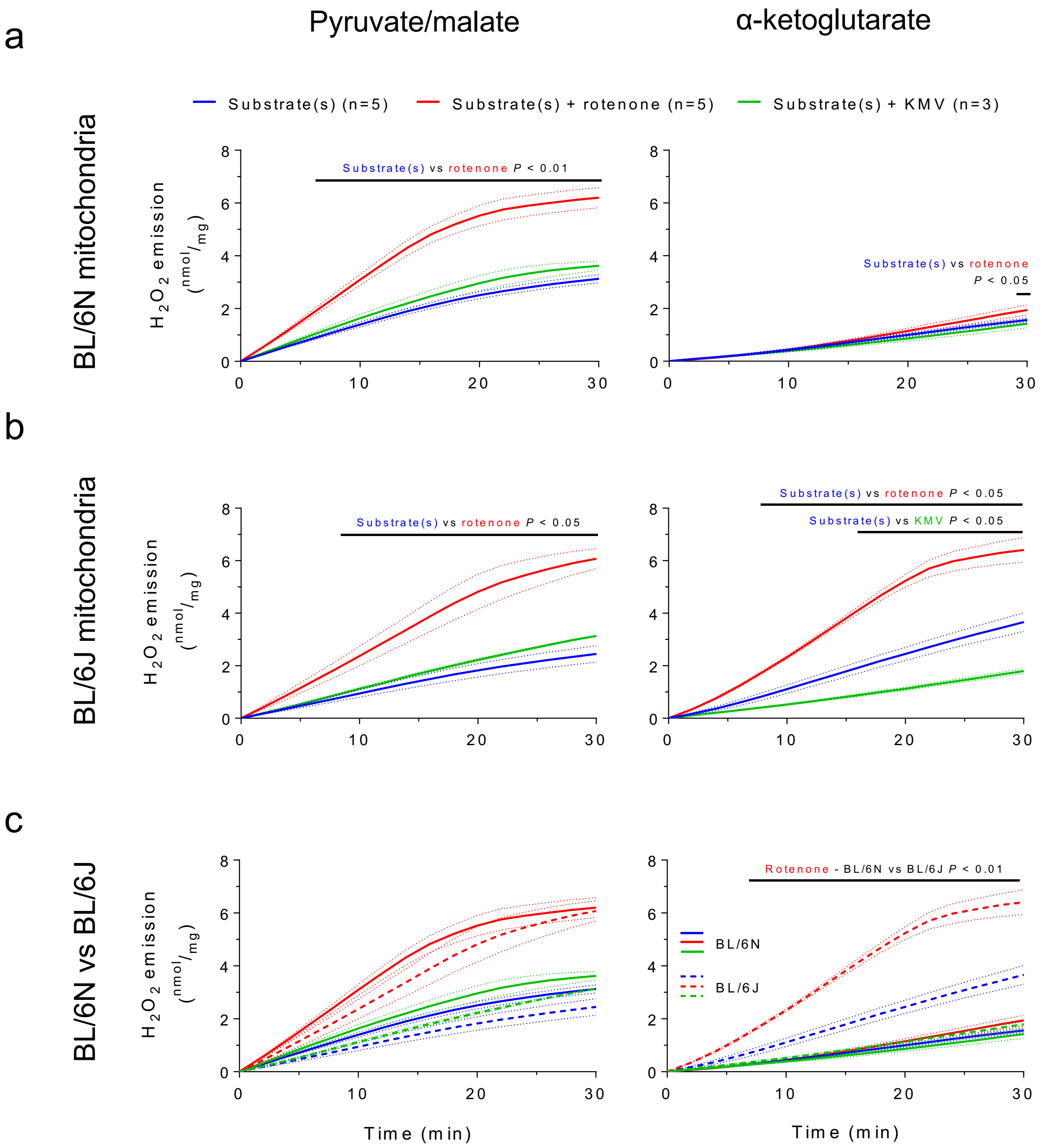

H_2O_2 emission (by Amplex® UltraRed) of isolated cardiac mitochondria harvested from BL/6N (**a**) or BL/6J (**b**) mice was measured after incubation with with 2,4-dinitrochlorobenzene, which binds covalently to glutathione. Pyruvate and malate (5 mM each) or α-ketoglutarate (5 mM) were used as substrates. H_2O_2 emission was measured in the presence of vehicle (black trace), substrate(s) alone (blue trace), rotenone (8 µM, red trace) or the α-ketoglutarate dehydrogenase inhibitor KMV (10 mM, green trace). The direct comparison between BL/6N and BL/6J mitochondria is shown in (**c**).

Results are shown as mean ± standard error of the mean; n = number of mice. Significance was calculated using two-way ANOVA with Bonferroni's post-hoc test. Continuous black lines above traces indicate statistically significant differences (defined as $P < 0.05$) between experimental groups by Bonferroni's post-hoc test.

Figure 4. NAD(P)H, membrane potential and respiration of cardiac mitochondria supplied with pyruvate/malate or α-ketoglutarate.

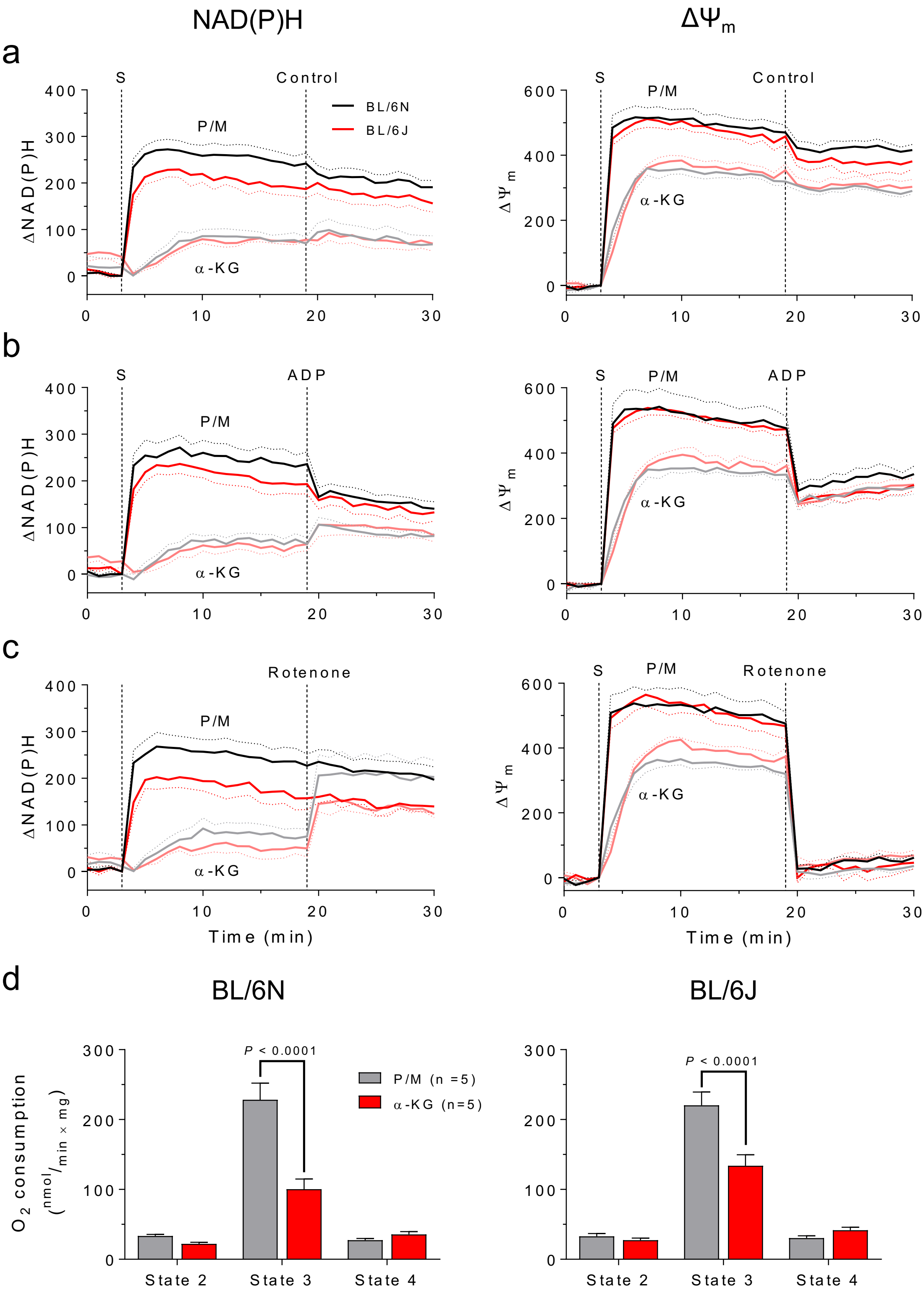

NAD(P)H autofluorescence (left) and mitochondrial membrane potential ($\Delta\Psi_m$, measured with the potentiometric dye TMRM, right) of cardiac mitochondria from BL/6N (black and gray traces) and BL/6J (red traces) mice supplied with pyruvate and malate (P/M, 5 mM each) or α-ketoglutarate (α-KG, 5 mM) as substrates (added at time point S). The effects of DMSO (as control, **a**), ADP (1 mM, **b**) and the complex I inhibitor rotenone (8 µM, **c**) on NAD(P)H autofluorescence and $\Delta\Psi_m$ did not differ between BL/6N and BL/6J mitochondria. (**d**) Respiration of isolated mitochondria from BL/6N (left) and BL/6J (right) mice supplied with P/M or α-KG. O_2 consumption was measured in the presence of substrate(s) alone (state 2), upon ADP addition (1 mM, state 3) and after inhibiting ADP phosphorylation with oligomycin (1.2 µM, state 4). Results are shown as mean ± standard error of the mean; n = number of mice. Significance was calculated using two-way ANOVA with Bonferroni's post-hoc test.

Figure 5. Mitochondrial respiration, redox state, and ROS production of isolated mitochondria and cardiac myocytes grouped based on α-ketoglutarate dehydrogenase activity.

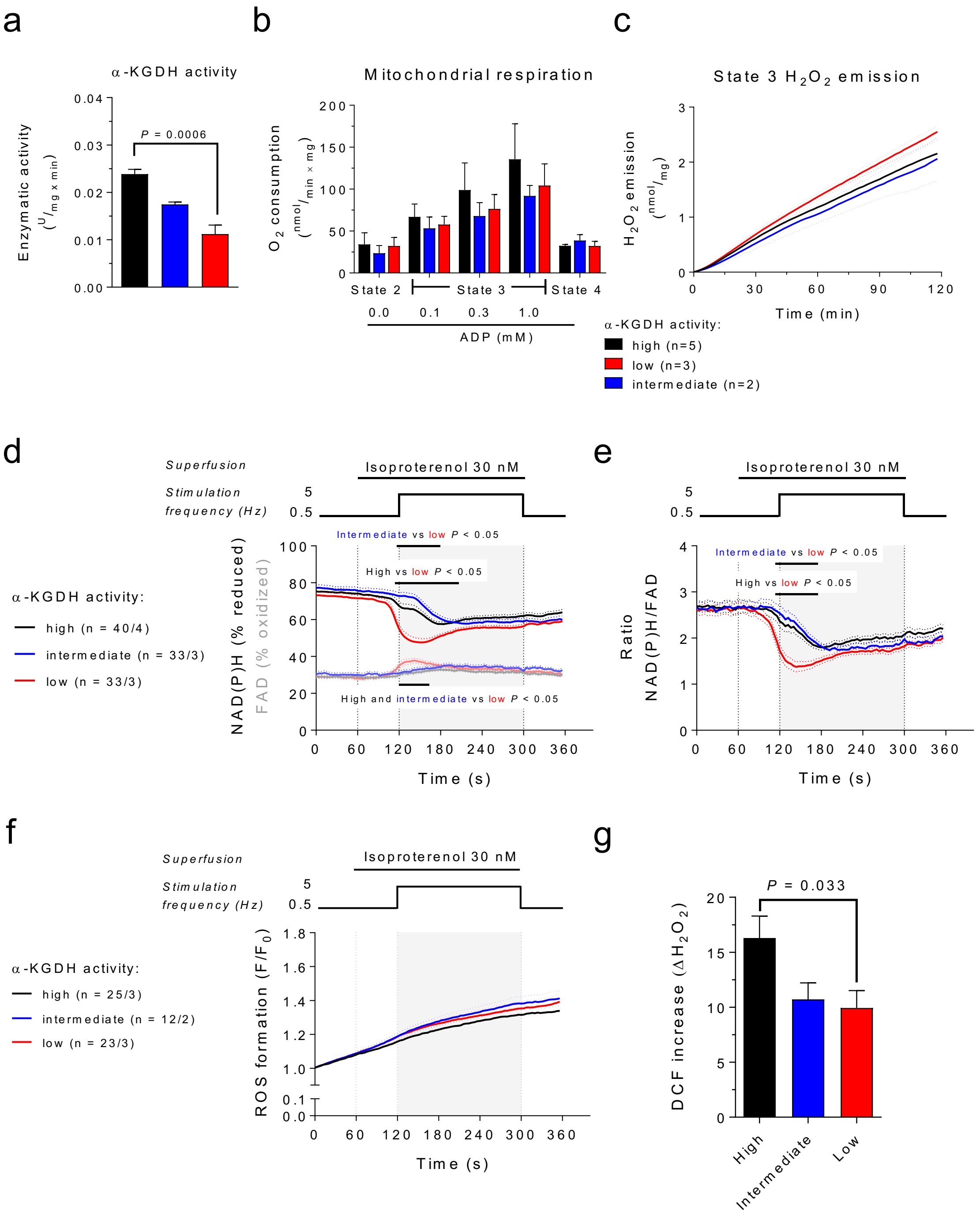

Enzymatic activity of α-KGDH (**a**) in the heart of *Dlst*$^{+/-}$ mice and wild-type littermates divided in groups of high, intermediate and low α-KGDH activity.

O_2 consumption (**b**) and H_2O_2 emission (by Amplex® UltraRed, **c**) of isolated cardiac mitochondria supplied with α-ketoglutarate as substrate and grouped based on their respective α-ketoglutarate dehydrogenase activity. In (**b**), O_2 consumption was measured in the presence of α-ketoglutarate alone (state 2), upon ADP addition (state 3) and after inhibiting ADP phosphorylation with oligomycin (1.2 µM, state 4). In (**c**), H_2O_2 emission was measured in the presence of saturating ADP (1 mM).

NAD(P)H and FAD autofluorescence (**d**), NAD(P)H/FAD ratio (**e**) and ROS production (with the fluorescent ROS indicator DCF, **f**) of isolated, field-stimulated cardiac myocytes grouped based on their α-ketoglutarate dehydrogenase (α-KGDH) activity. To simulate an increase in workload, cardiac myocytes were superfused with the β-agonist isoproterenol (30 nM) and stimulation frequency was increased from 0.5 to 5 Hz for 180 s (corresponding to the gray-shaded area). To assess H_2O_2-eliminating capacity, cardiac myocytes were superfused with external H_2O_2 (10 mM) and the increase in DCF fluorescence was measured (**g**).

Results are shown as mean ± standard error of the mean; n = number of mice for panels (**a**) to (**c**) and number of cells/number of mice for panels (**d**) to (**f**). Significance was calculated using one-way ANOVA with Bonferroni's post-hoc test for panels (**a**) and (**g**) and two-way ANOVA with Bonferroni's post-hoc test for panels (**b**) to (**f**). *P*-values in panels (**a**) and (**g**) indicate statistically significant differences (defined as $P < 0.05$) by Bonferroni's post-hoc test. In panels (**d**) and (**e**), continuous black lines above traces indicate statistically significant differences between experimental groups by Bonferroni's post-hoc test.

Supplementary Figures and Legends

Supplementary Figure 1.

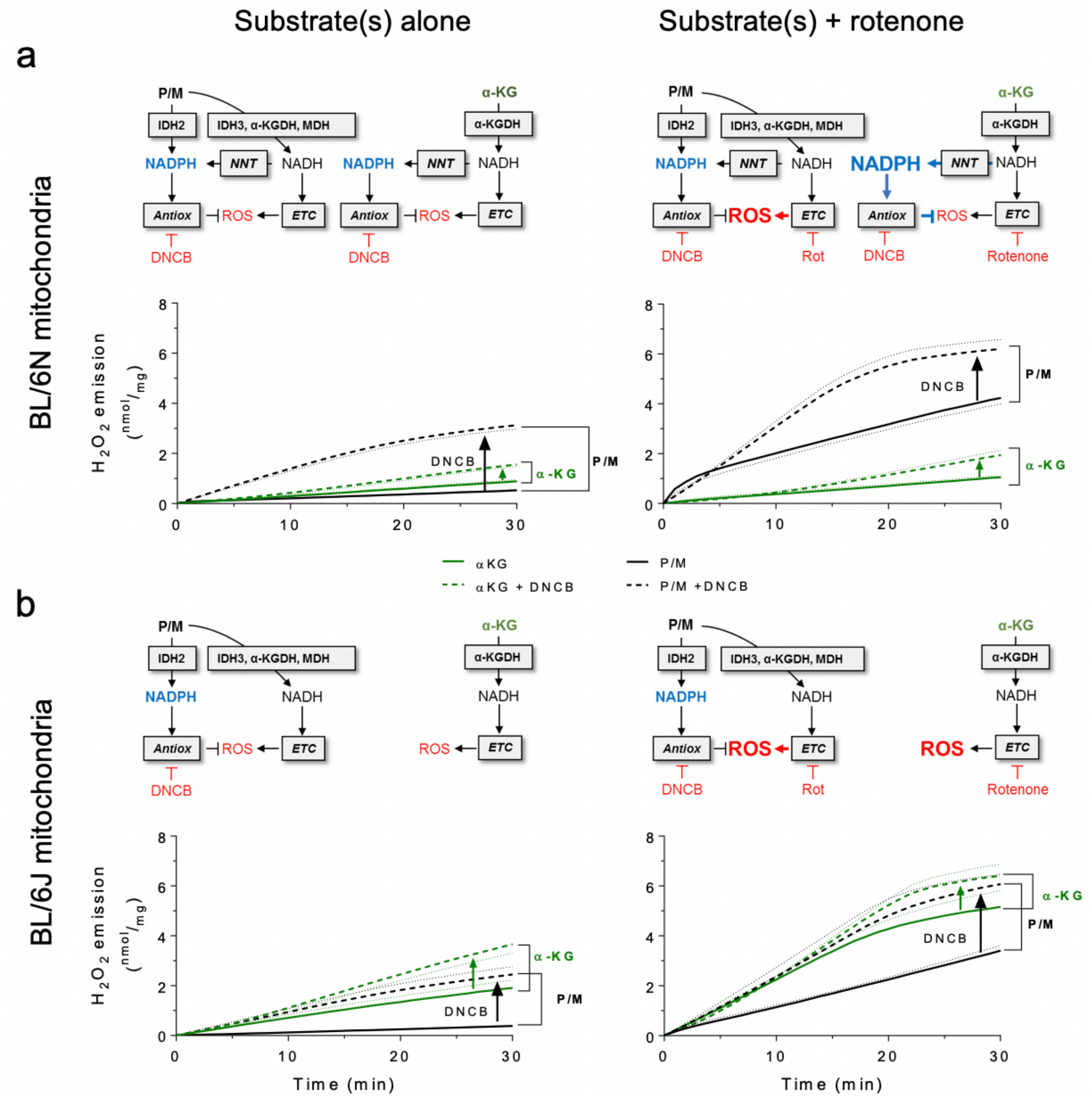

Direct comparison of traces shown in **Figure 1a** and **2a**. H_2O_2 emission (by Amplex® UltraRed) of isolated cardiac mitochondria harvested from BL/6N (**a**) or BL/6J (**b**) mice with preserved antioxidative capacity (solid lines) or after treatment with DNCB (dashed lines). Pyruvate and malate (5 mM each, black traces) or α-ketoglutarate (5 mM, green traces) were used as substrates, and H_2O_2 emission was measured in the presence of vehicle (left part) or rotenone (right part).

Supplementary Figure 2.

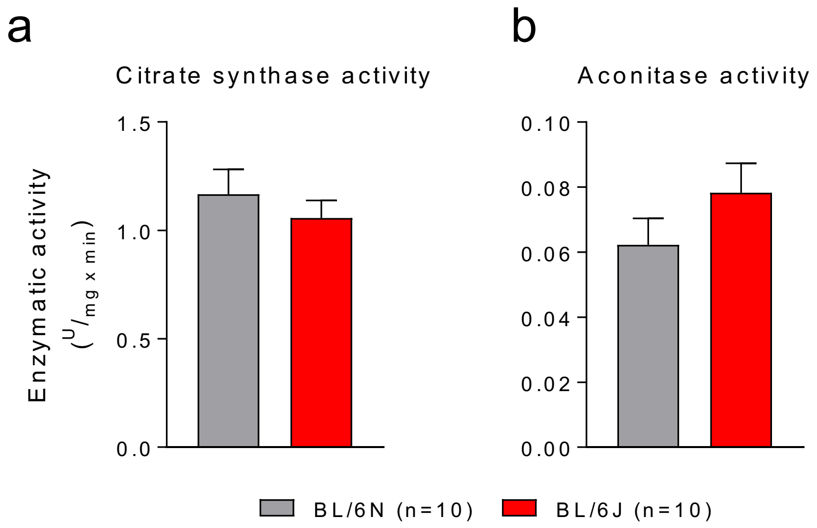

Enzymatic activity of citrate synthase (**a**) and aconitase (**b**) in cardiac mitochondria of BL/6N and BL/6J mice.

Significance was calculated using Student's t-test.

Supplementary Figure 3.

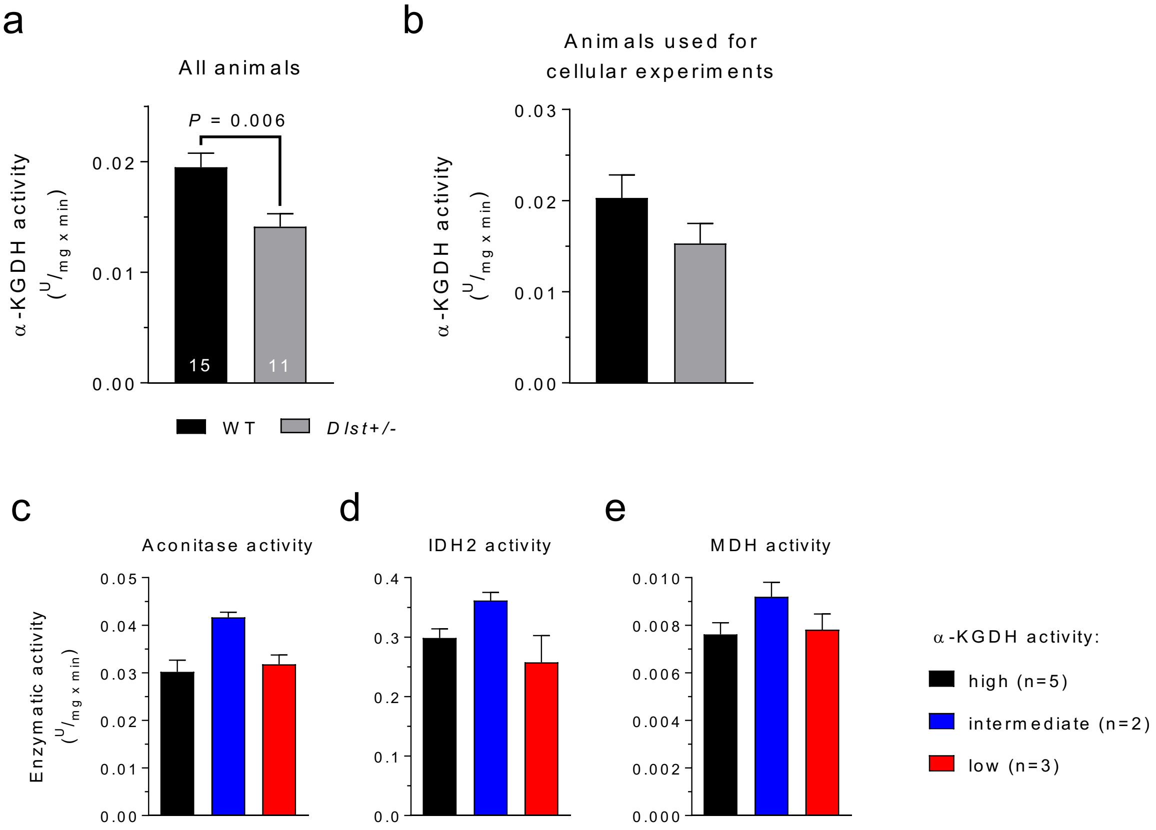

Enzymatic activity of α-KGDH in the heart of wild-type and *Dlst*$^{+/-}$ mice (**a**) and in the heart of mice used for cellular experiments shown in **Figure 5d** and **e** (**b**). Enzymatic activity of aconitase (**c**), isocitrate dehydrogenase type 2 (IDH2, **d**) and malate dehydrogenase (MDH, **e**) in the heart of *Dlst*$^{+/-}$ mice and wild-type littermates divided in groups of high, intermediate and low α-KGDH activity.

Significance was calculated using Student’s t-test for panel (**a**) and (**b**) and one-way ANOVA with Bonferroni post-hoc test for panels (**c**) to (**e**).

Supplementary Figure 4.

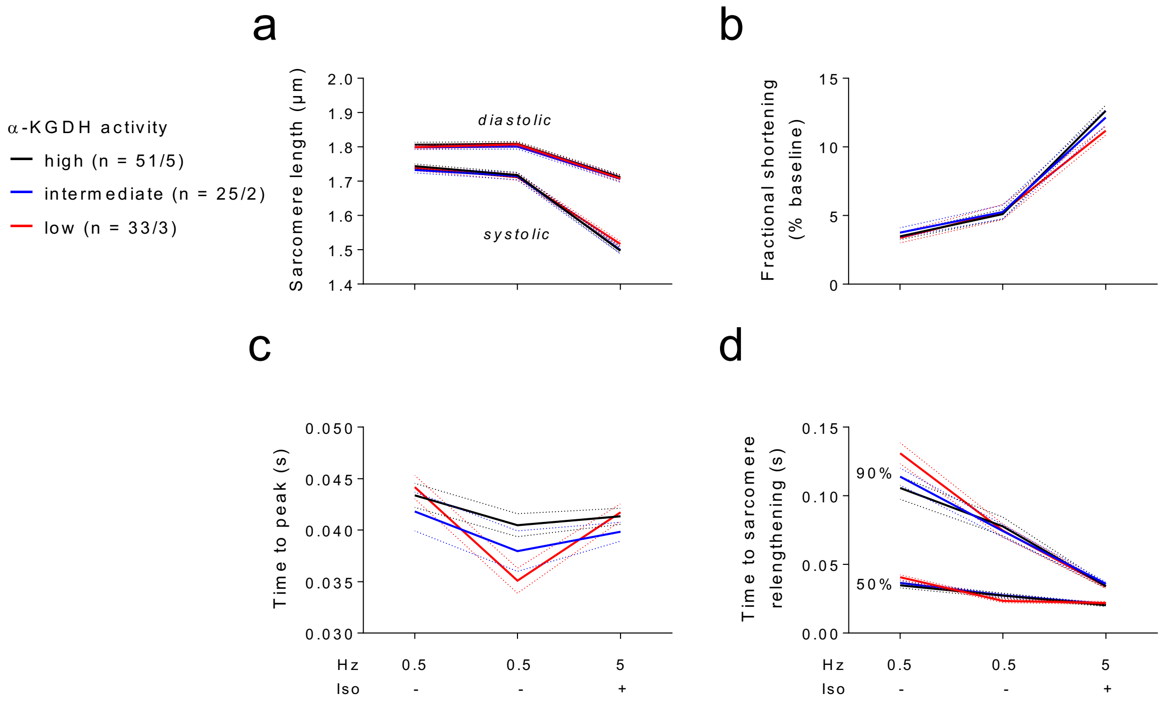

Sarcomere length (**a**), fractional sarcomeric shortening (**b**), time to peak sarcomere shortening (**c**) and sarcomere re-lengthening time (**d**) of isolated cardiac myocytes from *Dlst*$^{+/-}$ mice and wild-type littermates divided in groups of high, intermediate and low α-KGDH activity. Cardiac myocytes were subjected to the same experimental stress protocol described for **Figure 5d-g**.

Significance was calculated using two-way ANOVA with Bonferroni’s post-hoc test for panels (**b**) to (**f**).

Mechano-energetic uncoupling underlies lack of contractile reserve in Barth syndrome cardiomyopathy

Edoardo Bertero, Alexander Nickel, Michael Kohlhaas, Mathias Hohl, Vasco Sequeira, Carolin Krug, Julia Schwemmlein, Christopher Carlein, Kai Münker, Sarah Atighetchi, Andreas Müller, Andrey Kazakov, Reinhard Kappl, Karina von der Malsburg, Alexander von der Malsburg, Michael Böhm, Ulrich Laufs, Markus Hoth, Peter Rehling, Jan Dudek, Martin van der Laan, Leticia Prates Roma, Christoph Maack

As submitted on January 4th, 2021.

Abstract

Barth syndrome is associated with infantile onset of cardiac and skeletal muscle myopathy and caused by mutations of the gene encoding tafazzin, which catalyzes maturation of cardiolipin in the inner mitochondrial membrane. Cardiomyopathy was previously traced to disassembly of respiratory chain complexes with increased formation of reactive oxygen species (ROS). Here, we show that in tafazzin-deficient mice, loss of the Ca^{2+} uniporter in cardiac, but not skeletal muscle mitochondria prevents Ca^{2+}-mediated activation of Krebs cycle-related regeneration of NADH and $FADH_2$, compromising energetic adaptation of cardiac myocytes during hormonal and/or mechanical workload transitions. This mechano-energetic uncoupling prevents the physiological increase in systolic force generation and occurs in the absence of severe respiratory chain defects or increased mitochondrial ROS emission. These data provide a mechanistic explanation for the inability of Barth syndrome patients to adapt their cardiac output to the required demands during physical exercise and highlight tissue-specific consequences of disturbed cardiolipin remodeling.

Introduction

Barth syndrome (BTHS) is an X-linked multisystem disorder characterized by infantile onset of cardiomyopathy, skeletal myopathy, recurrent neutropenia, and growth retardation (51). It is caused by mutations in the gene encoding tafazzin (*Taz*), a transacylase catalyzing the final step in the maturation of cardiolipin (CL), a key phospholipid of the inner mitochondrial membrane (IMM) (52, 53, 61). CL is required for the structural organization of several protein complexes in the IMM, in particular the electron transport chain (ETC) super-complexes (so-called "respirasomes") (210). Defective CL maturation in BTHS destabilizes respirasomes (62-64, 78) and hampers production of adenosine triphosphate (ATP) by oxidative phosphorylation (62, 64, 103). Cellular models of BTHS revealed increased mitochondrial formation of reactive oxygen species (ROS) (87, 99, 103), and suppressing mitochondrial ROS prevented systolic dysfunction in a "heart-on-chip" inducible pluripotent stem cell (iPSC) model of BTHS (87), suggesting a causal role of mitochondrial ROS in BTHS pathophysiology. Since ROS formation and elimination in cardiac mitochondria are intimately coupled to the processes of excitation-contraction (EC) coupling (211), we here employed a mouse model with global short hairpin RNA (shRNA)-mediated knockdown (KD) of the *Taz* gene to analyze mitochondrial function integrated with ion handling in adult cardiac myocytes and hearts. While previous studies using this mouse model observed that cardiac dysfunction was associated with ultrastructural and functional abnormalities of cardiac (and skeletal) muscle mitochondria (88-92), it is still unresolved how these abnormalities mechanistically relate to the development of cardiomyopathy.

In cardiac myocytes, variations in energetic demand of EC coupling are tightly matched by oxidative phosphorylation under the control of calcium (Ca^{2+}) and adenosine diphosphate (ADP) (8), a process termed "mechano-energetic coupling" (212). While ATP consumption at myofilaments and ion transporters oxidizes Krebs cycle-derived NADH and $FADH_2$ through ADP-induced stimulation of respiration ("pull condition"), uptake of Ca^{2+} into mitochondria via the Ca^{2+} uniporter (MCU) stimulates Krebs cycle dehydrogenases to regenerate these pyridine nucleotides ("push" condition; **Graphical abstract**) (213). In addition, the Krebs cycle regenerates NADPH required for mitochondrial antioxidative capacity either directly (via NADP-linked isocitrate and malate dehydrogenases) or indirectly via the nicotinamide nucleotide transhydrogenase (NNT) reaction (47, 211, 214). Therefore, Ca^{2+}-driven metabolic adaptations sustain both ATP production and ROS elimination under conditions of increased workload (8, 46).

We reported previously that alterations of EC coupling occurring in heart failure (HF) with reduced ejection fraction (HFrEF), such as decreased Ca^{2+} release from the sarcoplasmic reticulum (SR) and elevated cytosolic sodium (Na^+), hamper mitochondrial Ca^{2+} accumulation and thereby, provoke energy supply-and-demand mismatch and excessive ROS emission from mitochondria (30, 43, 46). Furthermore, elevated cardiac afterload drains mitochondrial NADPH via (reverse-mode) NNT towards NADH and ATP production, but at the cost of NADPH-coupled antioxidative capacity, triggering oxidative stress that causes cell death, cardiac remodeling, and dysfunction (47). Consequently, targeting mitochondrial Ca^{2+} handling (209), ROS (215, 216), or CL (47, 217-219) ameliorates HF progression in various animal models.

Despite this increasingly detailed knowledge on mechano-energetic coupling and uncoupling in normal and failing hearts, hardly any detailed information is available on these aspects in BTHS cardiomyopathy. Here, we show that in agreement with clinical data on patients with BTHS (118, 220-222), cardiomyopathy in *Taz*-KD mice is in many aspects reminiscent of HF with *preserved* (HFpEF) rather than *reduced* ejection fraction, with increased myofilament Ca^{2+} affinity and slowed cross-bridge cycling velocity impairing myocardial relaxation and thereby, hindering the filling of the left ventricle (LV) during diastole. On the mitochondrial level, disruption of mechano-energetic coupling rather than defects in respiratory chain (62-64, 103) and/or increased formation of ROS (87, 99, 103) evolves as the primary energetic defect in BTHS cardiomyopathy. As a central mechanism, substantial downregulation of the MCU in cardiac (but not skeletal muscle) mitochondria blunts adaptation of Krebs cycle activity to ATP consumption, thereby limiting the contractile reserve during physiological elevations of cardiac workload (**Graphical abstract**). These data provide mechanistic insights into two major clinical problems in BTHS patients, i.e., the inability of the heart to increase LV ejection fraction (LVEF) during physical exercise (119) and, to some extent, the increased risk for arrhythmias (223).

Results

Diastolic dysfunction and moderate systolic dysfunction in *Taz*-KD cardiomyopathy

While mice with global shRNA-mediated KD of *Taz* (**Figures S1A-C**) thrived normally up to an age of 20 weeks, body weight was ~18% and heart weight (by tibia length) ~11% lower in 50-week-old (w/o) *Taz*-KD mice compared to wild-type (WT) littermates (**Figures 1A-C, Table S1**). Magnetic resonance imaging revealed that at 10 weeks of age, LVEF, cardiac output, ventricular volumes, and cardiac mRNA expression of atrial natriuretic peptide (*Anp*) were unchanged between *Taz*-KD and WT mice (**Figures 1D-H, Table S2**). However, peak LV radial and circumferential strain as more sensitive parameters of contractile function were mildly reduced in *Taz*-KD already at this young age (**Figures S1D-F**). Between 10 and 15 weeks, cardiac output and LVEF modestly deteriorated in *Taz*-KD mice, while LV cavity size remained unchanged at 20 and decreased at 50 weeks (**Figures 1D-G, Table S2**). Although LVEF remained "preserved" at >50% in Taz-KD mice even at 50 weeks, peak longitudinal, circumferential, and radial strain further deteriorated (**Figures S1G-I**) and *Anp* expression increased markedly after week 10 (**Figure 1H**), indicating elevated LV filling pressures. At 50 weeks, mitral inflow velocity assessed with Doppler echocardiography revealed that the E wave, reflecting early passive filling of the LV before atrial contraction, was lost in six of eight *Taz*-KD-, but not WT mice (**Figure 1I**), indicating impaired relaxation of the LV. Despite modestly increased gene expression of connective tissue growth factor (*Ctgf*, **Figure 1J**), no relevant increase in cardiac fibrosis occurred (**Figures 1K, L**). Therefore, impaired relaxation is unlikely related to extracellular matrix remodeling but rather to cardiac myocyte dysfunction.

Defects in excitation-contraction coupling in *Taz*-KD myocytes

To reveal the underlying mechanisms for cardiac dysfunction, sarcomere shortening was analyzed together with cytosolic Ca^{2+} concentrations ($[Ca^{2+}]_c$) in unloaded isolated, field-stimulated cardiac myocytes from 10 w/o mice. At baseline (0.5 Hz stimulation), *Taz*-KD myocytes displayed enhanced fractional sarcomere shortening compared to WT (**Figures 2A-C**), while the amplitude of $[Ca^{2+}]_c$ transients ($\Delta[Ca^{2+}]_c$) was unchanged (**Figures 2E, F**). Of note, the rate of $[Ca^{2+}]_c$ decay was faster in *Taz*-KD vs. WT myocytes (**Figures 2E, G**), while sarcomere re-lengthening kinetics were similar (**Figure 2D**). After simulating a physiological workload increase by β-adrenergic stimulation with isoproterenol (Iso; 30 nM) and increasing stimulation frequency to 5 Hz, fractional sarcomere shortening increased to similar values, while diastolic and systolic sarcomere lengths were shorter in *Taz*-KD vs. WT myocytes (**Figures 2A-C**). In contrast, the Iso/5 Hz-induced increase in diastolic and systolic $[Ca^{2+}]_c$ and thereby, also $\Delta[Ca^{2+}]_c$ were blunted in *Taz*-KD myocytes, while rates of $[Ca^{2+}]_c$ decay accelerated to similar maximal levels in both groups (**Figures 2E-G**).

In murine cardiac myocytes, ~90% of cytosolic Ca^{2+} are removed by the SR Ca^{2+} ATPase (SERCA) during steady-state $[Ca^{2+}]_c$ transients, while ~10% are removed by the sarcolemmal Na^+/Ca^{2+}-exchanger (NCX) (17, 18, 224). To determine the contribution of SERCA and NCX towards $[Ca^{2+}]_c$ removal and at the same time, assess SR Ca^{2+} load, we applied sequential caffeine pulses after pacing at 0.5 Hz and Iso/5 Hz, respectively. While caffeine-induced SR Ca^{2+} release and fractional SR Ca^{2+} release during steady-state $[Ca^{2+}]_c$ transients were similar between genotypes under either condition (**Figures 2I-K**), Iso/5 Hz-induced accumulation of diastolic $[Ca^{2+}]_c$ and net cellular Ca^{2+} load (i.e., maximal $[Ca^{2+}]_c$ after caffeine-induced SR Ca^{2+} release) were lower in *Taz*-KD vs. WT myocytes (**Figures 2L-N**). Again, rates of $[Ca^{2+}]_c$ decline during steady-state $[Ca^{2+}]_c$ transients (reflecting mostly SERCA activity) were faster in *Taz*-KD vs. WT myocytes at baseline, but increased to similar maximal rates in both genotypes at Iso/5 Hz (**Figures 2G, O**). Furthermore, also $[Ca^{2+}]_c$ decay kinetics after caffeine, reflecting mostly forward-mode NCX activity (224), were accelerated in *Taz*-KD vs. WT myocytes at baseline at 0.5 Hz (in trend) and Iso/5 Hz ($p<0.05$), respectively (**Figure 2P**), but yet these rates were an order of magnitude slower (τ values ~10-fold longer) than SERCA rates (**Figure 2O**). These data indicate that $[Ca^{2+}]_c$ decay is hastened by accelerated SERCA and NCX activities at baseline, with a reduced SERCA reserve being recruited during β-adrenergic stimulation in *Taz*-KD vs. WT myocytes.

In cardiac myocytes from aged (50 w/o) Taz-KD mice, a similar phenotype evolved as in young (10 w/o) mice, with shorter sarcomere length and enhanced fractional shortening at Iso/5 Hz despite a blunted increase of $\Delta[Ca^{2+}]_c$ (**Figures S2A-D**). In agreement with progressive diastolic dysfunction *in vivo* (**Figures 1H, I**), sarcomere re-lengthening substantially slowed in 50 w/o *Taz*-KD vs. WT myocytes at baseline and Iso/5 Hz (**Figure 2D**). When plotting sarcomere length against $[Ca^{2+}]_c$ in the same cells, respectively, sarcomeres were shorter at any given $[Ca^{2+}]_c$ at 10

(**Figure 2H**) or 50 weeks (**Figures S2E, F**), pinpointing increased Ca^{2+} affinity of myofilaments to underlie diastolic dysfunction in *Taz*-KD myocytes.

To resolve this, we assessed force-Ca^{2+} relationships in membrane-permeabilized and mechanically preloaded myocytes from young (10 w/o) mice. While cross-sectional area, maximal and passive forces, and Ca^{2+}-cooperative activation remained unchanged between genotypes (**Table S3**), *Taz*-KD myocytes displayed a leftward shift in the force/pCa relationship (**Figure 2Q**), confirming elevated myofilament Ca^{2+} sensitivity (EC_{50} 2.2±0.1 vs. 3.0±0.2 μM $[Ca^{2+}]$ for *Taz*-KD vs. WT, respectively; p=0.0002). Of note, rate constants of tension redevelopment after re-stretching (k_{TR}) plotted against corresponding isometric forces, indexing cross-bridge cycling velocity (225, 226), were (s)lower in *Taz*-KD than WT myocytes (**Figure 2R**).

In summary, increased myofilament Ca^{2+} sensitivity and decreased cross-bridge cycling velocity are early defects of EC coupling in *Taz*-KD hearts, which are partly compensated by accelerated SERCA- and NCX-dependent $[Ca^{2+}]_c$ decay kinetics at young age (**Graphical abstract**). This preactivation of Ca^{2+} handling, however, blunts the recruitable SERCA reserve during β-adrenergic stimulation already at young age. With aging, diastolic dysfunction *in vivo* (**Figure 1I**) and *in vitro* (**Figure 2D**) surfaces already in the absence of β-adrenergic stimulation, despite maintained preactivated SERCA activity (**Figure S3D**). Since cross-bridge cycling and SERCA activity are main cellular ATP consumers (224), these alterations are expected to pose an extra energetic burden on mitochondria in *Taz*-KD myocytes. Therefore, it is essential to evaluate mitochondrial function in an integrated manner in conjunction with the pathological alterations of EC coupling in *Taz*-KD myocytes.

Mild respiratory dysfunction, but unchanged ROS emission in cardiac *Taz*-KD mitochondria

Since *Taz* silencing affects mitochondrial CL synthesis, we first analyzed the structural organization and function of the ETC in cardiac mitochondria. Blue native gel electrophoresis (BN-PAGE) revealed destabilization of supercomplexes ($I\text{-}III_n\text{-}IV_n$) and increased abundance of monomeric cytochrome *c* oxidase in 10 w/o *Taz*-KD mitochondria, which was, however, not further aggravated after 50 weeks (**Figure 3A**). In line with previous studies (62, 64, 93), using pyruvate/malate as substrates, submaximal and maximal ADP-coupled ("state 3") respiration was lower in cardiac mitochondria from 10 w/o *Taz*-KD vs. WT mice (**Figure 3B**). However, at 20 and 50 weeks of age, respiratory capacity deteriorated in WT animals, but was no longer different in *Taz*-KD vs. WT mice (**Figures 3E; S3A, B**).

Since mitochondrial ROS formation was elevated in cellular models of BTHS (87, 99, 103), we determined superoxide ($^{\bullet}O_2^-$) and H_2O_2 formation/emission in isolated cardiac mitochondria. Neither mitochondrial $^{\bullet}O_2^-$ formation nor H_2O_2 emission were different in the absence or presence of ADP, at 10, 20 or 50 weeks of age, respectively (**Figures 3C, D, F, G; Figures S3C-E**). Therefore, despite evident remodeling of the ETC, ROS formation in- and emission from isolated cardiac mitochondria of *Taz*-KD mice unlikely underlies the pathogenesis of cardiac dysfunction.

Loss of the MCU abrogates Ca^{2+} uptake in cardiac mitochondria of *Taz*-KD mice

Since mitochondrial Ca^{2+} uptake plays a pivotal role in the dynamic regulation of mitochondrial ATP production and antioxidative capacity in cardiac myocytes (8), we determined Ca^{2+} retention capacity of isolated cardiac mitochondria from 10 w/o animals by applying Ca^{2+} pulses of 10 µM each to isolated mitochondria and determining extramitochondrial [Ca^{2+}]. In WT mitochondria, each elevation of extramitochondrial Ca^{2+} after a pulse was followed by an exponential decay, indicative of Ca^{2+} uptake into mitochondria (**Figure 4A**). After several pulses, the rate of Ca^{2+} uptake slowed and eventually, Ca^{2+} was released by mitochondria, which could be inhibited by pretreatment with cyclosporine A, an inhibitor of the permeability transition pore (PTP). Strikingly, Ca^{2+} uptake was virtually absent in *Taz*-KD mitochondria, which was unaffected by cyclosporine A (**Figure 4A**), ruling out premature PTP opening as the underlying mechanism. The same was observed in cardiac mitochondria from 20 w/o mice (**Figure S3F**).

To resolve the underlying mechanism for this substantial defect, we performed BN-PAGE analysis in cardiac mitochondria of *Taz*-KD and, for comparison, global *Mcu*-knockout (KO) mice (227). This revealed that all three MCU-specific bands decreased in 10 w/o *Taz*-KD mitochondria, reflecting structural remodeling of the MCU complex (**Figure 4B**). Western blot analyses confirmed strongly reduced protein levels of the pore-forming subunit MCUa in *Taz*-KD hearts at any age, while mRNA expression was unchanged (**Figure 4C, D and Figures S3G, H**). This observation was confirmed in iPSC-derived cardiac myocytes obtained from one BTHS patient compared to a healthy control, while voltage-dependent anion-selective channel 3 (VDAC3), NADH dehydrogenase 1β subcomplex subunit 8 (NDUFB8) and ribosome-associated membrane protein (LETM1) levels were unchanged (**Figure 4E**). In contrast, expression of the dominant-negative subunit MCUb, which inhibits MCU-dependent Ca^{2+} uptake (153, 228), increased (**Figure 4C and Figures S3G, H**). While protein levels of the regulatory subunit MCUR1 increased, the expression of other MCU complex members, i.e., MICU1, MICU2 and EMRE, were unchanged in 10 w/o *Taz*-KD mice (**Figure 4C**).

Mitochondrial Ca^{2+} uptake is preserved in skeletal muscle and brain of *Taz*-KD mice

Besides cardiomyopathy, BTHS patients develop skeletal myopathy with exercise intolerance and fatigue (229). At any age, ETC structure and H_2O_2 emission were largely unaffected, while at 50 weeks, ADP-stimulated state 3 respiration was reduced in *Taz*-KD vs. WT skeletal muscle mitochondria (**Figures S4A-F**). In contrast to cardiac-, skeletal muscle mitochondria displayed normal Ca^{2+} uptake at all ages (**Figures S5A-C**) despite modest structural remodeling of the MCU complex and a trend towards lower protein abundance of MCUa, with other MCU complex subunits unchanged (**Figures S5D, E**). In *Taz*-KD brain mitochondria, Ca^{2+} uptake, MCUa protein levels and MCU complex structure were preserved (**Figures S5F-H**). These data indicate that loss of MCUa protein primarily affects Ca^{2+} uptake in cardiac mitochondria, whereas in skeletal muscle mitochondria, Ca^{2+} accumulation is preserved despite modest changes in MCUa levels and MCU complex structure. These differences might be explained by tissue-specific CL composition of the IMM and by the higher MCU current density in murine skeletal muscle compared with cardiac mitochondria (230, 231).

Defective mitochondrial Ca^{2+} uptake provokes pyridine nucleotide oxidation during workload transitions in *Taz*-KD cardiac myocytes

To assess the consequences of MCU deficiency for mitochondrial Ca^{2+} uptake in mitochondria integrated into their physiological environment in intact cardiac myocytes, we employed a patch-clamp based technique that we previously developed to monitor $[Ca^{2+}]_c$ and mitochondrial Ca^{2+} concentrations ($[Ca^{2+}]_m$) in the same cells (30). In fact, despite unchanged $\Delta[Ca^{2+}]_c$, the amplitude of $[Ca^{2+}]_m$ transients was diminished in *Taz*-KD vs. WT myocytes and failed to further increase in response to Iso/5 Hz, blunting mitochondrial Ca^{2+} accumulation (**Figures 5A-C**).

During workload transitions, ADP accelerates electron flux along the ETC, thereby oxidizing NADH and $FADH_2$ (8). Under physiological conditions, $[Ca^{2+}]_m$

accumulation stimulates Krebs cycle dehydrogenases to maintain adequate supply of reducing equivalents to the ETC (8, 20). In WT myocytes, NAD(P)H and FAD redox states were largely maintained during workload transitions (**Figures 5D, E**). In contrast, these abruptly oxidized without any Ca^{2+}-mediated recovery during Iso/5 Hz in *Taz*-KD myocytes (**Figures 5D, E**). Despite NAD(P)H and FAD oxidation, mitochondrial membrane potential ($\Delta\Psi_m$) was maintained in both genotypes (**Figure 5F**). While baseline NAD(P)H/FAD redox states were similar in myocytes of 10 w/o mice (**Figures 5D, E**), these were more oxidized in 20 and 50 w/o *Taz*-KD vs. WT myocytes, which further aggravated during 5 Hz stimulation (**Figures S6A-D**). Of note, at 20 and 50, but not 10 weeks, *Taz*-KD myocytes displayed more spontaneous (i.e., non-stimulated) contractions compared to WT after stimulation was stepped back from 5 Hz to 0.5 Hz (**Figures 5G, H**).

To interrogate whether NAD(P)H/FAD oxidation and arrhythmias are related to defective mitochondrial Ca^{2+} uptake, Ca^{2+} extrusion via the mitochondrial Na^+/Ca^{2+} exchanger (NCLX) was inhibited with CGP-37157 (30). In fact, NCLX-inhibition reduced NAD(P)H and FAD redox states during the stress protocol (**Figure 5I**) and decreased the number of non-stimulated beats during the ensuing 0.5 Hz stimulation in *Taz*-KD myocytes (**Figure 5J**).

Mitochondrial ROS emission is prevented by upregulation of ROS-detoxifying capacity in *Taz*-KD cardiac myocytes

Since in our previous studies, inhibiting mitochondrial Ca^{2+} accumulation oxidized NAD(P)H and increased mitochondrial ROS emission (30, 46), we expected that also in *Taz*-KD myocytes, NAD(P)H oxidation would elevate mitochondrial ROS. However, oxidation of the non-selective ROS-indicator DCF was similar in myocytes from 10 w/o *Taz*-KD vs. WT mice at 0.5 Hz and Iso/5 Hz stimulation, respectively (**Figure 6A**). When myocytes were exposed to 1 mM extracellular H_2O_2, however, the increase in DCF fluorescence was ~50% lower in *Taz*-KD versus WT myocytes (**Figures 6B, C**), indicating augmented cellular H_2O_2-eliminating capacity. This was consistent with 2-fold increased protein expression of H_2O_2-eliminating catalase and glutathione peroxidase 1 (GPX1) at an age of 10 weeks, while expression of $^{\bullet}O_2^-$ eliminating superoxide dismutases (SOD) 1 and 2 as well as peroxiredoxin (PRDX) isoforms 1-3 were unchanged (**Figure 6D**). At 20 and 50 weeks of age, however, catalase and GPX1 upregulation ceased, and at 50 weeks, expression of the mitochondrial PRDX3 and SOD2 were reduced in *Taz*-KD vs. WT myocytes (**Figure 6D**).

To monitor H_2O_2 directly *in vivo*, we crossed WT and *Taz*-KD mice with mice expressing an H_2O_2-specific fluorescence reporter in the mitochondrial matrix (mito-roGFP2-Orp1) (132). The redox state of mito-roGFP2-Orp1 (reporting H_2O_2) was similar in WT and *Taz*-KD hearts at 20 weeks of age (**Figure 6E, F**) and was rather reduced in one *Taz*-KD vs. one WT heart at 50 weeks (**Figure 6E**). Also, nuclear staining of 8-hydroxy-2'-guanosine as a marker of intracellular oxidative stress was not significantly different between both genotypes (**Figure 6G**). Aconitase activity as an indirect, yet unspecific index of mitochondrial ROS formation was decreased in 50 w/o *Taz*-KD vs. WT hearts (**Figure 6H**). This, however, may also be related to disturbance of iron/sulfur cluster biogenesis in *Taz*-deficient tissues (232, 233).

In conclusion, these results suggest that while ROS formation at the respiratory chain is unaltered, the anticipated increase of H_2O_2 emission from mitochondria due to insufficient Ca^{2+}-stimulated and Krebs cycle-mediated NADPH regeneration in *Taz*-KD myocytes may be counterbalanced by compensatory upregulation of H_2O_2-detoxifying capacity through catalase and mitochondrial glutathione peroxidase at young age. Although this upregulation vanishes at older age, no clear increase in ROS occurs despite oxidation of NAD(P)H redox state in *Taz*-KD cardiac myocytes.

Energetic deficit underlies compromised systolic reserve in *Taz*-KD myocytes

A so far unresolved issue is that while *Taz*-KD mice had mildly impaired systolic function *in vivo* (**Figures 1E-G and Figures S1D-I**), isolated cardiac myocytes displayed preserved or even supranormal sarcomere shortening (**Figures 2A-C**), likely related to increased myofilament Ca^{2+} affinity (**Figure 2Q**). However, in *unloaded* myocytes, energetic demand is underestimated compared to the *in vivo* situation since mechanical preload of cardiac myocytes (or muscle) increases O_2 and ATP consumption (212). Sarcolemmal ATP-dependent K^+ channels (K_{ATP}) are sensors of the intracellular ATP/ADP ratio (234). When ATP levels drop (e.g., during ischemia), K_{ATP} channels open to conduct K^+ efflux that hyperpolarizes the cell membrane (212, 234). This shortens action potential duration and reduces trans-sarcolemmal Ca^{2+} influx via L-type Ca^{2+} channels, a mechanism preventing cellular damage by Ca^{2+} overload during metabolic stress (212, 234). In normoxic cardiac myocytes, K_{ATP} channels are mostly closed due to efficient cellular buffering of ATP by the creatine kinase system (212). However, K_{ATP} channels can be sensitized to diminished mitochondrial ATP production by the compound pinacidil, which reduces the sensitivity of K_{ATP} channels to ATP by interacting with the channel proteins at sites near the ATP binding site (235, 236).

To analyze whether compromised Ca^{2+}-dependent adaptation of mitochondrial Krebs cycle activity and thereby, ATP production during β-adrenergic stimulation and pacing may become limiting for systolic function in *Taz*-KD myocytes, we exposed myocytes to workload transitions as in **Figure 2** in the absence or presence of either pinacidil or the specific K_{ATP} channel blocker HMR-1098 (237). While in WT myocytes, neither of these affected basal or maximal systolic sarcomere shortening, pinacidil blunted the increase in sarcomere shortening in response to Iso/5 Hz in *Taz*-KD myocytes (**Figure 7A**), suggesting that drug-primed K_{ATP} channels are activated by a reduced cellular ATP/ADP ratio under these conditions, thereby decreasing Ca^{2+} influx. To investigate these energetic aspects further, we employed a technology developed by Prosser *et al.* (238) and further advanced by Helmes *et al.* (239) by which isolated cardiac myocytes are pre-stretched with glass fibers to exert isometric contractions (**Figure 7B**). Preload-dependent potentiation of force by the Frank-Starling mechanism is paralleled by a matching increase in O_2 (and therefore ATP) consumption (212). Accelerating stimulation rate from 1 to 4 Hz in pre-stretched myocytes (but in the absence of β-adrenergic stimulation) further increased systolic force generation in WT myocytes, a phenomenon known as the “Bowditch Treppe” which is caused by intracellular Ca^{2+} accumulation and subsequently, SR Ca^{2+} loading (224, 240) (**Figures 7B-E**). When stepping back from 4 to 1 Hz, the transient (“post-rest”-like) potentiation of force is explained by increased SR Ca^{2+} loading during the prior 4 Hz stimulation (224, 240). Strikingly, both the Bowditch Treppe and post-rest potentiation of force were completely blunted in *Taz*-KD myocytes (**Figures 7C-E**), in agreement with the lack of frequency-dependent cellular and SR Ca^{2+} loading in unloaded myocytes (**Figures 2I-N**). Furthermore, while in *unloaded* myocytes, systolic sarcomere shortening was preserved at Iso/5 Hz (**Figure 2C**), force generation was substantially decreased in mechanically *preloaded* *Taz*-KD myocytes at 4 Hz (**Figures 7C-E**). Therefore, mechanical preload, which substantially elevates ATP consumption of the cell (212), deteriorates systolic force generation in *Taz*-KD myocytes, while in the presence of saturating ATP and phosphocreatine in permeabilized myocytes, maximal force generation was maintained (**Figure 2Q**, **Table S3**). Together, these data suggest that metabolic adaptation during elevated workload rather than ATP-producing capacity of mitochondria *per se* contributes to systolic dysfunction in hearts of *Taz*-KD mice.

Discussion

BTHS can manifest with a severe form of cardiomyopathy, potentially lethal or requiring heart transplantation in infancy. The clinical phenotype of BTHS cardiomyopathy is both heterogeneous and dynamic, and its pathophysiology largely unresolved. The most commonly reported manifestation is dilated cardiomyopathy (DCM), but often in combination with morphological aspects of hypertrophic (HCM) and/or non-compaction cardiomyopathy (118, 220-222, 241). While in the first weeks of life, a phenotype of DCM with systolic dysfunction is more common, LV dilation often regresses and systolic function recovers during the first year(s) of life (220, 221). In fact, most patients eventually enter a phase in which LVEF is preserved (at ~50%) and remains stable (118) or only mildly deteriorates over the following two decades (222). However, although LVEF is preserved at rest, it does not increase during exercise (119), resembling the clinical phenotype of HFpEF (242-244) and likely contributing to exercise intolerance of BTHS patients (119). Finally, patients with BTHS can suffer or die from ventricular arrhythmias (223, 245). However, the defects of EC coupling and mechanisms of arrhythmias have neither been explored in more detail nor put into context with mitochondrial defects in BTHS.

Here, we show that cardiomyopathy of *Taz*-KD mice closely resembles that of BTHS patients, and that this phenotype is reminiscent of HFpEF rather than HFrEF (118, 220-222, 241). Progressive diastolic dysfunction *in vivo* in the absence of relevant fibrosis is readily explained by elevated myofilament Ca^{2+} affinity and slowed crossbridge cycling, a feature characteristic of hereditary forms of HCM, but not DCM (246). To compensate for sarcomeric relaxation deficits, cytosolic Ca^{2+} decay kinetics are constitutively accelerated in *Taz*-KD myocytes through increased SERCA and NCX activities already under “resting” conditions, which however largely exploits the inotropic and lusitropic reserve recruited by β-adrenergic stimulation and/or increased stimulation frequency, as it occurs during exertion *in vivo* (**Graphical abstract**). This is in stark contrast to the defects in EC coupling in myocytes from animal models (33) or patients (247) with HFrEF, where *reduced* SERCA activity and SR Ca^{2+} load are a central defect for systolic and diastolic dysfunction. Furthermore, our data contrast with a recent study on the same *Taz*-KD mouse model in which reduced SERCA activity (probed by biochemical assays) was suggested to underlie diastolic and systolic dysfunction in BTHS cardiomyopathy (248).

As the primary mitochondrial defect, we identified selective deficiency of MCU protein, but not mRNA, which destabilized the MCU complex and abrogated Ca^{2+} uptake into mitochondria from *Taz*-KD hearts (**Graphical abstract**). This is in agreement with a recent report that revealed that CL is required for MCU complex stability in yeast mitochondria and confirmed this in myocardium from patients with BTHS (249). However, this study was mostly based on a minimal MCUa-EMRE complex recombinantly expressed in the baker's yeast *Saccharomyces cerevisiae* that does not contain an intrinsic MCU-like transporter. Furthermore, the physiological implications and disease relevance of these results were not experimentally addressed in this paper. Our comprehensive *in vitro* and *in vivo* analyses, which we reported in a preliminary form (250) prior to the mentioned study (249), extend these observations by showing that the MCU defect is specific for *Taz*-deficiency in heart, but not skeletal muscle or brain mitochondria. In contrast, respiratory chain function deteriorates with age in skeletal muscle, but not cardiac mitochondria of *Taz*-KD mice, suggesting important tissue-specific differences of CL deficiency causing cardiomyopathy or skeletal muscle myopathy in BTHS, respectively.

During physiological workload transitions, lack of mitochondrial Ca^{2+} uptake prevents Krebs cycle activation and regeneration of reduced pyridine nucleotides in *Taz*-KD cardiac myocytes (**Graphical abstract**). This is in agreement with results of our previous studies in guinea pig cardiac myocytes with pharmacological inhibition of the MCU (46) or acceleration of NCLX-dependent mitochondrial Ca^{2+} extrusion (at elevated $[Na^+]_i$) (30), but also mice with genetic deletion of the MCU (22). Based on our previous studies, we anticipated increased emission of H_2O_2 from mitochondria due to depletion of antioxidative NADPH (46, 47). However, this was prevented at least to some extent by upregulation of H_2O_2-eliminating catalase and glutathione peroxidase 1, but not of $^{\bullet}O_2^-$-eliminating SOD1 or SOD2 in *Taz*-KD hearts. We also ruled out increased $^{\bullet}O_2^-$ formation at the respiratory chain and H_2O_2 emission from isolated cardiac and skeletal muscle mitochondria, which was further supported by a lack of mitochondrial H_2O_2 elevation in hearts *in vivo* as detected with the sensitive and specific H_2O_2 sensor mito-roGFP2-Orp1 (132).

These data are in contrast to previous reports of increased ROS formation in BTHS cell models (87, 99, 103), one of which assigned ROS a causal role for systolic dysfunction in an iPSC "heart-on-chip" model of BTHS (87). Furthermore, our data to some extent contrast with another study (93) reporting increased H_2O_2 emission from cardiac, but not skeletal muscle mitochondria respiring on succinate in the absence of rotenone, a condition which favors $^{\bullet}O_2^-$ formation at complex I via reverse electron transfer (9). In the mentioned study (93), *Taz* was knocked down in C57BL/6J mice, in which a loss-of-function mutation of the mitochondrial transhydrogenase favors H_2O_2 emission in working cardiac myocytes (47). Conversely, our data are in agreement with a recent study that observed no increase in ROS formation at eleven different sites within cardiac and skeletal muscle mitochondria of *Taz*-KD mice on a C57BL/6NJ background (251) which (in contrast to C57BL/6J) *does* contain a functional transhydrogenase (47). Taken together, our data generated by a broad spectrum of methods that also integrate mitochondrial function and ROS formation/emission with the processes of EC coupling *in vitro* and *in vivo* argue against a relevant role of mitochondrial ROS in the pathophysiology of BTHS cardioskeletal myopathy. This should discourage previously suggested strategies to treat BTHS patients with antioxidants (87, 106, 252) and is in line with the observation that overexpression of catalase does not alter the cardiac phenotype in *Taz*-KD mice (93).

Patients with BTHS are at risk for sudden cardiac death (223), but the mechanisms underlying ventricular arrhythmias are unknown. In a parallel study, we discovered that in mouse models of HCM, increased myofilament Ca^{2+} sensitivity *per se* causes ADP-induced oxidation of mitochondrial NADH and (via transhydrogenase) NADPH, increasing mitochondrial H_2O_2 emission that triggers and sustains arrhythmias *in vitro* and *in vivo* (Kohlhaas et al., accompanying manuscript). In that study, inhibition of NCLX-mediated mitochondrial Ca^{2+} export (with CGP-37157) prevented NAD(P)H oxidation and arrhythmias in isolated cardiac myocytes and whole hearts of mice with HCM-typical sarcomeric mutations. Since also in *Taz*-KD myocytes, NAD(P)H oxidation was ameliorated and cellular arrhythmias blunted by NCLX inhibition, we propose that in BTHS, lack of mitochondrial Ca^{2+} uptake and increased myofilament Ca^{2+} affinity conspire to induce mitochondrial redox mismatch and arrhythmias, potentially mediated by redox modifications of ryanodine receptors (253).

It has been a long-held concept that mitochondrial Ca^{2+} uptake matches metabolic output to cardiac workload by Ca^{2+}-induced activation of rate-limiting Krebs cycle dehydrogenases (**Graphical abstract**) (8, 20, 149, 254). However, direct experimental evidence for this concept is challenging. We approached this problem in two ways. First, by sensitizing sarcolemmal K_{ATP} channels to variations in mitochondrial ATP production with pinacidil, systolic sarcomere shortening was compromised in *Taz*-KD, but not WT myocytes, likely mediated by K_{ATP} channel-induced hyperpolarization of the cell membrane that limits cellular Ca^{2+} influx (212, 234). Second, by comparing maximal sarcomere shortening in *unloaded* cardiac myocytes with actual force generation in similarly intact, but mechanically *preloaded* cardiac myocytes, where only in preloaded myocytes, systolic dysfunction unfolds in *Taz*-KD vs. WT myocytes, although in the presence of sufficient (external) ATP and phosphocreatine, maximal sarcomeric force generation was similar between both genotypes in mechanically preloaded, but permeabilized cardiac myocytes. These data suggest that defective Ca^{2+}-dependent energy supply and demand matching limits ATP regeneration required for maximal (but not submaximal) force production. Support for this concept comes from studies in *Mcu*-KO animals, in which delayed metabolic adaptation caused by loss of the MCU abrogates the acute increase in contractile performance induced by isoproterenol infusion *in vivo* (22). Mitochondrial Ca^{2+}-driven metabolic adaptations, and thereby the bioenergetic mismatch resulting from MCU deficiency, might be even more relevant in humans than in rodents, since the high basal heart rate of mice prevents substantial (>0.5-fold) increases in cardiac output (181), whereas sympathetic activation in humans can increase cardiac output 4- to 5-fold (182).

Conclusions and clinical implications

Our data identify disruption of the mechano-energetic coupling reserve (**Graphical abstract**) rather than – as previously suggested – decreased respiration or oxidative stress as a primary defect in BTHS cardiomyopathy, which is characterized by diastolic rather than systolic dysfunction *in vitro* and *in vivo*. These data help explain two major clinical problems in BTHS patients, i.e., the inability of the heart to increase LVEF during physical exercise (119), which is specific for BTHS, but not other forms of mitochondrial cardiomyopathies (255), and to some extent, the increased risk for arrhythmias (223).

This has implications for the treatment of patients with BTHS, in whom the use of cardiac glycosides is still common (220), although these cause mechano-energetic uncoupling and ventricular tachycardia through hampering mitochondrial Ca^{2+} uptake (256). In fact, in a case series of five patients with BTHS who suffered from ventricular tachycardia or fibrillation, two of whom died suddenly while playing, all five had digoxin as the only common medication, although only one of these patients had a typical DCM-like phenotype with relevant systolic dysfunction, while the remaining four had largely preserved EF (223), comparable to the *Taz*-KD mouse model of the current study. Therefore, use of digoxin in BTHS should be discouraged, while future efforts should be directed at probing treatments that improve mechano-energetic coupling through lowering energetic demand (i.e., by myosin modulators (257)) and/or improve mitochondrial Ca^{2+} uptake (i.e., by SGLT2-inhibitors (258)).

Declarations

Author Contributions

EB, AN, MK, MHohl, VS, CK, JS, CC, KM, SA, AM, AK, RK, KvdM, AvdM, JD, LPR, and CM designed and conducted the experiments. EB, AN, MK, MHohl, VS, MHoth, JD, MvdL, LPR, and CM drafted and edited the manuscript. MB and UL gave important input to the manuscript and provided funding.

Acknowledgements

CM was supported by the German Heart Foundation (Margret Elisabeth Strauß-Projektförderung), the Barth Syndrome Foundation, the German Research Foundation (DFG; Ma 2528/7-1, SFB 894, TRR-219) and the German Federal Agency for Education and Research (BMBF; 01EO1504). JD is supported by the DFG (DU1839/2-1), the BMBF and the Barth Syndrome Foundation. MH is supported by the DFG (SFB 894 and SFB 1027). MvdL is supported by the Barth Syndrome Foundation and the DFG (SFB 894). PR is funded by the European Research Council (ERC) Advanced Grant (ERCAdG No. 339580), DFG (SFB1002, project A06), and the DFG under Germany's Excellence Strategy - EXC 2067/1- 390729940.
We thank Michelle Gulentz, Nina Schnellbach, and Annette Berbner for technical assistance.

Declaration of Interests

CM and UL received speaker and consultancy honoraria from Boehringer Ingelheim and AstraZeneca.

Figures and Legends

Figure 1. *Taz*-KD cardiomyopathy is characterized by diastolic and modest systolic dysfunction.

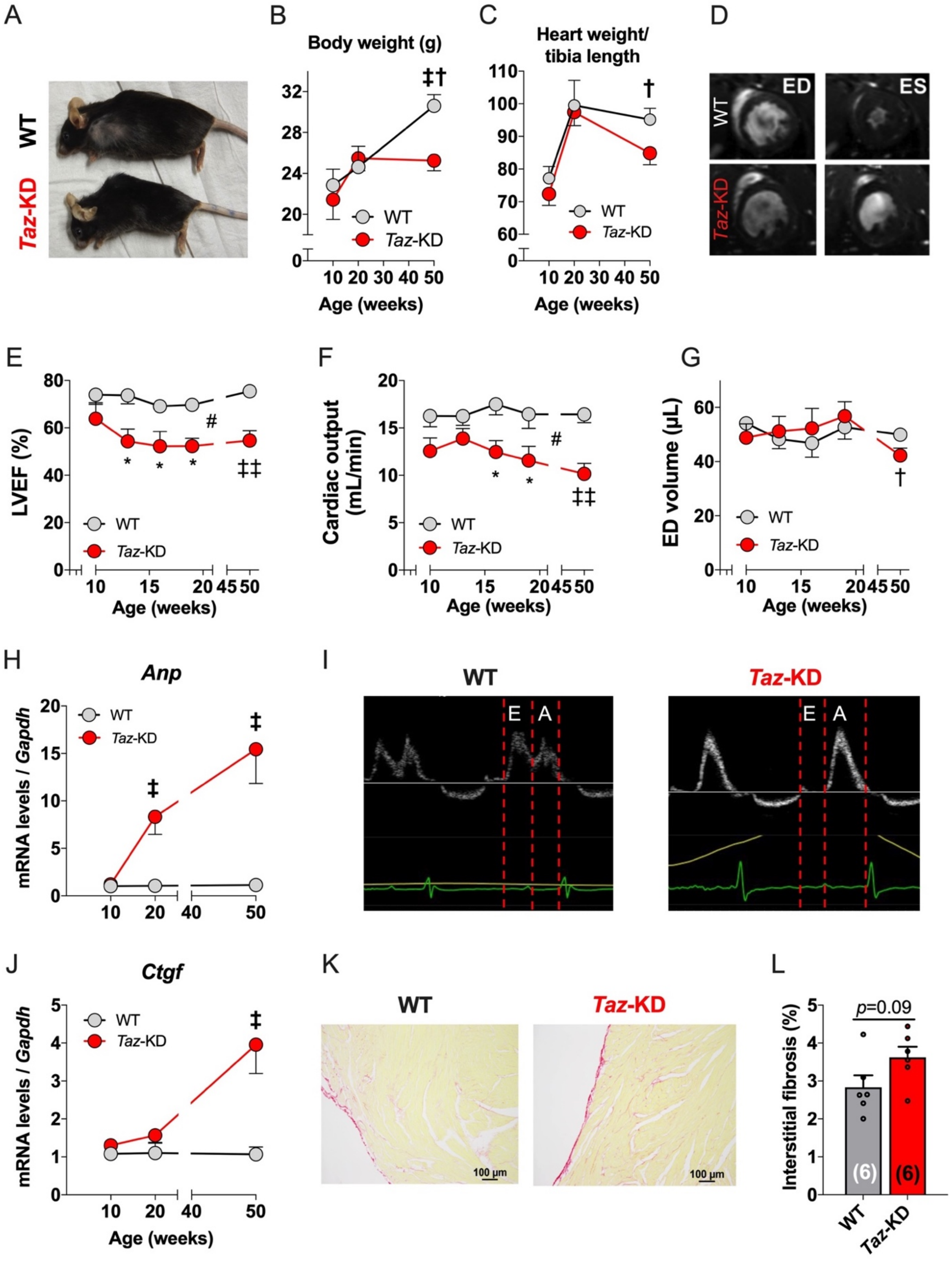

A) Representative image of one 50-week-old (w/o) *Taz*-KD mouse compared with a WT littermate.
B) Body weight and
C) heart weight/tibia length ratio of *Taz*-KD mice and WT littermates at 10, 20, and 50 weeks, respectively (10 weeks: WT n=5, *Taz*-KD n=6; 20 weeks: WT=10, *Taz*-KD=13; 50 weeks: WT=16, *Taz*-KD=12).
D) Representative short-axis MRI images of the left ventricle at end diastole (ED) and end systole (ES) of WT (top) and *Taz*-KD mice (bottom).
E) Left ventricular ejection fraction (LVEF),
F) cardiac output, and
G) end-diastolic (ED) volume, at 10, 13, 15, 18, 20, and 50 weeks, respectively (10 to 20 weeks: WT n=5, *Taz*-KD n=6; 50 weeks: WT=16, *Taz*-KD=12).
H) Cardiac mRNA levels of atrial natriuretic peptide (*Anp*) and normalized to WT in 10, 20, and 50 w/o mice (WT n=4, *Taz*-KD n=3).
I) Representative Doppler echocardiography images of mitral inflow velocity in 50 w/o mice.
J) Cardiac mRNA levels of connective tissue growth factor (*Ctgf*) normalized to WT in 10, 20, and 50 w/o mice (WT n=4, *Taz*-KD n=3).
K) Representative histology image of LV myocardium from 50 w/o mice stained with Picrosirius red to detect interstitial fibrosis (n=6 per group).
L) Quantification of LV interstitial fibrosis in 50 w/o mice (n=6 per group).

See also **Figure S1** and **Tables S1-S2**.

Data represent mean ± SEM (indicated by error bars); n-numbers are indicated as numbers of hearts or animals; statistical significance was determined by unpaired Student t-test in (B), (C), (H), (J), (L), and for the 50 week group in (E) to (G); and by 2-way ANOVA followed by Bonferroni post-test in (E) to (G), age group 10 to 20 weeks.

# indicates $p<0.05$ with 2-way ANOVA;
*,**,***,***,****: $p<0.05$, $p<0.01$, $p<0.001$, $p<0.0001$ with Bonferroni post-test;
†, ‡, †‡, ‡‡: $p<0.05$, $p<0.01$, $p<0.001$, $p<0.0001$ with unpaired Student t-test.

Figure 2. Alterations of excitation-contraction coupling in *Taz*-KD versus WT cardiac myocytes.

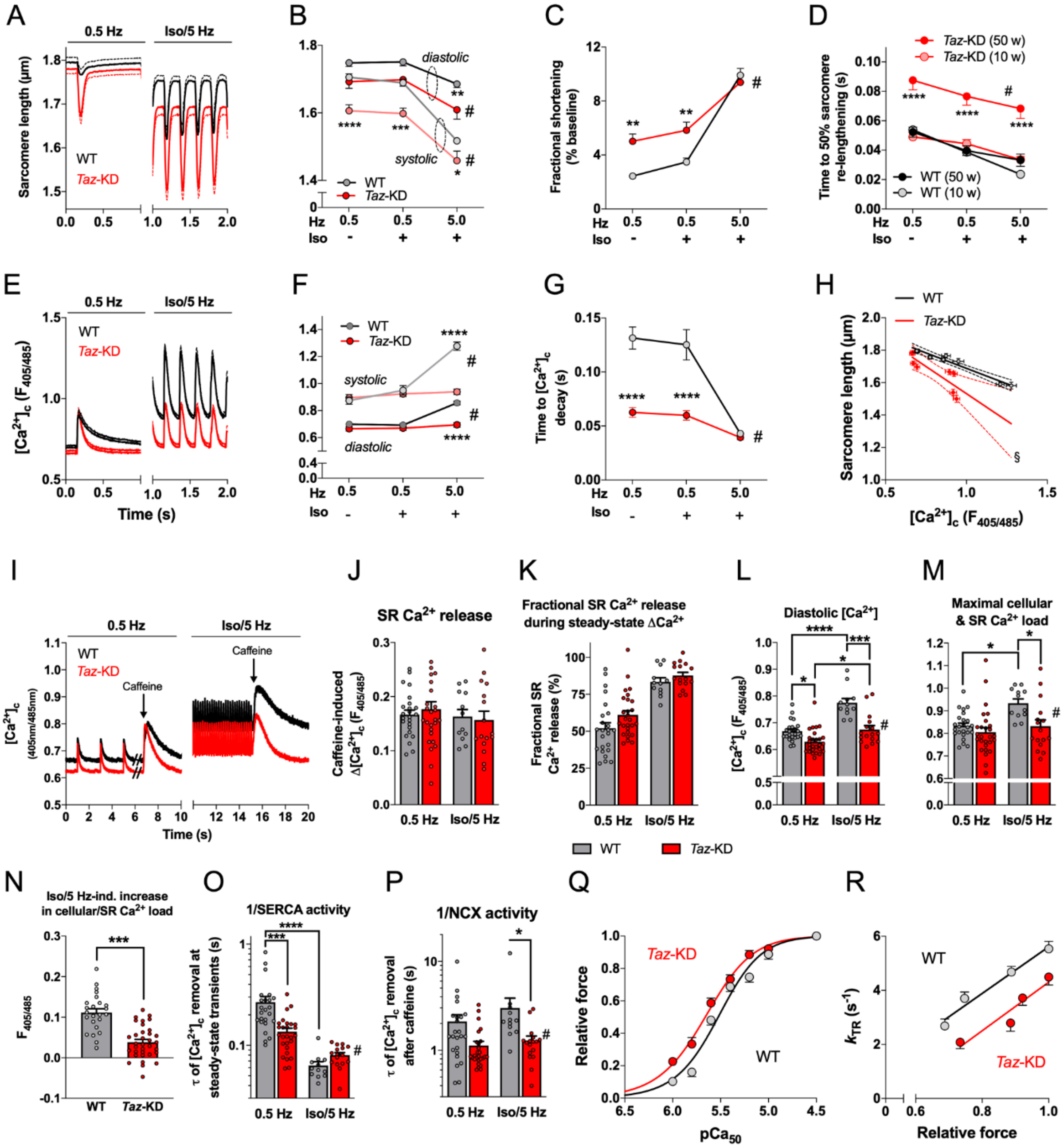

For experiments shown in (A) to (H), isolated cardiac myocytes isolated from 10 w/o WT or *Taz*-KD mice were field-stimulated at 0.5 Hz for 120 s, superfused with isoproterenol (Iso; 30 nM), and stimulation frequency was increased from 0.5 Hz to 5 Hz for 180 s.

A) Averaged original traces of sarcomere length of cardiac myocytes,
B) systolic and diastolic sarcomere length and
C) fractional sarcomere shortening of cardiac myocytes, respectively (WT n=38/3, *Taz*-KD n=28/3).
D) Time to 50% sarcomere re-lengthening of cardiac myocytes from 10 and 50 w/o mice (10 weeks: WT n=38/3, *Taz*-KD n=28/3; 50 weeks: WT n=30/4, *Taz*-KD n=26/4).
E) Averaged original traces of cytosolic Ca^{2+} transients ($[Ca^{2+}]_c$),
F) Systolic and diastolic cytosolic Ca^{2+} ($[Ca^{2+}]_c$), and
G) time to $[Ca^{2+}]_c$ decay of intact cardiac myocytes loaded with the cell-permeant ratiometric Ca^{2+} indicator Indo-1 AM (n=22/3 per group).
H) $[Ca^{2+}]_c$ levels plotted against sarcomere length. Data are extracted from the experiments shown in (E) to (G) (n=22/3 per group).

In the experiments shown in (I) to (P), caffeine (10 mM) pulses were applied to cardiac myocytes loaded with Indo-1 after 120 s of 0.5 Hz or combined Iso/5 Hz stimulation (0.5 Hz: WT n=24/2, *Taz*-KD; n=27/2; Iso/5 Hz: WT n=12/2, *Taz*-KD n=16/2).

I) Averaged original traces of cytosolic Ca^{2+} transients ($[Ca^{2+}]_c$).
J) Caffeine-induced increase in $[Ca^{2+}]_c$, indicating SR Ca^{2+} load after 0.5 Hz or Iso/5 Hz stimulation.
K) Fractional Ca^{2+} release from the SR calculated as the % amplitude of steady-state Ca^{2+} transients compared with the caffeine-induced increase in $[Ca^{2+}]_c$, respectively.
L) Diastolic $[Ca^{2+}]_c$ during steady-state 0.5 Hz or Iso/5 Hz stimulation, respectively.
M) Maximal cellular and SR Ca^{2+} load during pacing at 0.5 Hz or Iso/5 Hz, reflecting the maximal $[Ca^{2+}]_c$ after the caffeine pulse after the respective conditions.

N) Net change of total cellular and SR Ca^{2+} load induced by Iso/5 Hz stimulation, calculated as the difference between the values at 0.5 Hz and Iso/5Hz as indicated in (M).

O) Kinetics of $[Ca^{2+}]_c$ decay of steady-state $[Ca^{2+}]_c$ transients during 0.5 Hz or Iso/5 Hz stimulation, reporting largely Ca^{2+} removal by the SR Ca^{2+} ATPase.

P) Kinetics of $[Ca^{2+}]_c$ decay after caffeine pulses after 0.5 Hz or Iso/5 Hz stimulation as an indicator of Ca^{2+} removal by the sarcolemmal Na^+/Ca^{2+} exchanger (NCX).

In the experiments shown in (Q) and (R), permeabilized cardiac myocytes were used (WT n=18/4, *Taz*-KD n=15/4) and intracellular Ca^{2+} concentrations defined to assess Ca^{2+}-dependent force generation of myofilaments.

Q) Force-Ca^{2+} relations of permeabilized loaded cardiac myocytes.

R) Normalized rate constant of tension redevelopment (k_{TR}) as a function of Ca^{2+}-activated isometric force.

See also **Figure S2** and **Table S3**.

Data represent mean ± SEM [indicated by dotted lines in (A) and (H), by error bars in other panels]; n-numbers are indicated as numbers of cardiac myocytes / animals; statistical significance was determined by 2-way ANOVA followed by Bonferroni post-test.

# indicates $p<0.05$ with 2-way ANOVA;
*,**,***,***,****: $p<0.05$, $p<0.01$, $p<0.001$, $p<0.0001$ with Bonferroni post-test.

Figure 3. Structural remodeling of the respiratory chain impairs respiration, but does not increase ROS emission in cardiac mitochondria of *Taz*-KD mice.

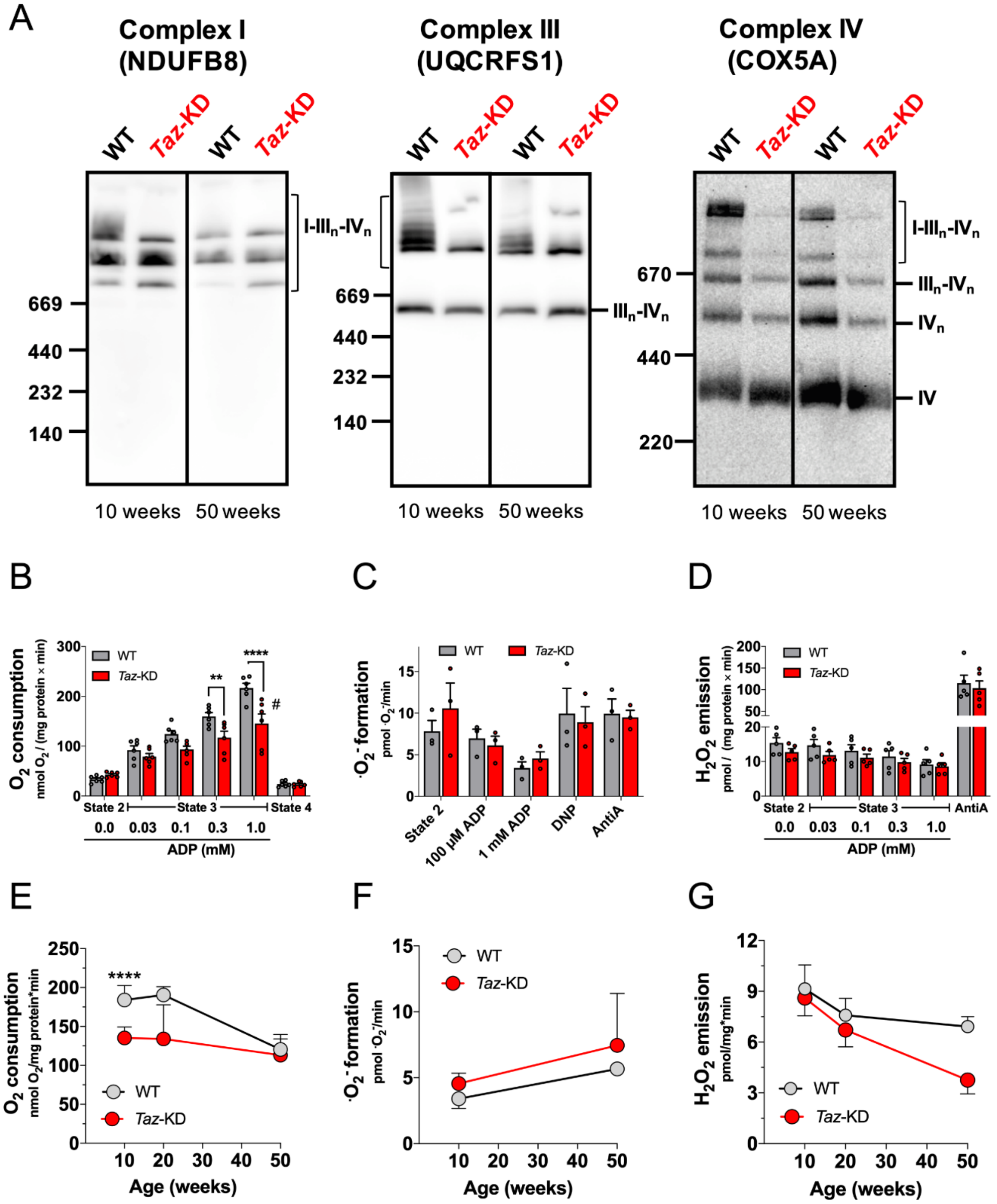

A) Blue native gel electrophoresis (BN-PAGE) analysis of isolated heart mitochondria from 10 and 50 w/o mice, respectively. Western blot and immunodecoration performed with antibodies against the following proteins (from left to right): NADH dehydrogenase 1β subcomplex subunit 8 (NDUFB8) of complex I, the complex III component Rieske (UQCRFS1), and the cytochrome *c* oxidase (complex IV) subunit 5a (COX5A).

B) O_2 consumption of isolated cardiac mitochondria from 10 w/o mice supplied with pyruvate and malate (5/5 mM) as substrates in the absence (State 2) and presence of different ADP concentrations (State 3). The complex V inhibitor oligomycin was added to inhibit phosphorylation-coupled respiration (State 4; n=6 per group).

C) Superoxide ($\cdot O_2^-$) formation of isolated cardiac mitochondria from 10 w/o mice supplied with pyruvate and malate (5/5 mM) and different ADP concentrations. The protonophore 2,4-dinitrophenol (DNP) and the complex III inhibitor antimycin A (AntiA) were added to uncouple respiration from ADP phosphorylation and as a positive control inducing $\cdot O_2^-$ formation at complex III, respectively (n=3 per group).

D) Hydrogen peroxide (H_2O_2) emission of isolated cardiac mitochondria from 10 w/o mice supplied with pyruvate and malate (5/5 mM) and different ADP concentrations. The complex III inhibitor antimycin A (AntiA) was added as a positive control (n=5 per group).

E) State 3 (ADP 1 mM) O_2 consumption of isolated cardiac mitochondria from 10, 20, and 50 w/o mice (10 weeks: n=6 per group; 20 weeks: WT=4, *Taz*-KD=3; 50 weeks: WT=7, *Taz*-KD=6).

F) State 3 (ADP 1 mM) $\cdot O_2^-$ formation of isolated cardiac mitochondria from 10 and 50 w/o mice (n=3 per group and age).

G) State 3 (ADP 1 mM) H_2O_2 emission of isolated cardiac mitochondria from 10, 20, and 50 w/o mice (10 weeks: n=5 per group; 20 weeks: WT=4, *Taz*-KD=3; 50 weeks: n=5 per group).

Data shown in (E), (F), and (G), summarize the results shown in (B), (C), and (D) together with those shown in **Figure S3**.

Data represent mean ± SEM (indicated by error bars); n-numbers are indicated as numbers of hearts or animals; statistical significance was determined by 2-way ANOVA followed by Bonferroni post-test.

# indicates $p<0.05$ with 2-way ANOVA;
*,**,***,***,****: $p<0.05$, $p<0.01$, $p<0.001$, $p<0.0001$ with Bonferroni post-test.

Figure 4. Loss of the mitochondrial Ca^{2+} uniporter abrogates Ca^{2+} uptake into cardiac mitochondria of *Taz*-KD mice.

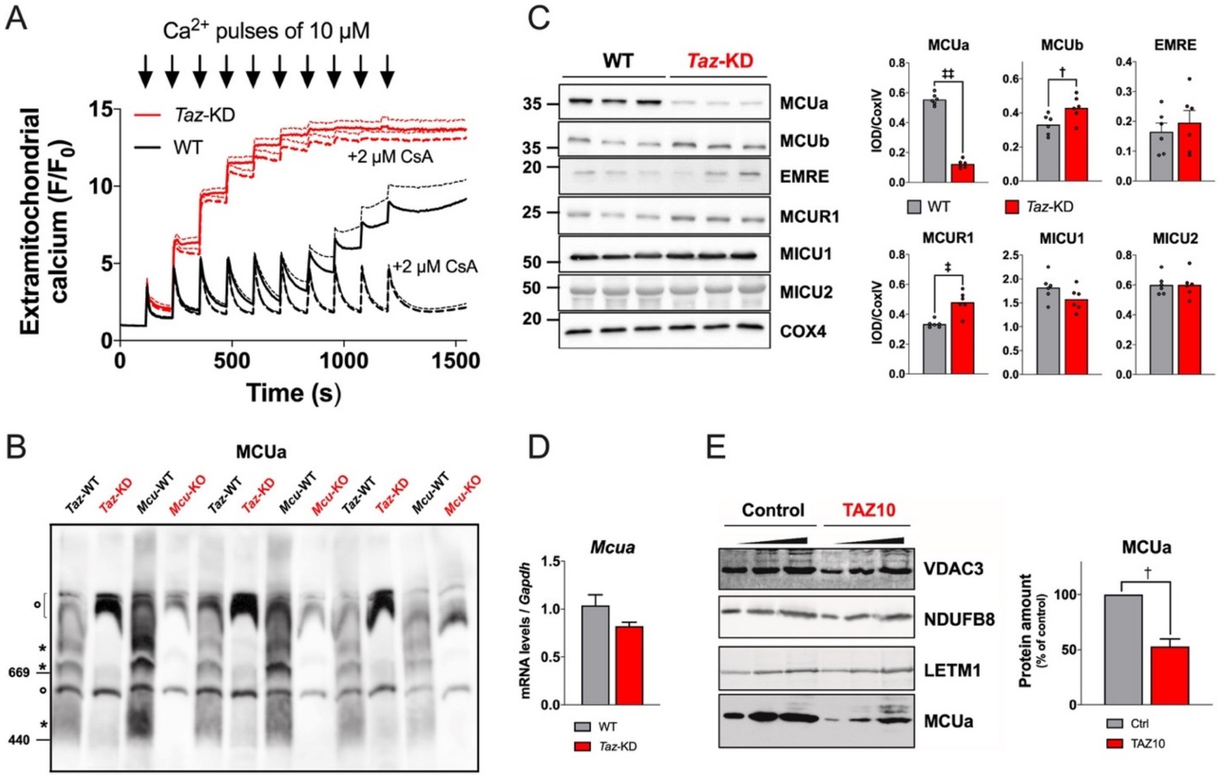

A) Ca^{2+} retention capacity of isolated cardiac mitochondria from 10 w/o mice exposed to repetitive 10 µM Ca^{2+} pulses at 120 s intervals. Extramitochondrial Ca^{2+} was monitored with CalciumGreen 5N. Cyclosporine A (CsA) was added to prevent mitochondrial permeability transition (dashed traces; WT n=5, *Taz*-KD n=4).

B) BN-PAGE analysis of MCUa in cardiac mitochondria of 3 independent pairs of 10 w/o *Taz*-KD, *Mcu* knockout (*Mcu*-KO), and WT littermates (*Taz*-WT and *Mcu*-WT, respectively). MCU-specific bands are indicated with stars (*), non-specific bands with circles (°).

C) Representative western blot and quantification of MCU complex subunits MCUa, MCUb, EMRE, MCUR1, MICU1, and MICU2 in hearts of 10 w/o *Taz*-KD mice (n=6 per group). Data are presented as intensity optical density (IOD) of the specific band to IOD of cytochrome oxidase subunit 4 (COX4).

D) Cardiac *Mcua* mRNA levels in 10 w/o mice (n=7 per group).

E) Western blot and quantification of MCUa, voltage-dependent anion-selective channel 3 (VDAC3), NADH dehydrogenase 1β subcomplex subunit 8 (NDUFB8), and mitochondrial H^+/Ca^{2+} exchanger (LETM1) levels in iPSC-derived cardiac myocytes obtained from a patient with Barth syndrome (indicated as TAZ10) and one healthy control.

See also **Figure S3**.

Data represent mean ± SEM [indicated by dotted lines in (A), by error bars in other panels]; n-numbers are indicated as numbers of hearts or animals; statistical significance was determined unpaired Student t-test.

†, ‡, †‡, ‡‡: $p<0.05$, $p<0.01$, $p<0.001$, $p<0.0001$ with unpaired Student t-test.

Figure 5. Defective mitochondrial Ca^{2+} uptake provokes mitochondrial oxidation and cellular arrhythmias during workload transitions in *Taz*-KD cardiac myocytes.

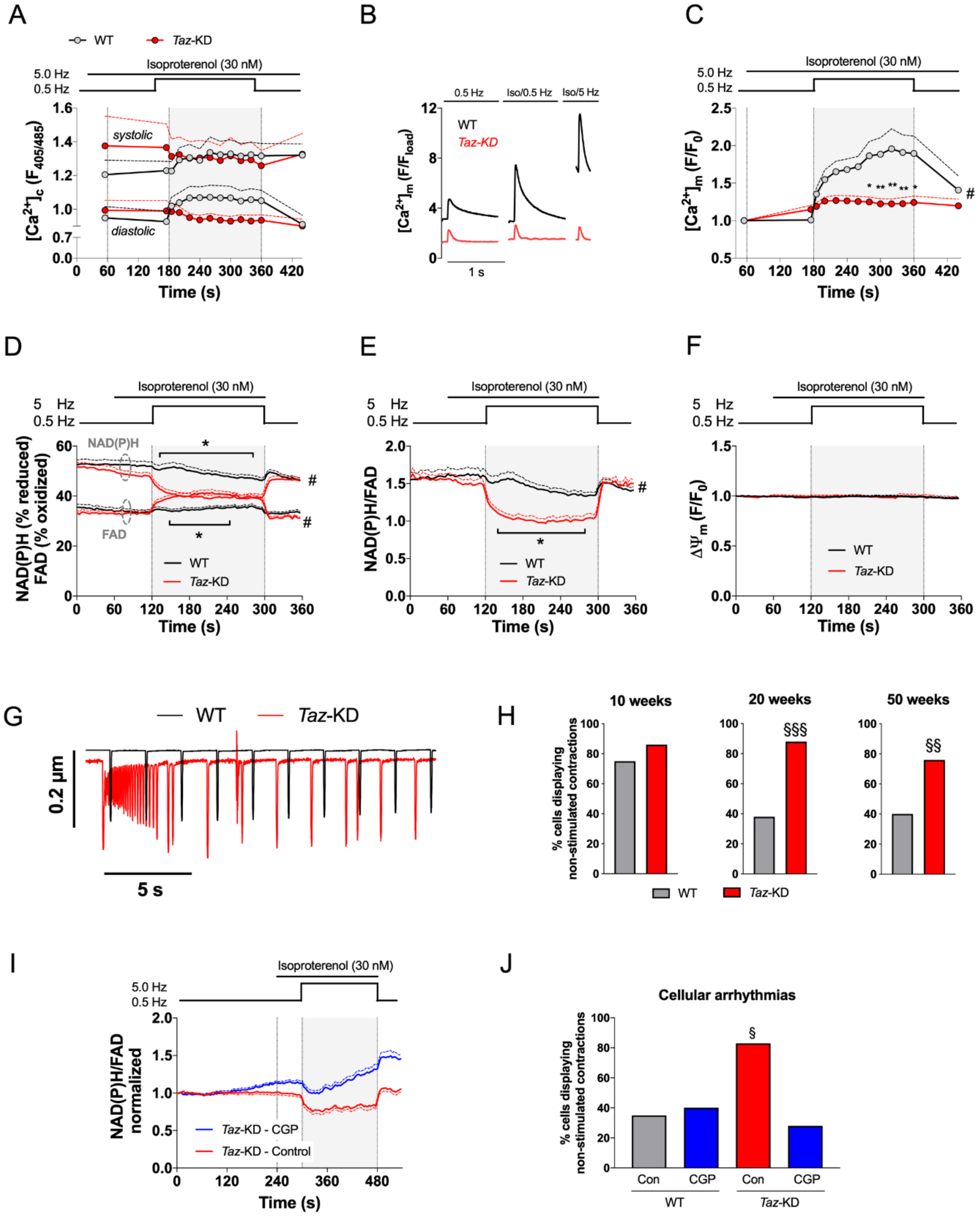

For experiments shown in (A) to (G), isolated cardiac myocytes from 10 w/o WT and *Taz*-KD mice were subjected to the same experimental protocol described for **Figure 2A-H** and cytosolic and mitochondrial Ca^{2+} concentrations were determined in the same cells, respectively. The gray-shaded area in the graphs indicate 5 Hz stimulation.

A) Cytosolic Ca^{2+} concentration ($[Ca^{2+}]_c$),
B) averaged original traces of mitochondrial Ca^{2+} transients and
C) diastolic mitochondrial Ca^{2+} concentration ($[Ca^{2+}]_m$) in the same patch-clamped cardiac myocytes, respectively (WT n=15/8, *Taz*-KD n=13/7).
D) Autofluorescence of NAD(P)H and FAD and
E) the ratio of NAD(P)H/FAD calculated from the data in (D) as an indicator of the mitochondrial pyridine nucleotide redox state in intact cardiac myocytes (WT n=29/3, *Taz*-KD n=24/3).
F) Mitochondrial membrane potential ($\Delta\Psi_m$) determined by TMRM in WT (n=20/3) and Taz-KD myocytes (n=18/3).
G) Two representative traces of sarcomere shortening in a WT and Taz-KD myocyte, respectively. Cells were captured during 0.5 Hz stimulation after the Iso/5Hz stress protocol. In WT, regular systolic sarcomere shortening in response to the triggered field stimulation pulses can be observed, while in the *Taz*-KD myocytes, autonomic sarcomere shortenings uncoupled from electrical stimulation occur, categorized as “cellular arrhythmias”
H) Percentage of cardiac myocytes showing non-stimulated sarcomere shortenings (“cellular arrhythmias” as indicated in H) after Iso/5 Hz at 10, 20, and 50 weeks of age, respectively. Data were extracted from experiments in (D) and Figure S6 (10 weeks: WT n=29/3, *Taz*-KD n=24/3; 20 weeks: WT n=13/3, *Taz*-KD n=24/3; 50 weeks: WT n=30/4, *Taz*-KD n=26/4).

In the experiments shown in (H) and (I), cardiac myocytes from 20 w/o mice were superfused with the mitochondrial Na^+/Ca^{2+} exchanger (NCLX) inhibitor CGP-37157 (CGP; 10 µM) or vehicle (DMSO) for 240 s before being subjected to Iso/5 Hz stimulation for 180 s (n=12/3 per group).

I) Normalized NAD(P)H/FAD ratio of intact cardiac myocytes from 20 w/o *Taz*-KD mice.

J) Percentage of cardiac myocytes showing non-stimulated sarcomere shortenings (“cellular arrhythmias”) after Iso/5 Hz and treatment with CGP or vehicle (Con) from the experiment shown in (H).

See also **Figure S6**.

Data represent mean ± SEM [indicated by dotted lines in (A), (C), (D), (E), (H)]; n-numbers are indicated as numbers of cardiac myocytes / animals; statistical significance was determined by 2-way ANOVA followed by Bonferroni post-test in (A), (C), (D), (E), (H), and by nonparametric tests in (G) and (I) [Fisher’s exact test in (G), Chi-square test in (I)].

# indicates $p<0.05$ with 2-way ANOVA;
*,**,***,***,****: $p<0.05$, $p<0.01$, $p<0.001$, $p<0.0001$ with Bonferroni post-test;
§, §§, §§§, §§§§: $p<0.05$, $p<0.01$, $p<0.001$, $p<0.0001$ with nonparametric tests [Fisher’s exact test in (G), Chi-square test in (I)].

Figure 6. Mitochondrial ROS emission is prevented by upregulation of ROS-detoxifying capacity in young *Taz*-KD cardiac myocytes.

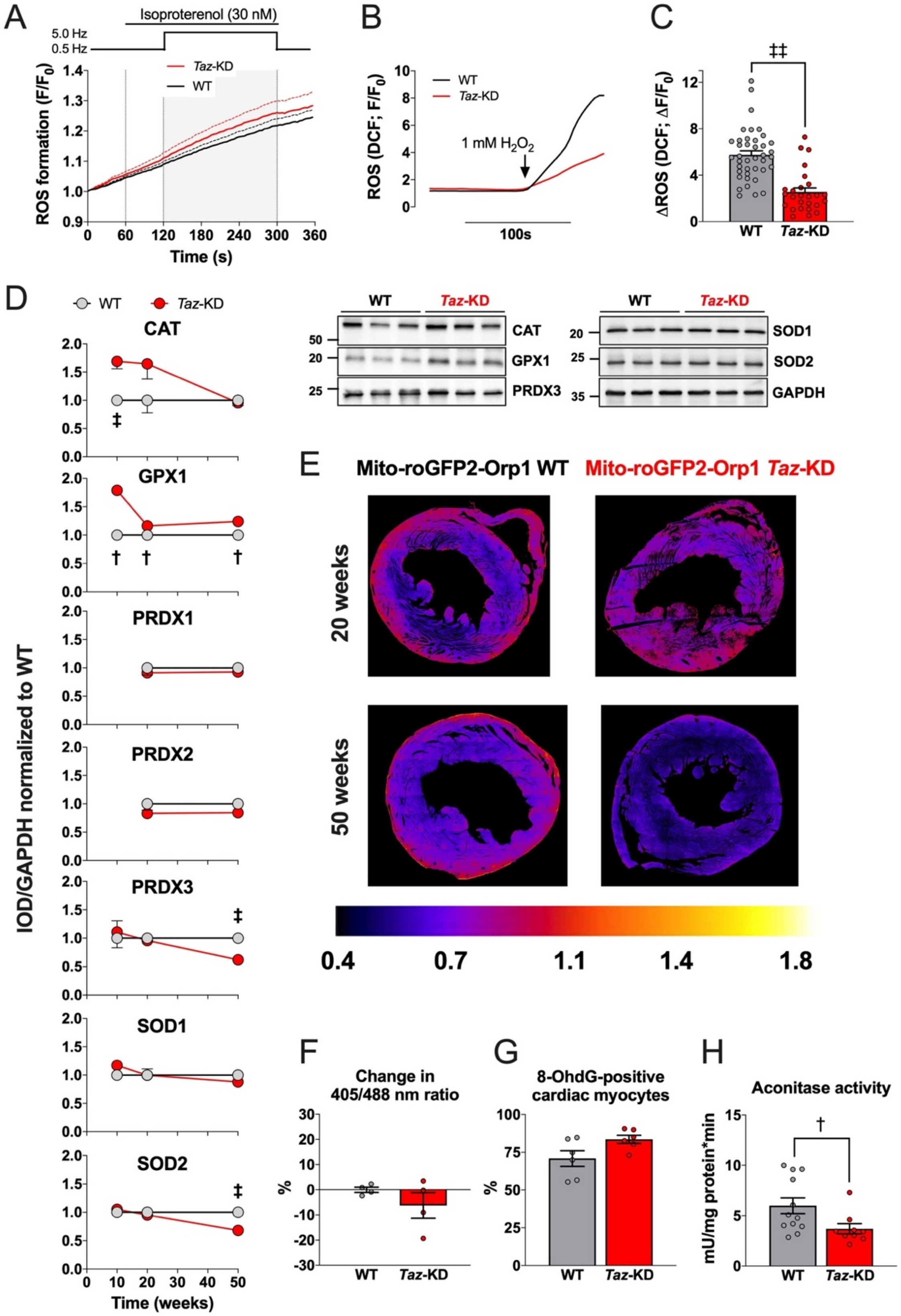

A) ROS emission determined with the fluorescent indicator DCF in intact cardiac myocytes from 10 w/o mice subjected to the same experimental protocol described for Figures 2A-H and 5A-G (WT n=40/4, *Taz*-KD n=26/4).
B) Representative measurement and (C) quantification of DCF fluorescence in response to superfusion with 1 mM H_2O_2 of intact cardiac myocytes from 10 w/o mice (WT n=40/4, *Taz*-KD n=26/4).
D) Protein levels of cardiac catalase (CAT), glutathione peroxidase 1 (GPX1), peroxiredoxin (PRDX) 1, 2, and 3, and superoxide dismutase (SOD) 1 and 2 related to the expression of GAPDH and normalized to WT in 10, 20, and 50 w/o mice (n=6 per group for 10 and 50 w/o; WT n=4, *Taz*-KD n=3 for 20 w/o). Representative blots are from 10 w/o hearts.
E) Representative ratiometric image (excitation: 405/488 nm; emission: 500-530 nm) of mito-roGFP2-Orp1/WT (left) and mito-roGFP2-Orp1/*Taz*-KD (right) heart histology slices at 20 (upper row) or 50 weeks (lower row).
F) Normalized fold change in ratio (%) of the redox state of the mito-roGFP2-Orp1 sensor in the hearts of 20 w/o mito-roGFP2-Orp1/WT and mito-roGFP2-Orp1/*Taz*-KD mice (n=4 per group).
G) Staining of 8-hydroxy-2'-deoxyguanosine (8-OHdG) in WT and *Taz*-KD hearts (n=6 per group).
H) Activity of aconitase in hearts of WT (n=12) and *Taz*-KD (n=9) mice.

Data represent mean ± SEM [indicated by dotted lines in (A), by error bars in other panels]; n-numbers are indicated as numbers of cardiac myocytes / animals in (A) and (C) and as number of hearts or animals for (D) to (H); statistical significance was determined by 2-way ANOVA followed by Bonferroni post-test in (A), and by unpaired Student t-test in (C) to (H).

†, ‡, †‡, ‡‡: $p<0.05$, $p<0.01$, $p<0.001$, $p<0.0001$ with unpaired Student t-test.

Figure 7. Lack of frequency-dependent potentiation of force development in *Taz*-KD cardiac myocytes.

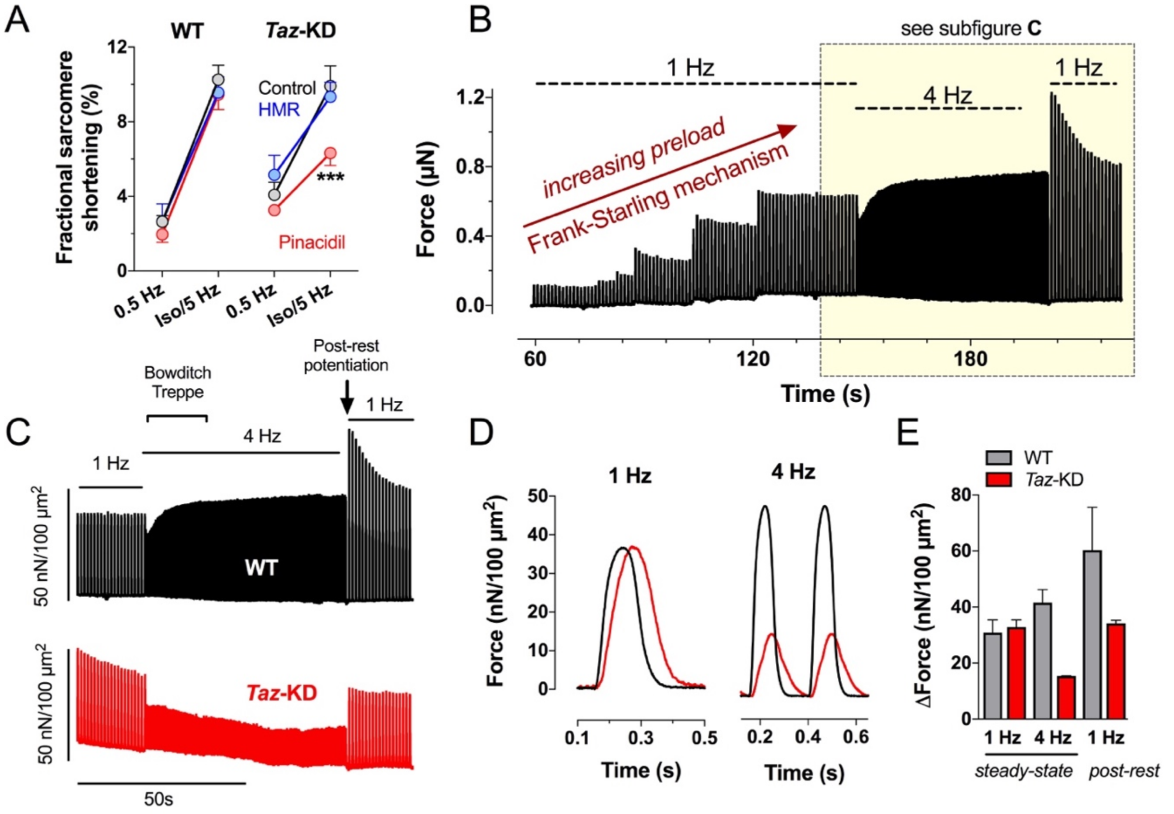

A) Fractional sarcomere shortening of isolated cardiac myocytes from 20 w/o WT and *Taz*-KD mice. Cardiac myocytes were field-stimulated at 0.5 Hz and superfused with the K_{ATP} channel sensitizer pinacidil (red trace; WT n=8/2, *Taz*-KD n=6/2), the K_{ATP} channel inhibitor HMR (blue; WT n=8/2, *Taz*-KD n=7/2), or vehicle (black; WT n=8/2, *Taz*-KD n=7/2) for 240 s before being subjected to Iso/5 Hz stimulation for 180 s.

B) Representative trace of force developed by one isolated cardiac myocyte pre-stretched with glass fibers to exert isometric contractions demonstrating the preload-dependent potentiation of force by the Frank-Starling mechanism.

C) Representative traces of force development of isolated pre-stretched cardiac myocytes from 20 w/o mice subjected to the protocol shown in (B).

D) Averaged original traces and

E) quantification of force developed by isolated cardiac myocytes subjected to the protocol shown in (B) (n=2/2 per group).

Data represent mean ± SEM [indicated by error bars); n-numbers are indicated as numbers of cardiac myocytes / animals; statistical significance was determined by 2-way ANOVA followed by Bonferroni post-test

*** *p*<0.001 with Bonferroni post-test.

Graphical Abstract

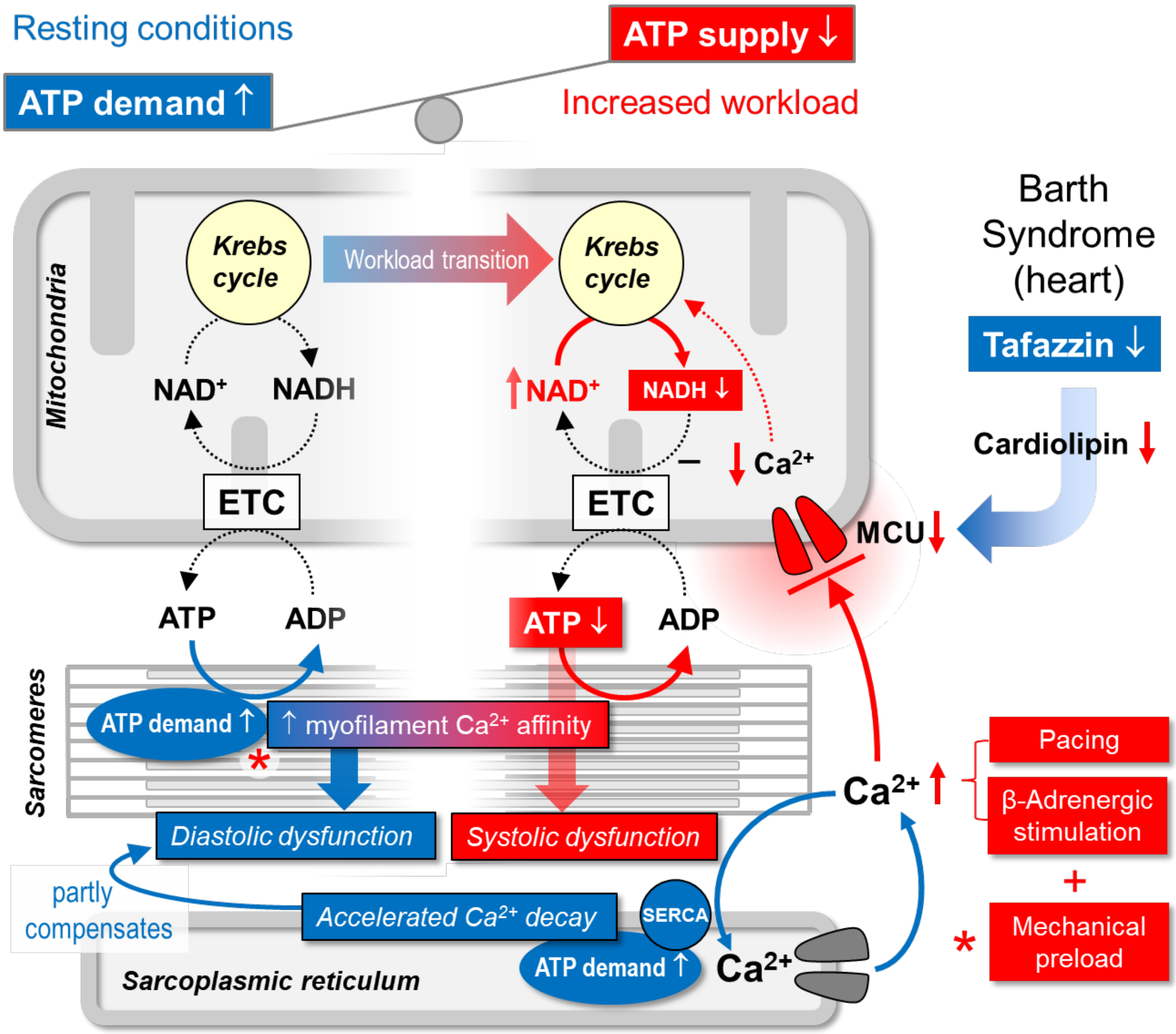

Supplementary Figures and Legends

Figure S1.

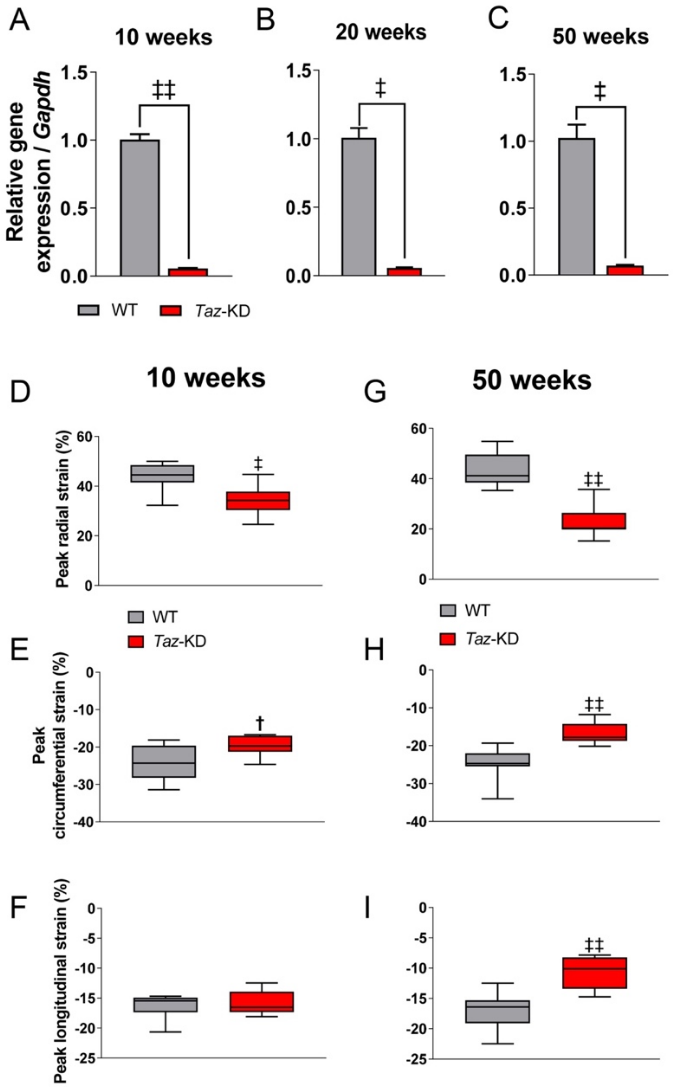

A) Tafazzin mRNA levels in 10, (B) 20, and (C) 50 w/o mice (n=6 per group).

D) Left ventricular peak radial, (E) circumferential, and (F) longitudinal strain in 10 w/o mice (WT n=8, *Taz*-KD n=10).

G) Left ventricular peak radial, (H) circumferential, and (I) longitudinal strain in 50 w/o mice (WT n=11, *Taz*-KD n=9).

This Figure refers to **Figure 1**.

Error bars indicate standard error of the mean (S. E.M.);
n-numbers are indicated as numbers of hearts or animals;
†, ‡, †‡, ‡‡: p<0.05, p<0.01, p<0.001, p<0.0001 with unpaired Student t-test.

Figure S2.

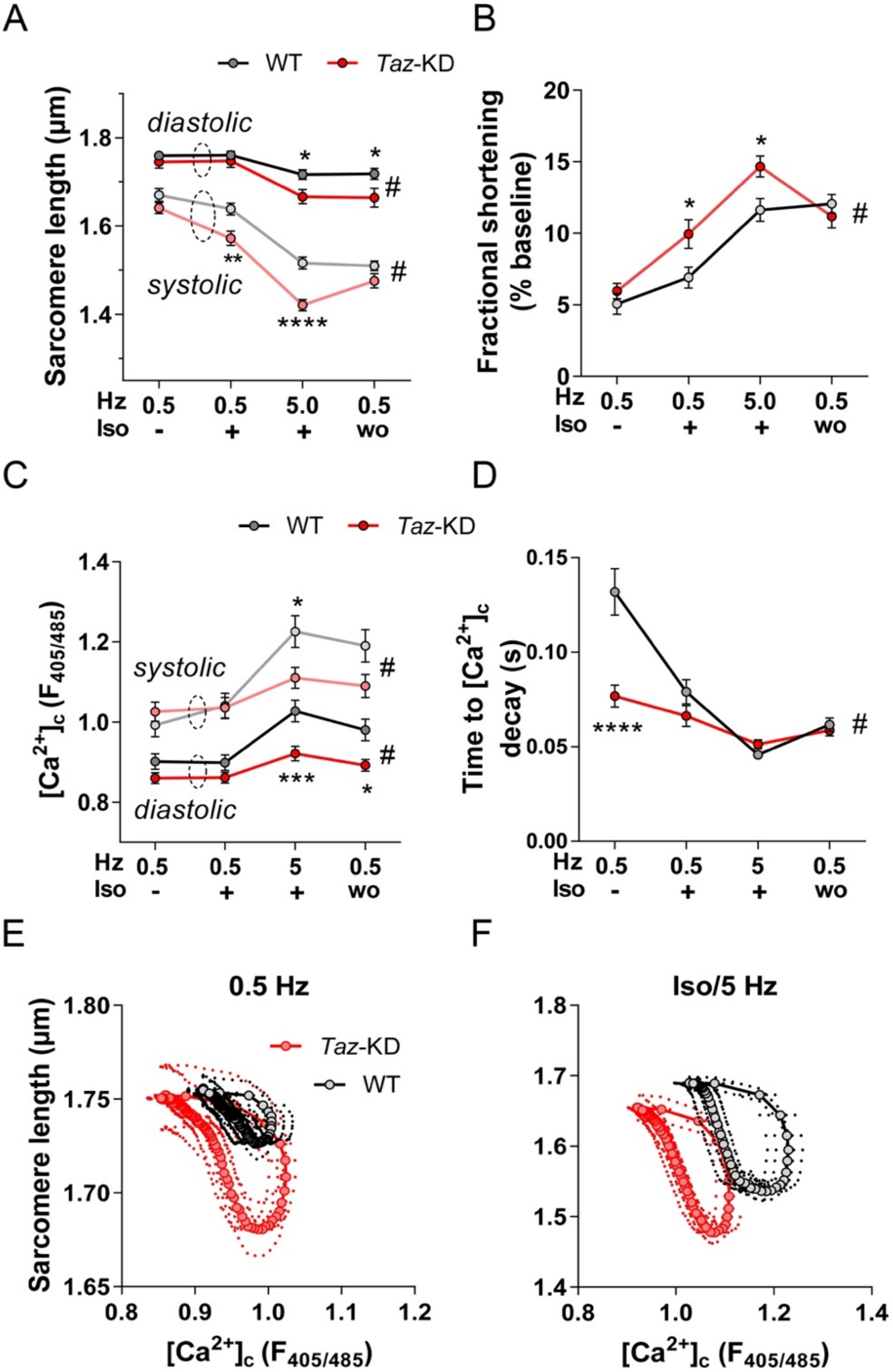
A
WT
Taz-KD
Sarcomere length (µm)
1.8
1.6
1.4
diastolic
systolic
*
*
#
**
#
****
Hz 0.5 0.5 5.0 0.5
Iso - + + wo
B
Fractional shortening (% baseline)
20
15
10
5
0
*
*
#
Hz 0.5 0.5 5.0 0.5
Iso - + + wo
C
WT
Taz-KD
$[Ca^{2+}]_c$ ($F_{405/485}$)
1.4
1.2
1.0
0.8
systolic
diastolic
*
#
#
***
*
Hz 0.5 0.5 5 0.5
Iso - + + wo
D
Time to $[Ca^{2+}]_c$ decay (s)
0.15
0.10
0.05
0.00
****
#
Hz 0.5 0.5 5 0.5
Iso - + + wo
E
0.5 Hz
Taz-KD
WT
Sarcomere length (µm)
1.80
1.75
1.70
1.65
0.8 0.9 1.0 1.1 1.2
$[Ca^{2+}]_c$ ($F_{405/485}$)
F
Iso/5 Hz
1.8
1.7
1.6
1.5
1.4
0.8 1.0 1.2 1.4
$[Ca^{2+}]_c$ ($F_{405/485}$)

A) Sarcomere length and (B) fractional shortening of intact cardiac myocytes isolated from 50 w/o animals (WT n=30/4, *Taz*-KD n=26/4).

C) Cytosolic Ca^{2+} ($[Ca^{2+}]_c$) and (D) time to $[Ca^{2+}]_c$ decay of intact cardiac myocytes isolated from 50 w/o animals and loaded with Indo-1 (WT n=21/3, *Taz*-KD n=19/3).

E) $[Ca^{2+}]_c$ plotted against sarcomere length of cardiac myocytes at 0.5 Hz and (F) Iso/5 Hz stimulation. Data extracted from experiments in (A) to (D) (WT n=21/3, *Taz*-KD n=19/3).

This Figure refers to **Figure 2**.

Error bars and dotted lines [in (E) and (F)] indicate standard error of the mean (S. E. M.);
n-numbers are indicated as numbers of cardiac myocytes / animals.
# indicates $p<0.05$ with 2-way ANOVA;
*,**,***,***,****: $p<0.05$, $p<0.01$, $p<0.001$, $p<0.0001$ with Bonferroni post-test.

Figure S3.

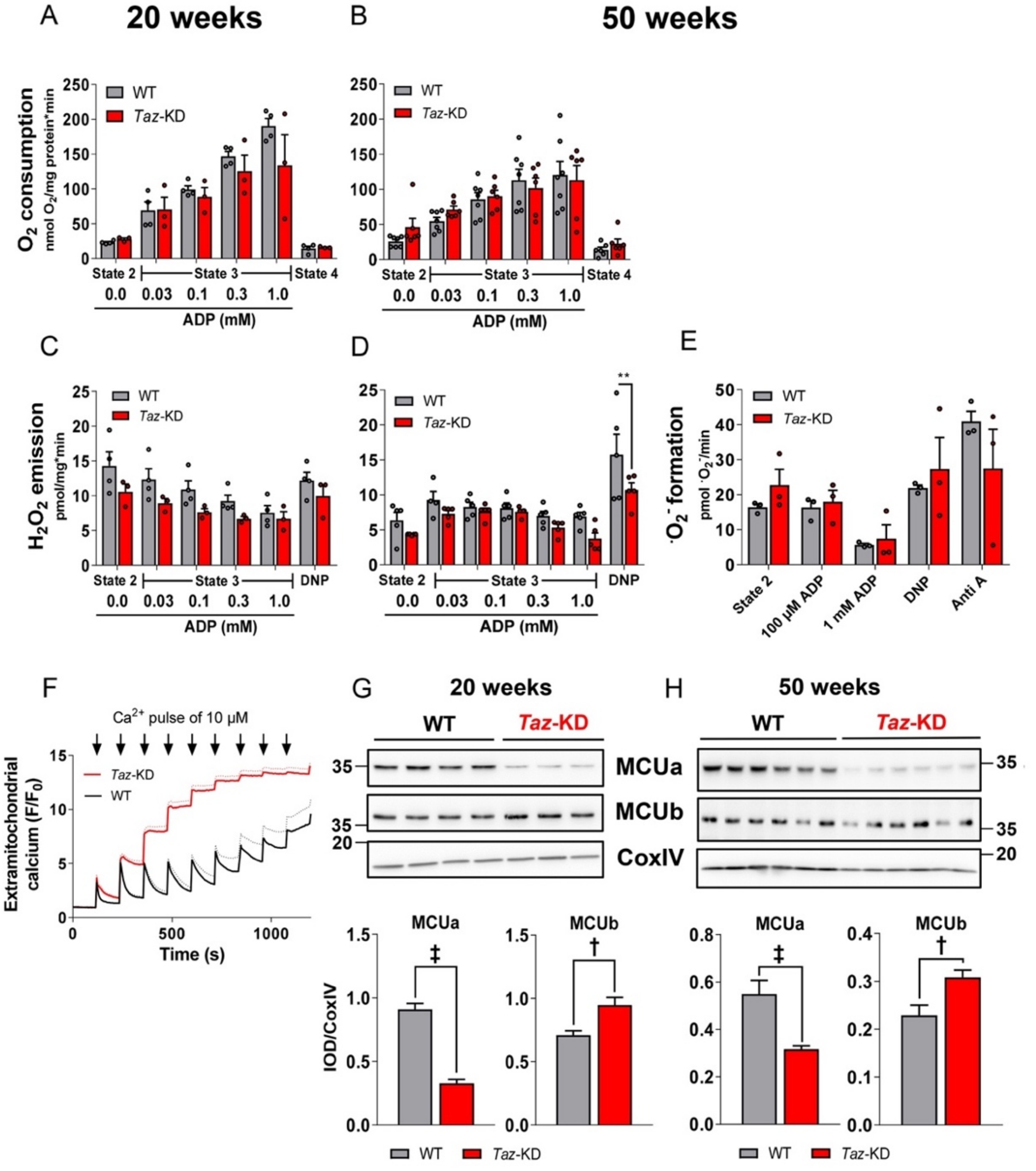
A
20 weeks
B
50 weeks
O2 consumption
nmol O2/mg protein*min
WT
Taz-KD
State 2
State 3
State 4
0.0
0.03
0.1
0.3
1.0
ADP (mM)
C
D
E
H2O2 emission
pmol/mg*min
DNP
**
·O2− formation
pmol ·O2−/min
State 2
100 μM ADP
1 mM ADP
DNP
Anti A
F
Ca2+ pulse of 10 μM
Extramitochondrial calcium (F/F0)
Time (s)
G
20 weeks
H
50 weeks
WT
Taz-KD
MCUa
MCUb
CoxIV
35
20
IOD/CoxIV
‡
†

A) O_2 consumption of cardiac mitochondria from 20 and (B) 50 w/o mice (20 weeks: WT n=4, *Taz*-KD n=3; 50 weeks: WT n=7, *Taz*-KD n=6).

C) H_2O_2 emission from cardiac mitochondria from 20 and (D) 50 w/o mice (20 weeks: WT n=4, *Taz*-KD n=3; 50 weeks: n=5 per group).

E) Superoxide ($\cdot O_2^-$) formation in cardiac mitochondria from 50 w/o mice (3 per group).

F) Ca^{2+} retention capacity of cardiac mitochondria from 20 w/o mice (WT n=4, *Taz*-KD n=3).

G) Protein levels of MCUa and MCUb in the heart of 20 and (H) 50 w/o mice (20 weeks: WT n=4, *Taz*-KD n=3; 50 weeks: n=6 per group).

This Figure refers to **Figures 3** and **4**.

Error bars and dotted lines [in (F)] indicate standard error of the mean (S. E. M.);
n-numbers are indicated as numbers of hearts or animals;
# indicates $p<0.05$ with 2-way ANOVA;
*,**,***,***,****: $p<0.05$, $p<0.01$, $p<0.001$, $p<0.0001$ with Bonferroni post-test;
†, ‡, †‡, ‡‡ = $p<0.05$, $p<0.01$, $p<0.001$, $p<0.0001$ with unpaired Student t-test.

Figure S4.

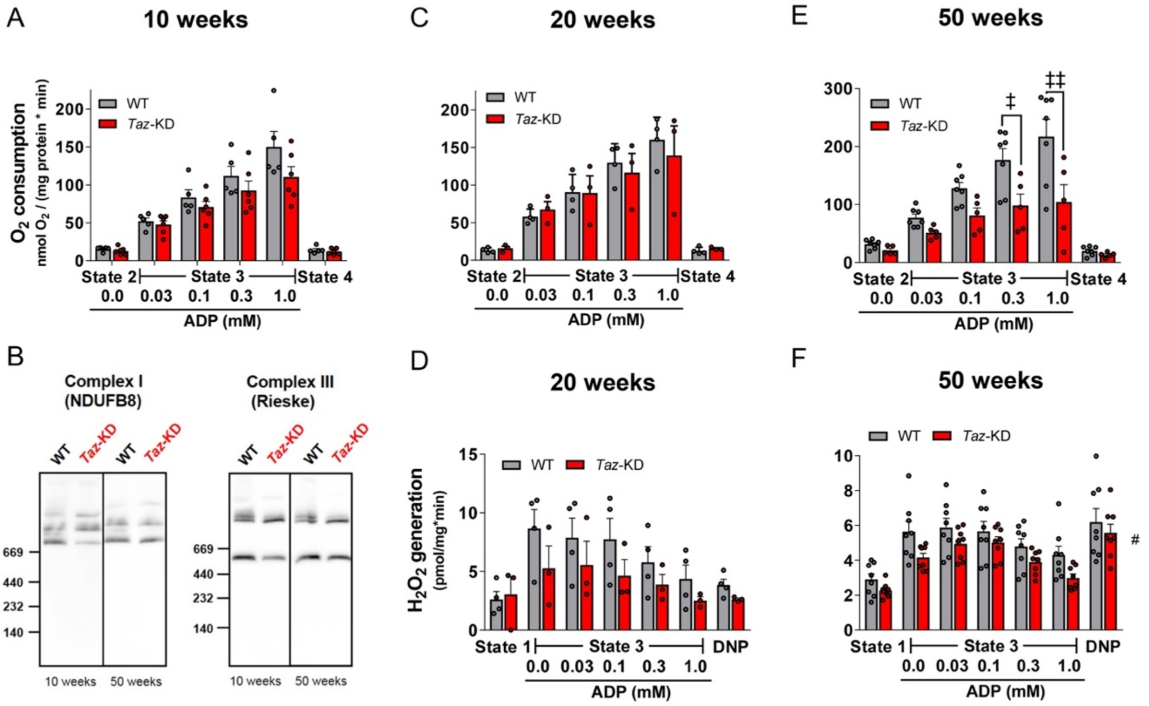

A) O_2 consumption of skeletal muscle mitochondria from 10 w/o mice (WT n=5, *Taz*-KD n=6).

B) BN-PAGE analysis of the NADH dehydrogenase 1 β subcomplex subunit 8 (NDUFB8) of complex I and the complex III component Rieske in skeletal muscle mitochondria from 10 and 50 w/o mice.

C) O_2 consumption and

D) H_2O_2 emission of skeletal muscle mitochondria from 20 w/o mice (WT n=4, *Taz*-KD n=3).

E) O_2 consumption and (F) H_2O_2 emission of skeletal muscle mitochondria from 50 w/o mice (O_2 consumption: WT n=7, *Taz*-KD n=5; H_2O_2 emission: n=8 per group).

Error bars indicate standard error of the mean (S. E. M.);
n-numbers are indicated as numbers of hearts or animals;
†, ‡, ††, ‡‡ = $p<0.05$, $p<0.01$, $p<0.001$, $p<0.0001$ with unpaired Student t-test.

Figure S5.

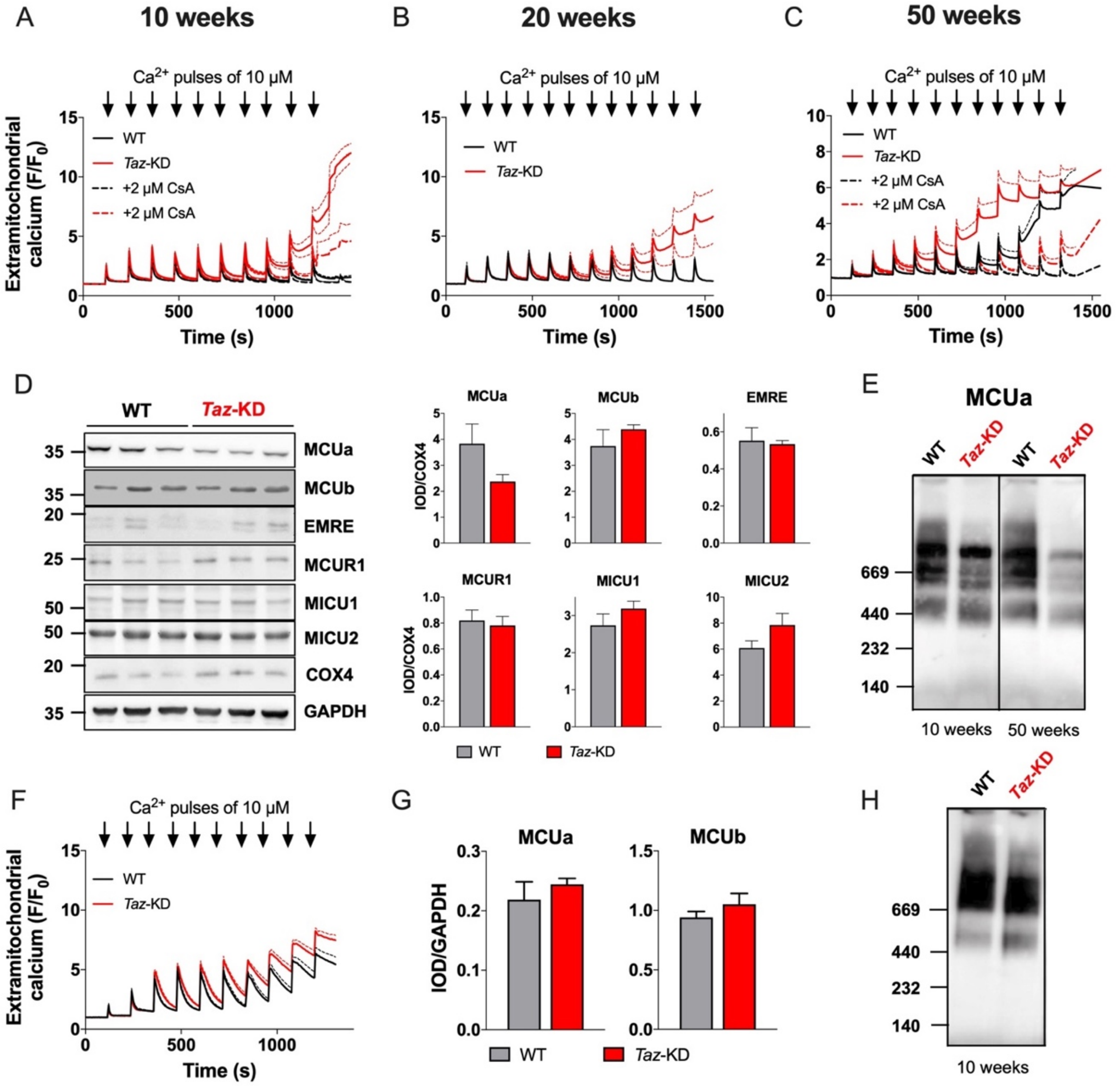

A) Ca^{2+} retention capacity of skeletal muscle mitochondria from 10, (B) 20, and (C) 50 w/o mice (10 weeks: WT n=6, *Taz*-KD n=4; 20 weeks: WT n=4, *Taz*-KD n=3; 50 weeks: n=8 per group).

D) Protein levels of the MCU complex subunits MCUa, MCUb, EMRE, MCUR1, MICU1, and MICU2 in skeletal muscle of 10 w/o mice (n=6 per group).

E) BN-PAGE analysis of MCUa in skeletal muscle of 10 and 50 w/o mice.

F) Ca^{2+} retention capacity of brain mitochondria from 10 w/o mice (n=4 per group).

G) Protein levels of MCUa and MCUb in brain of 10 w/o mice (n=6 per group).

H) BN-PAGE analysis of MCUa in brain from 10 w/o mice.

Error bars and dotted lines [in (A) to (C) and (F)] indicate standard error of the mean (S. E. M.); n-numbers are indicated as numbers of hearts or animals.

Figure S6.

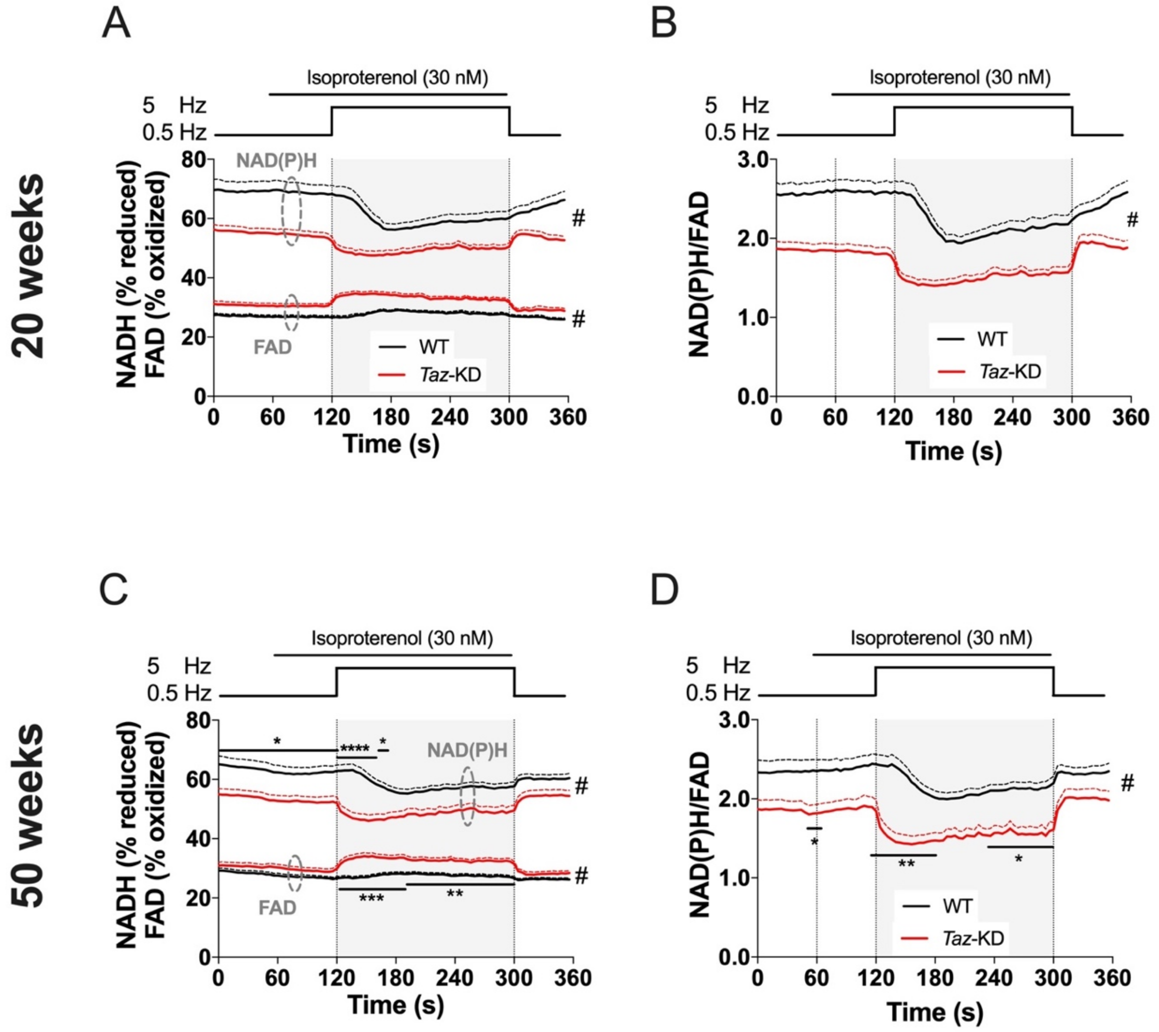

A) Autofluorescence of NAD(P)H and FAD and

B) NAD(P)H/FAD ratio in intact cardiac myocytes from 20 w/o mice (WT n=12/3, *Taz*-KD n=24/3).

C) Autofluorescence of NAD(P)H and FAD and

D) NAD(P)H/FAD ratio in intact cardiac myocytes from 50 w/o mice (WT n=30/4, *Taz*-KD n=26/4).

This Figure refers to **Figure 5**.

Dotted lines indicate standard error of the mean (SEM);
n-numbers are indicated as numbers of cardiac myocytes / animals;
# indicates $p<0.05$ with 2-way ANOVA;
*,**,***,***,****: $p<0.05$, $p<0.01$, $p<0.001$, $p<0.0001$ with Bonferroni post-test.

Table S1.

	10 weeks of age		**20 weeks of age**		**50 weeks of age**	
	WT (n=5)	***Taz*-KD** (n=6)	**WT** (n=5)	***Taz*-KD** (n=7)	**WT** (n=24)	***Taz*-KD** (n=19)
BW (g)	22.84±1.58	21.44±1.93	24.63±2.03	25.49±1.22	30.61±1.09	*25.25±0.99*†‡
HW (mg)	129.5±5.5	119.5±6.4	175.6±23.2	174.1±10.7	168.1±6.3	*147.9±6.4*†
HW/BW (mg/g)	5.71±0.17	5.67±0.25	7.04±0.45	6.85±0.31	5.51±0.11	5.94±0.25
Liver weight (mg)	1039±103	1058±130	1032±88	1267±69	1342±52	1214±59
Lung weight (mg)	141.7±5.67	135.2±6.9	155.3±9.3	151.9±10.0	161.1±3.1	150.5±3.8

Abbreviations. BW: body weight; HW: heart weight.

Table S2.

	10 weeks of age		**20 weeks of age**		**50 weeks of age**	
	WT (n=5)	***Taz*-KD** (n=4)	**WT** (n=5)	***Taz*-KD** (n=4)	**WT** (n=16)	***Taz*-KD** (n=12)
CO (mL/min)	16.26±1.14	12.57±1.37	16.45±1.49	*11.56±1.50**	16.31±0.80	*10.15±1.10*†‡
CO/BW (mL/min/g)	*NA*	*NA*	0.68±0.06	*0.44±0.05**	0.53±0.02	*0.40±0.03*†‡
HR (bpm)	433.20 ±28.66	423.25 ±13.52	436.60 ±27.60	410.75±45.6	433.4 ±12.76	444.5 ±13.18
LVEF (%)	73.95±3.99	63.83±6.80	69.68±1.78	*52.33±3.26**	75.42±1.38	*54.61±4.22*‡‡
LVEDV (µL)	51.40±3.20	46.75±3.12	54.20±3.63	54.00±3.08	49.94±2.04	*42.5±2.77*†
LVESV (µL)	13.80±2.97	17.25±3.86	16.60±1.81	26.00±3.14	12.31±0.89	*19.58±2.57*‡
SV (µL)	37.60±1.50	29.50±2.50	37.60±2.06	*28.00±1.00**	37.63±1.64	22.67±1.97
LVEDD (mm)	3.68±0.16	3.90±0.16	3.72±0.18	3.83±0.75	3.65±0.04	3.62±0.11
LVESD (mm)	2.26±0.10	2.67±0.37	2.28±0.06	2.68±0.14	2.05±0.06	*2.56±0.06*†‡
LVPW (mm)	0.68±0.02	0.77±0.12	0.70±0.05	0.73±0.05	0.78±0.03	0.72±0.04
IVS (mm)	1.00±0.03	1.07±0.07	0.96±0.05	1.08±0.09	0.98±0.04	1.06±0.05

Abbreviations. BW: body weight; HR: heart rate; IVS: interventricular septum; LVEDD: left ventricular end-diastolic diameter; LVESD: left ventricular end-systolic diameter; LVEDV: left ventricular end-diastolic volume; LVESV: left ventricular end-systolic volume; LVEF: left ventricular ejection fraction; LVPW: left ventricular posterior wall; NA: not available; SV: stroke volume; Taz-KD: tafazzin-knockdown; WT: wild-type.

Table S3.

	WT (n=18/4)	***Taz*-KD** (n=15/4)
Area (μm^2)	332 ± 50.5	315 ± 49.6
F_{max} (kN/m^2)	17.2 ± 1.6	15.2 ± 1.7
F_{pass} (kN/m^2)	2.3 ± 0.2	2.0 ± 0.4
nH	2.11±0.15	1.91±0.15

Abbreviations. F_{max}: maximal force development; F_{pass}: passive force development; nH: Hill´s coefficient for Ca^{2+} cooperative activation.

Errors are indicated as standard error of the mean (S. E. M.);
n-numbers are indicated as numbers of hearts or animals for **Tables S1-S2** and as numbers of cardiac myocytes / animals for **Table S3**.
\# indicates $p<0.05$ with 2-way ANOVA;
*,**,***,***,****: $p<0.05$, $p<0.01$, $p<0.001$, $p<0.0001$ with Bonferroni post-test;
†, ‡, †‡, ‡‡ = $p<0.05$, $p<0.01$, $p<0.001$, $p<0.0001$ with unpaired Student t-test.

Methods

Experimental model and subject details

Taz-KD mice

Generation and characterization of the *Taz*-KD mouse model has been described elsewhere (88). Mice were obtained from Jackson Laboratories (B6.Cg-Gt(ROSA)26Sor$^{tm37(H1/tet0\text{-}RNAi:Taz)Arte}$/ZkhuJ (stock No. 014648). This strain expresses shRNA against *Taz* mRNA in the ROSA26 locus under control of the tetracycline-response element (Tet-On). To generate *Taz*-KD mice, mouse embryonic stem cells containing an engineered recombinase-mediated cassette exchange (RMCE) locus on chromosome 6 were used to target insertion of Tet-On *Taz* shRNA cassettes in the *ROSA26* locus. Embryonic stem cell clones in which the Tet-On cassettes were correctly targeted were identified by Southern DNA blot. One embryonic stem cell clone achieving adequate suppression of *Taz* mRNA (assessed by RT-PCR) was injected into tetraploid blastocysts, giving rise to a line of transgenic mice from a single founder. The genetic background of these mice is C57BL/129S6.

Animal procedures were approved by the local animal ethics committees (RUF-55.2.2-2532-2-804) and conducted in accordance with institutional guidelines. Animals were fed with standard rodent chow enriched with doxycycline (625 mg/kg). For breeding, female mice were fed with this diet one week before and after mating. During mating, doxycycline was withdrawn to avoid male infertility. The genotype of the pups was assessed by RT-PCR. Mice were housed in a pathogen-free facility under 12 h light/darkness cycles and controlled temperature and humidity. Animals were maintained in IVC housing and manipulated in Class IIA laminar flow biosafety cabinets to prevent cross-contamination. Sentinel animals were regularly tested for pathogens using either serology or PCR on tissue, feces, and pelt swabs. Sentinel animals were housed 2 per cage on the bottom shelf of each ventilated rack. Cages were sampled systematically so that every cage was sampled over a 4-week period on any given rack. Sentinel mice were exposed to colony animal bedding for 6-8 consecutive months.

Animals were used for experiments at 10, 20, and 50 weeks of age. Since we did not identify gender-specific differences in cardiac function *in vivo* or in mitochondrial function in vitro, both male and female mice were used for the study.

iPSC-derived cardiac myocytes

The generation of cardiac myocytes from a control individual iPSCs (WT-D2) and a BTHS patient [TAZ10 (c.590 G>T)] was described previously (62, 259). Feeder-free adherent cultures of iPSCs were passaged every 4-5 days by using the non-enzymatic Versene solution. Differentiation of iPSCs into cardiac myocytes was induced by RPMI 1640 medium supplemented with 2 mM L-glutamine and B27 without insulin (260). The GSK3 inhibitor CHIR99021 (10 µM) was added to the culture for 24 hours, the Wnt inhibitor IWP2 (5 µM) was added at day 3 for 2 days and the culture medium was changed to RPMI+B27+insulin (RPMI 1640 medium supplemented with 2 mM L-glutamine and B27 with insulin, at day 7. At day 20, the cells were replated as monolayers into geltrex-coated culture dishes. Cardiac myocytes were selected by substituting glucose for 4 mM lactate in the culture medium for 6 days between days 20 and 30 (261).

Method details

Mitochondria isolation from mouse heart

Mitochondria isolation from mouse heart and skeletal muscle was described previously (47).

Mitochondria isolation from mouse brain

For mitochondria isolation from mouse brain, the brain was extracted, rinsed with isolation solution (same as used for mitochondria isolation from mouse heart) and minced with scissors. The tissue was divided in two parts and transferred to a 5 mL homogenizer (Teflon pestle) and manually homogenized in a buffer consisting of 1 ml isolation solution and 0.16 mg/mL bacterial protease type XXIV; using 10 strokes with a loose-fitting glass pestle followed by a tight-fitting pestle. The homogenate was centrifuged at 2000 g for 3 minutes at 4°C in a pre-cooled centrifuge. The pellet was resuspended in 1 mL of isolation solution and bacterial protease mixture and centrifuged again at 2000g for 3 minutes. The supernatant obtained from these two centrifugations were pooled and centrifuged at 12000 g for 8 minutes. The resulting pellet, containing mitochondria, was resuspended in 100 µL of mitochondrial suspension solution (same as used for mitochondria isolation from mouse heart).

Mitochondrial respiration and H_2O_2 emission

Assessment of mitochondrial respiration and H_2O_2 emission was performed as described previously (47).

Mitochondrial superoxide formation

Superoxide ($^{\bullet}O_2^-$) formation in isolated mitochondria was monitored by measuring the EPR spectra of the radical formed by the reaction of $^{\bullet}O_2^-$ with the redox-activated cyclic hydroxylamine spin trap 1-hydroxy-3-methoxycarbonyl-2,2,5,5-tetramethylpyrrolidine (CMH; 300 µM) using a Bruker spectrometer (ESP300e) equipped with a standard 4102ST cavity holding the capillary support quartz glass finger. The temperature of the finger was controlled and maintained at 37°C throughout the experiment. The sample containing mitochondria (12 µg per replicate), CMH, as well as different combinations of substrates/inhibitors was filled in a 50 µL glass capillary, which was immediately transferred into the capillary holder. To correct for unspecific radical production, control experiments were performed with single components of the assays and CMH. As described previously (47), the EPR spectra of the CMH radical were measured with modulation amplitude of 0.1 mT and a microwave power of 20 mW at a time constant of 20.48 ms for 8 times and evaluated with a customized program (Medeia) which measures the peak-to-peak intensity and width of one (or several) lines of a radical visible in a time series. In the absence of line width changes and saturation effects, the intensity information can be translated to radical concentration by calculating the integral of the monitored line and considering the multiplicity of the radical signal. This value is compared to a reference sample of known concentration (100 µM Tempol) recorded under identical conditions for quantitative measures.

Permeability transition pore (PTP) assay

Mitochondrial Ca^{2+} retention capacity was assessed as described previously (47).

Experiments with intact cardiac myocytes

Cardiac myocyte isolation from mouse heart was performed as described previously (47). Experiments with intact cardiac myocytes were performed using a customized IonOptix setup (IonOptix, Milton, MA, USA) coupled to an inverted epifluorescence microscope (Eclipse Ti, Nikon GmbH, Düsseldorf, Germany). All experiments were performed at 37°C. During the experiment, cells were continuously superfused with

Normal Tyrode´s (NT) solution containing (in mM): NaCl 130, KCl 5, $MgCl_2$ 1, $CaCl_2$ 1, Na-HEPES 10, glucose 10, sodium pyruvate 2 and ascorbic acid 0.3 (pH 7.54).

For experiments shown in **Figures 2A-H**, **5D-H, 6A-C**, **S2**, and **S6** adult ventricular myocytes were field-stimulated at 0.5 Hz for 120 s, subsequently superfused with NT solution containing isoproterenol (30 nM), and when the isoproterenol-induced increase in contractility became evident, stimulation frequency was increased to 5 Hz for 180s. For experiments shown in **Figures 5I**, **J** and **7A,** cardiac myocytes were superfused with NT solution containing the NCLX inhibitor CGP-37157 (10 µM; **Figures 5I**, **J**), the K_{ATP} channel sensitizer pinacidil (100 µM), the K_{ATP} channel blocker HMR-1098 (30 µM; **Figure 7A**), or vehicle (DMSO) before being subjected to Iso/5 Hz stimulation.

In the experiment shown in **Figures 2I-P**, cardiac myocytes were field-stimulated at 0.5 Hz for 120 s. Subsequently, field-stimulation was stopped and one pulse of caffeine (10 mM) was applied to induce Ca^{2+} release from the SR. Stimulation at 0.5 Hz was resumed until sarcomere shortening was again comparable to baseline conditions. Thereafter, cardiac myocytes were superfused with NT solution containing isoproterenol (30 nM) until a visible increase in sarcomere shortening could be observed, and stimulation frequency was increased to 5.0 Hz for 120 s. A second caffeine pulse was applied immediately after stopping field-stimulation.

During the experiments described above, sarcomere shortening was measured together with NAD(P)H and FAD autofluorescence (**Figures 5D-J**; **S2A**, **B**; **S6**), Indo-1-AM fluorescence to monitor $[Ca^{2+}]_c$ (**Figure 2A**, **E-P**; **S2C-F**), tetramethylrhodamine methyl ester (TMRM; 10 nM) to monitor mitochondrial membrane potential $\Delta\Psi_m$ (**Figure 5F**) or cellular ROS formation with 5-(-6)-chloromethyl-2,7-dichlorodihydrofluorescein diacetate (DCF; 1 µM; **Figure 6A-C**). Calibration of NAD(P)H and FAD signals was performed by applying carbonyl cyanide-p-trifluoromethoxyphenylhydrazone (FCCP; 5 µM) and cyanide (4 mM) to induce complete oxidation and reduction, respectively, of the mitochondrial pyridine nucleotide pools.

Patch clamp experiments

To determine mitochondrial and cytosolic Ca^{2+} levels in the same cardiac myocyte (**Figure 5A-C**), we employed a patch-clamp dual-fluorescence approach that we previously established (30). Briefly, cardiac myocytes were incubated for 2 hours with rhod-2-acetoxymethylesther (rhod-2-AM), a Ca^{2+} indicator that segregates primarily into mitochondria, and subsequently cytosolic remnants of rhod-2-AM were removed by dialyzing the cytosol with a pipette solution containing Indo-1 penta-K^+ salt (75 µM). Indo-1 penta-K^+ salt does not pass membranes and thus reports specifically $[Ca^{2+}]_c$ (30). Additionally, the pipette solution contained (in mM): potassium glutamate 130, KCl 19, $MgCl_2$ 0.5, Na-HEPES 15, Mg-ATP 5 (pH 7.2). Subsequently, cardiac myocytes were voltage-clamped in whole-cell configuration (37°C, pipette resistance 2-4 MΩ) and subjected to the experimental stress protocol described above by depolarizing the cell from -80 to +10 mV for 50 ms at 0.5 or 5 Hz, respectively.

Force measurements in intact cardiac myocytes

To monitor force development in isolated cardiac myocytes (**Figures 7B-E**), we used the IonOptix force transducers as described previously (239). In this experiment, cardiac myocytes were superfused with NT solution containing (in mM) NaCl 130, KCl 5, $MgCl_2$ 1, $CaCl_2$ 2, Na-HEPES 10, glucose 10, sodium pyruvate 2, and ascorbic acid 0.3 (pH 7.54). Briefly, cantilever of the force transducer and the piezo motor were covered first with “precoat” for a few seconds and thereafter coated with specially-formulated biocompatible adhesive (MyoTak). Subsequently, the holders were transferred into the chamber, in which cardiac myocytes were placed on a 2% BSA-laminated cover slip. Beating cells with the correct orientation were attached to both cantilevers and then stretched with the piezo motor up to a sarcomere length of 1.9 µm. The measurements were performed at room temperature. The stimulation frequency was 1 Hz, and after the final sarcomere length was reached, stimulation frequency was kept for 40 s at 1 Hz and then for 60 s at 4 Hz.

Force measurements in membrane-permeabilized cardiac myocytes

The composition of all solutions was calculated based on a computer software as previously described (226). The pH of all solutions was adjusted to 7.1 at 15°C by KOH and ionic strength was adjusted to 180 mM with KCl. The relaxing solution contained (in mM) free Mg^{2+} 2, MgATP 1, EGTA 20, BES 10, and phosphocreatine (PCr) 14.5. Maximal Ca^{2+} activating solution consisted of (in mM) 2 free Mg^{2+}, 1 MgATP, 20 EGTA, 10 BES and 32 µM free Ca^{2+}. Ca^{2+} activating solutions with lower free $[Ca^{2+}]$ were obtained by mixing of the Ca^{2+} activating and relaxing solutions and assuming an apparent stability constant of the Ca^{2+}-EGTA complex of $10^{6.35}$ (226).

Frozen cardiac tissue samples from 10 w/o *Taz*-KD and WT mice were thawed in relaxing solution and cardiac myocytes were mechanically isolated with a tissue ruptor (Qiagen). Cardiac myocytes were chemically permeabilized by incubation for 5 minutes in relaxing solution containing 0.5% (v/v) Triton-X100 and glued between a force transducer and a servo motor (Aurora Scientific). Isometric force measurements were subsequently performed in single cardiac myocytes at sarcomere length of 2.2 µm. Average sarcomere lengths were determined by means of a spatial Fourier transformation. Absolute tensions were normalized to cardiac myocyte cross-sectional area and expressed as developed tension (in kN/m^2). Passive force (F_{pass}) was determined by shortening the myocyte in relaxing solution by 30% of its length. Active tension (Ca^{2+}-F_{act}) was calculated as $F_{act}=F_{total}-F_{pass}$. In addition, the rate constant of tension redevelopment (k_{TR}) was determined using a slack-restretch test: after steady state force was reached, cardiac myocytes were shortened within 1 ms to 70% of their original length and restretched to the original length after 50 ms. A single exponential was fitted to the force redevelopment to determine the rate constant of force redevelopment: k_{TR} was determined at maximal and submaximal [Ca^{2+}] to assess cross-bridge cycling kinetics.

Force-Ca^{2+} relations were fit by a non-linear fit procedure to a modified Hill equation using GraphPad Prism 8 as follows:

$$P (Ca^{2+}) / P_0 = [Ca^{2+}]nH / (K\ nH + [Ca^{2+}]nH)$$

where P is steady-state force. P_0 denotes the steady isometric force at either saturating [Ca^{2+}], nH describes the steepness of the relationship, and K represents the [Ca^{2+}] at which force is half-maximal (0.5 x P0). Myofilament Ca^{2+}affinity is denoted as EC_{50}.

Redox histology

To map the *in vivo* redox status, the *Taz*-KD mouse model was crossbred with a transgenic model expressing the mitochondrial H_2O_2 sensor mito-roGFP2-Orp1 (132) on a C57BL/6N background. Mice were sacrificed via cervical dislocation. Immediately afterwards, the thorax was opened and cardiac perfusion was performed. Hereby, the circulatory system was perfused with 25 mL N-Ethylmaleimide (NEM, 50 mM, diluted in PBS) at ~5 mL/min. Thereafter, hearts were removed and dissected in 50 mM NEM solution. Fixation was done overnight at room temperature with 4% paraformaldehyde. On the following day, the samples were washed for 15 min in PBS, embedded in Tissue Tek OCT Compound (Fisher Scientific) rapidly frozen using liquid nitrogen-cooled isopentane and cut at 5 µM using a Leica CM 3050 S cryostat (Leica, Germany). For imaging, a filter-based fluorescence microscope (Axio Observer 7, Zeiss) with a 20x air objective was used. The roGFP2-Orp1 fluorescence was measured at 500 to 550 nm with either 405 (BP 430/60, Zeiss filter) or 488 nm (BP 470/40 HE, Zeiss filter) excitation.

The images obtained at 405 and 488 nm excitation were analyzed separately and individual thresholds for signal intensity were set to remove background and overexposed pixels (Fiji imaging software). Fluorescence ratio 405/488 images were calculated by combining the image masks resulting from 405 and 488 nm thresholds and displaying the ratio. The resulting image was visualized using ImageJ lookup table "Fire". Image analysis was performed using a macro coded by the investigator, thus minimizing the risk of bias. The presented change in ratio (**Figure 6F**) results from normalizing all ratios to the average of the WT ratio.

Gene expression analyses

RNA was prepared from mouse LV tissue using peqGold TriFast (PeqLab) extraction reagent per manufacturer´s protocol. For cDNA preparation 2 µg of RNA were digested with DNAse (Peqlab) and then reverse-transcribed using the HighCap cDNA RT Kit (Applied Biosystems) according to the manufacturer´s protocol. TaqMan PCR was conducted in a StepOne plus thermocycler (Applied Biosystems) using TaqMan GenEx Mastermix (Applied Biosystems). Signals were normalized to corresponding glyceraldehyde-3-phosphate dehydrogenase (*Gapdh*) controls. No template controls were used to monitor for contaminating amplifications. The ΔCt was used for statistical analysis and $2^{-\Delta\Delta Ct}$ for data presentation. Probes used to amplify the transcripts are listed in the **Key resources tables**.

SDS-page and Western blot

Western blot analysis was performed either to determine total protein content using complete tissue homogenate or to compare protein content in isolated mitochondria and cytosol (see mitochondrial isolation). Mouse LV myocardium, skeletal muscle, and brain tissue was homogenized in total lysis buffer containing Tris-HCl 100 mM, SDS 4%, and glycine 20%, complete protease inhibitors (Roche), and phosphatase inhibitors (Roche). The homogenate was centrifuged at 16.000 g for 20 minutes and protein concentration was estimated by BCA assay. For each lane, 50 µg of protein was separated on 10 or 12% SDS-PAGE gels and electrophoretically transferred to nitrocellulose membrane (0.2 µm pore size, Schleicher and Schuell). Membranes were blocked in Tris-buffered saline (TBS) containing 5% non-fat dry milk for 120 minutes at room temperature and exposed to the primary antibodies (listed in the **Key resources tables**) diluted 1:1000. Secondary antibodies (goat anti-mouse 1:2500; rabbit anti-goat 1:5000) were incubated for 60 minutes at room temperature. Proteins were visualized by enhanced chemiluminescence according to the manufacturer´s guidelines (Amersham Pharmacia Biotech, Freiburg, Germany). Quantification was performed using the high-resolution chemiluminescence Fusion SL Detection System (Peqlab, Erlangen, Germany) and analyzed by FusionCapture Advanced Software (Peqlab, Germany). Data are presented as intensity optical density (IOD).

Blue Native-PAGE and Western blot

Mitochondria were isolated from tissues as described above and the protein concentration was estimated by BCA assay. For BN-PAGE analysis, 100 µg (brain and heart) or 200 µg (skeletal muscle) of mitochondria were solubilized in digitonin buffer containing (in mM) Tris-HCl 20, NaCl 50, EDTA 0.1, PMSF 2, glycerol 10%, (w/v) digitonin 1%; pH 7.4, for 15 minutes on ice. After a clarifying spin, the samples were separated on a 4-13% BN-PAGE (262). Native protein complexes were transferred on a PVDF membrane (Immobilon-P 0.45 µM pore size, Merck Millipore) followed by immunoblotting with antibodies directed against NDUFB8, UQCRFS1, COX5A (all generated by Peter Rehling), and MCUa. In addition, expression levels of the proteins were analyzed by SDS-PAGE and immunoblotting using antibodies specific for OXPHOS proteins and MCUa.

Magnetic resonance imaging

All MRI experiments were performed using a 9.4 Tesla horizontal bore animal scanner (Bruker BioSpin 94/20, Ettlingen, Germany) equipped with Paravision 5.1 operating software, with a linear resonator and a receive only 2 × 2 element phased-array surface coil developed for imaging of the mouse heart.

During imaging experiments, animals were anesthetized using a mixture of isoflurane and oxygen (1.0 to 2.5 %/99.0 to 97.5 %), applied via a nose mask at a flow rate of 1.0 to 2.0 L/min. Mice were positioned prone in a dedicated cradle including the coil, and a water-heated blanket was placed over the body to prevent hypothermia.

Core temperature was measured using a rectal sensor. ECG signals were recorded with external electrodes attached to the front paws and a pressure transducer attached to the abdominal wall allowed for monitoring of the respiration rate.

For determination of end-diastolic and end-systolic volumes, a multi-slice retrospectively self-gated cine fast low angle shot (FLASH) sequence was employed in short axis orientation covering the entire left ventricle from base to apex (protocol Intragate-FLASH). Sequence settings were set to TR/TE of 5.6/1.5 ms, flip angle 20°, 8 consecutive slices, slice thickness 0.7 mm, 200 averages, field of view 25.6 × 25.6 mm, matrix 256 × 256 (resulting in a resolution in plane of 100 µm × 100 µm). For every slice position 20 cine image frames were reconstructed. With the same sequence, four-chamber cine images were acquired for strain analysis with imaging parameters set to TR/TE 5.6/1.4 ms, flip angle 20°, 1 slice, slice thickness 1.0 mm, 200 averages, field of view 20.0 × 20.0 mm, matrix 200 × 200 (resulting in a resolution in plane of 100 µm × 100 µm).

Images were exported from the scanner in DICOM format, and image analysis was performed by manually contouring LV images using the freely available software Segment (263). The investigator was blinded to the genotype of the animals during image analysis.

Echocardiography

Echocardiography was performed with the Visualsonics Vevo® 770 High-Resolution *in vivo* Micro-Imaging System (Visualsonics Inc., Scanhead: RMV707B, 15-45 MHz, cardiac mouse). Mice were anesthetized with a mixture of isoflurane (3%) and O_2 (97%) at a flow rate of 1 L/min. The animal was placed in a supine position on a pad with embedded ECG. During the measurement, anesthesia was maintained with a mixture of isoflurane (1-1.5%) and O_2 (98.5-99%) at a flow rate of 1 L/min using a rodent nose mask. Heart rate was maintained at ~500 beats per minute (bpm) with these regimens. Body temperature was monitored via a rectal probe and maintained at 37.0±1.5°C throughout the entire procedure via a heated platform and a heat lamp. Chest hair was removed and a layer of preheated ultrasound gel was applied to the chest.

Two-dimensional (B-mode) images were acquired in parasternal long- and short-axis view with guided one-dimensional (M-mode) recordings at the midventricular level apical of the papillary muscle in both views. Interventricular septum (IVS), left ventricular posterior wall (LVPW), and left ventricular internal diameter (LVID) were measured in parasternal long-axis projection during at least three cardiac cycles and averaged. ECG and respiration gating were used to suppress imaging artifacts due to respiration and cardiac movements.

Myocardial fibrosis

Interstitial fibrosis was assessed by Picro Sirius red staining as described in previous publications (264). In short, LV tissue samples were fixed using 4% formalin/PBS solution and embedded in paraffin. LV circumferential sections 6 µm thick were cut with a microtome. Subsequently, samples were deparaffinized, hydrated, and incubated in 0.1% Sirius red in a saturated solution of picric acid. Excess Sirius red was re- moved with 0.01 N HCl. Picro Sirius red staining identifies collagen type I and type III by yellow-red and green birefringence, respectively. Ten fields from the middle third of the left ventricle were photographed at 100x magnification with a Nikon E600 microscope. The quantification displayed in **Figure 1L** corresponds to the percent area of collagen on total myocardial tissue as analyzed with the digital software Lucia G.

8-hydroxy-2'-deoxyguanosine (8-OHdG) staining

Histology slices of LV myocardium were deparaffinized and pre-treated in Coplin jars with 0.05% citraconic anhydride solution (pH 7.4) for 1 hour at 98°C. Slices were then incubated overnight in primary antibody at 4°C and thereafter with the appropriate secondary antibody at 37°C for 40 minutes. To detect hydroxyl radical-induced DNA oxidation, slices were incubated with a polyclonal antibody against 8-OHdG (Abcam) diluted 1:300 in citrate buffer. To identify cardiac myocytes, a monoclonal antibody against α-sarcomeric actin (Sigma-Aldrich) was used. FITC- and TRITC-conjugated anti-goat IgG and anti-mouse IgM (Dianova) were used as secondary antibodies. Wash steps were performed with 4x saline-sodium citrate buffer. Sections were counterstained with DAPI (Calbiochem) and mounted with fluorescent mounting medium (Vectashield, Vector Laboratories). All sections were evaluated using a Nikon E600 epifluorescence microscope (Nikon, Germany) with appropriate filters.

Quantification and statistical analysis

Values are displayed as mean ± SEM. Statistical parametric analyses were used after confirming that values followed a normal distribution. Statistical tests used for analysis are specified in each Figure legend and include two-way ANOVA followed by Bonferroni's multiple comparisons test, unpaired t tests, Fisher's exact test, and Chi square test. If not specified otherwise in the respective Methods section, statistical analyses were performed using GraphPad Prism version 6.00 for Windows (GraphPad, http://www.graphpad.com). The n-numbers are indicated as numbers of cardiac myocytes / animals or as number of hearts or animals, depending on the Figure; the related information is provided in the Figure legend.

Discussion

Calcium (Ca^{2+}) is a highly versatile second messenger that regulates a number of cellular processes, transducing signals from the extracellular environment to the cytosol and from the cytosol and the endoplasmic reticulum to mitochondria. In the four studies comprised in this Thesis, we explored the Janus-faced role of mitochondrial Ca^{2+} uptake in cardiac myocytes.

Mitochondria do not survive calcium overload during transplantation

The sensitivity of mitochondria to Ca^{2+} was first reported in the 70s, when Bernardi and colleagues reported that "the permeability of isolated mitochondria varies sigmoidally with respect to Ca^{2+} concentration, with an apparent K_m of 16 µM at pH 7.0. […] In the presence of Ca^{2+}, both neutral and charged molecules of molecular weight <1000 pass readily through the membrane. This response to Ca^{2+} is interpreted as a gating effect at the internal end of hydrophilic channels which span the inner membrane" (265). Despite decades of investigation, the molecular identity of the pore that mediates the Ca^{2+}-induced increase in mitochondria permeability has been elucidated only in part; nevertheless, there is a wealth of evidence indicating that high Ca^{2+} concentrations ($[Ca^{2+}]$) induce activation of the permeability transition pore (266, 267). In line with these results, we observed a rapid abrogation of mitochondrial respiration accompanied by a collapse of $\Delta\psi_m$ when isolated skeletal muscle mitochondria were exposed to $[Ca^{2+}]$ comparable to that found in the extracellular environment.

The rationale behind our seemingly trivial experimental question was the widespread media attention gained by mitochondrial transplantation, a therapeutic approach consisting in the injection of autologous skeletal muscle mitochondria into the ischemic myocardium. Although evidence supporting the viability of transplanted mitochondria is still lacking, a single-armed trial was initiated to test this approach in paediatric patients (NCT02851758). Our results confirm that mitochondrial function is irreversibly hampered upon exposure to the millimolar $[Ca^{2+}]$ of the extracellular environment, and raise the question whether the beneficial effects observed in preclinical models of mitochondrial transplantation result from mechanisms other than ATP production from internalized mitochondria, e.g. molecules released from mitochondria during permeability transition.

CaMKII does not control mitochondrial Ca^{2+} uptake in cardiac myocytes

To protect mitochondria from Ca^{2+} overload, Ca^{2+} uptake via the MCU is modulated by the regulatory subunits of the complex, MICU1 and MICU2, which account for the cooperative activation of the MCU at high [Ca^{2+}] and at the same time function as a "gatekeeper", preventing Ca^{2+} accumulation in the matrix at low cytosolic [Ca^{2+}]. An important and so far unresolved question is whether additional mechanisms – such as phosphorylation of the MCU complex by cytosolic kinases – contribute to the regulation of the MCU current. One recent study published in *Nature* reported that the MCU is a target for CaMKII phosphorylation, which increases the MCU current and thus favours Ca^{2+} overload during ischemia/reperfusion injury (171).

In our study, we addressed this question by assessing mitochondrial function in two mouse models of genetic deletion of two major cardiac CaMKII isoforms, and demonstrated that cardiomyocyte-specific CaMKIIδ/γ or global CaMKIIδ knockout are inconsequential for mitochondrial Ca^{2+} uptake, respiration, and metabolic adaptation to elevated cardiac workload. On the one hand, CaMKII gene knockout overcomes the limitations associated with pharmacological CaMKII inhibitors used in previous studies; on the other hand, we did not investigate the consequences of CaMKII deletion in pathological conditions; therefore, it remains to be assessed whether CaMKII modulates MCU activity in response to cardiac stressors, such as ischemia/reperfusion.

Selective NADH communication from α-ketoglutarate dehydrogenase to mitochondrial transhydrogenase prevents reactive oxygen species formation under reducing conditions in the heart

Oxidative stress has been identified as one of the key factors implicated in the progression of heart failure, and mitochondria are considered the main source of reactive oxygen species (ROS) in the heart. ROS formation can take place at virtually any step of electron transfer from Krebs cycle intermediates to oxygen. While the electron transport chain is considered a major source of ROS, the α-ketoglutarate dehydrogenase (α-KGDH) complex also comprises a flavin group that might become a source of ROS. In particular, studies performed in skeletal muscle and brain mitochondria indicate that the ROS formation at the α-KGDH might become the main source of mitochondrial ROS under reducing conditions (5, 196, 197). On the other hand, α-KGDH also provides reducing equivalents to mitochondrial antioxidant systems. In fact, although α-KGDH cannot use $NADP^+$ as an electron acceptor, the NADH derived from the Krebs cycle dehydrogenases can regenerate reduced NADPH via the nicotinamide nucleotide transhydrogenase (NNT) reaction.

Our experiments comparing emission of the ROS hydrogen peroxide (H_2O_2) from NNT-competent or -deficient cardiac mitochondria supplied with either complex I substrates (i.e., pyruvate and malate) or α-KG reveal a privileged communication of the α-KGDH complex with the NNT. This model is supported by the central observation that the complex I inhibition with rotenone exacerbates ROS emission from mitochondria supplied with α-KG only in the absence of a functional NNT. In the presence of the NNT, electrons transported by NADH derived from the α-KGDH reaction can be shuttled to NADPH; without the NNT, NADH can donate electrons uniquely to complex I, and thus its inhibition with rotenone provokes a backup of electrons to O_2 to superoxide. Overall, these results indicate that α-KGDH is a sink, rather than a source of ROS in the heart. Future studies should be aimed to assess the molecular underpinnings of this preferential communication; the shuttling of electrons from α-KG to NADPH might be favoured by the spatial proximity of the α-KGDH complex and the NNT.

Mechano-energetic uncoupling underlies lack of contractile reserve in Barth syndrome cardiomyopathy

Barth syndrome (BTHS) is an X-linked disorder affecting primarily the cardiac and skeletal muscle. In BTHS, loss of the enzyme tafazzin alters the composition of cardiolipin, a phospholipid found in the inner mitochondrial membrane (IMM). The abnormal phospholipid composition of the IMM affects the structural organization of numerous membrane-embedded protein complexes, including the electron transport chain. In a mouse model of BTHS (*Taz*-KD mice) we identified remodeling of the MCU complex with complete abrogation of mitochondrial Ca^{2+} uptake as a primary defect in cardiac, but not skeletal muscle or brain mitochondria. This hinders Ca^{2+} uptake, Ca^{2+}-dependent Krebs cycle activation, and consequently the regeneration of reduced pyridine nucleotides during physiological workload transitions in cardiac myocytes, depleting the intracellular energetic reserve and causing cellular arrhythmias, which can be blunted by inhibiting mitochondrial Ca^{2+} efflux. In contrast to previous studies in cell models of BTHS (87, 99, 103), these defects occur in the absence of any increase of mitochondrial superoxide formation and/or H_2O_2 emission in isolated mitochondria, cardiac myocytes or the heart *in vivo*, and only mild early defects in mitochondrial respiration.

The role of mitochondrial Ca^{2+} uptake in matching metabolic output to cardiac workload by stimulating the activity of Krebs cycle dehydrogenases was first characterized in a series of landmark studies by Brandes and Bers (20). Their experiments demonstrated that the redox state of the mitochondrial pyridine nucleotide pool transiently shifts toward oxidation in response to an increase in energy demand, but this oxidation is rapidly rescued by Ca^{2+} accumulation in the mitochondrial matrix, which stimulates the Krebs cycle to regenerate the reduced forms of NAD^+ and FAD. In contrast, inhibiting the MCU with the ruthenium red derivative Ru360 or accelerating Ca^{2+} efflux from mitochondria by elevating cytosolic sodium leads to net oxidation of the $NADH/NAD^+$ and $FADH_2/FAD$ ratios (30). In recent years, the limitations associated with pharmacological inhibitors of the MCU were overcome by the discovery of the molecular identity of the uniporter (151, 152) and the subsequent development of mouse models in which the gene encoding the MCU pore-forming subunit (MCUa) was selectively deleted in cardiac myocytes (*Mcu*-KO mice) (22, 184). In *Mcu*-KO animals, the delayed metabolic adaptation caused by loss of MCUa abrogates the acute increase in contractile performance induced by isoproterenol infusion *in vivo* (22). In agreement with these studies, MCU deficiency in *Taz*-KD mice causes net oxidation of mitochondrial redox state, and thus prevents adequate delivery of electrons to the ETC, when cardiac myocytes are subjected to an increase in workload.

Overall, our observations confirm the relevance of MCU-dependent Ca^{2+} uptake as a driver of metabolic adaptation during cardiac workload transitions, and identify disruption of the mechano-energetic coupling reserve as a primary defect in BTHS cardiomyopathy. The impaired Ca^{2+}-dependent stimulation of the Krebs cycle oxidizes the redox state of mitochondria, thereby causing cellular arrhythmias, and limits ATP regeneration required for maximal force development. These data provide a mechanistic explanation for two central defects in BTHS cardiomyopathy, i.e. the impaired in contractile reserved during physical exercise and the increased risk of ventricular arrhythmias.

Declaration of Authorship

Statement of individual author contributions and of legal second publication rights

<table>
<tr><td colspan="6">Publication (complete reference): <i>Mitochondria Do Not Survive Calcium Overload During Transplantation</i>. Bertero E, O'Rourke B, Maack C. Circ Res. 2020 Mar 13;126(6):784-786. doi: 10.1161/CIRCRESAHA.119.316291. Epub 2020 Feb 6.</td></tr>
<tr><td>Participated in</td><td colspan="5">Author Initials, Responsibility decreasing from left to right</td></tr>
<tr><td>Study Design
Methods Development</td><td>CM</td><td>EB</td><td>BOR</td><td></td><td></td></tr>
<tr><td>Data Collection</td><td>EB</td><td></td><td></td><td></td><td></td></tr>
<tr><td>Data Analysis and Interpretation</td><td>EB</td><td></td><td></td><td></td><td></td></tr>
<tr><td>Manuscript Writing
Writing of Introduction
Writing of Materials & Methods
Writing of Discussion
Writing of First Draft</td><td>EB (all sections)</td><td>CM (all sections)</td><td></td><td></td><td></td></tr>
</table>

<table>
<tr><td colspan="6">Publication (complete reference): <i>CaMKII does not control mitochondrial Ca^{2+} uptake in cardiac myocytes</i>. Nickel AG*, Kohlhaas M*, Bertero E, Wilhelm D, Wagner M, Sequeira V, Kreusser MM, Dewenter M, Kappl R, Hoth M, Dudek J, Backs J, Maack C. J Physiol. 2020 Apr;598(7):1361-1376. doi: 10.1113/JP276766. Epub 2019 Mar 27.
*equally contributed</td></tr>
<tr><td>Participated in</td><td colspan="5">Author Initials, Responsibility decreasing from left to right</td></tr>
<tr><td>Study Design
Methods Development</td><td>CM</td><td>MK</td><td></td><td></td><td></td></tr>
<tr><td>Data Collection</td><td>AGN</td><td>MK</td><td>DW</td><td>MW</td><td>VS</td></tr>
<tr><td>Data Analysis and Interpretation</td><td>AGN</td><td>MK</td><td>EB</td><td>MW</td><td>VS</td></tr>
<tr><td>Manuscript Writing
Writing of Introduction
Writing of Materials & Methods
Writing of Discussion
Writing of First Draft</td><td>EB (all sections)</td><td>CM (all sections)</td><td></td><td></td><td></td></tr>
</table>

Publication (complete reference): *Selective NADH communication from α-ketoglutarate dehydrogenase to mitochondrial transhydrogenase prevents reactive oxygen species formation under reducing conditions in the heart*. Wagner M*, Bertero E*, Nickel A, Kohlhaas M, Gibson GE, Heggermont W, Heymans S, Maack C. Basic Res Cardiol. 2020 Aug 3;115(5):53. doi: 10.1007/s00395-020-0815-1.

*equally contributed

Participated in	**Author Initials,** Responsibility decreasing from left to right				
Study Design Methods Development	CM	MW			
Data Collection	MW	EB	AN	MK	
Data Analysis and Interpretation	MW	EB	AN	MK	
Manuscript Writing					
Writing of Introduction	EB	CM			
Writing of Materials & Methods	MW	EB			
Writing of Discussion	EB	CM			
Writing of First Draft	EB	MW			

Publication (complete reference): *Mechano-energetic uncoupling underlies lack of contractile reserve in Barth syndrome cardiomyopathy*. Bertero E, Nickel A, Kohlhaas M, Hohl M, Sequeira V, Krug C, Schwemmlein J, Carlein C, Münker K, Atighetchi S, Müller A, Kazakov A, Kappl R, von der Malsburg K, von der Malsburg A, Böhm M, Laufs U, Hoth M, Rehling P, Dudek J, van der Laan M, Prates Roma L, Maack C. Submitted.

Participated in	**Author Initials,** Responsibility decreasing from left to right				
Study Design Methods Development	CM				
Data Collection	MK	AN	MH	EB	
Data Analysis and Interpretation	AN	MK	EB	MH	
Manuscript Writing					
Writing of Introduction	EB	CM			
Writing of Materials & Methods	EB	AN	MK	CM	
Writing of Discussion	EB	CM			
Writing of First Draft	EB	AN	MK		

The doctoral researcher confirms that she/he has obtained permission from both the publishers and the co-authors for legal second publication.

The doctoral researcher and the primary supervisor confirm the correctness of the above mentioned assessment.

Edoardo Bertero		Genova	
Doctoral Researcher’s Name	Date	Place	Signature

Prof. Dr. Christoph Maack		Würzburg	
Primary Supervisor’s Name	Date	Place	Signature

Statement of individual author contributions to figures/tables/chapters included in the manuscripts

Publication (complete reference): *Mitochondria Do Not Survive Calcium Overload During Transplantation*. Bertero E, O'Rourke B, Maack C. Circ Res. 2020 Mar 13;126(6):784-786. doi: 10.1161/CIRCRESAHA.119.316291. Epub 2020 Feb 6.

Figure	**Author Initials,** Responsibility decreasing from left to right				
1	EB				

Publication (complete reference): *CaMKII does not control mitochondrial Ca^{2+} uptake in cardiac myocytes*. Nickel AG*, Kohlhaas M*, Bertero E, Wilhelm D, Wagner M, Sequeira V, Kreusser MM, Dewenter M, Kappl R, Hoth M, Dudek J, Backs J, Maack C. J Physiol. 2020 Apr;598(7):1361-1376. doi: 10.1113/JP276766. Epub 2019 Mar 27.

*equally contributed

Figure	**Author Initials,** Responsibility decreasing from left to right				
1	AN				
2	MK				
3	MK				
4	AN				
5	MK				
6	AN				
7	EB	MK			

Explanations: the Doctoral Researcher also contributed to this study with experiments that were not included in the final version, but only in the rebuttal letter.

Publication (complete reference): *Selective NADH communication from α-ketoglutarate dehydrogenase to mitochondrial transhydrogenase prevents reactive oxygen species formation under reducing conditions in the heart*. Wagner M*, Bertero E*, Nickel A, Kohlhaas M, Gibson GE, Heggermont W, Heymans S, Maack C. Basic Res Cardiol. 2020 Aug 3;115(5):53. doi: 10.1007/s00395-020-0815-1.

*equally contributed

Figure	**Author Initials,** Responsibility decreasing from left to right				
1	EB and MW				
2	EB and MW				
3	MW	AN			
4	MW	AN			
5	MW	MK			

Explanations (if applicable): the Doctoral Researcher also contributed to this study with experiments that were not included in the final version, but only in the rebuttal letter.

Publication (complete reference): *Mechano-energetic uncoupling underlies lack of contractile reserve in Barth syndrome cardiomyopathy*. Bertero E, Nickel A, Kohlhaas M, Hohl M, Sequeira V, Krug C, Schwemmlein J, Carlein C, Münker K, Atighetchi S, Müller A, Kazakov A, Kappl R, von der Malsburg K, von der Malsburg A, Böhm M, Laufs U, Hoth M, Rehling P, Dudek J, van der Laan M, Prates Roma L, Maack C. Submitted.					
Figure	**Author Initials,** Responsibility decreasing from left to right				
1	EB	AM	MH	AK	
2	CK	EB	JS	VS	MK
3	AN	KvdM	AvdM	EB	
4	MH	AN	JD		
5	EB	MK	CK		
6	MH	CC	CK	AN	
7	MK	JS			
S1	EB	MH			
S2	EB				
S3	AN	KM	SA		
S4	AN	KM	SA	KvdM	AvdM
S5	MH	AN	KvdM	AvdM	
S6	EB	CK			

I also confirm my primary supervisor's acceptance.

Edoardo Bertero Genova

Doctoral Researcher's Name Date Place Signature

Affidavit

I hereby confirm that my thesis entitled “*Mechano-energetic uncoupling in Barth syndrome cardiomyopathy*” is the result of my own work. I did not receive any help or support from commercial consultants. All sources and/or materials applied are listed and specified in the thesis.

Furthermore, I confirm that this thesis has not yet been submitted as part of another examination process neither in identical nor in similar form.

Place, date	Signature

Eidesstattliche Erklärung

Hiermit erkläre ich an Eides statt, die Dissertation „*Mechano-energetische Entkopplung bei der Barth Syndrom Kardiomyopathie*“ eigenständig, d.h. insbesondere selbständig und ohne Hilfe eines kommerziellen Promotionsberaters, angefertigt und keine anderen als die von mir angegeben Quellen und Hilfsmittel verwendet zu haben.

Ich erkläre außerdem, dass die Dissertation weder in gleicher noch in ähnlicher Form bereits in einem anderen Prüfungsverfahren vorgelegen hat.

Ort, Datum	Unterschrift

Acknowledgements

A huge thank you goes to all of my colleagues, for their continuous guidance and the great time we had together. First, my gratitude goes to the people I met in Homburg: Alexander Dietl, Michelle Gulentz, Mathias Hohl, Michael Kohlhaas, Alexander Nickel, Nina Schnellbach, and Michael Wagner. They made my first time in Germany an incredible experience and it wasn’t long before I decided to come back!

In Würzburg I saw our laboratory scale up to a large family of people, and I am deeply in depth with all of them: Khaled Alhussini, Berkan Arslan, Annette Berbner, Antonella Cellini, Elisabeth Danner, Jan Dudek, Manuela Erk, Kira Geiger, Mona Goebel, Marija Grgic, Annette Herrmann, Ilona Kutschka, Anne Neumaier, Jovana Nikolic, Kathrin Renoth, Anja Sauer, Julia Schwemmlein, Isabelle Simon, Christina Wasmus, Hannah Weiß, David Weissman, and Jana Werner.

A special thanks goes to my friends Vasco Sequeira and Anton Xu. The time I spent with you was always invaluable, and I think I was really blessed to meet you. Finally, the biggest thank you goes to Christoph Maack. A mentor, and a friend. May our paths meet again one day. *Aller guten Dinge sind drei!*

Bibliography

1. Mitchell P. Coupling of phosphorylation to electron and hydrogen transfer by a chemi-osmotic type of mechanism. *Nature.* 1961;191:144-8.
2. Pfeiffer K, Gohil V, Stuart RA, Hunte C, Brandt U, Greenberg ML, et al. Cardiolipin stabilizes respiratory chain supercomplexes. *J Biol Chem.* 2003;278(52):52873-80.
3. Murphy MP. How mitochondria produce reactive oxygen species. *Biochem J.* 2009;417(1):1-13.
4. Chouchani ET, Pell VR, Gaude E, Aksentijevic D, Sundier SY, Robb EL, et al. Ischaemic accumulation of succinate controls reperfusion injury through mitochondrial ROS. *Nature.* 2014;515(7527):431-5.
5. Quinlan CL, Goncalves RL, Hey-Mogensen M, Yadava N, Bunik VI, and Brand MD. The 2-oxoacid dehydrogenase complexes in mitochondria can produce superoxide/hydrogen peroxide at much higher rates than complex I. *The Journal of biological chemistry.* 2014;289(12):8312-25.
6. Rindler PM, Cacciola A, Kinter M, and Szweda LI. Catalase-dependent H2O2 consumption by cardiac mitochondria and redox-mediated loss in insulin signaling. *American journal of physiology Heart and circulatory physiology.* 2016;311(5):H1091-h6.
7. Kirkman HN, and Gaetani GF. Catalase: a tetrameric enzyme with four tightly bound molecules of NADPH. *Proceedings of the National Academy of Sciences of the United States of America.* 1984;81(14):4343-7.
8. Bertero E, and Maack C. Calcium Signaling and Reactive Oxygen Species in Mitochondria. *Circ Res.* 2018;122(10):1460-78.
9. Aon MA, Cortassa S, and O'Rourke B. Redox-optimized ROS balance: a unifying hypothesis. *Biochim Biophys Acta.* 2010;1797(6-7):865-77.
10. Lopaschuk GD, Ussher JR, Folmes CD, Jaswal JS, and Stanley WC. Myocardial fatty acid metabolism in health and disease. *Physiol Rev.* 2010;90(1):207-58.
11. Stanley WC, Recchia FA, and Lopaschuk GD. Myocardial substrate metabolism in the normal and failing heart. *Physiol Rev.* 2005;85(3):1093-129.
12. Murashige D, Jang C, Neinast M, Edwards JJ, Cowan A, Hyman MC, et al. Comprehensive quantification of fuel use by the failing and nonfailing human heart. *Science.* 2020;370(6514):364-8.
13. Bedi KC, Jr., Snyder NW, Brandimarto J, Aziz M, Mesaros C, Worth AJ, et al. Evidence for Intramyocardial Disruption of Lipid Metabolism and Increased Myocardial Ketone Utilization in Advanced Human Heart Failure. *Circulation.* 2016;133(8):706-16.
14. Mizuno Y, Harada E, Nakagawa H, Morikawa Y, Shono M, Kugimiya F, et al. The diabetic heart utilizes ketone bodies as an energy source. *Metabolism.* 2017;77:65-72.
15. Voros G, Ector J, Garweg C, Droogne W, Van Cleemput J, Peersman N, et al. Increased Cardiac Uptake of Ketone Bodies and Free Fatty Acids in Human Heart Failure and Hypertrophic Left Ventricular Remodeling. *Circ Heart Fail.* 2018;11(12):e004953.
16. Bertero E, and Maack C. Metabolic remodelling in heart failure. *Nat Rev Cardiol.* 2018;15(8):457-70.
17. Bers DM. Cardiac excitation-contraction coupling. *Nature.* 2002;415(6868):198-205.
18. Eisner DA, Caldwell JL, Kistamas K, and Trafford AW. Calcium and Excitation-Contraction Coupling in the Heart. *Circ Res.* 2017;121(2):181-95.
19. Li L, Desantiago J, Chu G, Kranias EG, and Bers DM. Phosphorylation of phospholamban and troponin I in beta-adrenergic-induced acceleration of cardiac relaxation. *Am J Physiol Heart Circ Physiol.* 2000;278(3):H769-79.
20. Brandes R, and Bers DM. Intracellular Ca2+ increases the mitochondrial NADH concentration during elevated work in intact cardiac muscle. *Circulation research.* 1997;80(1):82-7.

21. Marinelli F, Almagor L, Hiller R, Giladi M, Khananshvili D, and Faraldo-Gomez JD. Sodium recognition by the Na+/Ca2+ exchanger in the outward-facing conformation. *Proc Natl Acad Sci U S A.* 2014;111(50):E5354-62.
22. Luongo TS, Lambert JP, Yuan A, Zhang X, Gross P, Song J, et al. The Mitochondrial Calcium Uniporter Matches Energetic Supply with Cardiac Workload during Stress and Modulates Permeability Transition. *Cell reports.* 2015;12(1):23-34.
23. Kirichok Y, Krapivinsky G, and Clapham DE. The mitochondrial calcium uniporter is a highly selective ion channel. *Nature.* 2004;427(6972):360-4.
24. Rizzuto R, Pinton P, Carrington W, Fay FS, Fogarty KE, Lifshitz LM, et al. Close contacts with the endoplasmic reticulum as determinants of mitochondrial Ca2+ responses. *Science.* 1998;280(5370):1763-6.
25. de Brito OM, and Scorrano L. Mitofusin 2 tethers endoplasmic reticulum to mitochondria. *Nature.* 2008;456(7222):605-10.
26. Wu S, Lu Q, Wang Q, Ding Y, Ma Z, Mao X, et al. Binding of FUN14 Domain Containing 1 With Inositol 1,4,5-Trisphosphate Receptor in Mitochondria-Associated Endoplasmic Reticulum Membranes Maintains Mitochondrial Dynamics and Function in Hearts in Vivo. *Circulation.* 2017;136(23):2248-66.
27. Chen Y, Csordas G, Jowdy C, Schneider TG, Csordas N, Wang W, et al. Mitofusin 2-containing mitochondrial-reticular microdomains direct rapid cardiomyocyte bioenergetic responses via interorganelle Ca(2+) crosstalk. *Circ Res.* 2012;111(7):863-75.
28. Filadi R, Greotti E, Turacchio G, Luini A, Pozzan T, and Pizzo P. Mitofusin 2 ablation increases endoplasmic reticulum-mitochondria coupling. *Proc Natl Acad Sci U S A.* 2015;112(17):E2174-81.
29. Milani-Nejad N, and Janssen PM. Small and large animal models in cardiac contraction research: advantages and disadvantages. *Pharmacol Ther.* 2014;141(3):235-49.
30. Maack C, Cortassa S, Aon MA, Ganesan AN, Liu T, and O'Rourke B. Elevated cytosolic Na+ decreases mitochondrial Ca2+ uptake during excitation-contraction coupling and impairs energetic adaptation in cardiac myocytes. *Circ Res.* 2006;99(2):172-82.
31. Ponikowski P, Voors AA, Anker SD, Bueno H, Cleland JGF, Coats AJS, et al. 2016 ESC Guidelines for the diagnosis and treatment of acute and chronic heart failure: The Task Force for the diagnosis and treatment of acute and chronic heart failure of the European Society of Cardiology (ESC)Developed with the special contribution of the Heart Failure Association (HFA) of the ESC. *Eur Heart J.* 2016;37(27):2129-200.
32. Bonow RO, Mann D, Zipes D, and Libby P. *Braunwald's Heart Disease: A Textbook of Cardiovascular Medicine.* Saunders; 2011.
33. Hobai IA, and O'Rourke B. Decreased sarcoplasmic reticulum calcium content is responsible for defective excitation-contraction coupling in canine heart failure. *Circulation.* 2001;103(11):1577-84.
34. Bers DM. Altered cardiac myocyte Ca regulation in heart failure. *Physiology (Bethesda).* 2006;21:380-7.
35. Schwinger RH, Wang J, Frank K, Muller-Ehmsen J, Brixius K, McDonough AA, et al. Reduced sodium pump alpha1, alpha3, and beta1-isoform protein levels and Na+,K+-ATPase activity but unchanged Na+-Ca2+ exchanger protein levels in human heart failure. *Circulation.* 1999;99(16):2105-12.
36. Baartscheer A, Schumacher CA, van Borren MM, Belterman CN, Coronel R, and Fiolet JW. Increased Na+/H+-exchange activity is the cause of increased [Na+]i and underlies disturbed calcium handling in the rabbit pressure and volume overload heart failure model. *Cardiovasc Res.* 2003;57(4):1015-24.
37. Valdivia CR, Chu WW, Pu J, Foell JD, Haworth RA, Wolff MR, et al. Increased late sodium current in myocytes from a canine heart failure model and from failing human heart. *J Mol Cell Cardiol.* 2005;38(3):475-83.
38. Armoundas AA, Hobai IA, Tomaselli GF, Winslow RL, and O'Rourke B. Role of sodium-calcium exchanger in modulating the action potential of ventricular myocytes from normal and failing hearts. *Circ Res.* 2003;93(1):46-53.

39. Weber CR, Piacentino V, 3rd, Houser SR, and Bers DM. Dynamic regulation of sodium/calcium exchange function in human heart failure. *Circulation.* 2003;108(18):2224-9.
40. Pieske B, Maier LS, Piacentino V, 3rd, Weisser J, Hasenfuss G, and Houser S. Rate dependence of [Na+]i and contractility in nonfailing and failing human myocardium. *Circulation.* 2002;106(4):447-53.
41. Weisser-Thomas J, Piacentino V, 3rd, Gaughan JP, Margulies K, and Houser SR. Calcium entry via Na/Ca exchange during the action potential directly contributes to contraction of failing human ventricular myocytes. *Cardiovasc Res.* 2003;57(4):974-85.
42. Li Q, Su D, O'Rourke B, Pogwizd SM, and Zhou L. Mitochondria-derived ROS bursts disturb Ca(2)(+) cycling and induce abnormal automaticity in guinea pig cardiomyocytes: a theoretical study. *Am J Physiol Heart Circ Physiol.* 2015;308(6):H623-36.
43. Kohlhaas M, and Maack C. Adverse bioenergetic consequences of Na+-Ca2+ exchanger-mediated Ca2+ influx in cardiac myocytes. *Circulation.* 2010;122(22):2273-80.
44. Michels G, Khan IF, Endres-Becker J, Rottlaender D, Herzig S, Ruhparwar A, et al. Regulation of the human cardiac mitochondrial Ca2+ uptake by 2 different voltage-gated Ca2+ channels. *Circulation.* 2009;119(18):2435-43.
45. Pinali C, Bennett H, Davenport JB, Trafford AW, and Kitmitto A. Three-dimensional reconstruction of cardiac sarcoplasmic reticulum reveals a continuous network linking transverse-tubules: this organization is perturbed in heart failure. *Circ Res.* 2013;113(11):1219-30.
46. Kohlhaas M, Liu T, Knopp A, Zeller T, Ong MF, Bohm M, et al. Elevated cytosolic Na+ increases mitochondrial formation of reactive oxygen species in failing cardiac myocytes. *Circulation.* 2010;121(14):1606-13.
47. Nickel AG, von Hardenberg A, Hohl M, Loffler JR, Kohlhaas M, Becker J, et al. Reversal of Mitochondrial Transhydrogenase Causes Oxidative Stress in Heart Failure. *Cell Metab.* 2015;22(3):472-84.
48. Neubauer S. The failing heart--an engine out of fuel. *N Engl J Med.* 2007;356(11):1140-51.
49. McMurray J, Chopra M, Abdullah I, Smith WE, and Dargie HJ. Evidence of oxidative stress in chronic heart failure in humans. *Eur Heart J.* 1993;14(11):1493-8.
50. Barth PG, Van den Bogert C, Bolhuis PA, Scholte HR, van Gennip AH, Schutgens RB, et al. X-linked cardioskeletal myopathy and neutropenia (Barth syndrome): respiratory-chain abnormalities in cultured fibroblasts. *J Inherit Metab Dis.* 1996;19(2):157-60.
51. Barth PG, Scholte HR, Berden JA, Van der Klei-Van Moorsel JM, Luyt-Houwen IE, Van 't Veer-Korthof ET, et al. An X-linked mitochondrial disease affecting cardiac muscle, skeletal muscle and neutrophil leucocytes. *J Neurol Sci.* 1983;62(1-3):327-55.
52. Bione S, D'Adamo P, Maestrini E, Gedeon AK, Bolhuis PA, and Toniolo D. A novel X-linked gene, G4.5. is responsible for Barth syndrome. *Nat Genet.* 1996;12(4):385-9.
53. Houtkooper RH, Turkenburg M, Poll-The BT, Karall D, Perez-Cerda C, Morrone A, et al. The enigmatic role of tafazzin in cardiolipin metabolism. *Biochim Biophys Acta.* 2009;1788(10):2003-14.
54. Lecocq J, and Ballou CE. On the Structure of Cardiolipin. *Biochemistry.* 1964;3:976-80.
55. Ikon N, and Ryan RO. Cardiolipin and mitochondrial cristae organization. *Biochim Biophys Acta Biomembr.* 2017;1859(6):1156-63.
56. Schlame M, and Haldar D. Cardiolipin is synthesized on the matrix side of the inner membrane in rat liver mitochondria. *J Biol Chem.* 1993;268(1):74-9.
57. Houtkooper RH, Rodenburg RJ, Thiels C, van Lenthe H, Stet F, Poll-The BT, et al. Cardiolipin and monolysocardiolipin analysis in fibroblasts, lymphocytes, and tissues using high-performance liquid chromatography-mass spectrometry as a diagnostic test for Barth syndrome. *Anal Biochem.* 2009;387(2):230-7.
58. Hoch FL. Cardiolipins and biomembrane function. *Biochim Biophys Acta.* 1992;1113(1):71-133.

59. Schlame M, Kelley RI, Feigenbaum A, Towbin JA, Heerdt PM, Schieble T, et al. Phospholipid abnormalities in children with Barth syndrome. *Journal of the American College of Cardiology.* 2003;42(11):1994-9.
60. Kulik W, van Lenthe H, Stet FS, Houtkooper RH, Kemp H, Stone JE, et al. Bloodspot assay using HPLC-tandem mass spectrometry for detection of Barth syndrome. *Clin Chem.* 2008;54(2):371-8.
61. Bertero E, Kutschka I, Maack C, and Dudek J. Cardiolipin remodeling in Barth syndrome and other hereditary cardiomyopathies. *Biochim Biophys Acta Mol Basis Dis.* 2020;1866(8):165803.
62. Dudek J, Cheng IF, Balleininger M, Vaz FM, Streckfuss-Bomeke K, Hubscher D, et al. Cardiolipin deficiency affects respiratory chain function and organization in an induced pluripotent stem cell model of Barth syndrome. *Stem Cell Res.* 2013;11(2):806-19.
63. Chatzispyrou IA, Guerrero-Castillo S, Held NM, Ruiter JPN, Denis SW, L IJ, et al. Barth syndrome cells display widespread remodeling of mitochondrial complexes without affecting metabolic flux distribution. *Biochim Biophys Acta Mol Basis Dis.* 2018;1864(11):3650-8.
64. Dudek J, Cheng IF, Chowdhury A, Wozny K, Balleininger M, Reinhold R, et al. Cardiac-specific succinate dehydrogenase deficiency in Barth syndrome. *EMBO Mol Med.* 2016;8(2):139-54.
65. Li Y, Lou W, Raja V, Denis S, Yu W, Schmidtke MW, et al. Cardiolipin-induced activation of pyruvate dehydrogenase links mitochondrial lipid biosynthesis to TCA cycle function. *J Biol Chem.* 2019;294(30):11568-78.
66. Malhotra K, Modak A, Nangia S, Daman TH, Gunsel U, Robinson VL, et al. Cardiolipin mediates membrane and channel interactions of the mitochondrial TIM23 protein import complex receptor Tim50. *Sci Adv.* 2017;3(9):e1700532.
67. Francy CA, Clinton RW, Frohlich C, Murphy C, and Mears JA. Cryo-EM Studies of Drp1 Reveal Cardiolipin Interactions that Activate the Helical Oligomer. *Sci Rep.* 2017;7(1):10744.
68. Ban T, Ishihara T, Kohno H, Saita S, Ichimura A, Maenaka K, et al. Molecular basis of selective mitochondrial fusion by heterotypic action between OPA1 and cardiolipin. *Nat Cell Biol.* 2017;19(7):856-63.
69. Anton Z, Landajuela A, Hervas JH, Montes LR, Hernandez-Tiedra S, Velasco G, et al. Human Atg8-cardiolipin interactions in mitophagy: Specific properties of LC3B, GABARAPL2 and GABARAP. *Autophagy.* 2016;12(12):2386-403.
70. Lutter M, Fang M, Luo X, Nishijima M, Xie X, and Wang X. Cardiolipin provides specificity for targeting of tBid to mitochondria. *Nat Cell Biol.* 2000;2(10):754-61.
71. Tamura Y, Harada Y, Yamano K, Watanabe K, Ishikawa D, Ohshima C, et al. Identification of Tam41 maintaining integrity of the TIM23 protein translocator complex in mitochondria. *J Cell Biol.* 2006;174(5):631-7.
72. Frazier AE, Dudek J, Guiard B, Voos W, Li Y, Lind M, et al. Pam16 has an essential role in the mitochondrial protein import motor. *Nat Struct Mol Biol.* 2004;11(3):226-33.
73. Truscott KN, Voos W, Frazier AE, Lind M, Li Y, Geissler A, et al. A J-protein is an essential subunit of the presequence translocase-associated protein import motor of mitochondria. *J Cell Biol.* 2003;163(4):707-13.
74. Choi SY, Huang P, Jenkins GM, Chan DC, Schiller J, and Frohman MA. A common lipid links Mfn-mediated mitochondrial fusion and SNARE-regulated exocytosis. *Nat Cell Biol.* 2006;8(11):1255-62.
75. DeVay RM, Dominguez-Ramirez L, Lackner LL, Hoppins S, Stahlberg H, and Nunnari J. Coassembly of Mgm1 isoforms requires cardiolipin and mediates mitochondrial inner membrane fusion. *J Cell Biol.* 2009;186(6):793-803.
76. Huang KC, Mukhopadhyay R, and Wingreen NS. A curvature-mediated mechanism for localization of lipids to bacterial poles. *PLoS Comput Biol.* 2006;2(11):e151.
77. Rampelt H, Wollweber F, Gerke C, de Boer R, van der Klei IJ, Bohnert M, et al. Assembly of the Mitochondrial Cristae Organizer Mic10 Is Regulated by Mic26-Mic27 Antagonism and Cardiolipin. *J Mol Biol.* 2018;430(13):1883-90.

78. McKenzie M, Lazarou M, Thorburn DR, and Ryan MT. Mitochondrial respiratory chain supercomplexes are destabilized in Barth Syndrome patients. *J Mol Biol.* 2006;361(3):462-9.
79. Fry M, and Green DE. Cardiolipin requirement for electron transfer in complex I and III of the mitochondrial respiratory chain. *J Biol Chem.* 1981;256(4):1874-80.
80. Beyer K, and Nuscher B. Specific cardiolipin binding interferes with labeling of sulfhydryl residues in the adenosine diphosphate/adenosine triphosphate carrier protein from beef heart mitochondria. *Biochemistry.* 1996;35(49):15784-90.
81. Noel H, and Pande SV. An essential requirement of cardiolipin for mitochondrial carnitine acylcarnitine translocase activity. Lipid requirement of carnitine acylcarnitine translocase. *Eur J Biochem.* 1986;155(1):99-102.
82. Chu CT, Ji J, Dagda RK, Jiang JF, Tyurina YY, Kapralov AA, et al. Cardiolipin externalization to the outer mitochondrial membrane acts as an elimination signal for mitophagy in neuronal cells. *Nat Cell Biol.* 2013;15(10):1197-205.
83. Petrosillo G, Casanova G, Matera M, Ruggiero FM, and Paradies G. Interaction of peroxidized cardiolipin with rat-heart mitochondrial membranes: induction of permeability transition and cytochrome c release. *FEBS Lett.* 2006;580(27):6311-6.
84. Hanske J, Toffey JR, Morenz AM, Bonilla AJ, Schiavoni KH, and Pletneva EV. Conformational properties of cardiolipin-bound cytochrome c. *Proc Natl Acad Sci U S A.* 2012;109(1):125-30.
85. Sorice M, Circella A, Cristea IM, Garofalo T, Di Renzo L, Alessandri C, et al. Cardiolipin and its metabolites move from mitochondria to other cellular membranes during death receptor-mediated apoptosis. *Cell Death Differ.* 2004;11(10):1133-45.
86. Lovell JF, Billen LP, Bindner S, Shamas-Din A, Fradin C, Leber B, et al. Membrane binding by tBid initiates an ordered series of events culminating in membrane permeabilization by Bax. *Cell.* 2008;135(6):1074-84.
87. Wang G, McCain ML, Yang L, He A, Pasqualini FS, Agarwal A, et al. Modeling the mitochondrial cardiomyopathy of Barth syndrome with induced pluripotent stem cell and heart-on-chip technologies. *Nature medicine.* 2014;20(6):616-23.
88. Acehan D, Vaz F, Houtkooper RH, James J, Moore V, Tokunaga C, et al. Cardiac and skeletal muscle defects in a mouse model of human Barth syndrome. *J Biol Chem.* 2011;286(2):899-908.
89. Huang Y, Powers C, Madala SK, Greis KD, Haffey WD, Towbin JA, et al. Cardiac metabolic pathways affected in the mouse model of barth syndrome. *PloS one.* 2015;10(6):e0128561.
90. Kim J, Lee K, Fujioka H, Tandler B, and Hoppel CL. Cardiac mitochondrial structure and function in tafazzin-knockdown mice. *Mitochondrion.* 2018;43:53-62.
91. Powers C, Huang Y, Strauss A, and Khuchua Z. Diminished Exercise Capacity and Mitochondrial bc1 Complex Deficiency in Tafazzin-Knockdown Mice. *Frontiers in physiology.* 2013;4:74.
92. Soustek MS, Falk DJ, Mah CS, Toth MJ, Schlame M, Lewin AS, et al. Characterization of a transgenic short hairpin RNA-induced murine model of Tafazzin deficiency. *Hum Gene Ther.* 2011;22(7):865-71.
93. Johnson JM, Ferrara PJ, Verkerke ARP, Coleman CB, Wentzler EJ, Neufer PD, et al. Targeted overexpression of catalase to mitochondria does not prevent cardioskeletal myopathy in Barth syndrome. *J Mol Cell Cardiol.* 2018;121:94-102.
94. Phoon CK, Acehan D, Schlame M, Stokes DL, Edelman-Novemsky I, Yu D, et al. Tafazzin knockdown in mice leads to a developmental cardiomyopathy with early diastolic dysfunction preceding myocardial noncompaction. *J Am Heart Assoc.* 2012;1(2).
95. Kiebish MA, Yang K, Liu X, Mancuso DJ, Guan S, Zhao Z, et al. Dysfunctional cardiac mitochondrial bioenergetic, lipidomic, and signaling in a murine model of Barth syndrome. *J Lipid Res.* 2013;54(5):1312-25.
96. Le CH, Benage LG, Specht KS, Li Puma LC, Mulligan CM, Heuberger AL, et al. Tafazzin deficiency impairs CoA-dependent oxidative metabolism in cardiac mitochondria. *J Biol Chem.* 2020;295(35):12485-97.

97. Goncalves RLS, Schlame M, Bartelt A, Brand MD, and Hotamisligil GS. Cardiolipin deficiency in Barth syndrome is not associated with increased superoxide/H2 O2 production in heart and skeletal muscle mitochondria. *FEBS Lett.* 2020.

98. Suzuki-Hatano S, Sriramvenugopal M, Ramanathan M, Soustek M, Byrne BJ, Cade WT, et al. Increased mtDNA Abundance and Improved Function in Human Barth Syndrome Patient Fibroblasts Following AAV-TAZ Gene Delivery. *Int J Mol Sci.* 2019;20(14).

99. Chowdhury A, Aich A, Jain G, Wozny K, Luchtenborg C, Hartmann M, et al. Defective Mitochondrial Cardiolipin Remodeling Dampens HIF-1alpha Expression in Hypoxia. *Cell reports.* 2018;25(3):561-70 e6.

100. He Q, Wang M, Harris N, and Han X. Tafazzin knockdown interrupts cell cycle progression in cultured neonatal ventricular fibroblasts. *Am J Physiol Heart Circ Physiol.* 2013;305(9):H1332-43.

101. Valianpour F, Mitsakos V, Schlemmer D, Towbin JA, Taylor JM, Ekert PG, et al. Monolysocardiolipins accumulate in Barth syndrome but do not lead to enhanced apoptosis. *J Lipid Res.* 2005;46(6):1182-95.

102. Xu Y, Sutachan JJ, Plesken H, Kelley RI, and Schlame M. Characterization of lymphoblast mitochondria from patients with Barth syndrome. *Lab Invest.* 2005;85(6):823-30.

103. Gonzalvez F, D'Aurelio M, Boutant M, Moustapha A, Puech JP, Landes T, et al. Barth syndrome: cellular compensation of mitochondrial dysfunction and apoptosis inhibition due to changes in cardiolipin remodeling linked to tafazzin (TAZ) gene mutation. *Biochim Biophys Acta.* 2013;1832(8):1194-206.

104. Gonzalvez F, Schug ZT, Houtkooper RH, MacKenzie ED, Brooks DG, Wanders RJ, et al. Cardiolipin provides an essential activating platform for caspase-8 on mitochondria. *J Cell Biol.* 2008;183(4):681-96.

105. Mejia EM, Zegallai H, Bouchard ED, Banerji V, Ravandi A, and Hatch GM. Expression of human monolysocardiolipin acyltransferase-1 improves mitochondrial function in Barth syndrome lymphoblasts. *J Biol Chem.* 2018;293(20):7564-77.

106. He Q, Harris N, Ren J, and Han X. Mitochondria-targeted antioxidant prevents cardiac dysfunction induced by tafazzin gene knockdown in cardiac myocytes. *Oxid Med Cell Longev.* 2014;2014:654198.

107. Li Y, Lou W, Grevel A, Bottinger L, Liang Z, Ji J, et al. Cardiolipin-deficient cells have decreased levels of the iron-sulfur biogenesis protein frataxin. *J Biol Chem.* 2020;295(33):11928-37.

108. Fatica EM, DeLeonibus GA, House A, Kodger JV, Pearce RW, Shah RR, et al. Barth Syndrome: Exploring Cardiac Metabolism with Induced Pluripotent Stem Cell-Derived Cardiomyocytes. *Metabolites.* 2019;9(12).

109. Malhotra A, Edelman-Novemsky I, Xu Y, Plesken H, Ma J, Schlame M, et al. Role of calcium-independent phospholipase A2 in the pathogenesis of Barth syndrome. *Proc Natl Acad Sci U S A.* 2009;106(7):2337-41.

110. Khuchua Z, Yue Z, Batts L, and Strauss AW. A zebrafish model of human Barth syndrome reveals the essential role of tafazzin in cardiac development and function. *Circulation research.* 2006;99(2):201-8.

111. Soustek MS, Baligand C, Falk DJ, Walter GA, Lewin AS, and Byrne BJ. Endurance training ameliorates complex 3 deficiency in a mouse model of Barth syndrome. *J Inherit Metab Dis.* 2015;38(5):915-22.

112. Schafer C, Moore V, Dasgupta N, Javadov S, James JF, Glukhov AI, et al. The Effects of PPAR Stimulation on Cardiac Metabolic Pathways in Barth Syndrome Mice. *Front Pharmacol.* 2018;9:318.

113. Suzuki-Hatano S, Saha M, Rizzo SA, Witko RL, Gosiker BJ, Ramanathan M, et al. AAV-Mediated TAZ Gene Replacement Restores Mitochondrial and Cardioskeletal Function in Barth Syndrome. *Hum Gene Ther.* 2019;30(2):139-54.

114. Suzuki-Hatano S, Saha M, Soustek MS, Kang PB, Byrne BJ, Cade WT, et al. AAV9-TAZ Gene Replacement Ameliorates Cardiac TMT Proteomic Profiles in a Mouse Model of Barth Syndrome. *Mol Ther Methods Clin Dev.* 2019;13:167-79.

115. Cole LK, Mejia EM, Sparagna GC, Vandel M, Xiang B, Han X, et al. Cardiolipin deficiency elevates susceptibility to a lipotoxic hypertrophic cardiomyopathy. *J Mol Cell Cardiol.* 2020;144:24-34.

116. Wang S, Li Y, Xu Y, Ma Q, Lin Z, Schlame M, et al. AAV Gene Therapy Prevents and Reverses Heart Failure in a Murine Knockout Model of Barth Syndrome. *Circ Res.* 2020;126(8):1024-39.

117. Cosson L, Toutain A, Simard G, Kulik W, Matyas G, Guichet A, et al. Barth syndrome in a female patient. *Mol Genet Metab.* 2012;106(1):115-20.

118. Spencer CT, Bryant RM, Day J, Gonzalez IL, Colan SD, Thompson WR, et al. Cardiac and clinical phenotype in Barth syndrome. *Pediatrics.* 2006;118(2):e337-46.

119. Spencer CT, Byrne BJ, Bryant RM, Margossian R, Maisenbacher M, Breitenger P, et al. Impaired cardiac reserve and severely diminished skeletal muscle O(2) utilization mediate exercise intolerance in Barth syndrome. *American journal of physiology Heart and circulatory physiology.* 2011;301(5):H2122-9.

120. Spencer CT, Byrne BJ, Gewitz MH, Wechsler SB, Kao AC, Gerstenfeld EP, et al. Ventricular arrhythmia in the X-linked cardiomyopathy Barth syndrome. *Pediatr Cardiol.* 2005;26(5):632-7.

121. Cade WT, Bohnert KL, Peterson LR, Patterson BW, Bittel AJ, Okunade AL, et al. Blunted fat oxidation upon submaximal exercise is partially compensated by enhanced glucose metabolism in children, adolescents, and young adults with Barth syndrome. *J Inherit Metab Dis.* 2019;42(3):480-93.

122. Roberts AE, Nixon C, Steward CG, Gauvreau K, Maisenbacher M, Fletcher M, et al. The Barth Syndrome Registry: distinguishing disease characteristics and growth data from a longitudinal study. *Am J Med Genet A.* 2012;158A(11):2726-32.

123. Kelley RI, Cheatham JP, Clark BJ, Nigro MA, Powell BR, Sherwood GW, et al. X-linked dilated cardiomyopathy with neutropenia, growth retardation, and 3-methylglutaconic aciduria. *J Pediatr.* 1991;119(5):738-47.

124. Finsterer J. Barth syndrome: mechanisms and management. *Appl Clin Genet.* 2019;12:95-106.

125. Wortmann SB, Duran M, Anikster Y, Barth PG, Sperl W, Zschocke J, et al. Inborn errors of metabolism with 3-methylglutaconic aciduria as discriminative feature: proper classification and nomenclature. *J Inherit Metab Dis.* 2013;36(6):923-8.

126. Vernon HJ, Sandlers Y, McClellan R, and Kelley RI. Clinical laboratory studies in Barth Syndrome. *Mol Genet Metab.* 2014;112(2):143-7.

127. Christodoulou J, McInnes RR, Jay V, Wilson G, Becker LE, Lehotay DC, et al. Barth syndrome: clinical observations and genetic linkage studies. *Am J Med Genet.* 1994;50(3):255-64.

128. Toye AA, Lippiat JD, Proks P, Shimomura K, Bentley L, Hugill A, et al. A genetic and physiological study of impaired glucose homeostasis control in C57BL/6J mice. *Diabetologia.* 2005;48(4):675-86.

129. Backs J, Backs T, Neef S, Kreusser MM, Lehmann LH, Patrick DM, et al. The delta isoform of CaM kinase II is required for pathological cardiac hypertrophy and remodeling after pressure overload. *Proc Natl Acad Sci U S A.* 2009;106(7):2342-7.

130. Kreusser MM, Lehmann LH, Keranov S, Hoting MO, Oehl U, Kohlhaas M, et al. Cardiac CaM Kinase II genes delta and gamma contribute to adverse remodeling but redundantly inhibit calcineurin-induced myocardial hypertrophy. *Circulation.* 2014;130(15):1262-73.

131. Heggermont WA, Papageorgiou AP, Quaegebeur A, Deckx S, Carai P, Verhesen W, et al. Inhibition of MicroRNA-146a and Overexpression of Its Target Dihydrolipoyl Succinyltransferase Protect Against Pressure Overload-Induced Cardiac Hypertrophy and Dysfunction. *Circulation.* 2017;136(8):747-61.

132. Fujikawa Y, Roma LP, Sobotta MC, Rose AJ, Diaz MB, Locatelli G, et al. Mouse redox histology using genetically encoded probes. *Science Signaling.* 2016;9(419):rs1-rs.

133. Mela L, and Seitz S. Isolation of mitochondria with emphasis on heart mitochondria from small amounts of tissue. *Methods Enzymol.* 1979;55:39-46.

134. Chappell JB, and Perry SV. Biochemical and osmotic properties of skeletal muscle mitochondria. *Nature.* 1954;173(4414):1094-5.
135. Wagner M, Bertero E, Nickel A, Kohlhaas M, Gibson GE, Heggermont W, et al. Selective NADH communication from alpha-ketoglutarate dehydrogenase to mitochondrial transhydrogenase prevents reactive oxygen species formation under reducing conditions in the heart. *Basic Res Cardiol.* 2020;115(5):53.
136. Nickel AG, Kohlhaas M, Bertero E, Wilhelm D, Wagner M, Sequeira V, et al. CaMKII does not control mitochondrial Ca(2+) uptake in cardiac myocytes. *J Physiol.* 2020;598(7):1361-76.
137. Bertero E, O'Rourke B, and Maack C. Mitochondria Do Not Survive Calcium Overload During Transplantation. *Circ Res.* 2020;126(6):784-6.
138. Chance B, and Williams GR. Respiratory enzymes in oxidative phosphorylation. III. The steady state. *J Biol Chem.* 1955;217(1):409-27.
139. Chance B, and Williams GR. Respiratory enzymes in oxidative phosphorylation. IV. The respiratory chain. *J Biol Chem.* 1955;217(1):429-38.
140. Chance B, and Williams GR. Respiratory enzymes in oxidative phosphorylation. II. Difference spectra. *J Biol Chem.* 1955;217(1):395-407.
141. Chance B, and Williams GR. A simple and rapid assay of oxidative phosphorylation. *Nature.* 1955;175(4469):1120-1.
142. McCully JD, Cowan DB, Emani SM, and Del Nido PJ. Mitochondrial transplantation: From animal models to clinical use in humans. *Mitochondrion.* 2017;34:127-34.
143. Bertero E, Maack C, and O'Rourke B. Mitochondrial transplantation in humans: "magical" cure or cause for concern? *J Clin Invest.* 2018;128(12):5191-4.
144. McCully JD, Emani SM, and Del Nido PJ. Response to Bertero, Maack and O’Rourke. *The Journal of clinical investigation.* 2018.
145. Zhang Q, Raoof M, Chen Y, Sumi Y, Sursal T, Junger W, et al. Circulating mitochondrial DAMPs cause inflammatory responses to injury. *Nature.* 2010;464(7285):104-7.
146. Vagnozzi RJ, Maillet M, Sargent MA, Khalil H, Johansen AK, Schwanekamp JA, et al. An acute immune response underlies the benefit of cardiac stem-cell therapy. *Nature.* 2019.
147. Münzel T, Camici GG, Maack C, Bonetti NR, Fuster V, and Kovacic JC. Impact of Oxidative Stress on the Heart and Vasculature: Part 2 of a 3-Part Series. *Journal of the American College of Cardiology.* 2017;70(2):212-29.
148. Nickel A, Kohlhaas M, and Maack C. Mitochondrial reactive oxygen species production and elimination. *Journal of molecular and cellular cardiology.* 2014;73:26-33.
149. Balaban RS. Cardiac energy metabolism homeostasis: role of cytosolic calcium. *J Mol Cell Cardiol.* 2002;34(10):1259-71.
150. Halestrap AP, and Richardson AP. The mitochondrial permeability transition: a current perspective on its identity and role in ischaemia/reperfusion injury. *Journal of molecular and cellular cardiology.* 2015;78:129-41.
151. De Stefani D, Raffaello A, Teardo E, Szabo I, and Rizzuto R. A forty-kilodalton protein of the inner membrane is the mitochondrial calcium uniporter. *Nature.* 2011;476(7360):336-40.
152. Baughman JM, Perocchi F, Girgis HS, Plovanich M, Belcher-Timme CA, Sancak Y, et al. Integrative genomics identifies MCU as an essential component of the mitochondrial calcium uniporter. *Nature.* 2011;476(7360):341-5.
153. Raffaello A, De Stefani D, Sabbadin D, Teardo E, Merli G, Picard A, et al. The mitochondrial calcium uniporter is a multimer that can include a dominant-negative pore-forming subunit. *The EMBO journal.* 2013;32(17):2362-76.
154. Sancak Y, Markhard AL, Kitami T, Kovacs-Bogdan E, Kamer KJ, Udeshi ND, et al. EMRE is an essential component of the mitochondrial calcium uniporter complex. *Science.* 2013;342(6164):1379-82.
155. Mallilankaraman K, Doonan P, Cardenas C, Chandramoorthy HC, Muller M, Miller R, et al. MICU1 is an essential gatekeeper for MCU-mediated mitochondrial Ca(2+) uptake that regulates cell survival. *Cell.* 2012;151(3):630-44.

156. Plovanich M, Bogorad RL, Sancak Y, Kamer KJ, Strittmatter L, Li AA, et al. MICU2, a paralog of MICU1, resides within the mitochondrial uniporter complex to regulate calcium handling. *PloS one.* 2013;8(2):e55785.
157. Payne R, Hoff H, Roskowski A, and Foskett JK. MICU2 Restricts Spatial Crosstalk between InsP3R and MCU Channels by Regulating Threshold and Gain of MICU1-Mediated Inhibition and Activation of MCU. *Cell reports.* 2017;21(11):3141-54.
158. Kohlhaas M, and Maack C. Calcium release microdomains and mitochondria. *Cardiovascular research.* 2013;98(2):259-68.
159. Beckendorf J, van den Hoogenhof MMG, and Backs J. Physiological and unappreciated roles of CaMKII in the heart. *Basic research in cardiology.* 2018;113(4):29.
160. Erickson JR, Joiner ML, Guan X, Kutschke W, Yang J, Oddis CV, et al. A dynamic pathway for calcium-independent activation of CaMKII by methionine oxidation. *Cell.* 2008;133(3):462-74.
161. Erickson JR, Nichols CB, Uchinoumi H, Stein ML, Bossuyt J, and Bers DM. S-Nitrosylation Induces Both Autonomous Activation and Inhibition of Calcium/Calmodulin-dependent Protein Kinase II delta. *The Journal of biological chemistry.* 2015;290(42):25646-56.
162. Erickson JR, Pereira L, Wang L, Han G, Ferguson A, Dao K, et al. Diabetic hyperglycaemia activates CaMKII and arrhythmias by O-linked glycosylation. *Nature.* 2013;502:372.
163. Tombes RM, Faison MO, and Turbeville JM. Organization and evolution of multifunctional Ca(2+)/CaM-dependent protein kinase genes. *Gene.* 2003;322:17-31.
164. Burgos JI, Yeves AM, Barrena JP, Portiansky EL, Vila-Petroff MG, and Ennis IL. Nitric oxide and CaMKII: Critical steps in the cardiac contractile response To IGF-1 and swim training. *Journal of molecular and cellular cardiology.* 2017;112:16-26.
165. Anderson ME, Brown JH, and Bers DM. CaMKII in myocardial hypertrophy and heart failure. *Journal of molecular and cellular cardiology.* 2011;51(4):468-73.
166. Backs J, Song K, Bezprozvannaya S, Chang S, and Olson EN. CaM kinase II selectively signals to histone deacetylase 4 during cardiomyocyte hypertrophy. *The Journal of clinical investigation.* 2006;116(7):1853-64.
167. Hohl M, Wagner M, Reil JC, Muller SA, Tauchnitz M, Zimmer AM, et al. HDAC4 controls histone methylation in response to elevated cardiac load. *The Journal of clinical investigation.* 2013;123(3):1359-70.
168. Zhu WZ, Wang SQ, Chakir K, Yang D, Zhang T, Brown JH, et al. Linkage of beta1-adrenergic stimulation to apoptotic heart cell death through protein kinase A-independent activation of Ca2+/calmodulin kinase II. *The Journal of clinical investigation.* 2003;111(5):617-25.
169. Little GH, Saw A, Bai Y, Dow J, Marjoram P, Simkhovich B, et al. Critical role of nuclear calcium/calmodulin-dependent protein kinase IIdeltaB in cardiomyocyte survival in cardiomyopathy. *The Journal of biological chemistry.* 2009;284(37):24857-68.
170. Zhang R, Khoo MS, Wu Y, Yang Y, Grueter CE, Ni G, et al. Calmodulin kinase II inhibition protects against structural heart disease. *Nature medicine.* 2005;11(4):409-17.
171. Joiner ML, Koval OM, Li J, He BJ, Allamargot C, Gao Z, et al. CaMKII determines mitochondrial stress responses in heart. *Nature.* 2012;491(7423):269-73.
172. Fieni F, Johnson DE, Hudmon A, and Kirichok Y. Mitochondrial Ca2+ uniporter and CaMKII in heart. *Nature.* 2014;513(7519):E1-2.
173. Grundy D. Principles and standards for reporting animal experiments in The Journal of Physiology and Experimental Physiology. *J Physiol.* 2015;593(12):2547-9.
174. Weinreuter M, Kreusser MM, Beckendorf J, Schreiter FC, Leuschner F, Lehmann LH, et al. CaM Kinase II mediates maladaptive post-infarct remodeling and pro-inflammatory chemoattractant signaling but not acute myocardial ischemia/reperfusion injury. *EMBO molecular medicine.* 2014;6(10):1231-45.

175. Kreusser MM, Lehmann LH, Wolf N, Keranov S, Jungmann A, Grone HJ, et al. Inducible cardiomyocyte-specific deletion of CaM kinase II protects from pressure overload-induced heart failure. *Basic research in cardiology.* 2016;111(6):65.
176. Kohlhaas M, Nickel AG, Bergem S, Casadei B, Laufs U, and Maack C. Endogenous nitric oxide formation in cardiac myocytes does not control respiration during beta-adrenergic stimulation. *J Physiol.* 2017;595(12):3781-98.
177. Aon MA, Cortassa S, Marban E, and O'Rourke B. Synchronized whole cell oscillations in mitochondrial metabolism triggered by a local release of reactive oxygen species in cardiac myocytes. *The Journal of biological chemistry.* 2003;278(45):44735-44.
178. Bernardi P, Rasola A, Forte M, and Lippe G. The Mitochondrial Permeability Transition Pore: Channel Formation by F-ATP Synthase, Integration in Signal Transduction, and Role in Pathophysiology. *Physiol Rev.* 2015;95(4):1111-55.
179. Ling H, Zhang T, Pereira L, Means CK, Cheng H, Gu Y, et al. Requirement for Ca2+/calmodulin-dependent kinase II in the transition from pressure overload-induced cardiac hypertrophy to heart failure in mice. *J Clin Invest.* 2009;119(5):1230-40.
180. Westenbrink BD, Ling H, Divakaruni AS, Gray CB, Zambon AC, Dalton ND, et al. Mitochondrial reprogramming induced by CaMKIIdelta mediates hypertrophy decompensation. *Circulation research.* 2015;116(5):e28-39.
181. Desai KH, Sato R, Schauble E, Barsh GS, Kobilka BK, and Bernstein D. Cardiovascular indexes in the mouse at rest and with exercise: new tools to study models of cardiac disease. *The American journal of physiology.* 1997;272(2 Pt 2):H1053-61.
182. Chapman CB, Fisher JN, and Sproule BJ. Behavior of stroke volume at rest and during exercise in human beings. *The Journal of clinical investigation.* 1960;39:1208-13.
183. Garcia-Rivas Gde J, Carvajal K, Correa F, and Zazueta C. Ru360, a specific mitochondrial calcium uptake inhibitor, improves cardiac post-ischaemic functional recovery in rats in vivo. *British journal of pharmacology.* 2006;149(7):829-37.
184. Kwong JQ, Lu X, Correll RN, Schwanekamp JA, Vagnozzi RJ, Sargent MA, et al. The Mitochondrial Calcium Uniporter Selectively Matches Metabolic Output to Acute Contractile Stress in the Heart. *Cell reports.* 2015;12(1):15-22.
185. Bertero E, and Maack C. Metabolic remodelling in heart failure. *Nat Rev Cardiol.* 2018.
186. Neubauer S, Horn M, Cramer M, Harre K, Newell JB, Peters W, et al. Myocardial phosphocreatine-to-ATP ratio is a predictor of mortality in patients with dilated cardiomyopathy. *Circulation.* 1997;96(7):2190-6.
187. Maack C, Kartes T, Kilter H, Schafers HJ, Nickenig G, Bohm M, et al. Oxygen free radical release in human failing myocardium is associated with increased activity of rac1-GTPase and represents a target for statin treatment. *Circulation.* 2003;108(13):1567-74.
188. Ide T, Tsutsui H, Kinugawa S, Utsumi H, Kang D, Hattori N, et al. Mitochondrial electron transport complex I is a potential source of oxygen free radicals in the failing myocardium. *Circulation research.* 1999;85(4):357-63.
189. Heymes C, Bendall JK, Ratajczak P, Cave AC, Samuel JL, Hasenfuss G, et al. Increased myocardial NADPH oxidase activity in human heart failure. *J Am Coll Cardiol.* 2003;41(12):2164-71.
190. Cappola TP, Kass DA, Nelson GS, Berger RD, Rosas GO, Kobeissi ZA, et al. Allopurinol improves myocardial efficiency in patients with idiopathic dilated cardiomyopathy. *Circulation.* 2001;104(20):2407-11.
191. Balaban RS, Nemoto S, and Finkel T. Mitochondria, oxidants, and aging. *Cell.* 2005;120(4):483-95.
192. Kirkman HN, Galiano S, and Gaetani GF. The function of catalase-bound NADPH. *The Journal of biological chemistry.* 1987;262(2):660-6.
193. Liu T, and O'Rourke B. Enhancing mitochondrial Ca2+ uptake in myocytes from failing hearts restores energy supply and demand matching. *Circulation research.* 2008;103(3):279-88.
194. Nickel AG, von Hardenberg A, Hohl M, Löffler JR, Kohlhaas M, Becker J, et al. Reversal of Mitochondrial Transhydrogenase Causes Oxidative Stress in Heart Failure. *Cell metabolism.* 2015;22(3):472-84.

195. Cooney GJ, Taegtmeyer H, and Newsholme EA. Tricarboxylic acid cycle flux and enzyme activities in the isolated working rat heart. *The Biochemical journal.* 1981;200(3):701-3.

196. Starkov AA, Fiskum G, Chinopoulos C, Lorenzo BJ, Browne SE, Patel MS, et al. Mitochondrial alpha-ketoglutarate dehydrogenase complex generates reactive oxygen species. *The Journal of neuroscience : the official journal of the Society for Neuroscience.* 2004;24(36):7779-88.

197. Tretter L, and Adam-Vizi V. Generation of reactive oxygen species in the reaction catalyzed by alpha-ketoglutarate dehydrogenase. *The Journal of neuroscience : the official journal of the Society for Neuroscience.* 2004;24(36):7771-8.

198. Tanaka N, Koike K, Hamada M, Otsuka KI, Suematsu T, and Koike M. Mammalian -keto acid dehydrogenase complexes. VII. Resolution and reconstitution of the pig heart 2-oxoglutarate dehydrogenase complex. *The Journal of biological chemistry.* 1972;247(12):4043-9.

199. Huennekens FM, Basford RE, and Gabrio BW. An oxidase for reduced diphosphopyridine nucleotide. *The Journal of biological chemistry.* 1955;213(2):951-67.

200. Starkov AA. An update on the role of mitochondrial alpha-ketoglutarate dehydrogenase in oxidative stress. *Mol Cell Neurosci.* 2013;55:13-6.

201. Lawlis VB, and Roche TE. Regulation of bovine kidney alpha-ketoglutarate dehydrogenase complex by calcium ion and adenine nucleotides. Effects on S0.5 for alpha-ketoglutarate. *Biochemistry.* 1981;20(9):2512-8.

202. Gardner PR, Nguyen DD, and White CW. Aconitase is a sensitive and critical target of oxygen poisoning in cultured mammalian cells and in rat lungs. *Proceedings of the National Academy of Sciences of the United States of America.* 1994;91(25):12248-52.

203. Ronchi JA, Francisco A, Passos LA, Figueira TR, and Castilho RF. The Contribution of Nicotinamide Nucleotide Transhydrogenase to Peroxide Detoxification Is Dependent on the Respiratory State and Counterbalanced by Other Sources of NADPH in Liver Mitochondria. *The Journal of biological chemistry.* 2016;291(38):20173-87.

204. Rydström J. Mitochondrial NADPH, transhydrogenase and disease. *Biochimica et Biophysica Acta (BBA) - Bioenergetics.* 2006;1757(5):721-6.

205. McMurray JJ, and Pfeffer MA. Heart failure. *Lancet.* 2005;365(9474):1877-89.

206. Ponikowski P, Voors AA, Anker SD, Bueno H, Cleland JGF, Coats AJS, et al. 2016 ESC Guidelines for the diagnosis and treatment of acute and chronic heart failure: The Task Force for the diagnosis and treatment of acute and chronic heart failure of the European Society of Cardiology (ESC)Developed with the special contribution of the Heart Failure Association (HFA) of the ESC. *Eur Heart J.* 2016;37(27):2129-200.

207. Brown DA, Hale SL, Baines CP, del Rio CL, Hamlin RL, Yueyama Y, et al. Reduction of early reperfusion injury with the mitochondria-targeting peptide bendavia. *Journal of cardiovascular pharmacology and therapeutics.* 2014;19(1):121-32.

208. Kloner RA, Hale SL, Dai W, Gorman RC, Shuto T, Koomalsingh KJ, et al. Reduction of ischemia/reperfusion injury with bendavia, a mitochondria-targeting cytoprotective Peptide. *Journal of the American Heart Association.* 2012;1(3):e001644.

209. Liu T, Takimoto E, Dimaano VL, DeMazumder D, Kettlewell S, Smith G, et al. Inhibiting mitochondrial Na+/Ca2+ exchange prevents sudden death in a Guinea pig model of heart failure. *Circulation research.* 2014;115(1):44-54.

210. Zhang M, Mileykovskaya E, and Dowhan W. Cardiolipin is essential for organization of complexes III and IV into a supercomplex in intact yeast mitochondria. *J Biol Chem.* 2005;280(33):29403-8.

211. Nickel A, Kohlhaas M, and Maack C. Mitochondrial reactive oxygen species production and elimination. *J Mol Cell Cardiol.* 2014;73C:26-33.

212. Saks V, Dzeja P, Schlattner U, Vendelin M, Terzic A, and Wallimann T. Cardiac system bioenergetics: metabolic basis of the Frank-Starling law. *The Journal of physiology.* 2006;571(Pt 2):253-73.

213. Cortassa S, Aon MA, Marbán E, Winslow RL, and O'Rourke B. An integrated model of cardiac mitochondrial energy metabolism and calcium dynamics. *Biophysical journal.* 2003;84(4):2734-55.
214. Kembro JM, Aon MA, Winslow RL, O'Rourke B, and Cortassa S. Integrating mitochondrial energetics, redox and ROS metabolic networks: a two-compartment model. *Biophysical journal.* 2013;104(2):332-43.
215. Dai DF, Johnson SC, Villarin JJ, Chin MT, Nieves-Cintrón M, Chen T, et al. Mitochondrial oxidative stress mediates angiotensin II-induced cardiac hypertrophy and Galphaq overexpression-induced heart failure. *Circ Res.* 2011;108(7):837-46.
216. Dey S, DeMazumder D, Sidor A, Foster DB, and O'Rourke B. Mitochondrial ROS Drive Sudden Cardiac Death and Chronic Proteome Remodeling in Heart Failure. *Circ Res.* 2018;123(3):356-71.
217. Dai DF, Hsieh EJ, Chen T, Menendez LG, Basisty NB, Tsai L, et al. Global proteomics and pathway analysis of pressure-overload-induced heart failure and its attenuation by mitochondrial-targeted peptides. *Circulation Heart failure.* 2013;6(5):1067-76.
218. Dai DF, Chen T, Szeto H, Nieves-Cintrón M, Kutyavin V, Santana LF, et al. Mitochondrial targeted antioxidant Peptide ameliorates hypertensive cardiomyopathy. *Journal of the American College of Cardiology.* 2011;58(1):73-82.
219. Sabbah HN, Gupta RC, Kohli S, Wang M, Hachem S, and Zhang K. Chronic Therapy With Elamipretide (MTP-131), a Novel Mitochondria-Targeting Peptide, Improves Left Ventricular and Mitochondrial Function in Dogs With Advanced Heart Failure. *Circulation Heart failure.* 2016;9(2):e002206.
220. Rigaud C, Lebre A-S, Touraine R, Beaupain B, Ottolenghi C, Chabli A, et al. Natural history of Barth syndrome: a national cohort study of 22 patients. *Orphanet journal of rare diseases.* 2013;8(1):70.
221. Kang S-L, Forsey J, Dudley D, Steward CG, and Tsai-Goodman B. Clinical Characteristics and Outcomes of Cardiomyopathy in Barth Syndrome: The UK Experience. *Pediatric Cardiology.* 2016;37(1):167-76.
222. Roberts AE, Nixon C, Steward CG, Gauvreau K, Maisenbacher M, Fletcher M, et al. The Barth Syndrome Registry: Distinguishing disease characteristics and growth data from a longitudinal study. *American Journal of Medical Genetics Part A.* 2012;158A(11):2726-32.
223. Spencer CT, Byrne BJ, Gewitz MH, Wechsler SB, Kao AC, Gerstenfeld EP, et al. Ventricular Arrhythmia in the X-linked Cardiomyopathy Barth Syndrome. *Pediatric Cardiology.* 2005;26(5):632-7.
224. Bers DM. *Excitation-contraction coupling and cardiac contractile force.* Dordrecht, The Netherlands: Kluwer Academic Publisher; 2001.
225. Brenner B. Effect of Ca2+ on cross-bridge turnover kinetics in skinned single rabbit psoas fibers: implications for regulation of muscle contraction. *Proceedings of the National Academy of Sciences of the United States of America.* 1988;85(9):3265-9.
226. Sequeira V, Najafi A, McConnell M, Fowler ED, Bollen IA, Wust RC, et al. Synergistic role of ADP and Ca(2+) in diastolic myocardial stiffness. *The Journal of physiology.* 2015;593(17):3899-916.
227. Pan X, Liu J, Nguyen T, Liu C, Sun J, Teng Y, et al. The physiological role of mitochondrial calcium revealed by mice lacking the mitochondrial calcium uniporter. *Nature cell biology.* 2013;15(12):1464-72.
228. Lambert JP, Luongo TS, Tomar D, Jadiya P, Gao E, Zhang X, et al. MCUB Regulates the Molecular Composition of the Mitochondrial Calcium Uniporter Channel to Limit Mitochondrial Calcium Overload During Stress. *Circulation.* 2019;140(21):1720-33.
229. Bashir A, Bohnert KL, Reeds DN, Peterson LR, Bittel AJ, de Las Fuentes L, et al. Impaired cardiac and skeletal muscle bioenergetics in children, adolescents, and young adults with Barth syndrome. *Physiol Rep.* 2017;5(3).
230. Williams GS, Boyman L, Chikando AC, Khairallah RJ, and Lederer WJ. Mitochondrial calcium uptake. *Proceedings of the National Academy of Sciences of the United States of America.* 2013;110(26):10479-86.

231. Fieni F, Lee SB, Jan YN, and Kirichok Y. Activity of the mitochondrial calcium uniporter varies greatly between tissues. *Nature communications.* 2012;3:1317.
232. Li Y, Lou W, Grevel A, Böttinger L, Liang Z, Ji J, et al. Cardiolipin-deficient cells have decreased levels of the iron-sulfur biogenesis protein frataxin. *J Biol Chem.* 2020;295(33):11928-37.
233. Patil VA, Fox JL, Gohil VM, Winge DR, and Greenberg ML. Loss of cardiolipin leads to perturbation of mitochondrial and cellular iron homeostasis. *J Biol Chem.* 2013;288(3):1696-705.
234. Nichols CG, and Lederer WJ. Adenosine triphosphate-sensitive potassium channels in the cardiovascular system. *American Journal of Physiology-Heart and Circulatory Physiology.* 1991;261(6):H1675-H86.
235. Sasaki N, Sato T, Marbán E, and O'Rourke B. ATP consumption by uncoupled mitochondria activates sarcolemmal K(ATP) channels in cardiac myocytes. *American journal of physiology Heart and circulatory physiology.* 2001;280(4):H1882-8.
236. Hiraoka M, Fan Z, Furukawa T, Nakayama K, and Sawanobori T. Activation and reactivation of the ATP-sensitive K+ channel of the heart can be modified by drugs. *Cardiovascular Drugs and Therapy.* 1993;7(3):593-8.
237. Liu Y, Ren G, O'Rourke B, Marbán E, and Seharaseyon J. Pharmacological comparison of native mitochondrial K(ATP) channels with molecularly defined surface K(ATP) channels. *Molecular pharmacology.* 2001;59(2):225-30.
238. Prosser BL, Ward CW, and Lederer WJ. X-ROS signaling: rapid mechano-chemo transduction in heart. *Science.* 2011;333(6048):1440-5.
239. Helmes M, Najafi A, Palmer BM, Breel E, Rijnveld N, Iannuzzi D, et al. Mimicking the cardiac cycle in intact cardiomyocytes using diastolic and systolic force clamps; measuring power output. *Cardiovascular Research.* 2016;111(1):66-73.
240. Bers DM, Bassani RA, Bassani JW, Baudet S, and Hryshko LV. Paradoxical twitch potentiation after rest in cardiac muscle: increased fractional release of SR calcium. *J Mol Cell Cardiol.* 1993;25(9):1047-57.
241. Thompson WR, DeCroes B, McClellan R, Rubens J, Vaz FM, Kristaponis K, et al. New targets for monitoring and therapy in Barth syndrome. *Genetics in Medicine.* 2016;18(10):1001-10.
242. Abudiab MM, Redfield MM, Melenovsky V, Olson TP, Kass DA, Johnson BD, et al. Cardiac output response to exercise in relation to metabolic demand in heart failure with preserved ejection fraction. *Eur J Heart Fail.* 2013;15(7):776-85.
243. Borlaug BA, Melenovsky V, Russell SD, Kessler K, Pacak K, Becker LC, et al. Impaired chronotropic and vasodilator reserves limit exercise capacity in patients with heart failure and a preserved ejection fraction. *Circulation.* 2006;114(20):2138-47.
244. Kraigher-Krainer E, Shah AM, Gupta DK, Santos A, Claggett B, Pieske B, et al. Impaired systolic function by strain imaging in heart failure with preserved ejection fraction. *Journal of the American College of Cardiology.* 2014;63(5):447-56.
245. Ferreira C, Thompson R, and Vernon H. In: Adam MP, Ardinger HH, Pagon RA, Wallace SE, Bean LJH, Stephens K, et al. eds. *GeneReviews((R)).* Seattle (WA); 2014.
246. Watkins H, Ashrafian H, and Redwood C. Inherited cardiomyopathies. *The New England journal of medicine.* 2011;364(17):1643-56.
247. Piacentino V, Weber CR, Chen X, Weisser-Thomas J, Margulies KB, Bers DM, et al. Cellular Basis of Abnormal Calcium Transients of Failing Human Ventricular Myocytes. *Circulation Research.* 2003;92(6):651-8.
248. Braun JL, Hamstra SI, Messner HN, and Fajardo VA. SERCA2a tyrosine nitration coincides with impairments in maximal SERCA activity in left ventricles from tafazzin-deficient mice. *Physiol Rep.* 2019;7(16):e14215.
249. Ghosh S, Basu Ball W, Madaris TR, Srikantan S, Madesh M, Mootha VK, et al. An essential role for cardiolipin in the stability and function of the mitochondrial calcium uniporter. *Proceedings of the National Academy of Sciences of the United States of America.* 2020;117(28):16383-90.

250. Bertero E, Nickel A, Kohlhaas M, Hohl M, Krug C, Mueller A, et al. Downregulation of the mitochondrial calcium uniporter hinders cardiac energy supply-and-demand matching in Barth syndrome. *Eur J Heart Fail* 2018;20:518-.
251. Goncalves RLS, Schlame M, Bartelt A, Brand MD, and Hotamışlıgil GS. Cardiolipin deficiency in Barth syndrome is not associated with increased superoxide/H(2) O(2) production in heart and skeletal muscle mitochondria. *FEBS Lett.* 2020.
252. Saric A, Andreau K, Armand AS, Møller IM, and Petit PX. Barth Syndrome: From Mitochondrial Dysfunctions Associated with Aberrant Production of Reactive Oxygen Species to Pluripotent Stem Cell Studies. *Frontiers in genetics.* 2015;6:359.
253. Nikolaienko R, Bovo E, and Zima AV. Redox Dependent Modifications of Ryanodine Receptor: Basic Mechanisms and Implications in Heart Diseases. *Frontiers in physiology.* 2018;9(1775).
254. Denton RM, and McCormack JG. Ca2+ transport by mammalian mitochondria and its role in hormone action. *The American journal of physiology.* 1985;249(6 Pt 1):E543-54.
255. Taivassalo T, Dysgaard Jensen T, Kennaway N, DiMauro S, Vissing J, and Haller RG. The spectrum of exercise tolerance in mitochondrial myopathies: a study of 40 patients. *Brain.* 2003;126(2):413-23.
256. Liu T, Brown DA, and O'Rourke B. Role of mitochondrial dysfunction in cardiac glycoside toxicity. *J Mol Cell Cardiol.* 2010;49(5):728-36.
257. Green EM, Wakimoto H, Anderson RL, Evanchik MJ, Gorham JM, Harrison BC, et al. A small-molecule inhibitor of sarcomere contractility suppresses hypertrophic cardiomyopathy in mice. *Science.* 2016;351(6273):617-21.
258. Baartscheer A, Schumacher CA, Wüst RC, Fiolet JW, Stienen GJ, Coronel R, et al. Empagliflozin decreases myocardial cytoplasmic Na(+) through inhibition of the cardiac Na(+)/H(+) exchanger in rats and rabbits. *Diabetologia.* 2017;60(3):568-73.
259. Streckfuss-Bomeke K, Wolf F, Azizian A, Stauske M, Tiburcy M, Wagner S, et al. Comparative study of human-induced pluripotent stem cells derived from bone marrow cells, hair keratinocytes, and skin fibroblasts. *Eur Heart J.* 2013;34(33):2618-29.
260. Lian X, Zhang J, Azarin SM, Zhu K, Hazeltine LB, Bao X, et al. Directed cardiomyocyte differentiation from human pluripotent stem cells by modulating Wnt/beta-catenin signaling under fully defined conditions. *Nature protocols.* 2013;8(1):162-75.
261. Tohyama S, Hattori F, Sano M, Hishiki T, Nagahata Y, Matsuura T, et al. Distinct metabolic flow enables large-scale purification of mouse and human pluripotent stem cell-derived cardiomyocytes. *Cell Stem Cell.* 2013;12(1):127-37.
262. Ryan MT, Voos W, and Pfanner N. Assaying protein import into mitochondria. *Methods Cell Biol.* 2001;65:189-215.
263. Heiberg E, Sjogren J, Ugander M, Carlsson M, Engblom H, and Arheden H. Design and validation of Segment--freely available software for cardiovascular image analysis. *BMC medical imaging.* 2010;10:1.
264. Seeland U, Selejan S, Engelhardt S, Muller P, Lohse MJ, and Bohm M. Interstitial remodeling in beta1-adrenergic receptor transgenic mice. *Basic Res Cardiol.* 2007;102(2):183-93.
265. Haworth RA, and Hunter DR. The Ca2+-induced membrane transition in mitochondria: II. Nature of the Ca2+ trigger site. *Archives of Biochemistry and Biophysics.* 1979;195(2):460-7.
266. Bernardi P, Rasola A, Forte M, and Lippe G. The Mitochondrial Permeability Transition Pore: Channel Formation by F-ATP Synthase, Integration in Signal Transduction, and Role in Pathophysiology. *Physiological Reviews.* 2015;95(4):1111-55.
267. Bernardi P. Mitochondrial Transport of Cations: Channels, Exchangers, and Permeability Transition. *Physiological Reviews.* 1999;79(4):1127-55.